







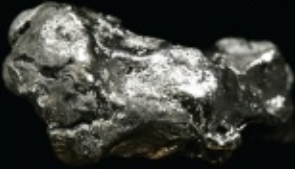
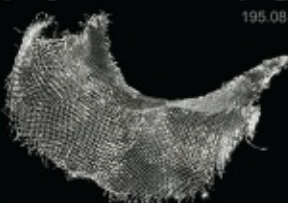

Конденсированные среды и межфазные границы

РЕЦЕНЗИРУЕМЫЙ НАУЧНЫЙ ЖУРНАЛ

Condensed Matter and Interphases

PEER-REVIEWED SCIENTIFIC JOURNAL

Том 26, № 3
Vol. 26, No. 3
2024

<p>Co 27 58.933</p>  <p>Cobalt</p>	<p>Ni 28 58.693</p>  <p>Nickel</p>	<p>Cu 29 63.546</p>  <p>Copper</p>
<p>Rh 45 102.91</p>  <p>Rhodium</p>	<p>Pd 46 106.42</p>  <p>Palladium</p>	<p>Ag 47 107.87</p>  <p>Silver</p>
<p>Ir 77 192.22</p>  <p>Iridium</p>	<p>Pt 78 195.08</p>  <p>Platinum</p>	<p>Au 79 196.97</p>  <p>Gold</p>

Condensed Matter and Interphases

Kondensirovannye sredy i mezhfaznye granitsy

Peer-reviewed scientific journal

Published since January 1999

Periodicity: Quarterly

Volume 26, No. 3, 2024

Full-text version is available in the Russian language on the website: <https://journals.vsu.ru/kcmf>

Condensed Matter and Interphases (Kondensirovannye Sredy i Mezhfaznye Granitsy) publishes articles in Russian and English dedicated to key issues of condensed matter and physicochemical processes at interfaces and in volumes.

The mission of the journal is to provide open access to the results of original research (theoretical and experimental) at the intersection of contemporary condensed matter physics and chemistry, material science and nanoindustry, solid state chemistry, inorganic chemistry, and physical chemistry, and to share scientific data in the **following sections**: atomic, electron, and cluster structure of solids, liquids, and interphase boundaries; phase equilibria and defect formation processes; structure and physical and chemical properties of interphases; laser thermochemistry and photostimulated processes on solid surfaces; physics and chemistry of surface, thin films and heterostructures; kinetics and mechanism of formation of film structures; electrophysical processes in interphase boundaries; chemistry of surface phenomena in sorbents; devices and new research methods.

The journal accepts for publication: reviews, original articles, short communications by leading Russian scientists, foreign researchers, lecturers, postgraduate and undergraduate students.

FOUNDER AND PUBLISHER:

Voronezh State University

The journal is registered by the Russian Federal Service for Supervision of Communications, Information Technology and Mass Media, Certificate of Registration ПИ № ФС77-78771 date 20.07.2020

The journal is included in the List of peer reviewed scientific journals published by the Higher Attestation Commission in which major research results from the dissertations of Candidates of Sciences (PhD) and Doctor of Science (DSc) degrees are to be published. Scientific specialties of dissertations and their respective branches of science are as follows: 1.4.1. – Inorganic Chemistry (Chemical sciences); 1.4.4. – Physical Chemistry (Chemical sciences); 1.4.6. – Electrochemistry (Chemical sciences); 1.4.15. – Solid State Chemistry (Chemical sciences); 1.3.8. – Condensed Matter Physics (Physical sciences).

The journal is indexed and archived in: Russian Scientific Index Citations, Scopus, Chemical Abstract, EBSCO, DOAJ, CrossRef

Editorial Board and Publisher Office:
1 Universitetskaya pl., Voronezh 394018
Phone: +7 (432) 2208445
<https://journals.vsu.ru/kcmf>
E-mail: kcmf@main.vsu.ru

When reprinting the materials, a reference to the Condensed Matter and Interphases must be cited

The journal's materials are available under the Creative Commons "Attribution" 4.0 Global License



© Voronezh State University, 2024

EDITOR-IN-CHIEF:

Victor N. Semenov, Dr. Sci. (Chem.), Full Professor, Voronezh State University, (Voronezh, Russian Federation)

VICE EDITORS-IN-CHIEF:

Evelina P. Domashevskaya, Dr. Sci. (Phys.–Math.), Full Professor, Voronezh State University, (Voronezh, Russian Federation)

Polina M. Volovitch, Ph.D. (Chem.), Associate Professor, Institut de Recherche de Chimie (Paris, France)

EDITORIAL BOARD:

Nikolay N. Afonin, Dr. Sci. (Chem.), Voronezh State Pedagogical University (Voronezh, Russian Federation)

Vera I. Vasil'eva, Dr. Sci. (Chem.), Full Professor, Voronezh State University, (Voronezh, Russian Federation)

Aleksandr V. Vvedenskii, Dr. Sci. (Chem.), Full Professor, Voronezh State University, (Voronezh, Russian Federation)

Victor V. Gusarov, Dr. Sci. (Chem.), Associate Member of the RAS, Ioffe Physical-Technical Institute RAS (St. Petersburg, Russian Federation)

Vladimir E. Guterman, Dr. Sci. (Chem.), Full Professor, Southern Federal University (Rostov-on-Don, Russian Federation)

Boris M. Darinskii, Dr. Sci. (Phys.–Math.), Full Professor, Voronezh State University, (Voronezh, Russian Federation)

Vladimir P. Zlomanov, Dr. Sci. (Chem.), Full Professor, Moscow State University, (Moscow, Russian Federation)

Valentin M. Levlev, Dr. Sci. (Phys.–Math.), Full Member of the RAS, Moscow State University, (Moscow, Russian Federation)

Oleg A. Kozaderov, Dr. Sci. (Chem.), Associate Professor, Voronezh State University, (Voronezh, Russian Federation)

Andrey I. Marshakov, Dr. Sci. (Chem.), Full Professor, Frumkin Institute of Physical Chemistry and Electrochemistry RAS (Moscow, Russian Federation)

Irina Ya. Mittova, Dr. Sci. (Chem.), Full Professor, Voronezh State University, (Voronezh, Russian Federation)

Victor V. Nikonenko, Dr. Sci. (Chem.), Full Professor, Kuban State University (Krasnodar, Russian Federation)

Oleg V. Ovchinnikov, Dr. Sci. (Phys.–Math.), Full Professor, Voronezh State University, (Voronezh, Russian Federation)

Sergey N. Saltykov, Dr. Sci. (Chem.), Associate Professor, Novolipetsk Steel (Lipetsk, Russian Federation)

Vladimir F. Selemenev, Dr. Sci. (Chem.), Full Professor, Voronezh State University, (Voronezh, Russian Federation)

Vladimir A. Terekhov, Dr. Sci. (Phys.–Math.), Full Professor, Voronezh State University, (Voronezh, Russian Federation)

Evgeny A. Tutov, Dr. Sci. (Chem.), Associate Professor, Voronezh State Technical University (Voronezh, Russian Federation)

Pavel P. Fedorov, Dr. Sci. (Chem.), Full Professor, Prokhorov General Physics Institute RAS (Moscow, Russian Federation)

Vitaly A. Khonik, Dr. Sci. (Phys.–Math.), Full Professor, Voronezh State Pedagogical University (Voronezh, Russian Federation)

Andrey B. Yaroslavtsev, Dr. Sci. (Chem.), Full Member of the RAS, Kurnakov Institute of General and Inorganic Chemistry RAS (Moscow, Russian Federation)

INTERNATIONAL MEMBERS OF THE EDITORIAL BOARD:

Mahammad Babanly, Dr. Sci. (Chem.), Associate Member of the ANAS, Institute of Catalysis and Inorganic Chemistry ANAS (Baku, Azerbaijan)

Tiziano Bellezze, Dr. Sci. (Chem.), Marche Polytechnic University (Ancona, Italy)

Mane Rahul Maruti, Ph.D. (Chem.), Shivaji University (Kolhapur, India)

Nguyen Anh Tien, Ph.D. (Chem.), Associate Professor, University of Pedagogy (Ho Chi Minh City, Vietnam)

Vladimir V. Pankov, Dr. Sci. (Chem.), Full Professor, Belarusian State University (Minsk, Belarus)

Fritz Scholz, Dr. Sci., Professor, Institut für Biochemie Analytische Chemie und Umweltchemie (Greifswald, Germany)

Mathias S. Wickleder, Dr. Sci., Professor, University of Cologne (Cologne, Germany)

Vladimir Sivakov, Dr. rer. nat., Leibniz Institute of Photonic Technology (Jena, Germany)

EXECUTIVE SECRETARY:

Vera A. Logacheva, Cand. Sci. (Chem.), Voronezh State University, (Voronezh, Russian Federation)

CONTENTS

Original articles

- Azeez Y. H., Othman K. A., Omer R. A., Qader A. F.
Probing molecular interactions, electronic properties, and reactivity of monoamine neurotransmitters in different protonation states via quantum chemical investigation 379
- Barkov K. A., Terekhov V. A., Nesterov D. N., Velichko K. E., Ivkov S. A., Buylov N. S., Kannykin S. V., Zanin I. E., Agapov B. V., Rodivilov S. V., Kersnovsky E. S., Polshin I. V., Ryabtsev S. V., Grechkina M. V., Sitnikov A. V.
Formation of silver nanocrystals in Ag-Si composite films obtained by ion beam sputtering 407
- Vasilkova E. I., Pirogov E. V., Shubina K. Yu., Voropaev K. O., Vasil'ev A. A., Karachinsky L. Ya., Novikov I. I., Barantsev O. V., Sobolev M. S.
Electrophysical properties of PIN photodiodes of the 2.2-2.6 μm range based on InGa(Al)As/InP heterostructures with a metamorphic buffer layer 417
- Grevtseva I. G., Ovchinnikov O. V., Smirnov M. S., Aslanov S. V., Latyshev A. N., Astashkina M. S.
Effect of plasmonic Au nanoparticles on IR luminescence of Ag₂S quantum dots 424
- Zvyagin A. I., Chevychelova T. A., Smirnov M. S., Ovchinnikov O. V., Latyshev A. N.
Formation of hybrid nanostructures based on Zn_{0.5}Cd_{0.5}S quantum dots and silver nanoparticles for nonlinear optical applications in the near ultraviolet 431
- Ismailov A. M., Muslimov A. E.
Formation of smooth and microporous ZnO-based substrate material 440
- Karpenko T. V., Shramenko V. V., Sheldeshov N. V.
Influence of the nature of the organic acid salt on the current-voltage characteristics and electrochemical impedance spectra of anion-exchange membranes 447
- Meshcheryakova A. A., Tomina E. V., Titov S. A., Nguyen Anh Tien, Dmitrenkov A. I.
Synthesis of nanoscale nickel (II) ferrite and a study of its catalytic and sorption activities towards methyl orange 456
- Minakova T. A., Kaluzhina S. A., Akseyonova E. N.
Features of the local activation of aluminum in the presence of bicarbonate ions 464
- Morozova N. B., Dontsov A. I., Pogorelova D. A., Dubovitskaya T. V.
The effect of the chemical compositions of palladium alloys on their hydrogen permeability 474
- Morozova N. B., Dontsov A. I., Khmelevskaya T. N.
Mechanical properties and catalytic activity of the Cu-36Pd (at. %) alloy foil surface after cleaning 483
- Nikitina E. V., Sobolev M. S., Pirogov E. V., Makhov I. S., Nadtochiy A. M., Vasilkova E. I., Kryzhanovskaya N. V.
Photoluminescence of GaPNAs/GaP(N) superlattices and bulk GaPN layers on GaP substrates 490
- Polkovnikova Yu. A., Belal M., Slivkin A. I.
A molecular dynamics simulation of the release of desloratadine from alloys containing polyvinylpyrrolidone 496
- Pospelov A. V., Kasach A. A., Tsyganov A. R., Kurilo I. I.
Preparation and properties of conversion phosphate-containing coatings on magnesium alloys doped with rare earth elements 504
- Seredin P. V., Sharofidinov Sh. Sh., Goloshchapov D. L., Buylov N. S., Ereemeev K. A., Yusupova S. A., Kukushkin S. A.
Residual strain evaluation in GaN/AlN multiperiod superlattices grown on SiC/Si 518
- Seredin P. V., Goloshchapov D. L., Kostomakha D. E., Peshkov Y. A., Buylov N. S., Gaivoronskaya A. A., Mizerov A. M., Timoshnev S. N., Sobolev M. S., Ubyivovk E. V., Zemlyakov V. I., Kutsko P. P., Parmon P. L.
Structural and spectroscopic studies of epitaxially overgrown GaN, n-GaN, and n⁺-GaN contact layers 526
- Yakimchuk M. A., Eliseeva E. S., Kostryukov V. F.
Nanocrystalline films based on YCrO₃ and LaCrO₃ yttrium and lanthanum chromites doped with strontium ions Sr²⁺ as a basis for semiconductor gas sensors 536
- Yakupov R. P., Buzko V. Yu., Ivanin S. N., Papezhuk M. V.
Preparation of composite micro-nanofibers based on nano-sized magnetite by electrospinning 547
- Chuvenkova O. A., Boikov N. I., Ryabtsev S. V., Parinova E. V., Chumakov R. G., Lebedev A. M., Smirnov D., Makarova A., Titova S. S., Fateev K. A., Turishchev S. Yu.
XPS investigations of thin epitaxial and magnetron tin layers surface physico-chemical state 558



Original articles

Research article

<https://doi.org/10.17308/kcmf.2024.26/12214>

Probing molecular interactions, electronic properties, and reactivity of monoamine neurotransmitters in different protonation states via quantum chemical investigation

Y. H. Azeez¹, K. A. Othman², R. A. Omer^{2,3}, A. F. Qader^{2✉}¹University of Halabja, College of Science, Department of Physics, Halabja, Iraq²Department of Chemistry, Faculty of Science and Health, Koya University, Danielle Mitterrand Boulevard, Koya KOY45, Kurdistan Region – F.R., Iraq³Knowledge University, College of Pharmacy, Department of Pharmacy, Erbil 44001, Iraq

Abstract

Amphetamine, dopamine, norepinephrine, serotonin, and tryptamine are a group of monoamine neurotransmitters that regulate diverse brain functions. This work examined these compounds' neutral, protonated, and deprotonated, structural, energetic, and optical properties using quantum chemistry methods. Noncovalent interactions (NCI) and reduced density gradient (RDG) investigations revealed weak intermolecular forces and electron density distribution. The RDG values were observed to span from 0.12 to 0.43, indicating varying degrees of repulsion or attraction. The hydrogen bonding patterns and their strength and nature were also investigated using the Atoms in Molecules (AIM) and B3LYP methods. The quantification was done using $\nabla^2 \rho(r)$, $H(r)$, and energy density values, which showed a variation from -0.014 to 0.026 Hartree/Bohr³, reflecting covalent or electrostatic interactions. A comparison was made between the compounds based on their physical and chemical attributes, such as polar surface area (ranging from 41.81 to 86.71 Å²), rotatable bonds (which were identical), and proton affinity (a measure of stability). Lewis structures and natural bond orbital (NBO) analysis showed resonance and electron delocalization. The study also examined their molecular orbitals (MOs) and found that protonation and deprotonation could significantly change their electronic characteristics, including the energies of the highest occupied (HOMO) and lowest unoccupied (LUMO), the energy gap, and the shape and size of their lobes. The nonlinear optical properties were also assessed, affected by polarizability and hyperpolarizability indices, ranging from 2.267 a.u. (Dopamine) to 7.891 a.u. (Protonated Serotonin). These properties pointed to the applications of these compounds in optical devices.

Keywords: Quantum chemistry, Molecular interactions, Monoamine neurotransmitters, electronic properties, and Protonation states

Acknowledgments: We would like to thank the heads of the chemistry departments at Koya University for their support.

For citation: Azeez Y. H., Othman Kh. A., Omer R. A., Qader A. F. Probing molecular interactions, electronic properties, and reactivity of monoamine neurotransmitters in different protonation states via quantum chemical investigation. *Condensed Matter and Interphases*. 2024;26(3): 379–406. <https://doi.org/10.17308/kcmf.2024.26/12214>

Для цитирования: Азиз Ю. Х., Осман Х. А., Омер Р. А., Кадер А. Ф. Квантово-химическое исследование молекулярных взаимодействий, электронных свойств и реакционной способности моноаминных нейромедиаторов в различных состояниях протонирования. *Конденсированные среды и межфазные границы*. 2024;26(3): 379–406. <https://doi.org/10.17308/kcmf.2024.26/12214>

✉ Aryan F. Qader, aryan.qader@koyauniversity.org

© Azeez Y. H., Othman Kh. A., Omer R. A., Qader A. F., 2024



The content is available under Creative Commons Attribution 4.0 License.

1. Introduction

Amphetamines, a class of psychoactive compounds, exert profound effects on the central nervous system. Notably, amphetamine, a potent stimulant, triggers the release of key neurotransmitters-dopamine, norepinephrine, and serotonin-crucial for mood, attention, and physiological processes. Dopamine relates to pleasure, norepinephrine to alertness, and serotonin to emotional well-being. Tryptamine, a fundamental neurotransmitter component, underscores their interconnected role in cognition and sensation, affecting normal brain function and psychoactive substance effects [1–5]. Noncovalent interactions (NCIs), encompassing weak molecular forces, hold vast significance across chemistry, biology, and material science, notably in drug discovery for optimized interactions [6]. Recent strides in methodologies like Reduced Density Gradient (RDG) analysis and Noncovalent Interaction (NCI) indices are pivotal for deciphering these interactions and enhancing tailored drug-target binding for therapeutic efficacy. The Reduced Density Gradient (RDG) method, rooted in electron density, unveils spatial distribution insights for Non-covalent interactions like hydrogen bonds and van der Waals forces, refining drug binding and selectivity. This study employs RDG and NCI methods to explore Non-covalent interactions, spotlighting their role in drug design. Objectives encompass characterizing interactions, assessing protonation effects, and examining resulting molecular properties, promising refined drug design for potent therapeutic agents [7–9]. The investigation extends to topological parameters via the Atoms in Molecules (AIM) approach, vital for understanding drug-receptor interactions and enhancing binding affinity [10, 11]. By utilizing advanced computational techniques, including Density Functional Theory (DFT), this study uncovers the distribution of attractive/repulsive forces depicted through RDG scatter plots and topological parameters [12]. The exploration also delves into nonlinear optical properties (NLO) and quantum parameters, offering multifaceted insights [13, 14].

This study delves into the intricate world of molecular interactions, bridging neurochemistry and computational chemistry to advance

our comprehension of the human mind and pharmaceutical development.

2. Computational Details

In this study, the computational investigations were conducted using the Gaussian software package, a prominent suite of quantum chemistry tools [15–17]. The Density Functional Theory (DFT) calculations used the accurate 6-31G(d,p) and 6-311++G(d,p) basis sets, enabling a precise exploration of molecular interactions, electron densities, and energy profiles. These aspects are crucial for optimizing drug-receptor binding and enhancing the understanding of non-covalent interactions [18–20].

3. Results and discussion

3.1. RDG and NCI Analysis

Noncovalent interactions (NCI) and reduced density gradient (RDG) studies are novel methodologies used for the characterization of weak intermolecular interactions [55–58]. The NCI index is used for characterizing intermolecular interactions and evaluating the characteristics of weak interactions. The NCI index is derived from the reduced density gradient (RDG) and provides further support for non-covalent interactions. The reduced density gradient (RDG) is a fundamental dimensionless quantity that includes the density and its initial derivative. The colorful RDG scatter plots were produced using the Multiwfn program, whereas the 3D isosurface was shown employing the VMD software [21, 22]. The NCI studies were conducted using an isosurface threshold of 0.5. The isosurface range for the Reduced Density Gradient (RDG) extends from -0.035 to 0.02 atomic units. Fig. 1 displays the two-dimensional representation of the reaction-diffusion grid (RDG) plots, as well as the three-dimensional isosurface.

The determination of the electron density of the $\text{sign}(\lambda_2)\rho$ peaks concerning RDG provides valuable insights into the characteristics and intensity of the molecular interactions. Within the molecular system, the color blue shows attractive interactions, whereas the colour red signifies repulsive interactions. The sign of the product between the sign of λ_2 and the charge $\rho(r)$ is crucial in determining the characteristics of the interaction. Specifically, when the sign of λ_2

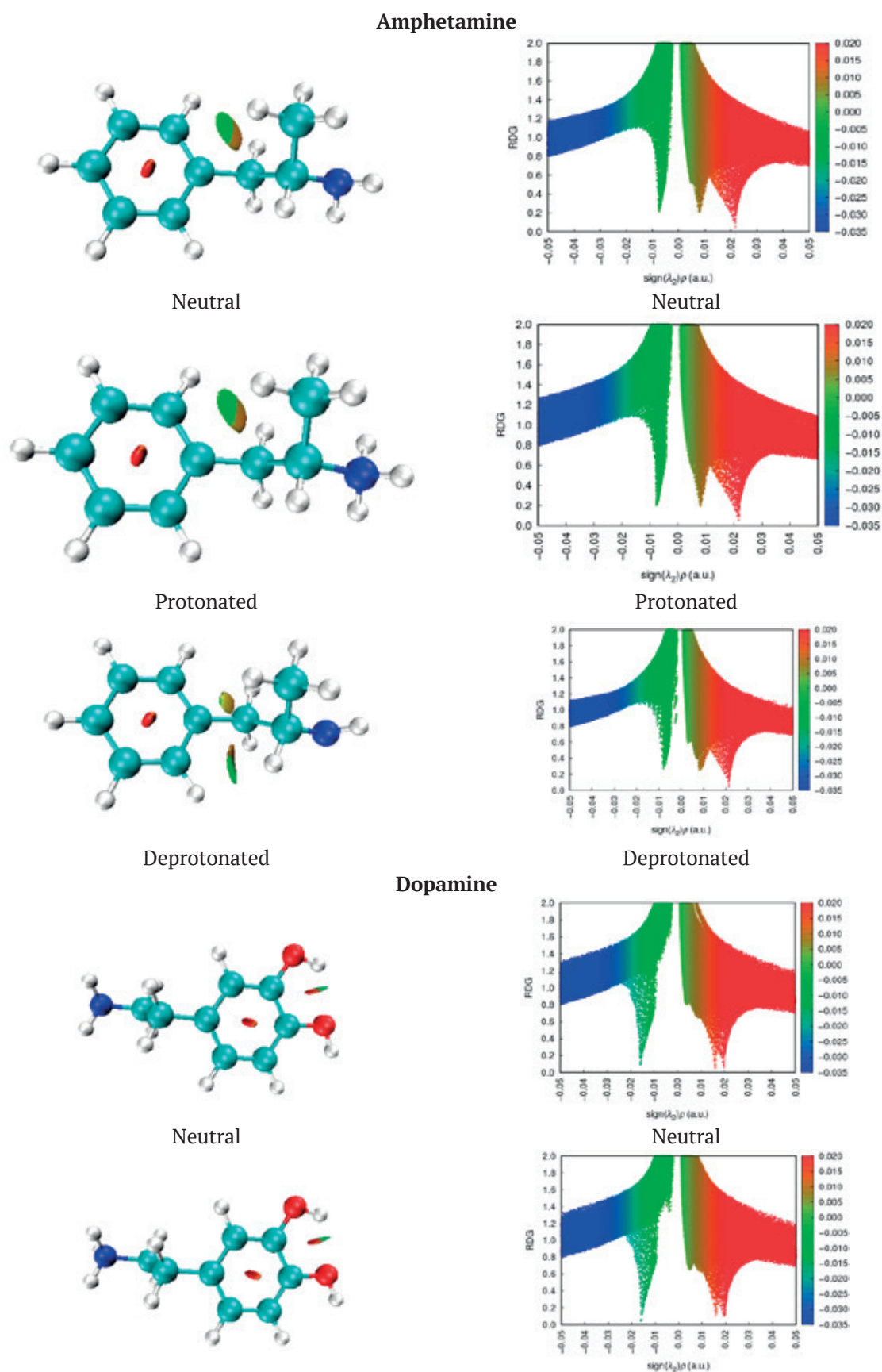


Fig. 1. Reduced Density Gradient (RDG) analysis showing weak and strong interaction of all compounds

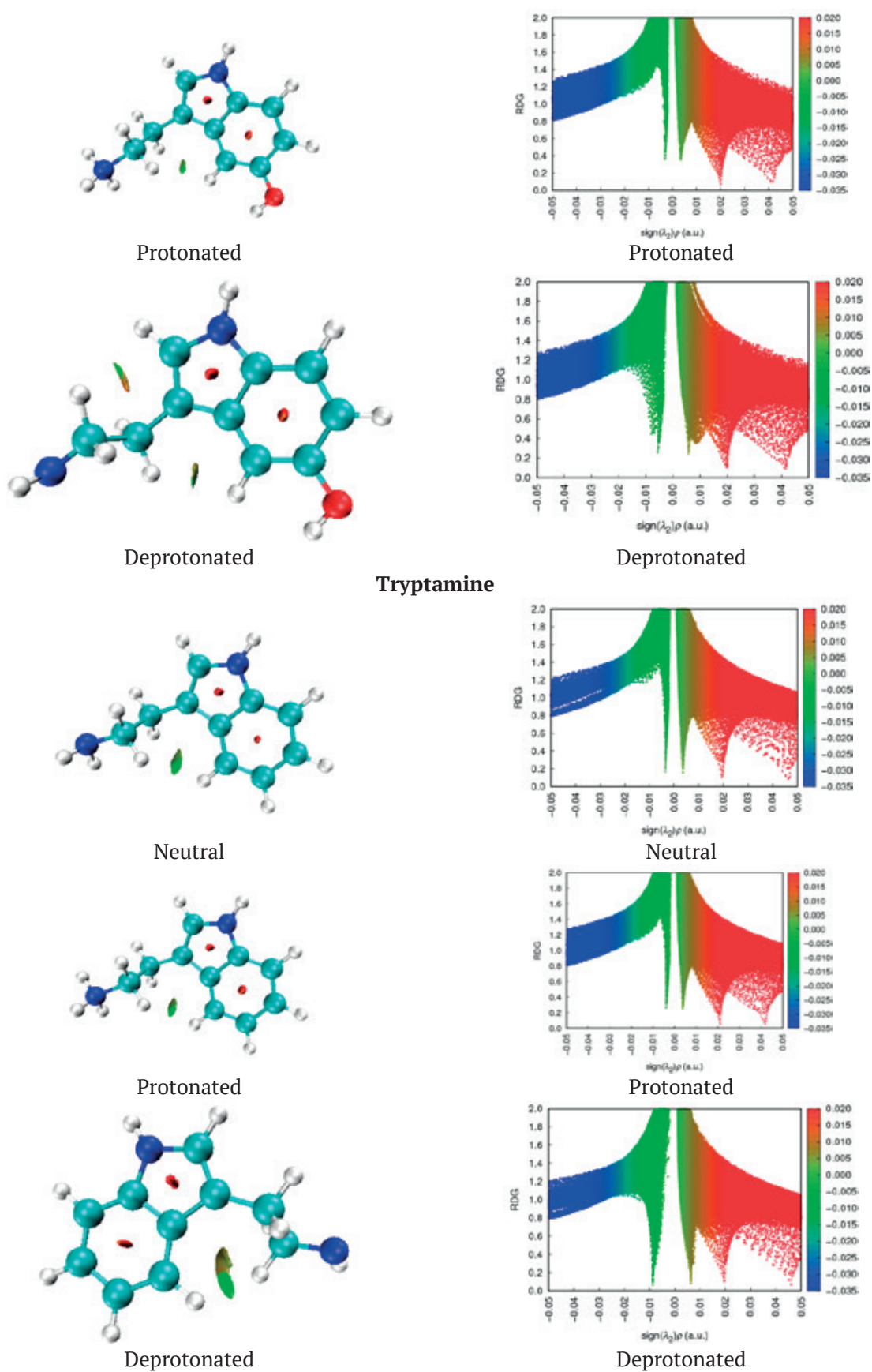


Fig. 1.

$\rho(r)$ is negative, it signifies a repulsive interaction that is bonded. Conversely, when the sign (λ_2) ρ is positive, along with the corresponding symbol, it shows a repulsive interaction that is non-bonded.

The scatter graphs of the RDG complexes are shown on the right side of Fig. 1. As seen on the left side of Fig. 1, the color red is assigned to denote strong repulsion resulting from steric effects, blue is used to show hydrogen bonding interactions, and green is employed to signify van der Waals interactions [23, 24]. As seen on the left side of Fig. 1, the blue coloration signifies the occurrence of hydrogen bonding. The green coloration correlates to van der Waals interactions, while the red coloration shows steric or cyclic effects. It is observed that all deprotonated compounds possess a low density and have a limited hydrogen interaction. Conversely, all protonated compounds show a larger density and display hydrogen bond interactions.

Serotonin and tryptamine have a pronounced repulsive behavior compared to other compounds, as seen by their red color in Fig. 1. The existence of a weak hydrogen bond interaction, together with additional contacts between the two hydrogen atoms (H–H), is shown by the observation of a green-colored isosurface for the serotonin and tryptamine complex. This green-colored isosurface may be attributed to van der Waals interactions. The identification of this isosurface position suggests the existence of van der Waals interactions.

3.2. Topological parameters

Using the atoms in molecules (AIM) analysis is a widely used approach for the detection and characterization of non-covalent interactions present in molecular systems, particularly emphasizing intra- and intermolecular hydrogen bonding. The determination of hydrogen bonds in molecular complexes is accomplished by conducting a thorough examination of electron density using topological techniques [25–28]. The B3LYP [29, 30] technique was used to calculate the topological characteristics, such as the Laplacian of electron density and the electron density, potential energy density, and ellipticity at bond critical sites (BCP). The computations have been succinctly presented in Table 1, while Fig. 2 provides a visual representation of the BCP.

Based on the findings presented in reference [27], the quantification of hydrogen bond interaction can be determined using the following criteria: weak hydrogen bonding is shown when the second derivative of the electron density regarding the distance is positive and the value of the Hamiltonian ($H(r)$) is positive; medium hydrogen bonding is categorized by a positive and a negative $H(r)$; and strong hydrogen bonding is classified by a negative and a negative $H(r)$.

The strong covalent connection between oxygen and hydrogen is shown by the significant negative values for O1-H21 (–2.170) for protonated dopamine, as displayed in Table 1 and Fig. 2.

If the energy density at the critical sites is negative ($HBCPs < 0$), the hydrogen bond exhibits a covalent nature. Conversely, if the energy density is positive ($HBCPs > 0$), the hydrogen bond has an electrostatic character.

3.3. Drug likeness

Table 2 succinctly compares the physico-chemical attributes of five compounds – Amphetamine, dopamine, norepinephrine, serotonin, and tryptamine – in neutral, protonated, and deprotonated forms, shedding light on their potential utility in drug design. Notably, norepinephrine and dopamine exhibit a relatively higher number of hydrogen bond donors and acceptors compared to the expected range of < 5 , suggesting their propensity for strong interactions [31]. Norepinephrine boasts the largest polar surface area (PSA) of 86.71 \AA^2 , indicative of extensive interaction potential, while Tryptamine possesses a smaller PSA of 41.81 \AA^2 , suggesting a more focused interaction profile [32]. The variations in molecular weight among the compounds reflect Norepinephrine's relatively higher mass and Amphetamine's and Dopamine's lighter nature, potentially affecting their absorption and distribution properties [33]. Interestingly, all compounds share the same number of rotatable bonds (2), showing comparable flexibility [34]. The higher molar refractivity observed in dopamine and tryptamine implies their favorable interaction with polar environments [35]. Upon protonation, hydrogen bonding properties remain relatively stable across the compounds, with minor decreases in PSA values and minimal changes in molecular

Table 1. Topological parameters (all in a.u) at the bond critical point (BCP) of title compound [Electron density (ρ), Laplacian of electron density ($\nabla^2\rho$), and Ellipticity (τ)], The units of V , G , and H are in a.u. For a – in a protonated state, and b – in a deprotonated state

1	2	3	4	5	6	7
a						
Amphetamine						
Связи				V	G	H
C2 – H11	0.295	-1.088	0.028	-0.346	0.037	-0.309
C3 – H12	0.283	-0.979	0.011	-0.331	0.043	-0.288
C3 – H13	0.283	-0.982	0.010	-0.332	0.043	-0.289
C5 – H16	0.282	-0.987	0.016	-0.331	0.042	-0.289
C5 – H14	0.287	-1.049	0.010	-0.340	0.039	-0.301
C5 – H15	0.280	-0.976	0.017	-0.328	0.042	-0.286
C6 – H17	0.288	-1.013	0.033	-0.344	0.045	-0.299
C7 – H18	0.289	-1.031	0.026	-0.345	0.043	-0.301
N1 – H19	0.336	-1.852	0.004	-0.539	0.038	-0.501
N1 – H20	0.336	-1.850	0.004	-0.539	0.038	-0.501
C8 – H21	0.292	-1.061	0.023	-0.349	0.042	-0.307
C9 – H22	0.292	-1.059	0.027	-0.350	0.042	-0.307
C10 – H23	0.292	-1.062	0.025	-0.349	0.042	-0.308
N1 – H24	0.336	-1.848	0.004	-0.538	0.038	-0.500
Dopamine						
N3 – H23	0.335	-1.851	0.003	0.500	0.000	0.500
C4 – H13	0.283	-0.983	0.011	0.288	0.000	0.288
C6 – H14	0.292	-1.086	0.031	0.308	0.000	0.308
C6 – H15	0.293	-1.089	0.031	0.308	0.000	0.308
C7 – H16	0.288	-1.021	0.036	0.300	0.000	0.301
C8 – H17	0.289	-1.030	0.027	0.301	0.000	0.301
C10 – H18	0.289	-1.032	0.029	0.302	0.000	0.302
N3 – H19	0.335	-1.853	0.003	0.501	0.000	0.501
N3 – H20	0.336	-1.853	0.003	0.501	0.000	0.501
O1 – H21	0.366	-2.170	0.021	0.601	0.001	0.602
O2 – H22	0.367	-2.166	0.019	0.602	0.001	0.603
Norepinephrine						
O1 – H24	0.025	0.128	0.320	-0.028	0.030	0.002
C5 – H13	0.289	-1.033	0.027	-0.332	0.037	-0.295
C7 – H14	0.292	-1.089	0.028	-0.344	0.036	-0.308
C7 – H15	0.293	-1.092	0.029	-0.345	0.036	-0.309
C8 – H16	0.290	-1.034	0.034	-0.348	0.045	-0.303
C9 – H17	0.289	-1.038	0.023	-0.345	0.043	-0.302
C11 – H18	0.290	-1.034	0.030	-0.346	0.044	-0.302
O1 – H19	0.363	-2.165	0.020	-0.658	0.058	-0.599
N4 – H20	0.337	-1.856	0.003	-0.541	0.039	-0.503
N4 – H24	0.326	-1.815	0.002	-0.522	0.034	-0.488
N4 – H21	0.337	-1.860	0.003	-0.542	0.038	-0.503
O2 – H22	0.366	-2.171	0.020	-0.659	0.058	-0.601
O3 – H23	0.367	-2.168	0.019	-0.662	0.060	-0.602

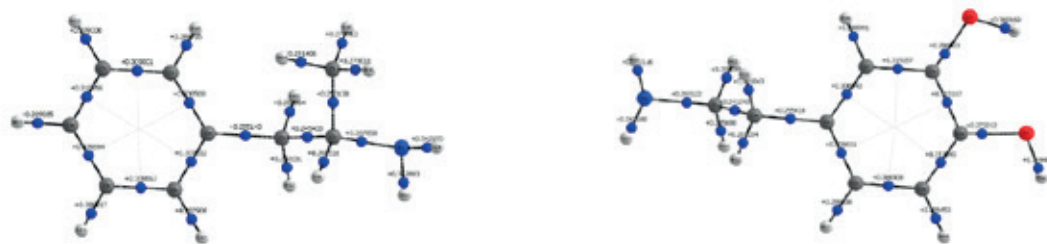
Table 1.

1	2	3	4	5	6	7
Serotonin						
C6 – H14	0.284	-0.986	0.012	-0.332	0.043	-0.289
C11 – H21	0.290	-1.044	0.023	-0.347	0.043	-0.304
C11 – C13	0.316	-0.822	0.507	-0.439	0.117	-0.322
C13 – H22	0.293	-1.065	0.026	-0.350	0.042	-0.308
C6 – H15	0.282	-0.974	0.013	-0.328	0.042	-0.286
C8 – H16	0.290	-1.076	0.026	-0.345	0.038	-0.307
N2 – H17	0.348	-1.841	0.057	-0.579	0.059	-0.520
C9 – H18	0.292	-1.087	0.032	-0.344	0.036	-0.308
C9 – H19	0.293	-1.090	0.032	-0.344	0.036	-0.308
C10 – H20	0.282	-0.964	0.045	-0.340	0.050	-0.290
N3 – H23	0.335	-1.851	0.003	-0.538	0.038	-0.501
N3 – H24	0.336	-1.853	0.004	-0.539	0.038	-0.501
O1 – H25	0.372	-2.146	0.021	-0.665	0.064	-0.601
N3 – H26	0.336	-1.853	0.003	-0.539	0.038	-0.501
C6 – H14	0.284	-0.986	0.012	-0.332	0.043	-0.289
Tryptamine						
C5 – H13	0.284	-0.987	0.012	-0.332	0.043	-0.290
C10 – H20	0.290	-1.036	0.029	-0.346	0.044	-0.303
C11 – H21	0.291	-1.050	0.025	-0.348	0.043	-0.305
C12 – H22	0.292	-1.057	0.024	-0.349	0.042	-0.307
C5 – H14	0.282	-0.976	0.013	-0.328	0.042	-0.286
C7 – H15	0.290	-1.077	0.027	-0.345	0.038	-0.307
N1 – H16	0.348	-1.840	0.057	-0.578	0.059	-0.519
C8 – H17	0.292	-1.085	0.032	-0.343	0.036	-0.307
C8 – H18	0.293	-1.093	0.031	-0.344	0.036	-0.309
C9 – H19	0.286	-0.996	0.031	-0.342	0.046	-0.295
N2 – H23	0.336	-1.852	0.003	-0.538	0.038	-0.501
N2 – H24	0.336	-1.853	0.003	-0.538	0.038	-0.501
N2 – H25	0.336	-1.852	0.003	-0.539	0.038	-0.501
b						
Amphetamine						
Связи				V	G	H
C2 – H11	0.253	-0.751	0.016	-0.265	0.039	-0.226
C3 – H12	0.282	-0.972	0.018	-0.331	0.044	-0.287
C3 – H13	0.280	-0.947	0.020	-0.329	0.046	-0.283
C5 – H16	0.273	-0.911	0.006	-0.321	0.047	-0.274
C5 – H14	0.271	-0.906	0.001	-0.315	0.044	-0.271
C5 – H15	0.272	-0.911	0.004	-0.318	0.045	-0.273
C6 – H17	0.289	-1.017	0.041	-0.348	0.047	-0.301
C7 – H18	0.287	-1.008	0.027	-0.342	0.045	-0.297
N1 – H19	0.327	-1.366	0.076	-0.517	0.088	-0.430
C8 – H20	0.285	-0.995	0.024	-0.340	0.045	-0.294
C9 – H21	0.285	-0.988	0.030	-0.340	0.047	-0.294
C10 – H22	0.284	-0.985	0.033	-0.340	0.047	-0.293
Dopamine						
O2 – H20	0.019	0.090	1.083	-0.022	0.022	0.000
C4 – H12	0.280	-0.954	0.027	-0.332	0.047	-0.285

Table 1.

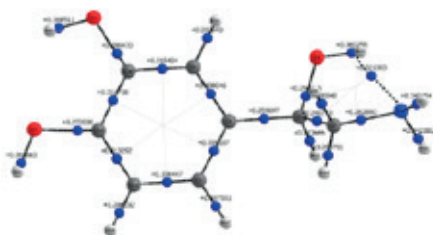
1	2	3	4	5	6	7
C4 – H13	0.278	-0.934	0.028	-0.329	0.048	-0.281
C6 – H14	0.274	-0.915	0.022	-0.313	0.042	-0.271
C6 – H15	0.260	-0.818	0.024	-0.284	0.040	-0.244
C7 – H16	0.287	-1.002	0.044	-0.345	0.047	-0.298
C8 – H17	0.286	-1.005	0.030	-0.342	0.045	-0.297
C10 – H18	0.284	-0.989	0.025	-0.339	0.046	-0.293
N3 – H19	0.328	-1.379	0.073	-0.520	0.087	-0.432
O1 – H20	0.367	-2.128	0.022	-0.656	0.062	-0.594
O2 – H21	0.369	-2.105	0.023	-0.660	0.067	-0.593
Norepinephrine						
O3 – H22	0.371	-2.131	0.021	-0.666	0.067	-0.599
O2 – H21	0.371	-2.141	0.022	-0.664	0.064	-0.600
N4 – H20	0.338	-1.671	0.036	-0.541	0.061	-0.479
N4 – H19	0.330	-1.747	0.027	-0.531	0.047	-0.484
C8 – H16	0.291	-1.069	0.025	-0.346	0.039	-0.307
C9 – H17	0.285	-0.984	0.045	-0.342	0.048	-0.294
C11 – H18	0.281	-0.958	0.029	-0.334	0.047	-0.287
C7 – H14	0.279	-0.953	0.018	-0.326	0.044	-0.282
C7 – H15	0.276	-0.933	0.018	-0.320	0.044	-0.277
C5 – H13	0.260	-0.814	0.023	-0.277	0.037	-0.240
O1 – H19	0.022	0.100	0.528	-0.025	0.025	0.000
O1 – H16	0.017	0.080	1.566	-0.016	0.018	0.002
O3 – H22	0.371	-2.131	0.021	-0.666	0.067	-0.599
Serotonin						
N3 – H23	0.327	-1.383	0.076	-0.520	0.087	-0.433
C11 – H21	0.284	-0.991	0.023	-0.339	0.046	-0.293
C11 – C13	0.307	-0.775	0.496	-0.414	0.110	-0.304
C13 – H22	0.287	-1.007	0.030	-0.343	0.046	-0.298
C6 – H14	0.280	-0.958	0.015	-0.327	0.044	-0.283
C6 – H15	0.280	-0.948	0.017	-0.329	0.046	-0.283
C8 – H16	0.288	-1.046	0.046	-0.347	0.043	-0.304
N2 – H17	0.349	-1.794	0.064	-0.580	0.066	-0.514
C9 – H18	0.246	-0.721	0.024	-0.257	0.038	-0.218
C9 – H19	0.259	-0.812	0.021	-0.283	0.040	-0.243
C10 – H20	0.284	-0.986	0.034	-0.340	0.047	-0.293
O1 – H24	0.372	-2.127	0.022	-0.664	0.066	-0.598
Tryptamine						
C5 – H13	0.276	-0.930	0.018	-0.326	0.047	-0.279
N2 – H23	0.320	-1.359	0.054	-0.507	0.084	-0.424
H18 – H19	0.009	0.025	0.233	-0.004	0.005	0.001
C10 – H20	0.278	-0.955	0.034	-0.334	0.047	-0.286
C11 – H21	0.280	-0.972	0.031	-0.336	0.047	-0.290
C12 – H22	0.280	-0.971	0.026	-0.336	0.046	-0.289
C5 – H14	0.273	-0.909	0.019	-0.322	0.047	-0.275
C7 – H15	0.285	-1.024	0.064	-0.343	0.044	-0.299
N1 – H16	0.347	-1.826	0.051	-0.570	0.057	-0.513
C8 – H17	0.253	-0.758	0.010	-0.284	0.047	-0.237
C8 – H18	0.244	-0.693	0.014	-0.268	0.047	-0.221
C9 – H19	0.285	-1.033	0.020	-0.340	0.041	-0.299

Neutral

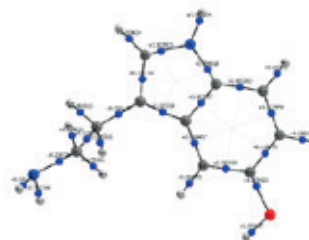


Amphetamine

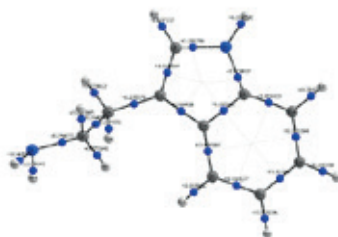
Dopamine



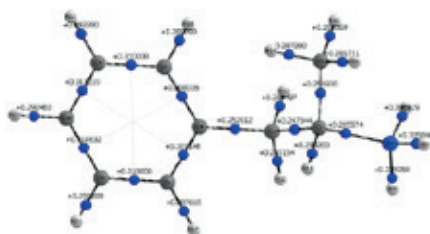
Norepinephrine



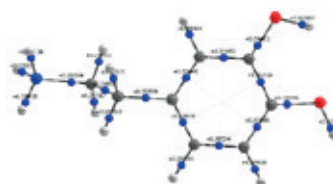
Serotonin



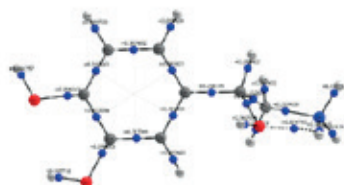
Tryptamine
Protonated



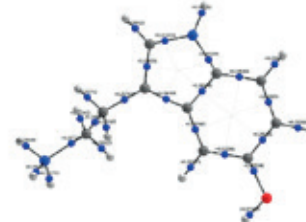
Amphetamine



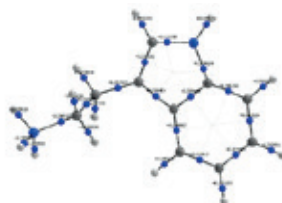
Dopamine



Norepinephrine

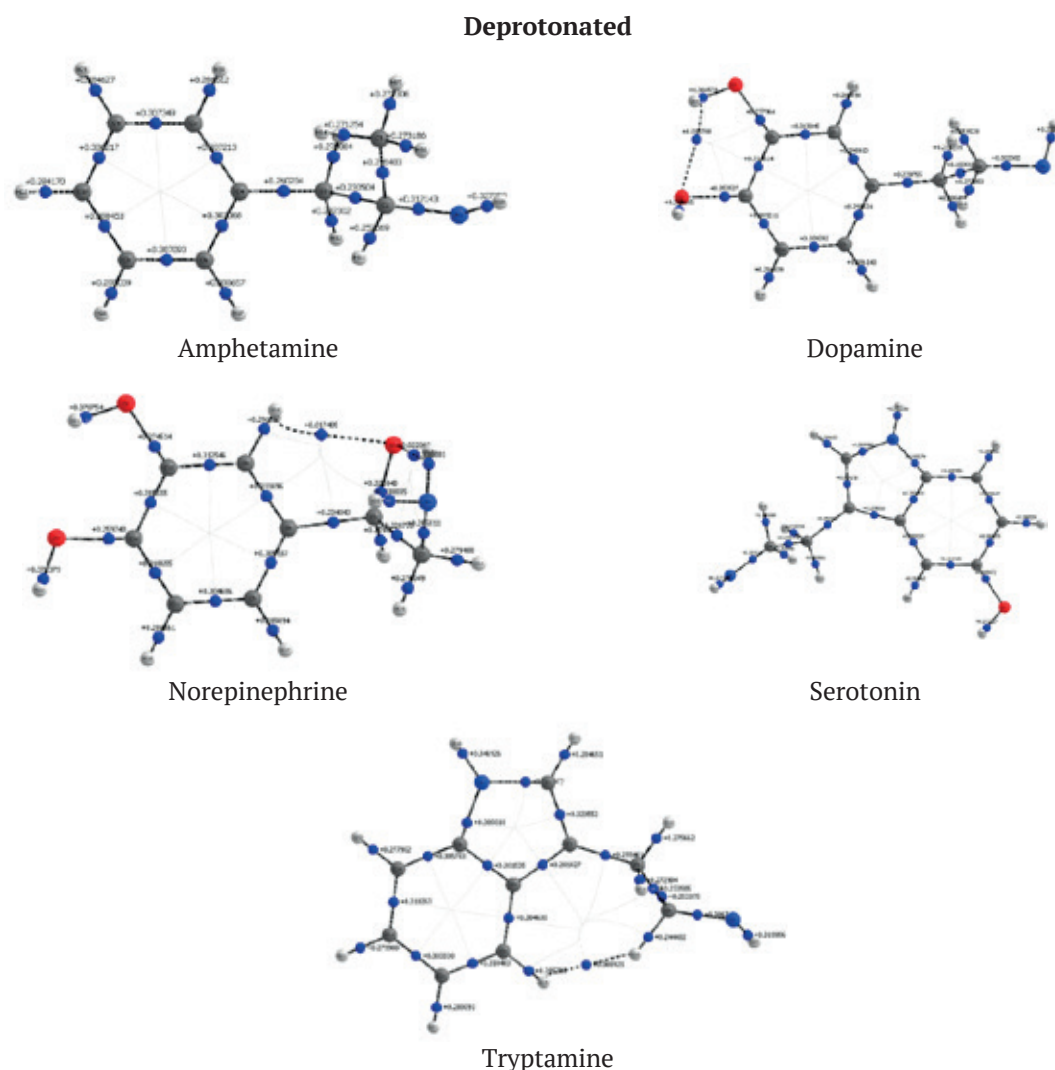


Serotonin



Tryptamine

Fig. 2. Electron density of the title compounds

**Fig. 2.**

weights. Remarkably, all measured values align with the expected ranges for drug-like molecules, highlighting the compounds' suitability for further drug design efforts. In summary, this concise yet informative analysis underscores how a diverse range of physicochemical properties can effectively guide molecular design, ensuring favorable interactions and the potential development of efficacious therapeutic agents.

3.4. Natural Bond Order (NBO) analysis

The investigation included the examination of the Lewis structures of all compounds in their neutral, protonated, and deprotonated forms. This examination was conducted using the B3LYP/6-311+G(d, p) technique and theoretical approaches based on the NBO analysis, as shown in Table 3-7. The NBO analysis is a significant technique used for examining the Lewis structure of a

molecule. It offers essential insights into several aspects, including resonance delocalization, bond order, hybridization type, and donor-acceptor interactions. The DFT calculations were used to conduct a comprehensive study, including the entire NBO analysis and the analysis of the second-order Fock matrix perturbation theory. As well as, the second order energy predicts the stabilization energy, which represents the strength of the delocalization interactions, for each donor NBO (i), acceptor NBO (j), and the $E(2)$ associated with the electron delocalization between the donor and the acceptor [36-40].

In the above equation, the symbol " q_i " represents the occupancy of the donor orbital, while " ϵ_i " and " ϵ_j " denote the diagonal elements. " $F(i, j)$ " represents the off-diagonal NBO Fock matrix element. A greater value of $E(2)$ signifies

Table 2. Physiochemical property values of study compounds and standard drug molecules

Descriptors	Am- phet- amine	Dopa- mine	Norepi- neph- rine	Sero- tonin	Trypt- amine	Expect- ed range
Hydrogen bond donor (HBD)	1	3	4	2	2	< 5
Hydrogen bond acceptors (HBA)	1	3	4	2	1	< 10
Polar surface area (PSA)	26.02	66.48	86.71	62.04	41.81	< 140
Molecular weight	135.21	153.18	169.18	176.22	160.22	< 500
Number of rotatable bonds	2	2	2	2	2	< 10
Molar refractivity	43.73	42.97	44.13	52.80	50.78	40–160
Protonated						
Hydrogen bond donor (HBD)	1	3	4	3	2	< 5
Hydrogen bond acceptors (HBA)	0	2	3	1	0	< 10
Polar surface area (PSA)	3.24	43.70	63.93	39.26	19.03	< 140
Molecular weight	136.21	154.19	170.19	177.22	161.22	< 500
Number of rotatable bonds	2	2	2	2	2	< 10
Molar refractivity	44.69	43.93	45.09	53.13	51.74	40–160
Deprotonated						
Hydrogen bond donor (HBD)	1	3	4	3	2	< 5
Hydrogen bond acceptors (HBA)	1	3	4	2	1	< 10
Polar surface area (PSA)	26.02	64.31	171.19	62.04	41.81	< 140
Molecular weight	137.22	153.18	86.71	178.23	160.22	< 500
Number of rotatable bonds	2	0	2	2	2	< 10
Molar refractivity	43.73	45.97	44.13	52.80	50.78	40–160

an increased level of interaction between electron donors and electron acceptors.

In this work, the NBO analysis reveals that the highest lone pair of electrons on oxygen (N2) inside the carboxylic group undergoes delocalization towards the π^* antibonding molecular orbital of the C4-C8 bond within the same carboxylic group for protonated serotonin compounds. This delocalization process results in a significant stabilization energy of 42.97 kcal/mol, as seen in Table 1.

The delocalization interaction $\pi^*(C 11 - C 13)$ to $\pi^*(C 5 - C 7)$ in protonated serotonin is of significant importance, with a stabilization energy of 261.16 kcal/mol. Similarly, with the neutral norepinephrine molecule, the interaction between $\pi^*(C 11 - C 12)$ and $\pi^*(C 8 - C 10)$ is noteworthy, with a stabilization energy of 256.38 kcal/mol. The findings show that $\sigma \rightarrow \sigma^*$ interactions have a lower delocalization energy compared to $\pi \rightarrow \pi^*$ interactions. The electron density attributed to σ bonds exhibits greater magnitude when compared to that of π bonds.

3.5. Nonlinear optical properties (NLO)

Nonlinear optical (NLO) materials are of significant importance in nonlinear optics, particularly because of their significant effect on information technology and industrial applications. The first static analysis was performed on the geometry that has undergone optimization using the B3LYP/6-311G++(d,p) method. The initial static hyperpolarizability, represented as: is a tensor of three dimensions with a rank of three, which may be mathematically represented by a $3 \times 3 \times 3$ matrix. The total static dipole moment mean polarizability, and initial static hyperpolarizability may be determined by using the equations that include the x, y, and z component [38, 41].

A high value of a particular component of the polarizability and hyperpolarizability indices indicates that there has been a considerable delocalization of charge in one or more specific directions [42, 43]. The total molecular dipole moment, mean polarizability, and first hyperpolarizability of the title have been calculated and are presented in Table 8.

Table 3. Second-order Perturbation Theory Analysis of Fock Matrix in NBO for Amphetamine

Donor NBO (i)	Acceptor NBO (j)	$E(2)$, kcal/mol	$E(j)-E(i)$, a.u.	$F(i,j)$, a.u.
Neutral				
π C 4 – C 7	π^* C 6 – C 8	19.64	0.28	0.066
π C 4 – C 7	π^* C 9 – C 10	21.47	0.28	0.069
π C 6 – C 8	π^* C 4 – C 7	20.68	0.29	0.069
π C 6 – C 8	π^* C 9 – C 10	19.62	0.28	0.067
σ C 6 – H 17	σ^* C 4 – C 7	3.95	1.1	0.059
σ C 7 – H 18	σ^* C 4 – C 6	4.01	1.09	0.059
σ C 7 – H 18	σ^* C 9 – C 10	3.53	1.1	0.056
π C 9 – C 10	π^* C 4 – C 7	19.38	0.29	0.067
π C 9 – C 10	π^* C 6 – C 8	20.76	0.28	0.068
σ C 9 – H 22	σ^* C 4 – C 7	3.79	1.1	0.058
Protonated				
π C 4 – C 7	π^* C 6 – C 8	19.23	0.29	0.067
π C 4 – C 7	π^* C 9 – C 10	18.18	0.3	0.066
σ C 5 – H 14	σ^* N 1 – C 2	5.68	0.68	0.056
π C 6 – C 8	π^* C 4 – C 7	21.44	0.27	0.069
π C 6 – C 8	π^* C 9 – C 10	18.87	0.29	0.067
σ C 6 – H 17	σ^* C 4 – C 7	4.11	1.1	0.06
σ C 7 – H 18	σ^* C 4 – C 6	4.17	1.09	0.06
π C 9 – C 10	π^* C 4 – C 7	22.53	0.27	0.069
π C 9 – C 10	π^* C 6 – C 8	20.99	0.27	0.069
π^* C 4 – C 7	π^* C 9 – C 10	171.97	0.02	0.082
Deprotonated				
π C 4 – C 6	π^* C 7 – C 9	20.47	0.26	0.066
π C 4 – C 6	π^* C 8 – C 10	26.03	0.25	0.073
π C 7 – C 9	π^* C 4 – C 6	18.9	0.3	0.068
π C 7 – C 9	π^* C 8 – C 10	18.96	0.28	0.066
π C 8 – C 10	π^* C 4 – C 6	15.76	0.3	0.063
π C 8 – C 10	π^* C 7 – C 9	19.11	0.29	0.067
σ C 9 – H 21	σ^* C 4 – C 7	3.65	1.12	0.057
LP (2) N 1	σ^* C 2 – H 11	20.35	0.48	0.092
π^* C 7 – C 9	π^* C 4 – C 6	196.57	0.02	0.084
π^* C 8 – C 10	π^* C 4 – C 6	133.51	0.02	0.08

Table 4. Second Order Perturbation Theory Analysis of Fock Matrix in NBO for dopamine

Donor NBO (i)	Acceptor NBO (j)	$E(2)$, kcal/mol	$E(j)-E(i)$, a.u.	$F(i,j)$, a.u.
1	2	3	4	5
Neutral				
σ O 1 – H 21	σ^* C 7 – C 9	5.47	1.31	0.076
π C 5 – C 8	π^* C 7 – C 9	18.23	0.28	0.064
π C 5 – C 8	π^* C 10 – C 11	20.8	0.27	0.068
π C 7 – C 9	π^* C 5 – C 8	20.73	0.3	0.071
π C 7 – C 9	π^* C 10 – C 11	19.68	0.28	0.068
σ C 8 – C 10	σ^* O 2 – C 11	5.08	1.02	0.064
π C 10 – C 11	π^* C 5 – C 8	17.09	0.31	0.066
π C 10 – C 11	π^* C 7 – C 9	18.6	0.3	0.068

Table 4.

1	2	3	4	5
LP (2) O 1	$\pi^* C 7 - C 9$	28.74	0.35	0.095
$\pi^* C 10 - C 11$	$\pi^* C 5 - C 8$	179.74	0.02	0.08
Protonated				
$\sigma O 1 - H 21$	$\sigma^* C 7 - C 9$	5.64	1.3	0.077
$\sigma O 2 - H 22$	$\sigma^* C 9 - C 11$	4.29	1.27	0.067
$\pi C 5 - C 8$	$\pi^* C 7 - C 9$	17.38	0.29	0.065
$\pi C 5 - C 8$	$\pi^* C 10 - C 11$	17.4	0.29	0.065
$\pi C 7 - C 9$	$\pi^* C 5 - C 8$	20.91	0.29	0.07
$\pi C 7 - C 9$	$\pi^* C 10 - C 11$	18.74	0.29	0.066
$\sigma C 8 - C 10$	$\sigma^* O 2 - C 11$	4.88	1.05	0.064
$\pi C 10 - C 11$	$\pi^* C 5 - C 8$	19.58	0.29	0.069
$\pi C 10 - C 11$	$\pi^* C 7 - C 9$	18.85	0.29	0.067
LP (2) O 1	$\pi^* C 7 - C 9$	32.29	0.33	0.098
Deprotonated				
$\sigma N 3 - H 19$	$\sigma^* C 6 - H 14$	5.9	0.94	0.067
$\sigma C 4 - C 6$	$\sigma^* C 5 - C 7$	7.11	0.47	0.057
$\pi C 5 - C 7$	$\pi^* C 8 - C 10$	18.2	0.26	0.061
$\pi C 5 - C 7$	$\pi^* C 9 - C 11$	30.11	0.24	0.079
$\pi C 8 - C 10$	$\pi^* C 5 - C 7$	17.25	0.3	0.067
$\pi C 8 - C 10$	$\pi^* C 9 - C 11$	16.07	0.27	0.063
$\pi C 9 - C 11$	$\pi^* C 8 - C 10$	21.98	0.3	0.073
LP (2) O 1	$\pi^* C 9 - C 11$	26.91	0.35	0.095
$\pi^* C 8 - C 10$	$\pi^* C 5 - C 7$	227.99	0.01	0.082
$\pi^* C 9 - C 11$	$\pi^* C 8 - C 10$	254.9	0.01	0.079

Table 5. Second Order Perturbation Theory Analysis of Fock Matrix in NBO for Norepinephrine

Donor NBO (i)	Acceptor NBO (j)	$E(2)$, kcal/mol	$E(j)-E(i)$, a.u.	$F(i,j)$, a.u.
1	2	3	4	5
Neutral				
$\sigma O 2 - H 22$	$\sigma^* C 8 - C 10$	5.43	1.31	0.076
$\pi C 6 - C 9$	$\pi^* C 8 - C 10$	18.14	0.28	0.065
$\pi C 6 - C 9$	$\pi^* C 11 - C 12$	20.41	0.27	0.068
$\pi C 8 - C 10$	$\pi^* C 6 - C 9$	21.08	0.29	0.071
$\pi C 8 - C 10$	$\pi^* C 11 - C 12$	20.66	0.28	0.069
$\sigma C 9 - C 11$	$\sigma^* O 3 - C 12$	5.03	1.02	0.064
$\pi C 11 - C 12$	$\pi^* C 8 - C 10$	17.97	0.3	0.067
LP (2) O 2	$\pi^* C 8 - C 10$	28.2	0.35	0.094
$\pi^* C 11 - C 12$	$\pi^* C 6 - C 9$	179.59	0.02	0.08
$\pi^* C 11 - C 12$	$\pi^* C 8 - C 10$	256.38	0.01	0.083
Protonated				
$\sigma O 2 - H 22$	$\sigma^* C 8 - C 10$	5.66	1.3	0.077
$\pi C 6 - C 9$	$\pi^* C 8 - C 10$	17.55	0.29	0.065
$\pi C 6 - C 9$	$\pi^* C 11 - C 12$	16.78	0.29	0.063
$\pi C 8 - C 10$	$\pi^* C 6 - C 9$	20.33	0.28	0.069
$\pi C 8 - C 10$	$\pi^* C 11 - C 12$	18.85	0.29	0.066
$\sigma C 9 - H 17$	$\sigma^* C 6 - C 8$	4.34	1.09	0.061
$\pi C 11 - C 12$	$\pi^* C 6 - C 9$	20.31	0.29	0.07
$\pi C 11 - C 12$	$\pi^* C 8 - C 10$	18.53	0.29	0.066
LP (2) O 2	$\pi^* C 8 - C 10$	32.64	0.33	0.098
LP (2) O 3	$\pi^* C 11 - C 12$	28.84	0.35	0.096

Table 5.

1	2	3	4	5
Deprotonated				
σ O 2 – H 21	σ^* C 8 – C 10	5.17	1.34	0.074
π C 8 – C 10	π^* C 6 – C 9	20.78	0.3	0.071
π C 8 – C 10	π^* C 11 – C 12	22.32	0.26	0.07
σ C 9 – C 11	σ^* O 3 – C 12	5.13	0.99	0.064
LP (2) O 1	σ^* C 5 – C 6	19.19	0.55	0.093
LP (3) O 1	σ^* C 5 – H 13	16.01	0.56	0.086
LP (1) O 2	σ^* C 10 – C 12	5.71	1.15	0.073
LP (2) O 2	π^* C 8 – C 10	23.94	0.37	0.09
π^* C 8 – C 10	π^* C 6 – C 9	212.92	0.02	0.085
π^* C 11 – C 12	π^* C 8 – C 10	131.19	0.03	0.083

Table 6. Second-order Perturbation Theory Analysis of Fock Matrix in NBO for Serotonin

Donor NBO (i)	Acceptor NBO (j)	$E(2)$, kcal/mol	$E(j)-E(i)$, a.u.	$F(i,j)$, a.u.
Neutral				
σ C 4 – C 8	σ^* C 5 – C 10	5.02	1.27	0.071
π C 4 – C 8	π^* C 5 – C 7	16.32	0.29	0.068
π C 5 – C 7	π^* C 4 – C 8	18.11	0.28	0.065
π C 5 – C 7	π^* C 10 – C 12	17.78	0.27	0.063
π C 5 – C 7	π^* C 11 – C 13	21.14	0.27	0.069
π C 10 – C 12	π^* C 5 – C 7	18.2	0.29	0.069
π C 10 – C 12	π^* C 11 – C 13	16.1	0.29	0.062
σ C 11 – C 13	σ^* N 2 – C 7	6.15	1.16	0.075
π C 11 – C 13	π^* C 10 – C 12	19.25	0.29	0.069
LP (1) N 2	π^* C 4 – C 8	35.4	0.3	0.093
Protonated				
σ C 5 – C 7	σ^* C 4 – C 6	5.29	1.06	0.067
π C 5 – C 7	π^* C 4 – C 8	19.79	0.26	0.064
π C 10 – C 12	π^* C 5 – C 7	19.4	0.29	0.071
π C 10 – C 12	π^* C 11 – C 13	14.93	0.3	0.06
σ C 11 – C 13	σ^* N 2 – C 7	6.27	1.15	0.076
π C 11 – C 13	π^* C 10 – C 12	20.35	0.28	0.069
LP (2) O 1	π^* C 10 – C 12	31.11	0.34	0.098
LP (1) N 2	π^* C 4 – C 8	42.97	0.28	0.099
π^* C 5 – C 7	π^* C 11 – C 13	233.04	0.01	0.082
π^* C 10 – C 12	π^* C 11 – C 13	254.27	0.01	0.082
Deprotonated				
σ C 4 – C 8	σ^* C 5 – C 10	5.29	1.25	0.073
π C 5 – C 7	π^* C 4 – C 8	17.65	0.29	0.066
π C 5 – C 7	π^* C 10 – C 12	18.89	0.26	0.063
π C 5 – C 7	π^* C 11 – C 13	24.39	0.25	0.07
σ C 6 – H 15	σ^* C 4 – C 8	5.06	1.05	0.065
π C 10 – C 12	π^* C 11 – C 13	16.24	0.28	0.063
π C 11 – C 13	π^* C 10 – C 12	19.18	0.29	0.069
LP (1) N 2	π^* C 5 – C 7	31.23	0.3	0.091
π^* C 5 – C 7	π^* C 4 – C 8	111.28	0.02	0.067
π^* C 11 – C 13	π^* C 5 – C 7	261.16	0.02	0.083

Table 7. Second-order Perturbation Theory Analysis of Fock Matrix in NBO for Tryptamine

Donor NBO (<i>i</i>)	Acceptor NBO (<i>j</i>)	<i>E</i> (2), kcal/mol	<i>E</i> (<i>j</i>)- <i>E</i> (<i>i</i>), a.u.	<i>F</i> (<i>i</i> , <i>j</i>), a.u.
Neutral				
s C 4 – C 6	s* C 3 – C 5	4.43	1.1	0.063
p C 4 – C 6	p* C 3 – C 7	18.35	0.28	0.065
p C 4 – C 6	p* C 9 – C 11	19.82	0.28	0.068
p C 4 – C 6	p* C 10 – C 12	19.01	0.27	0.065
s C 5 – H 13	s* C 3 – C 4	4.86	1.02	0.063
p C 9 – C 11	p* C 4 – C 6	16.63	0.28	0.065
p C 9 – C 11	p* C 10 – C 12	19.45	0.28	0.067
p C 10 – C 12	p* C 4 – C 6	18.9	0.28	0.069
p C 10 – C 12	p* C 9 – C 11	17.12	0.29	0.064
LP (1) N 1	p* C 4 – C 6	35.26	0.3	0.094
Protonated				
s C 4 – C 6	s* C 3 – C 5	5.16	1.06	0.066
p C 4 – C 6	p* C 3 – C 7	19.81	0.26	0.065
p C 4 – C 6	p* C 9 – C 11	18.58	0.28	0.066
p C 9 – C 11	p* C 10 – C 12	18.24	0.29	0.066
s C 10 – C 12	s* N 1 – C 6	6.36	1.14	0.076
p C 10 – C 12	p* C 4 – C 6	20.46	0.27	0.07
p C 10 – C 12	p* C 9 – C 11	18.7	0.28	0.065
LP (1) N 1	p* C 3 – C 7	41.22	0.28	0.098
p* C 4 – C 6	p* C 9 – C 11	249.47	0.01	0.079
p* C 4 – C 6	p* C 10 – C 12	207.04	0.02	0.081
Deprotonated				
p C 3 – C 7	p* C 4 – C 9	13.95	0.31	0.061
p C 4 – C 9	p* C 3 – C 7	10.81	0.31	0.052
p C 4 – C 9	p* C 6 – C 10	13.27	0.3	0.057
p C 4 – C 9	p* C 11 – C 12	12.49	0.28	0.053
p C 6 – C 10	p* C 11 – C 12	11.52	0.3	0.053
p C 11 – C 12	p* C 6 – C 10	8.44	0.31	0.047
LP (1) N 1	p* C 6 – C 10	16.18	0.38	0.072
LP (2) N 2	s* C 8 – H 18	9.75	0.6	0.072
p* C 6 – C 10	p* C 4 – C 9	115.66	0.02	0.073
p* C 11 – C 12	p* C 6 – C 10	85.65	0.01	0.061

The polarizabilities and the hyperpolarizabilities that were acquired from the GAUSSIAN 09 output were initially represented in atomic units (a.u.). These computed values have been translated into electrostatic units (e.s.u.) for making comparisons and interpretations more straightforward. For polarizabilities, 1 a.u. is equal to $0.1482 \cdot 10^{-24}$ e.s.u., and for hyperpolarizabilities, 1 a.u. is equal to $8.6393 \cdot 10^{-35}$ e.s.u.

As observed in Table 8, the computed dipole moment values for the compounds under investigation, both in their protonated and deprotonated states, are higher than the dipole

moment of urea, which is equal to 1.3732 D. When exploring the nonlinear optical (NLO) features of molecular systems, urea is often used as a model molecule because of its well-characterized nonlinear optical behavior. Because of this, it has often been used as a benchmark in many comparative studies.

The polarizability values were calculated for all compounds in their neutral, protonated, and deprotonated states. These values are reported in Table 8. The findings show that the polarizability is reduced in the deprotonated state as compared with the corresponding protonated and neutral states.

Table 8. NLO parameters for all compounds

Parameters	Neutral	Protonated	Deprotonated	Neutral	Protonated	Deprotonated
1	2	3	4	5	6	7
Amphetamine			Dopamine			
μ_r	1.26	11.90	9.25	2.86	14.82	12.42
α_{xx}	-57.96	-2.26	-106.59	-58.06	30.59	-131.00
α_{yy}	-56.53	-50.44	-65.72	-60.58	-55.79	-70.20
α_{zz}	-62.99	57.11	-69.70	-68.66	-62.17	-70.06
α_r	-59.16	1.47	-80.67	-62.43	-29.13	-90.42
$\alpha(esu) * 10^{-24}$	-8.77	0.22	-11.96	-9.25	-4.32	-13.40
β_{xxx}	0.97	165.11	-121.75	76.32	-293.07	-314.64
β_{yyy}	3.67	11.87	11.87	7.37	-0.96	-4.65
β_{zzz}	7.24	22.15	-5.74	10.86	-16.95	-31.93
β_x	11.88	199.13	-115.62	94.54	-310.98	-351.22
β_{yyy}	-4.21	-5.31	0.89	-9.86	-8.35	-6.61
β_{xyy}	-13.78	-19.99	20.46	-21.18	6.97	10.76
β_{yzz}	-0.83	0.11	0.13	2.91	5.32	0.49
β_y	-18.83	-25.19	21.48	-28.13	3.94	4.65
β_{zzz}	0.34	0.85	-1.72	-2.77	-9.10	7.08
β_{xxz}	21.92	2.49	30.89	28.10	-38.04	-25.57
β_{yyz}	-2.49	-1.12	-2.19	-2.62	-3.70	1.97
β_z	19.76	2.22	26.99	22.71	-50.84	-16.52
$\beta_0(esu) * 10^{-33}$	29.77	200.73	120.66	101.22	315.13	351.64
Norepinephrine			Serotonin			
μ_r	4.37	11.51	10.82	1.10	16.41	12.51
α_{xx}	-48.16	11.56	-102.27	-84.18	-1.57	-155.02
α_{yy}	-68.01	-61.36	-78.14	-56.30	-44.08	-74.40
α_{zz}	-72.25	-62.33	-82.33	-78.32	-74.52	-83.09
α_r	-62.80	-37.38	-87.58	-72.93	-40.06	-104.17
$\alpha(esu) * 10^{-24}$	-9.31	-5.54	-12.98	-10.81	-5.94	-15.44
β_{xxx}	1.81	188.37	-141.20	27.98	-311.06	264.60
β_{yyy}	-9.96	-1.25	-23.60	-12.03	-37.53	38.08
β_{zzz}	6.77	27.16	-32.30	-9.79	-21.39	4.74
β_x	-1.39	214.28	-197.10	6.17	-369.98	307.42
β_{yyy}	-7.85	6.67	-7.18	4.00	-6.17	15.89
β_{xyy}	-33.69	7.75	-29.43	5.65	-75.10	98.86
β_{yzz}	3.40	-8.23	3.11	-8.20	-12.22	-3.66
β_y	-38.14	6.19	-33.50	1.45	-93.49	111.10
β_{zzz}	9.01	7.39	0.64	2.28	5.37	-0.97
β_{xxz}	23.32	-54.05	-10.11	18.24	28.03	3.51

Table 8.

1	2	3	4	5	6	7
β_{yyz}	0.43	-2.69	7.69	-0.58	0.87	3.37
β_z	32.77	-49.35	-1.78	19.94	34.28	5.92
$\beta_0 (esu) * 10^{-33}$	50.34	219.98	199.93	20.92	383.15	326.93
Tryptamine						
μ_t	1.35	14.48	11.70			
α_{xx}	-70.12	10.12	-134.08			
α_{yy}	-57.78	-49.61	-76.20			
α_{zz}	-73.26	-69.73	-77.43			
α_t	-67.05	-36.41	-95.90			
$\alpha (esu) * 10^{-24}$	-9.94	-5.40	-14.21			
β_{xxx}	30.27	-285.98	-231.75			
β_{yyy}	-0.31	-11.74	-20.72			
β_{zzz}	-15.30	-26.16	1.77			
β_x	14.67	-323.88	-250.69			
β_{yyy}	24.41	19.17	14.72			
β_{xyy}	-16.25	-52.43	67.38			
β_{yzz}	-0.27	-2.65	3.40			
β_y	7.88	-35.92	85.50			
β_{zzz}	3.01	5.81	-0.35			
β_{xxz}	17.98	28.07	-9.63			
β_{yyz}	1.67	3.63	-8.61			
β_z	22.67	37.51	-18.59			
$\beta_0 (esu) * 10^{-33}$	-70.12	10.12	-134.08			

The determination of the size has significant importance within the context of a nonlinear optical (NLO) system. The values of the deprotonated dopamine and protonated serotonin molecules are found to be relatively greater than urea. Specifically, the β value of urea is measured to be $343.272 \cdot 10^{-33}$ esu, but other findings show that the initial hyperpolarizability value is less than the hyperpolarizability value of urea. The findings show that deprotonated dopamine and protonated serotonin have promise for uses in Nonlinear Optical (NLO) systems.

3.6. Quantum chemical parameters and Molecular orbitals (MOs)

Table 9 presents a detailed overview of the quantum chemical parameters for Amphetamine, Dopamine, Norepinephrine, Serotonin, and Tryptamine, in their neutral, protonated, and

deprotonated states. These parameters provide valuable insights into the compounds' electronic properties, reactivity, and stability, all of which are crucial considerations in evaluating their potential as drug candidates [44, 45].

Examining the Highest Occupied Molecular Orbital (HOMO) and Lowest Unoccupied Molecular Orbital (LUMO) energies reveals important details about the compounds' ionization potential and electron affinity [46]. For example, Amphetamine's neutral state shows a HOMO energy of -6.304 eV, showing its ability to donate electrons, while its LUMO energy of 0.049 eV suggests a lower tendency to accept electrons. Similar trends are observed across the compounds, with Tryptamine displaying a comparable pattern.

The energy gap, representing the difference between HOMO and LUMO energies, reflects the compounds' stability and their capacity

Table 9. Quantum chemical parameters for title compounds

Parameters	Neutral	Protonated	Deprotonated
1	2	3	4
Amphetamine			
HOMO, (eV)	-6.304	-9.798	1.868
LUMO, (eV)	0.049	-4.235	3.585
Ionization energy, (eV)	6.304	9.798	-1.868
Electron Affinity, (eV)	-0.049	4.235	-3.585
Energy gap, (eV)	6.353	5.563	1.717
Hardness, (eV)	3.177	2.782	0.859
Softness, (eV) ⁻¹	0.157	0.180	0.582
Electronegativity, (eV)	3.128	7.017	-2.727
Chemical potential, (eV)	-3.128	-7.017	2.727
Electrophilicity, (eV)	1.540	8.850	4.330
Nucleophilicity, (eV) ⁻¹	0.650	0.113	0.231
Back-donation, (eV)	-0.794	-0.695	-0.215
Electron transfer	0.985	2.523	-3.176
Total energy T.E., (a.u)	-405.559	-405.936	-404.895
Dopamine			
HOMO, (eV)	-5.522	1.492	1.492
LUMO, (eV)	0.173	3.653	3.653
Ionization energy, (eV)	5.522	-1.492	-1.492
Electron Affinity, (eV)	-0.173	-3.653	-3.653
Energy gap, (eV)	5.695	2.161	2.161
Hardness, (eV)	2.848	1.081	1.081
Softness, (eV) ⁻¹	0.176	0.463	0.463
Electronegativity, (eV)	2.675	-2.573	-2.573
Chemical potential, (eV)	-2.675	2.573	2.573
Electrophilicity, (eV)	1.256	3.062	3.062
Nucleophilicity, (eV) ⁻¹	0.796	0.327	0.327
Back-donation, (eV)	-0.712	-0.270	-0.270
Electron transfer	0.939	-2.381	-2.381
Total energy T.E., (a.u)	-516.681	-515.018	-515.017
Norepinephrine			
HOMO, (eV)	-5.45	-8.761	0.25
LUMO, (eV)	-0.313	-3.903	3.972
Ionization energy, (eV)	5.450	8.761	-0.250
Electron Affinity, (eV)	0.313	3.903	-3.972
Energy gap, (eV)	5.137	4.858	3.722
Hardness, (eV)	2.569	2.429	1.861
Softness, (eV) ⁻¹	0.195	0.206	0.269
Electronegativity, (eV)	2.882	6.332	-2.111
Chemical potential, (eV)	-2.882	-6.332	2.111
Electrophilicity, (eV)	1.616	8.253	1.197
Nucleophilicity, (eV) ⁻¹	0.619	0.121	0.835
Back-donation, (eV)	-0.642	-0.607	-0.465
Electron transfer	1.122	2.607	-1.134
Total energy T.E., (a.u)	-591.899	-592.282	-591.286
Serotonin			
HOMO, (eV)	-5.184	-8.095	1.902
LUMO, (eV)	-0.125	-4.355	3.005
Ionization energy, (eV)	5.184	8.095	-1.902

Table 9.

1	2	3	4
Electron Affinity, (eV)	0.125	4.355	-3.005
Energy gap, (eV)	5.059	3.740	1.103
Hardness, (eV)	2.530	1.870	0.552
Softness, (eV) ⁻¹	0.198	0.267	0.907
Electronegativity, (eV)	2.655	6.225	-2.454
Chemical potential, (eV)	-2.655	-6.225	2.454
Electrophilicity, (eV)	1.393	10.361	5.458
Nucleophilicity, (eV) ⁻¹	0.718	0.097	0.183
Back-donation, (eV)	-0.632	-0.468	-0.138
Electron transfer	1.049	3.329	-4.449
Total energy T.E., (a.u)	-573.030	-573.460	-572.361
Tryptamine			
HOMO, (eV)	-5.284	-8.41	2.122
LUMO, (eV)	-0.086	-4.343	3.14
Ionization energy, (eV)	5.284	8.410	-2.122
Electron Affinity, (eV)	0.086	4.343	-3.140
Energy gap, (eV)	5.198	4.067	1.018
Hardness, (eV)	2.599	2.034	0.509
Softness, (eV) ⁻¹	0.192	0.246	0.982
Electronegativity, (eV)	2.685	6.377	-2.631
Chemical potential, (eV)	-2.685	-6.377	2.631
Electrophilicity, (eV)	1.387	9.997	6.800
Nucleophilicity, (eV) ⁻¹	0.721	0.100	0.147
Back-donation, (eV)	-0.650	-0.508	-0.127
Electron transfer	1.033	3.136	-5.169
Total energy T.E., (a.u)	-497.713	-498.190	-497.140

for electronic transitions [47]. Importantly, all compounds exhibit energy gap values that fall within the expected range, underscoring their potential stability and reactivity. For instance, Norepinephrine's neutral state boasts an energy gap of 5.137 eV, highlighting its suitability for electronic transitions and reactivity.

Regarding hardness, a measure of resistance to electron addition or removal, values range from 0.509 eV (Tryptamine) to 3.177 eV (Amphetamine). These values signify the compounds' ability to maintain stability during chemical interactions. Electronegativity, indicative of electron-attracting ability, provides insights into polarity and reactivity [48, 49]. Dopamine's electronegativity of 2.675 eV aligns with expectations and underscores its balanced electron-attracting behavior.

Comparing the compounds' parameter values to the expected ranges underscores their suitability for drug design. Ionization energy values within the expected ranges show their

readiness for electron donation and participation in chemical reactions. Similarly, electron transfer energies suggest their potential for electron donation or acceptance during reactions, with Amphetamine displaying a value of 0.985 in its neutral state.

Molecular Orbitals (MOs) (Fig. 3–7), particularly HOMO and LUMO, are pivotal for understanding electronic structure and reactivity. In Gaussian software, these MOs can be visualized by using different signs and colours to denote the wave function and the electron density of the orbital. The HOMO depicts regions of high electron density, where electrons are prone to be donated or transferred, implying nucleophilic reactivity. The LUMO depicts regions of low electron density, where electrons are prone to be accepted or received, implying electrophilic reactivity [50–53]. Protonation and deprotonation are processes where a molecule gains or loses a proton (H⁺), respectively. This alters the charge, shape, and reactivity of the molecule, as well

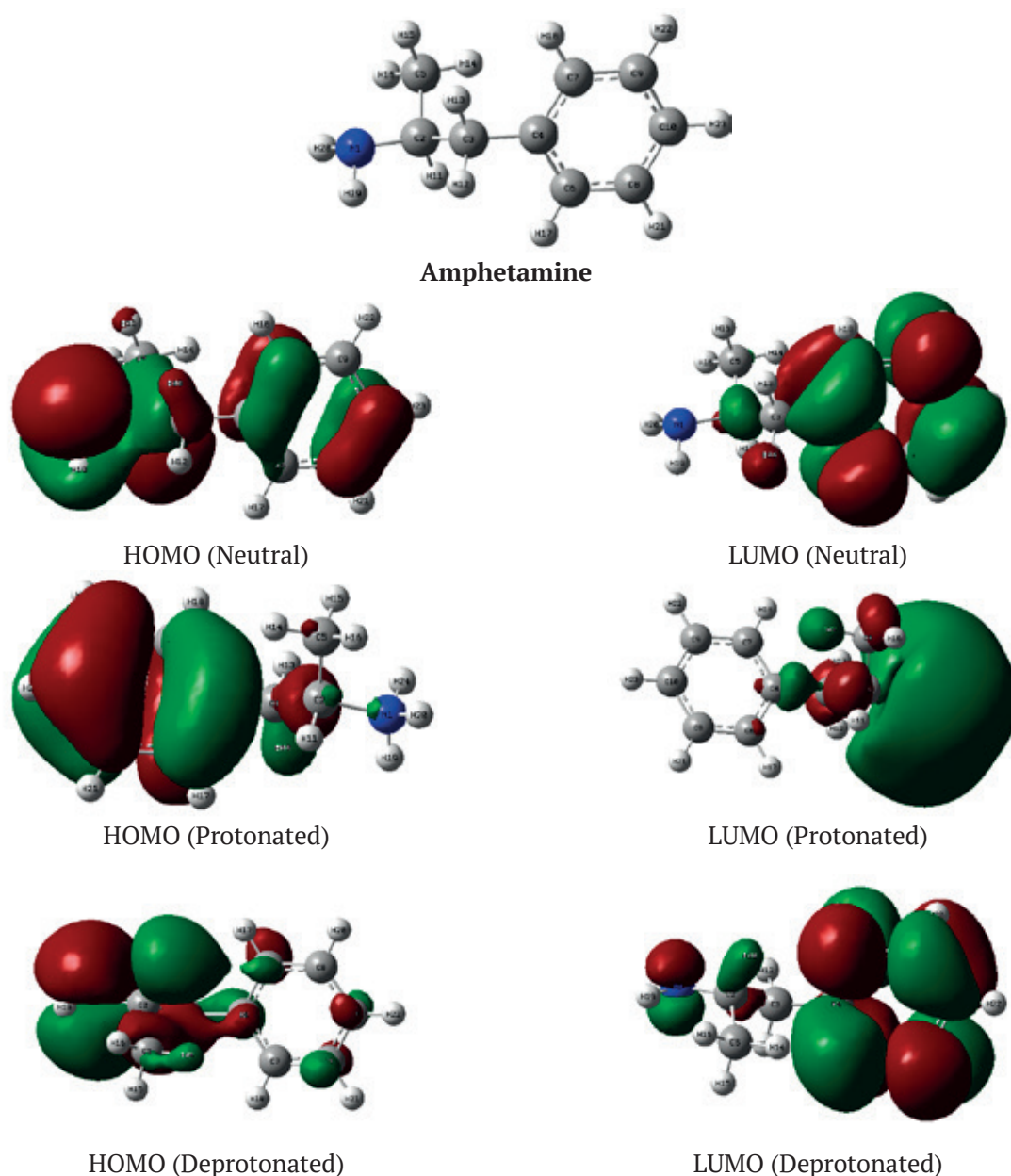


Fig. 3. Optimized structures, HOMO, and LUMO energies for Neutral, protonated, deprotonated

as the MOs, which are the regions where the electrons are distributed in the molecule.

For example, the quantum chemical parameters in Table 9 reveal the impact of protonation and deprotonation on amphetamine's electronic properties. Protonation causes the HOMO to shift to lower energy levels (from -6.304 to -9.798 eV) and the LUMO to lower energy levels (from 0.049 to -4.235 eV), leading to a reduced energy gap (from 6.353 to 5.563 eV). In contrast, deprotonation shifts the HOMO to

higher energy levels (from -6.304 to 1.868 eV) and the LUMO to higher energy levels (from 0.049 to 3.585 eV), resulting in a narrower energy gap (from 6.353 to 1.717 eV). These changes highlight how protonation and deprotonation influence amphetamine's reactivity and electron-donating or -accepting properties. Similar patterns of energy shifts are observed for Dopamine, Norepinephrine, Serotonin, and Tryptamine.

Also, In the Fig. 3, you can see how protonation and deprotonation modify the shape and size of

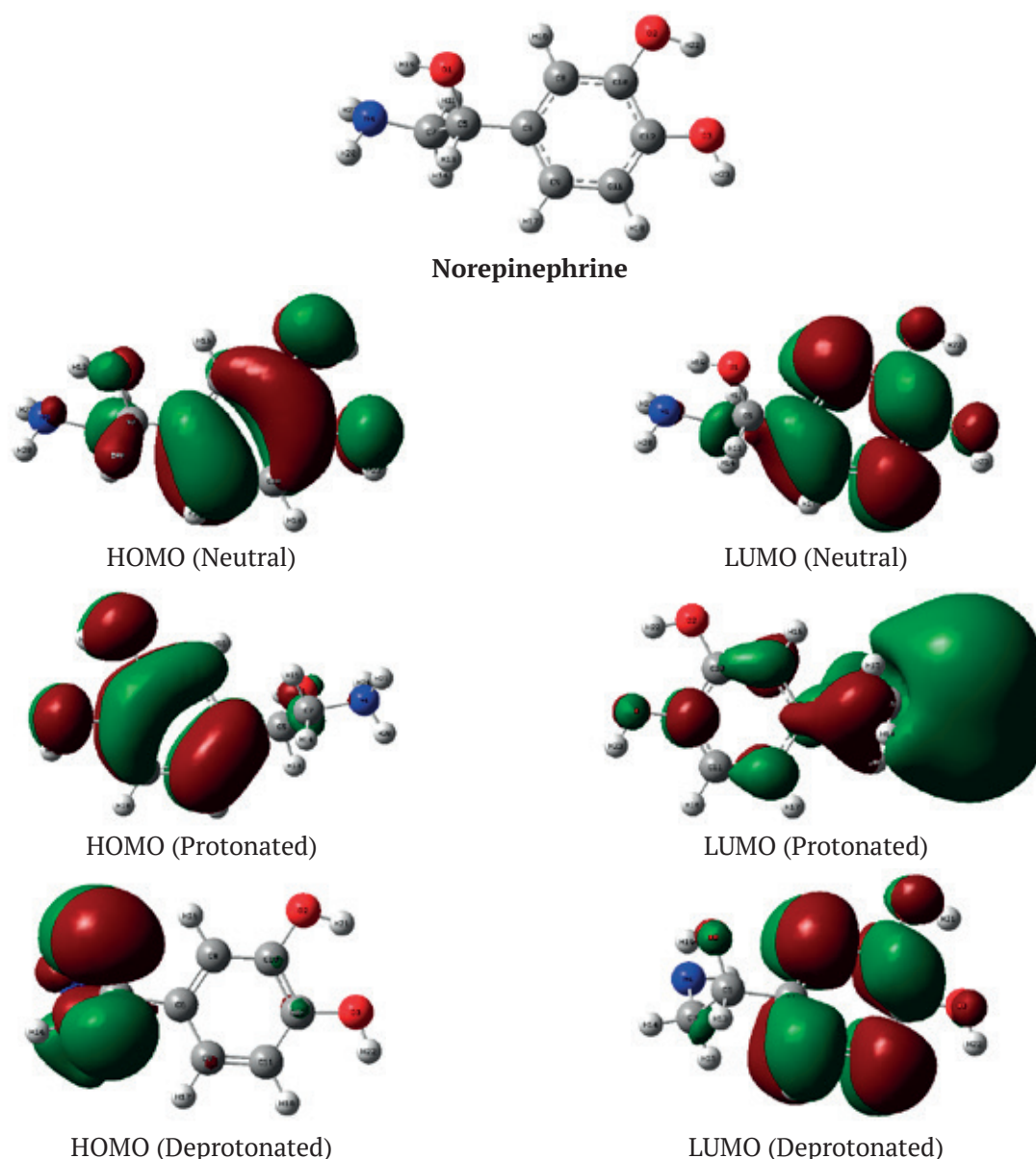


Fig. 4. Optimized structures, HOMO, and LUMO energies for Neutral, -protonated, and deprotonated

the lobes in the HOMO and LUMO of amphetamine. For example, in the protonated form, the nitrogen atom has a positive charge and a smaller lobe in the HOMO, while in the deprotonated form, the nitrogen atom has a negative charge and a larger lobe in the LUMO. The electron density is more pronounced in regions with larger and same-signed lobes. For instance, in amphetamine's HOMO, electron density concentrates on the nitrogen atom and its double-bond-connected carbon atoms. Conversely, in amphetamine's LUMO, electron density mostly concentrates on

its double-bond-connected carbon atoms on a benzene ring. Regions with smaller or oppositely-signed lobes have lower electron density.

4. Conclusions

This work investigated the reactivity, electronic characteristics, and molecular interactions of five different forms of monoamine neurotransmitters: deprotonated, protonated, and neutral. Various quantum chemical methods were used to analyze their structural, energetic, and optical characteristics. The protonation states of these

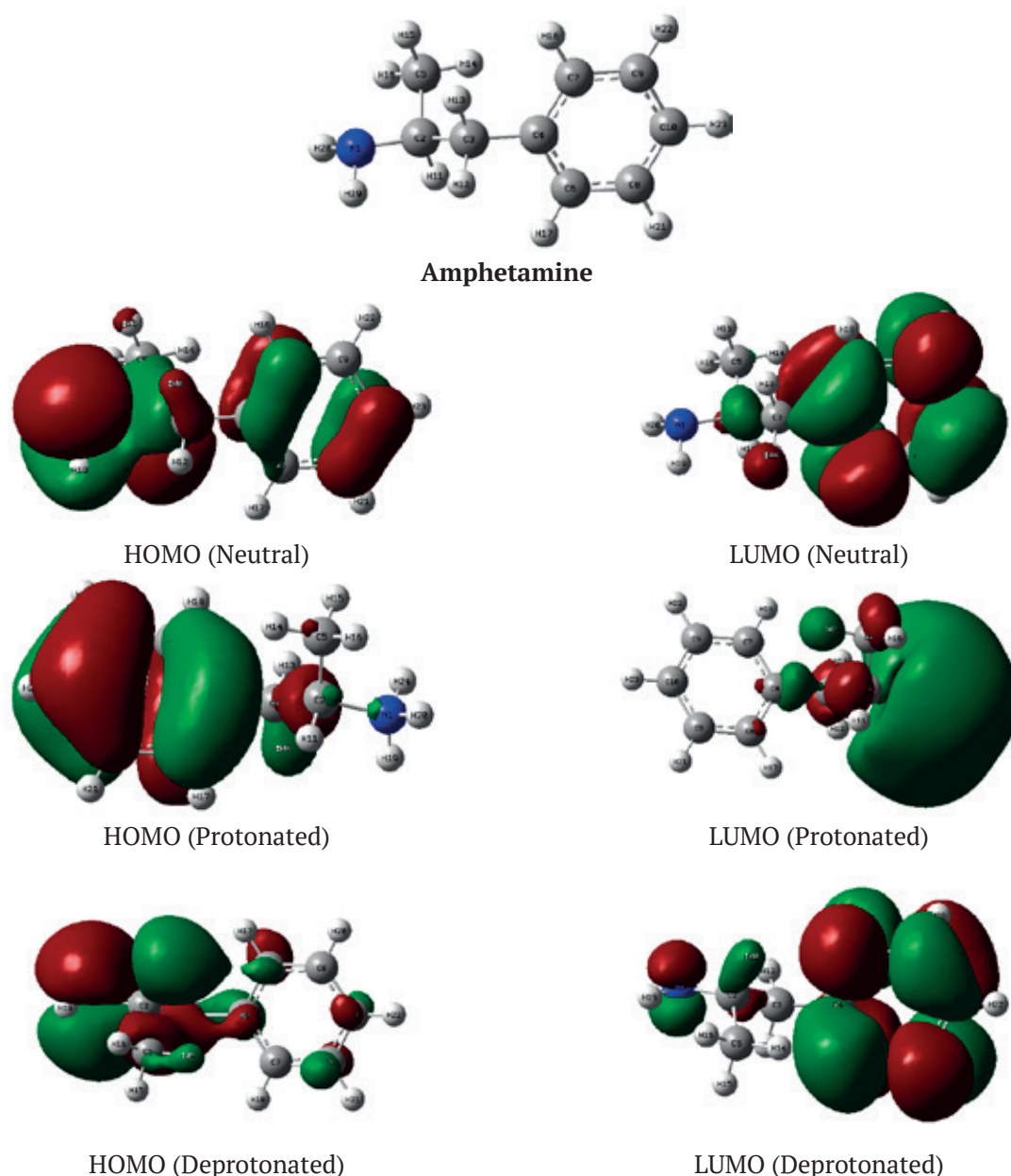


Fig. 5. Optimized structures, HOMO, and LUMO energies for Neutral, -protonated, and deprotonated

compounds changed the weak intermolecular forces and hydrogen bonding patterns that they showed. Lewis structures and NBO analysis were demonstrated to be effective tools for observing their resonance and the motion of the electrons. It was demonstrated that protons added or removed altered the molecular orbitals and energy gaps of these compounds, potentially affecting their reaction. It was also found that their nonlinear optical properties changed depending on their polarizability and hyperpolarizability indices.

This meant that they could be used in optical devices. The results provided insights into the molecular mechanisms and functions of these neurotransmitters in the brain and suggested new avenues for their applications in nanotechnology.

Contribution of the authors

The authors contributed equally to this article.

Conflict of interests

The authors declare that they have no known competing financial interests or personal

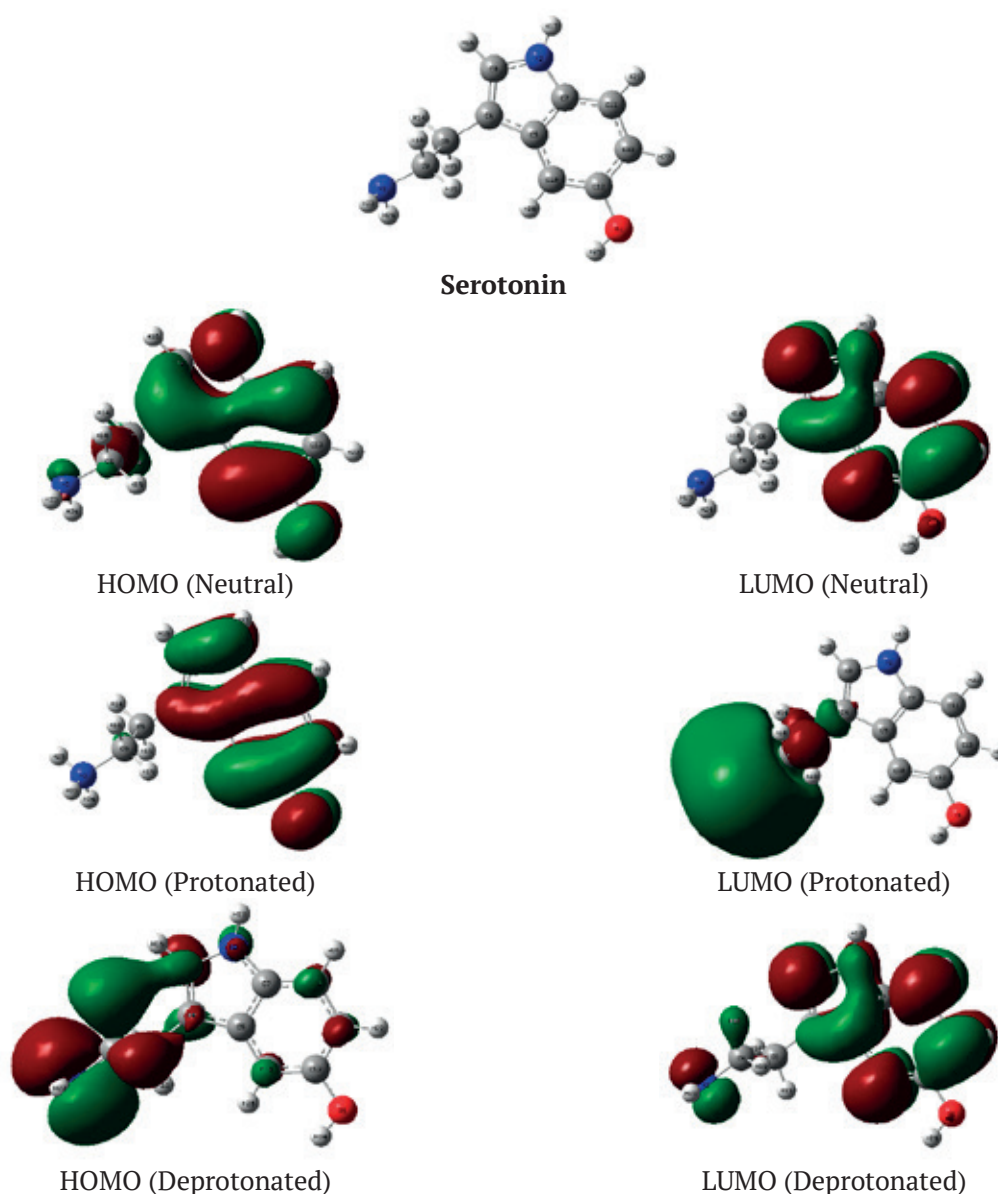


Fig. 6. Optimized structures, HOMO, and LUMO energies for Neutral, -protonated, and deprotonated

relationships that could have influenced the work reported in this paper.

References

1. Fleckenstein A. E., Volz T. J., Riddle E. L., Gibb J. W., Hanson G. R. New insights into the mechanism of action of amphetamines. *Annual Review of Pharmacology and Toxicology*. 2007;47: 681–698. <https://doi.org/10.1146/annurev.pharmtox.47.120505.105140>
2. Sulzer D., Sonders M. S., Poulsen N. W., Galli A. Mechanisms of neurotransmitter release by amphetamines: a review. *Progress in Neurobiology*. 2005;75: 406–433. <https://doi.org/10.1016/j.pneurobio.2005.04.003>
3. Kahlig K. M., Binda F., Khoshbouei H., ... Galli A. Amphetamine induces dopamine efflux through a dopamine transporter channel. *Proceedings of the National Academy of Sciences*. 2005;102: 3495–3500. <https://doi.org/10.1073/pnas.0407737102>
4. Gatley S. J., Pan D., Chen R., Chaturvedi G., Ding Y.-S. Affinities of methylphenidate derivatives for dopamine, norepinephrine and serotonin transporters. *Life Sciences*. 1996;58: PL231–PL239. [https://doi.org/10.1016/0024-3205\(96\)00052-5](https://doi.org/10.1016/0024-3205(96)00052-5)
5. Jones R. S. G. Tryptamine: a neuromodulator or neurotransmitter in mammalian brain? *Progress in Neurobiology*. 1982;19: 117–139. [https://doi.org/10.1016/0301-0082\(82\)90023-5](https://doi.org/10.1016/0301-0082(82)90023-5)

Tryptamine

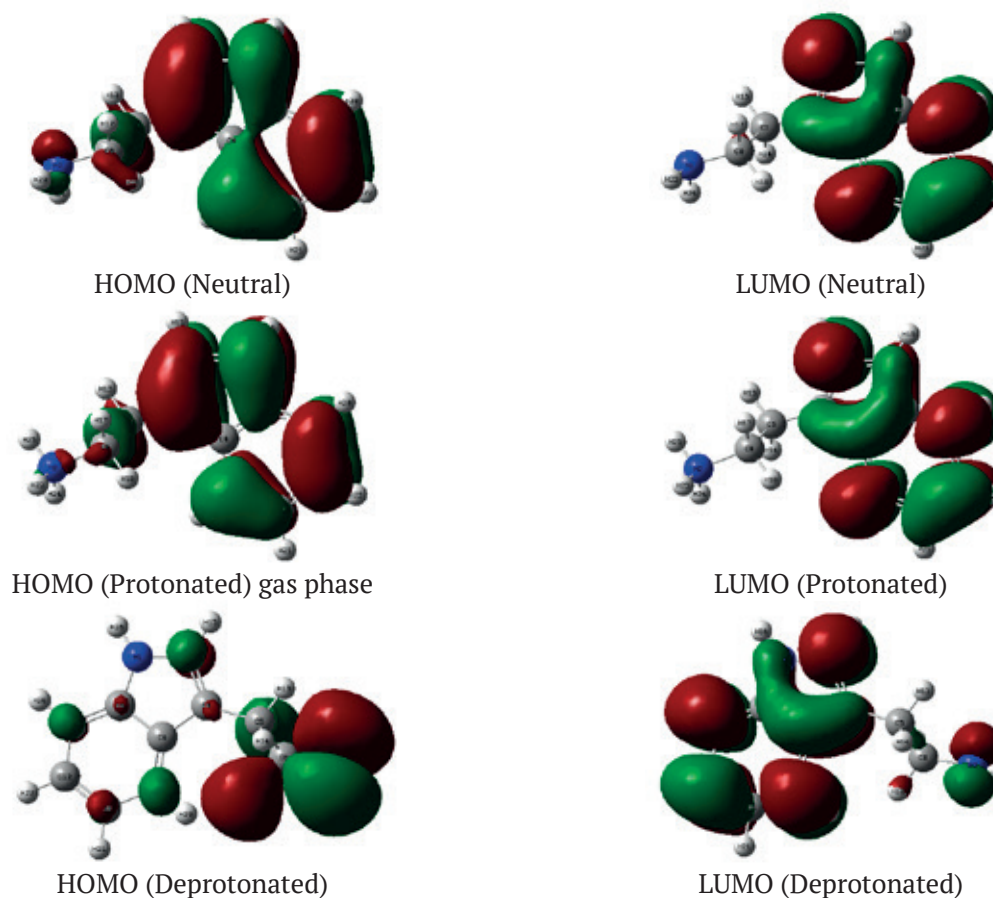


Fig. 7. Optimized structures, HOMO, and LUMO energies for Neutral, protonated, and deprotonated

6. Hobza P., Rezac J. Introduction: noncovalent interactions. *Chemical Reviews*. 2016;116: 4911–4912. <https://doi.org/10.1021/acs.chemrev.6b00247>

7. Lu T., Chen Q. Independent gradient model based on Hirshfeld partition: A new method for visual study of interactions in chemical systems. *Journal of Computational Chemistry*. 2022;43: 539–555. <https://doi.org/10.1002/jcc.26812>

8. Raffa R. B., Stagliano G. W., Spencer S. D. Protonation effect on drug affinity. *European Journal of Pharmacology*. 2004;483: 323–324. <https://doi.org/10.1016/j.ejphar.2003.10.019>

9. Saleh G., Gatti C., Presti L. L. Non-covalent interaction via the reduced density gradient: Independent atom model vs experimental multipolar electron densities. *Computational and Theoretical Chemistry*. 2012;998: 148–163. <https://doi.org/10.1016/j.comptc.2012.07.014>

10. Parameswari A. R., Rajalakshmi G., Kumaradhas P. A combined molecular docking and charge density analysis is a new approach for medicinal research to understand drug–receptor interaction: Curcumin–AChE model. *Chemico-Biological*

Interactions. 2015;225: 21–31. <https://doi.org/10.1016/j.cbi.2014.09.011>

11. Destro R., Soave R., Barzaghi M., Lo Presti L. Progress in the understanding of drug–receptor interactions. Part 1: experimental charge-density study of an angiotensin II receptor antagonist ($C_{30}H_{30}N_6O_3S$) at $T = 17$ K. *Chemistry – A European Journal*. 2005;11: 4621–4634. <https://doi.org/10.1002/chem.200400964>

12. Oliveira V. P., Marcial B. L., Machado F. B., Kraka E. Metal–halogen bonding seen through the eyes of vibrational spectroscopy. *Materials*. 2019;13: 55. <https://doi.org/10.3390/ma13010055>

13. Chandola P., Dwivedi J., Jamali M. C. Non-linear optical activity and biological evaluation of organic compounds by experimental and theoretical techniques. *European Chemical Bulletin*. 2023;12(4): 19608–19619. <https://doi.org/10.48047/ecb/2023.12.si4.1741>

14. Bhattacharya P. *Nonlinear optical probes for organic field effect transistors and halide perovskites*. Thesis. University of Missouri--Columbia: 2023, 142 p. Available at: <https://hdl.handle.net/10355/96071>

15. Mamad D. M., Rasul H. H., Awla A. H., Omer R. A. Insight into corrosion inhibition efficiency of imidazole-based molecules: a quantum chemical study. *Doklady Physical Chemistry*. 2023;511(2): 125–133. <https://doi.org/10.1134/s0012501623600043>
16. Rasul H. H., Mamad D. M., Azeez Y. H., Omer R. A., Omer K. A. Theoretical investigation on corrosion inhibition efficiency of some amino acid compounds *Computational and Theoretical Chemistry*. 2023;1225: 114177. <https://doi.org/10.1016/j.comptc.2023.114177>
17. Parlak A. E., Omar R. A., Koparir P., Salih M. I. Experimental, DFT and theoretical corrosion study for 4-(((4-ethyl-5-(thiophen-2-yl)-4H-1, 2, 4-triazole-3-yl) thio) methyl)-7, 8-dimethyl-2H-chromen-2-one. *Arabian Journal of Chemistry*. 2022;15: 104088. <https://doi.org/10.1016/j.arabjc.2022.104088>
18. Steinmann S. N., Corminboeuf C. Exploring the limits of density functional approximations for interaction energies of molecular precursors to organic electronics. *Journal of Chemical Theory and Computation*. 2012;8: 4305–4316. <https://doi.org/10.1021/ct300657h>
19. Anwar Omar R., Koparir P., Koparir M., Safin D. A. A novel cyclobutane-derived thiazole-thiourea hybrid with a potency against COVID-19 and tick-borne encephalitis: synthesis, characterization, and computational analysis. *Journal of Sulfur Chemistry*. 2023;45(1): 120–137. <https://doi.org/10.1080/17415993.2023.2260918>
20. Mamad D. M., Omer R. A., Othman K. A. Quantum chemical analysis of amino acids as anti-corrosion agents *Corrosion Reviews*. 2023;41(6), 703–717. <https://doi.org/10.1515/correv-2023-0031>
21. Boukabcha N., Benmohammed A., Belhachemi M. H. M., ... Djafri A. Spectral investigation, TD-DFT study, Hirshfeld surface analysis, NCI-RDG, HOMO-LUMO, chemical reactivity and NLO properties of 1-(4-fluorobenzyl)-5-bromolindolin-2,3-dione. *Journal of Molecular Structure*. 2023;1285: 135492. <https://doi.org/10.1016/j.molstruc.2023.135492>
22. Omer R. A., Koparir P., Ahmed L. O. Characterization and inhibitor activity of two newly synthesized thiazole. *Journal of Bio-and Tribo-Corrosion*. 2022;8: 28. <https://doi.org/10.1007/s40735-021-00625-1>
23. Saidj M., Djafri A., Rahmani R., ... Chouaih A. Molecular structure, experimental and theoretical vibrational spectroscopy, (HOMO-LUMO, NBO) investigation, (RDG, AIM) analysis, (MEP, NLO) study and molecular docking of Ethyl-2-[[4-Ethyl-5-(Quinolin-8-yloxyMethyl)-4H-1, 2, 4-Triazol-3-yl] Sulfanyl] acetate. *Polycyclic Aromatic Compounds*. 2023;43: 2152–2176. <https://doi.org/10.1080/10406638.2022.2039238>
24. Omar R. A., Koparir P., Sarac K., Koparir M., Safin D. A. A novel coumarin-triazole-thiophene hybrid: synthesis, characterization, ADMET prediction, molecular docking and molecular dynamics studies with a series of SARS-CoV-2 proteins. *Journal of Chemical Sciences*. 2023;135(1): 6. <https://doi.org/10.1007/s12039-022-02127-0>
25. Tang L., Zhu W. Computational design of high energy RDX-based derivatives: property prediction, intermolecular interactions, and decomposition mechanisms. *Molecules*. 2021;26(23): 7199. <https://doi.org/10.3390/molecules26237199>
26. Jumabaev A., Holikulov U., Hushvaktov H., Issaoui N., Absanov A. Intermolecular interactions in ethanol solution of OABA: Raman, FTIR, DFT, M062X, MEP, NBO, FMO, AIM, NCI, RDG analysis. *Journal of Molecular Liquids*. 2023;377: 121552. <https://doi.org/10.1016/j.molliq.2023.121552>
27. Bader R. F., Definition of molecular structure: by choice or by appeal to observation? *The Journal of Physical Chemistry A*. 2010;114: 7431–7444. <https://doi.org/10.1021/jp102748b>
28. Rozas I., Alkorta I., Elguero J. Behavior of ylides containing N, O, and C atoms as hydrogen bond acceptors. *Journal of the American Chemical Society*. 2000;122: 11154–11161. <https://doi.org/10.1021/ja0017864>
29. Omer R. A., Koparir P., Ahmed L. Theoretical determination of corrosion inhibitor activities of 4-allyl-5-(pyridin-4-yl)-4H-1, 2, 4-triazole-3-thiolthione tautomerism. *Indian Journal of Chemical Technology (IJCT)*. 2022;29: 75–81. <https://doi.org/10.56042/ijct.v29i1.51231>
30. Omer R., Koparir P., Koparir M., Rashid R., Ahmed L., Hama J. Synthesis, characterization and DFT study of 1-(3-Mesityl-3-methylcyclobutyl)-2-((4-phenyl-5-(thiophen-2-yl)-4H-1, 2, 4-triazol-3-yl) thio) ethan-1-one. *Protection of Metals and Physical Chemistry of Surfaces*. 2022;58: 1077–1089. <https://doi.org/10.1134/s2070205122050185>
31. Sandhu B., McLean A., Sinha A. S., ... Aakeröy C. B. Evaluating competing intermolecular interactions through molecular electrostatic potentials and hydrogen-bond propensities. *Crystal Growth & Design*. 2018;18: 466–478. <https://doi.org/10.1021/acs.cgd.7b01458>
32. Clark D. E. What has polar surface area ever done for drug discovery? *Future Medicinal Chemistry*. 2011;3: 469–484. <https://doi.org/10.4155/fmc.11.1>
33. Lipinski C. A. Drug-like properties and the causes of poor solubility and poor permeability. *Journal of Pharmacological and Toxicological Methods*. 2000;44: 235–249. [https://doi.org/10.1016/s1056-8719\(00\)00107-6](https://doi.org/10.1016/s1056-8719(00)00107-6)
34. Jain A. N. Surflex: fully automatic flexible molecular docking using a molecular similarity-based search engine. *Journal of Medicinal Chemistry*. 2003;46: 499–511. <https://doi.org/10.1021/jm020406h>

35. Silberstein L. L. Molecular refractivity and atomic interaction. II. *The London, Edinburgh, and Dublin Philosophical Magazine and Journal of Science*. 1917;3(198): 521–533. <https://doi.org/10.1080/14786440608635666>
36. Ranjith P., Ignatious A., Panicker C. Y., ... Anto P. Spectroscopic investigations, DFT calculations, molecular docking and MD simulations of 3-[(4-Carboxyphenyl) carbamoyl]-4-hydroxy-2-oxo-1, 2-dihydroxy quinoline-6-carboxylic acid. *Journal of Molecular Structure*. 2022;1264: 133315. <https://doi.org/10.1016/j.molstruc.2022.133315>
37. Sumathi D., Thanikachalam V., Bharanidharan S., Saleem H., Babu N. R. Vibrational spectroscopy (FT-IR, FT-Raman and UV) studies of E-[1-Methyl-2, 6-diphenyl-3-(propan-2-yl) piperidin-4-ylidene] amino 3-methylbenzoate] using DFT method. *International Journal of Scientific Reseach*. 2016;5(3): 694–713. Available at: [https://www.worldwidejournals.com/international-journal-of-scientific-research-\(IJSR\)/fileview.php?val=March_2016_1492757409_217.pdf](https://www.worldwidejournals.com/international-journal-of-scientific-research-(IJSR)/fileview.php?val=March_2016_1492757409_217.pdf)
38. Abbaz T., Bendjeddou A., Villemin D. Structure, electronic properties, NBO, NLO and chemical reactivity of bis (1, 4-dithiafulvalene) derivatives: functional density theory study. *International Journal of Advanced Chemistry*. 2017;6: 18–25. <https://doi.org/10.14419/ijac.v6i1.8668>
39. Villemin D., Abbaz T., Bendjeddou A. Molecular structure, HOMO, LUMO, MEP, natural bond orbital analysis of benzo and anthraquinodimethane derivatives. *Pharmaceutical and Biological Evaluations*. 2018;5(2), 27. <https://doi.org/10.26510/2394-0859.pbe.2018.04>
40. Abbaz T., Bendjeddou A., Villemin D. Molecular structure, NBO analysis, first hyper polarizability, and homo-lumo studies of π -extended tetrathiafulvalene (EXTTF) derivatives connected to π -nitro phenyl by density functional method. *International Journal of Advanced Chemistry*. 2018;6(1), 114–120. <https://doi.org/10.14419/ijac.v6i1.11126>
41. Rebaz O., Ahmed L., Koparir P., Jwameer H. Impact of solvent polarity on the molecular properties of dimetridazole. *El-Cezeri Fen ve Mühendislik Dergisi*. 2022;9: 740–747. <https://doi.org/10.31202/ecjse.1000757>
42. Khan M. U., Khalid M., Asim S., ... Imran M. Exploration of nonlinear optical properties of triphenylamine-dicyanovinylene coexisting donor- π -acceptor architecture by the modification of π -conjugated linker. *Frontiers in Materials*. 2021;8: 719971. <https://doi.org/10.3389/fmats.2021.719971>
43. Al-Shamiri H. A., Sakr M. E., Abdel-Latif S. A., ... Elwahy A. H. Experimental and theoretical studies of linear and non-linear optical properties of novel fused-triazine derivatives for advanced technological applications. *Scientific Reports*. 2022;12: 19937. <https://doi.org/10.1038/s41598-022-22311-z>
44. Atlam F. M., Awad M. K., El-Bastawissy E. A. Computational simulation of the effect of quantum chemical parameters on the molecular docking of HMG-CoA reductase drugs. *Journal of Molecular Structure*. 2014;1075: 311–326. <https://doi.org/10.1016/j.molstruc.2014.06.045>
45. Oldfield E. Chemical shifts in amino acids, peptides, and proteins: from quantum chemistry to drug design *Annual Review of Physical Chemistry*. 2002;53: 349–378. <https://doi.org/10.1002/chin.200249272>
46. Gallo M., Favila A., Glossman-Mitnik D. DFT studies of functionalized carbon nanotubes and fullerenes as nanovectors for drug delivery of antitubercular compounds. *Chemical Physics Letters*. 2007;447: 105–109. <https://doi.org/10.1016/j.cplett.2007.08.098>
47. Akbas E., Othman K. A., Çelikezen F. Ç., ... Mardinoglu A. Synthesis and biological evaluation of novel benzylidene thiazolo pyrimidin-3(5H)-one derivatives. *Polycyclic Aromatic Compounds*. 2023; 1–18. <https://doi.org/10.1080/10406638.2023.2228961>
48. Al-Fahemi J. H., Abdallah M., Gad E. A., Jahdaly B., Experimental and theoretical approach studies for melatonin drug as safely corrosion inhibitors for carbon steel using DFT. *Journal of Molecular Liquids*. 2016; 222: 1157–1163. <https://doi.org/10.1016/j.molliq.2016.07.085>
49. Bani-Yaseen A. D. Investigation on the impact of solvent on the photochemical properties of the photoactive anticancer drug Vemurafenib: a computational study. *Journal of Molecular Liquids*. 2021;322: 114900. <https://doi.org/10.1016/j.molliq.2020.114900>
50. Sustmann R. Orbital energy control of cycloaddition reactivity. *Physical Organic Chemistry–2*. 1974; 569–593. <https://doi.org/10.1016/b978-0-408-70681-0.50009-9>
51. Perveen M., Nazir S., Arshad A. W., ... Iqbal J. Therapeutic potential of graphitic carbon nitride as a drug delivery system for cisplatin (anticancer drug): a DFT approach. *Biophysical Chemistry*. 2020;267: 106461. <https://doi.org/10.1016/j.bpc.2020.106461>
52. Jaffar K., Riaz S., Afzal Q. Q., ... Al-Buriahi M. A. DFT approach towards therapeutic potential of phosphorene as a novel carrier for the delivery of felodipine (cardiovascular drug). *Computational and Theoretical Chemistry*. 2022;1212: 113724. <https://doi.org/10.1016/j.comptc.2022.113724>
53. Lewis D. F. Frontier orbitals in chemical and biological activity: quantitative relationships and

mechanistic implications. *Drug Metabolism Reviews*. 1999;31: 755–816. <https://doi.org/10.1081/dmr-100101943>

Information about the authors

Yousif Hussein Azeez, MSc in Advanced Materials Science, Lecturer at the Department of physics, Halabja University (Iraq).

<https://orcid.org/0000-0001-5357-7856>

yousif.husain@uoh.edu.iq

Khdar Ahmed Othman, MSc In Organic Chemistry, Lecturer at the Department of Chemistry, Faculty of Science and Health, Koya University, (Kurdistan Region – F.R., Iraq).

<https://orcid.org/0000-0002-7763-2976>

khdar.ahmed@koyauniversity.org

Rebaz Anwar Omer, PhD in Organic Chemistry, Head of Chemistry Department, Faculty of Science and Health, Koya University (Kurdistan Region – F.R., Iraq), Department of Pharmacy, College of Pharmacy, Knowledge University (Erbil, Iraq).

<https://orcid.org/0000-0002-3774-6071>

rebaz.anwar@koyauniversity.org

Aryan Fathulla Qader, PhD in Analytical Chemistry, Lecturer at the Department of Chemistry, Faculty of Science and Health, Koya University (Kurdistan Region – F.R., Iraq).

<https://orcid.org/0000-0002-2547-7708>

aryan.qader@koyauniversity.org

Received 28.10.2023; approved after reviewing 22.12.2023; accepted for publication 15.01.2024; published online 01.10.2024.



Original articles

Research article

<https://doi.org/10.17308/kcmf.2024.26/12215>**Formation of silver nanocrystals in Ag-Si composite films obtained by ion beam sputtering**K. A. Barkov¹✉, V. A. Terekhov¹, D. N. Nesterov¹, K. E. Velichko^{1,2}, S. A. Ivkov¹, N. S. Buylov^{1,2}, S. V. Kannykin¹, I. E. Zanin¹, B. V. Agapov^{1,2}, S. V. Rodivilov², E. S. Kersnovsky¹, I. V. Polshin¹, S. V. Ryabtsev¹, M. V. Grechkina¹, A. V. Sitnikov³¹Voronezh State University,
1 Universitetskaya pl., Voronezh 394018, Russian Federation²Research Institute of Electronic Technology,
5 Staryh Bolshevikov st., Voronezh 394033, Russian Federation³Voronezh State Technical University,
84 20 letiya Oktyabrya st., Voronezh 394006, Russian Federation**Abstract**

Nanostructured composite films based on Ag-Si containing silver nanoparticles are used as a material for SERS (Surface-enhanced Raman spectroscopy) substrates, plasmonic back reflector, nanoplasmonic sensors, nonlinear optics devices, memristor structures, etc. Due to the widespread use of nanocomposite films based on Ag-Si, there is a need to develop simple and affordable methods for their production compatible with semiconductor technology. Therefore, this work is devoted to the production of an Ag₈₀Si₂₀ nanocomposite film with a high silver content (80 at.%) by ion-beam sputtering with simultaneous control of the morphology, structure, phase composition and electrical properties of the manufactured sample. As a result of complex studies using X-ray diffraction, ultra-soft X-ray emission spectroscopy, SEM and AFM microscopy, it was found that the film is a nanocomposite material based on silver nanoparticles with an average size of ~15÷30 nm. At the same time, some silver nanoparticles are in direct contact, while some Ag nanoparticles are isolated from each other by a shell of silicon dioxide SiO₂ and amorphous silicon *a*-Si. Such a nanogranulated structure of the Ag₈₀Si₂₀ film causes the presence in the test sample of the effect of switching from a high-resistance state (880 Ohm) to a low-resistance state (~1 Ohm) under the action of a voltage of ~0.2 V. As a result of the formation of conductive filaments (CF) of Ag atoms in the dielectric layer between the silver granules.

Keywords: Silver nanoparticles, Ag NPs, Ag-Si films, Ultra-soft X-ray emission spectroscopy, Ion-beam sputtering**Funding:** This work was funded by the Russian Science Foundation, under grant number 23-79-10294, <https://rscf.ru/project/23-79-10294/>**Acknowledgments:** The research results were partially obtained using the equipment of the Voronezh State University's Center for Collective Use. URL: <http://ckp.vsu.ru>**For citation:** Barkov K. A., Terekhov V. A., Nesterov D. N., Velichko K. E., Ivkov S. A., Buylov N. S., Kannykin S. V., Zanin I. E., Agapov B. V., Rodivilov S. V., Kersnovsky E. S., Polshin I. V., Ryabtsev S. V., Grechkina M. V., Sitnikov A. V. Formation of silver nanocrystals in Ag-Si composite films obtained by ion beam sputtering. *Condensed Matter and Interphases*. 2024;26(3): 407–416. <https://doi.org/10.17308/kcmf.2024.26/12215>**Для цитирования:** Барков К. А., Терехов В. А., Нестеров Д. Н., Величко К. Е., Ивков С. А., Буйлов Н. С., Канныкин С. В., Занин И. Е., Агапов Б. В., Родивилов С. В., Керсновский Е. С., Польшин И. В., Рябцев С. В., Гречкина М. В., Ситников А. В. Формирование нанокристаллов серебра в композитных пленках Ag-Si, полученных ионно-лучевым распылением. *Конденсированные среды и межфазные границы*. 2024;26(3): 407–416. <https://doi.org/10.17308/kcmf.2024.26/12215>✉ Konstantin A. Barkov, e-mail: barkov@phys.vsu.ru

© Barkov K. A., Terekhov V. A., Nesterov D. N., Velichko K. E., Ivkov S. A., Buylov N. S., Kannykin S. V., Zanin I. E., Agapov B. V., Rodivilov S. V., Kersnovsky E. S., Polshin I. V., Ryabtsev S. V., Grechkina M. V., Sitnikov A. V., 2024



The content is available under Creative Commons Attribution 4.0 License.

1. Introduction

Nanostructured composite materials containing silver nanoparticles, due to their ability to amplify the electromagnetic field near the surface of metal nanoparticles when interacting with light (surface plasmon resonance), are a promising material for the manufacturing technology of SERS substrates used for high-precision diagnostics and detection of very low concentrations of material by Raman spectroscopy [1–3]. In addition, silver nanoparticles are used to create structures with a plasmonic back reflectors in order to increase the efficiency of solar cells [4,5], nanoplasmonic sensors [6] and nonlinear optics devices [7,8]. In addition, silicon decorated with silver nanoparticles is considered one of the candidates as an anode material for next-generation lithium-ion batteries with high energy density [9–11]. Despite the high theoretical capacity of 4200 mA·h/g of silicon, a strong volume change (> 300%) of the silicon anode occurs during the lithiation–delithiation process, which leads to its destruction and deterioration of electrochemical characteristics. Surface nanostructuring of a silicon anode using silver nanoparticles makes it possible to improve the conductivity of a silicon anode and reduce internal stresses when the volume of silicon changes, which leads to a significant increase in electrochemical characteristics [9–11]. It was shown in [9] that when using an Ag-Si nanocomposite film with a silver content of about 20% as an anode, the Coulomb efficiency reaches 95%, due to a decrease in the polarization of the anode due to the presence of silver nanoparticles. Currently, nanostructured Ag-Si and Ag-SiO_x films are of interest for creating random access memory (RAM), since they have the effect of switching from a high-resistance to a low-resistance state (memristor effect) [12–15]. Moreover, such structures are used as artificial electrical synapses for building neuromorphic computing systems. [16–18].

The widespread use of nanocomposite films based on Ag-Si leads to the need to develop simple and affordable methods for their production compatible with semiconductor technology. At the same time, additional difficulties are in the formation of metal nanoparticles in films with a high metal content as a result of their

coalescence into larger particles [19]. Therefore, this work is devoted to the production of an Ag₈₀Si₂₀ nanocomposite film with a high silver content (80 at.%) by ion-beam sputtering with simultaneous control of the morphology, structure, phase composition and electrical properties of the resulting sample.

2. Experimental

2.1 Preparation of the Ag₈₀Si₂₀ film by ion-beam sputtering

The Ag₈₀Si₂₀ film with a thickness of about 1.5 μm was obtained on a Si (100) substrate of the KDB-12 brand by ion-beam sputtering of a composite target (size 100x200 mm) made of pure silver Ag (99.99%) and Si (KDB-12) silicon strips with a size of 100x10 mm. To obtain the Ag₈₀Si₂₀ film of the desired atomic composition, silicon strips with a width of 10 mm were placed at a distance of 20 mm on the surface of the silver plate. The deposition was realized in a vacuum chamber (10⁻⁶ Topp) filled with Ar (purity 99.992%) up to the total gas pressure 8·10⁻⁴ Topp. A magnetic system consisting of permanent magnets, a magnetic circuit and an anode was used as a source of ion-beam sputtering. Argon ionization is carried out in the gap of the magnetic circuit located in the immediate vicinity of the anode, to which a positive displacement of 4 kV is applied. The optimal plasma current is ~170 μA. The sputtering coefficients of Ag and Si were 11.8 [20] and 1.5 [21], respectively. This mode ensures the deposition rate of the Ag₈₀Si₂₀ film ~1.5 μ/h. The ion beam sputtering technique is described in more detail in the works [20,21].

2.2 Methods of characterization of the Ag₈₀Si₂₀ ion-beam film

The atomic composition of the film was determined using a JEOL JSM-6380LV scanning electron microscope (SEM) with an INCA Energy 250 microanalysis attachment at a primary electron energy of 5 keV.

The structure of the sample was analyzed using a PANalytical Empyrean B.V. X-ray diffractometer with Cu Kα_{1,2}-radiation λ = 1.542 Å.

The surface morphology of the Ag₈₀Si₂₀ ion-beam film was analyzed using the Solver P47 NT-MDT scanning atomic force microscope (AFM) in the 1x1 μm scanning area.

The phase composition of the $\text{Ag}_{80}\text{Si}_{20}$ film was determined using a unique technique of ultra-soft X-ray emission spectroscopy (USXES) implemented on the RSM-500 spectrometer. This method allows recording the characteristic X-ray $\text{Si } L_{2,3}$ radiation resulting from electron transitions from the valence band to the $\text{Si } 2p$ core level. As a result, the USXES method provides information about the density of electronic states in the valence band, which makes it possible to detect the presence of Si-Si or Si-O bonds, regardless of the degree of ordering of the atomic structure of the film [22,23]. Modeling using reference spectra makes it possible to determine the contribution of amorphous, crystalline and oxide/suboxide phases of silicon in experimental $\text{Si } L_{2,3}$ -spectra [24]. The excitation of X-ray emission $\text{Si } L_{2,3}$ -spectra was carried out by an electron beam with an energy E from 1 to 3 keV, which provided an analysis depth of 10 to 60 nm [25].

The electrophysical properties of the film were studied using the current-voltage characteristics (I-V) obtained using a probe installation and a digital oscilloscope Aktakom ASK-4106 in the range from -0.6 to +0.6 V.

3. Results and discussion

3.1 Surface morphology of the $\text{Ag}_{80}\text{Si}_{20}$ ion-beam film

As a result of ion-beam sputtering of a composite target based on Ag and Si, a sufficiently thick film ~ 1.6 microns thick is formed under these conditions, as can be seen in the cross

section SEM image (Fig. 1a). The analysis of the elemental composition by energy dispersive spectroscopy (EDS) shows that the resulting ion-beam film has an atomic composition of Ag 79 at.% and Si 21 at.% ($\text{Ag}_{79}\text{Si}_{21}$) close to the technologically specified $\text{Ag}_{80}\text{Si}_{20}$. The elemental composition was analyzed at a primary electron energy of 5 keV in order to limit the depth of the analyzed layer to the thickness of the film. The surface of the $\text{Ag}_{80}\text{Si}_{20}$ film has a continuous and homogeneous structure (Fig. 1b). At the same time, according to AFM data, the surface of the $\text{Ag}_{80}\text{Si}_{20}$ film is granular with an average granule size of ~30 nm, which is clearly visible in the three-dimensional AFM image obtained by scanning a $1 \times 1 \mu\text{m}$ surface area (Fig. 2a). On the surface of the $\text{Ag}_{80}\text{Si}_{20}$ film, both individual granules and conglomerates formed by these granules reaching sizes of ~100–200 nm are clearly distinguishable (Fig. 2a). The average surface roughness of the $\text{Ag}_{80}\text{Si}_{20}$ film is in the range of $2.5 \div 3 \text{ nm}$, while some local relief inhomogeneities reach a height of $40 \div 70 \text{ nm}$.

The formation of granular nanoparticles in the $\text{Ag}_{80}\text{Si}_{20}$ film is clearly visible in the AFM image obtained in phase contrast mode with a scanning area of $1 \times 1 \mu\text{m}$ (Fig. 2b). At the same time, it is clearly visible from Fig. 2b that some nanoparticles are in direct contact, while some of the nanoparticles are surrounded by a shell with a different kind of contrast (light areas in Fig. 2b). Based on the atomic composition and AFM images of the $\text{Ag}_{80}\text{Si}_{20}$ film, it can be assumed that the nanogranules are formed on

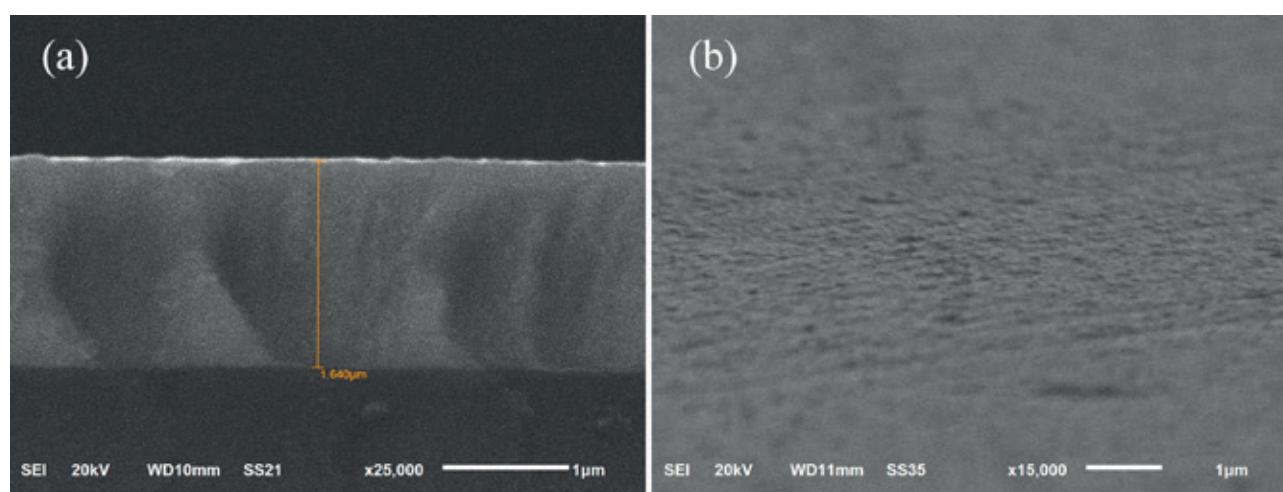


Fig. 1. SEM images of the cross section (a) and the surface (b) of the $\text{Ag}_{80}\text{Si}_{20}$ ion-beam film

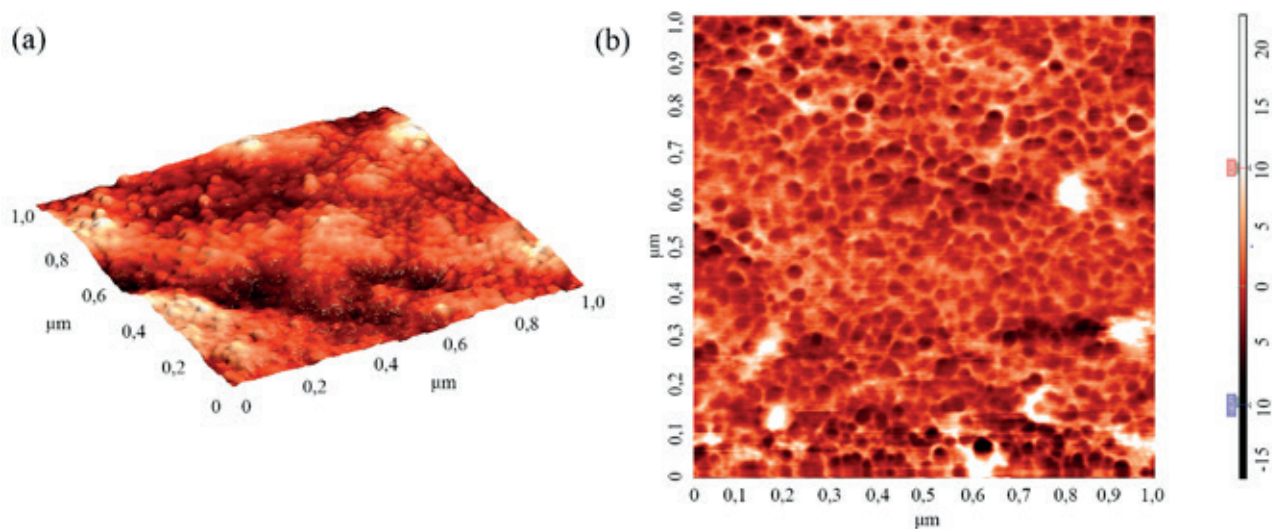


Fig. 2. Three-dimensional AFM image of the surface of the $\text{Ag}_{80}\text{Si}_{20}$ film (a) and phase contrast (b) obtained with a scanning area of $1 \times 1 \mu\text{m}$

the basis of silver, and the shell separating them is formed by silicon. Therefore, X-ray diffraction and X-ray spectroscopic studies were carried out to unambiguously answer the question about the phase composition of granules and shells in the $\text{Ag}_{80}\text{Si}_{20}$ film.

3.2. Structure and phase composition of the $\text{Ag}_{80}\text{Si}_{20}$ ion-beam film

Fig. 3 shows XRD patterns of the $\text{Ag}_{80}\text{Si}_{20}$ ion-beam film, as well as pure silver (99.99%) and polycrystalline silicon (poly-Si). The X-ray diffraction pattern of the $\text{Ag}_{80}\text{Si}_{20}$ ion-beam film shows XRD lines at values $2\theta = 38.20^\circ, 44.10^\circ, 64.30^\circ, 77.15^\circ$, corresponding to the values of d -spacings 2.356 Å, 2.054 Å, 1.448 Å, 1.236 Å, respectively. All of these XRD lines are associated with reflections from the crystallographic planes Ag (111), Ag (200), Ag (220), Ag (222) and Ag (400) (ICDD PDF-2, Card No. 00-004-0783). At the same time, all XRD reflexes in the $\text{Ag}_{80}\text{Si}_{20}$ film are greatly expanded compared to similar reflexes in the pure Ag standard, which indicates a small size of the crystallites. To estimate the average size of the crystallites by broadening the diffraction line, a section of the XRD pattern in the area of the Ag (111) line was recorded separately in a step-by-step mode with a long accumulation time in pure silver (Fig. 4a) and an $\text{Ag}_{80}\text{Si}_{20}$ ion-beam film (Fig. 4b). The Ag (111) XRD lines obtained in this way were decomposed on

the double line $\text{CuK}\alpha_1, \text{K}\alpha_2$ by Lorentz functions according to the standard procedure described in the [26–28]. Fig. 4 shows that the half-width $\text{K}\alpha_1$ of the Ag (111) reflex ($0.35 \text{ } 2\theta \text{ deg.}$) is significantly larger compared to the same reflex in pure silver ($0.12 \text{ } 2\theta \text{ deg.}$). Using the values of the half-width and position of the $\text{K}\alpha_1$ component, the average sizes of silver crystallites in the $\text{Ag}_{80}\text{Si}_{20}$ film were determined using the Debye-Scherrer formula, which amounted to $\sim 15 \text{ nm}$, which is consistent with AFM data. Thus, according to the results of X-ray diffraction analysis, silver in the ion-beam film $\text{Ag}_{80}\text{Si}_{20}$ is in a nanocrystalline state. At the same time, no crystalline phases based on silicon were detected in this film according to XRD data. Therefore, further studies of the phase composition of this sample will be carried out using the USXES method.

X-ray emission Si $L_{2,3}$ -spectra of the $\text{Ag}_{80}\text{Si}_{20}$ film obtained at analysis depths of 10, 35 and 60 nm are shown in Fig. 5. Two intensity peaks are observed in all X-ray spectra at $E = 89$ and 94.5 eV . The presence of these intensity maxima is due to the presence of Si 3s and O 2p states and is characteristic of the SiO_2 silicon dioxide spectrum [29,30], the spectrum of which is shown in the same figure for clarity. In addition, the formation of the silicon oxide phase in the $\text{Ag}_{80}\text{Si}_{20}$ film is additionally evidenced by the presence of a long-wavelength satellite in the X-ray spectrum at 77 eV. However, in all X-ray

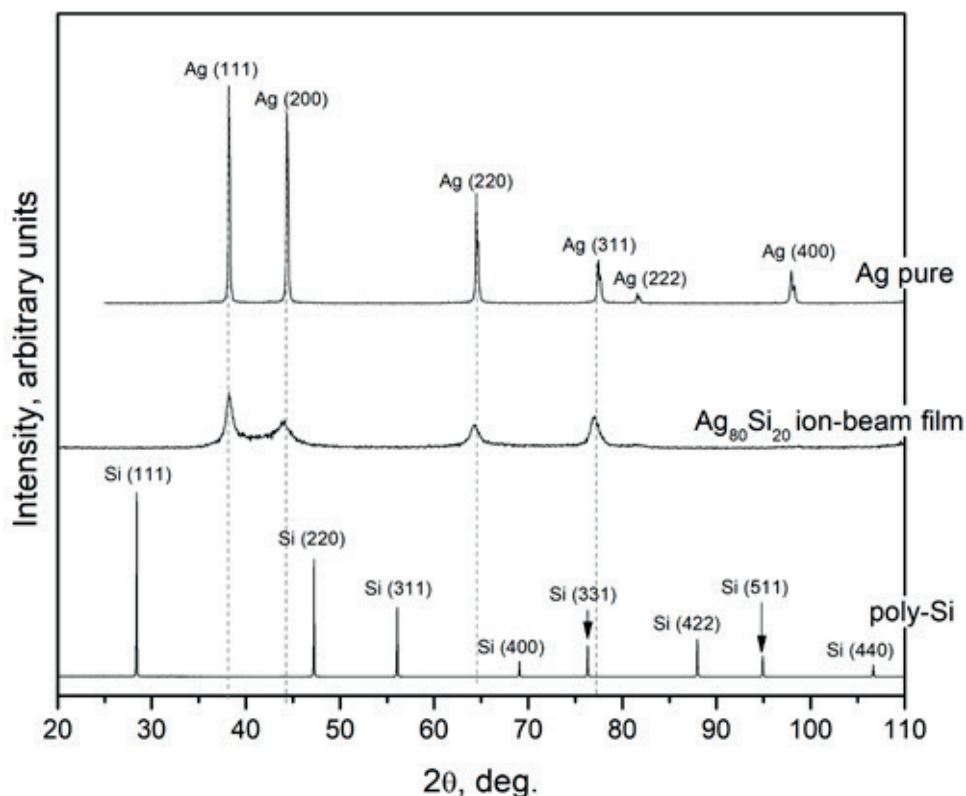


Fig. 3. XRD patterns of the $Ag_{80}Si_{20}$ ion-beam film, as well as polysilicon and pure silver standards

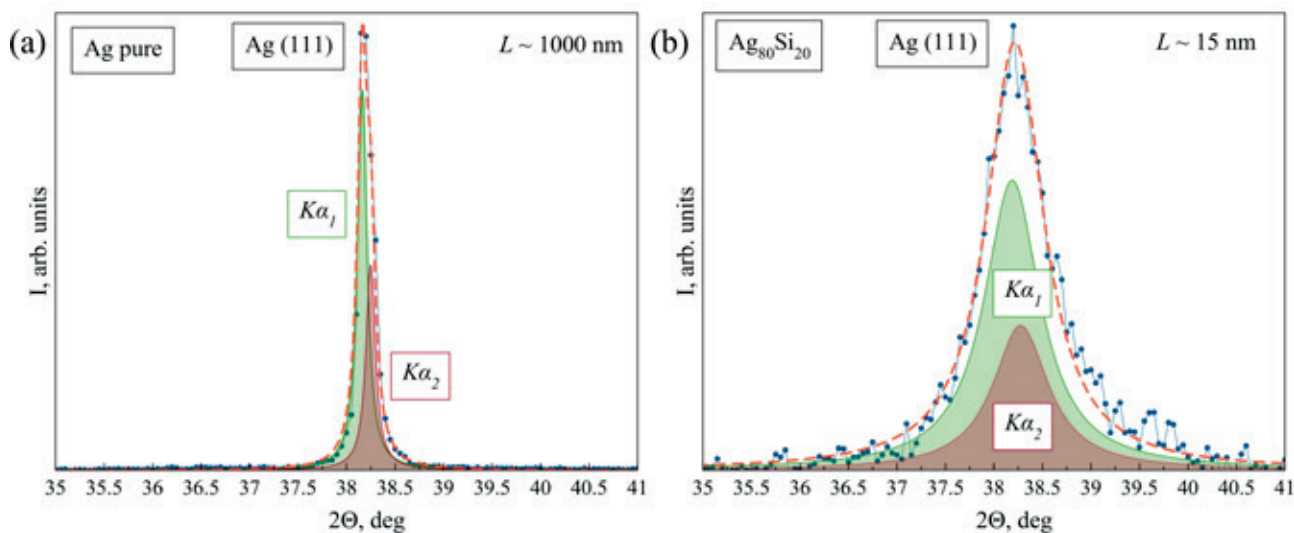


Fig. 4. XRD patterns of the $Ag_{80}Si_{20}$ ion-beam film and pure silver, recorded with a long accumulation time in the area of the Ag (111) line, as well as the result of their decomposition into components Ka_1 and Ka_2 by Lorentz functions

spectra of the $Ag_{80}Si_{20}$ film, the intensity in the region of 92 eV is noticeably higher compared to the SiO_2 spectrum. Such an increase in the intensity of the spectrum at 92 eV is due to the presence of a non-oxidized silicon phase in the $Ag_{80}Si_{20}$ film, the maximum of which is in this

energy region. To identify the phase of non-oxidized silicon in the $Ag_{80}Si_{20}$ film, experimental X-ray spectra based on standards were simulated [24]. The simulated spectra are shown in Fig. 5 as solid red lines. The simulation results show that in the surface layer of the $Ag_{80}Si_{20}$ film

with a depth of 10 nm, silicon is indeed mainly contained in the form of the SiO_2 phase, however, part of the silicon atoms (about 10%) is in the amorphous silicon a -Si phase. At the same time, with an increase in the depth of analysis to 35 nm, it leads to an increase in the a -Si content to 35%, which may be due to a decrease in the influence of the surface oxide. A further increase in the depth of analysis to 60 nm does not lead to a change in the shape of the X-ray spectrum, which indicates the uniformity of the phase composition of the $\text{Ag}_{80}\text{Si}_{20}$ film in depth. Thus, according to X-ray diffraction and ultra-soft X-ray emission spectroscopy, the $\text{Ag}_{80}\text{Si}_{20}$ ion-beam film is a nanocomposite material containing silver nanogranelles with an average size of about 15 nm, separated by a layer based on silicon dioxide and amorphous silicon.

3.3. Electrical properties of $\text{Ag}_{80}\text{Si}_{20}$ ion beam film

To study the electrical properties of the $\text{Ag}_{80}\text{Si}_{20}$ ion beam film, the current-voltage characteristics in the plane geometry of the sample were measured (Fig. 6). It can be seen from Figure 6 that with an increase in voltage from 0 to 0.6 V on the I-V characteristic in the 0.2 V region, there is an abrupt change in the recorded current values from $1.5 \cdot 10^{-4}$ to 0.1 A (by almost three orders of magnitude), the value of which increases smoothly with a further increase in the applied voltage, which is clearly visible on a logarithmic scale, shown in the box to Fig. 6. The evaluation of the resistance values R of the $\text{Ag}_{80}\text{Si}_{20}$ film in two linear sections reveals the effect of switching at 0.2 V from the high-resistance state of the film (~ 880 Ohm) to the low-resistance (~ 1 Ohm). At

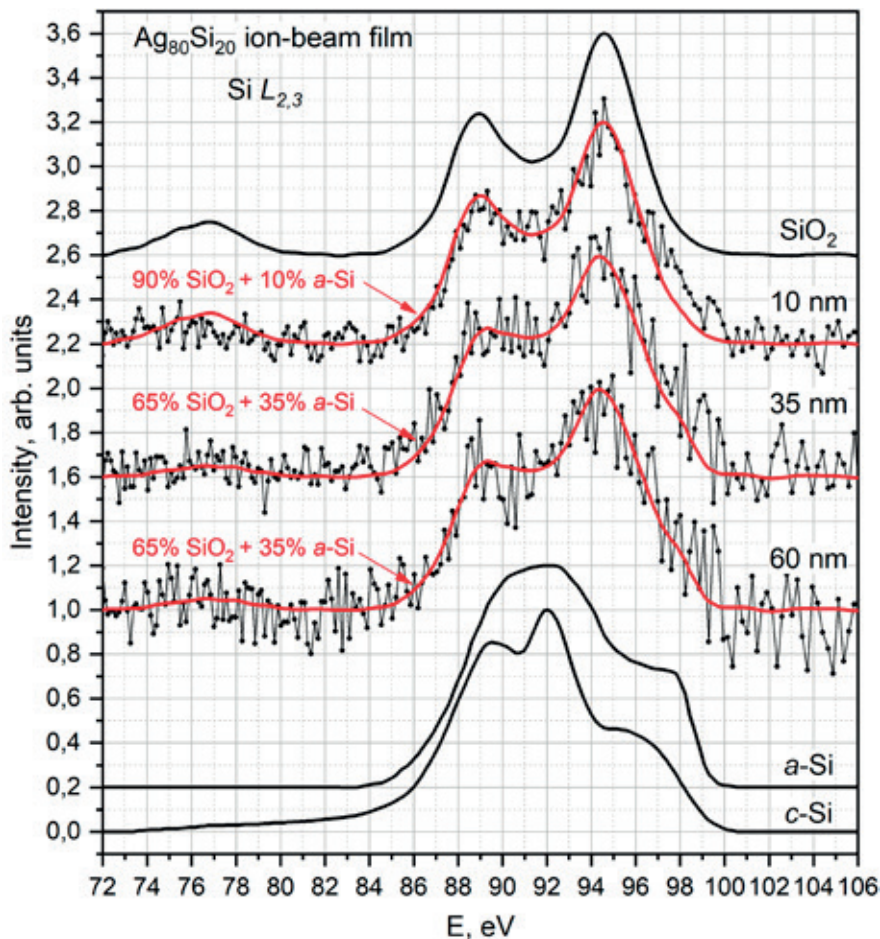


Fig. 5. X-ray emission $\text{Si } L_{2,3}$ -spectra of the $\text{Ag}_{80}\text{Si}_{20}$ film obtained at analysis depths of 10, 35 and 60 nm, as well as spectra of standards of crystalline silicon (c -Si), amorphous silicon (a -Si) and silicon dioxide (SiO_2). The experimental spectrum is represented by dots, the model is represented by a solid red line

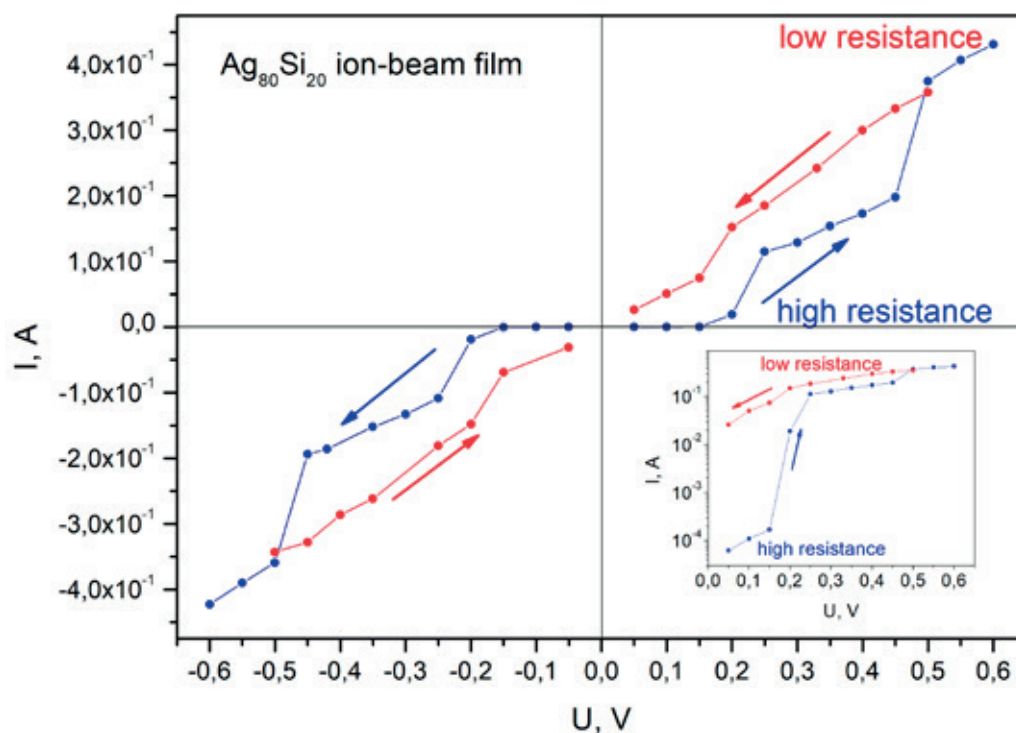


Fig. 6. Current-voltage curve of the ion beam film $\text{Ag}_{80}\text{Si}_{20}$. The insert shows a straight branch of the I - V curve on a logarithmic scale

the same time, in the case of a decrease in the voltage applied to the film from 0.6 to 0.05 V, the film remains in a low-resistance state until the current polarity changes, and hysteresis can be seen on the I - V characteristic. A similar character of the I - V curves was observed in the case of nanogranulated silver films obtained by thermal evaporation followed by oxidation at 100 °C [31], in Ag-SiO_2 nanocomposite films obtained by the sol-gel method with an Ag content of ~50% [14], in Ag-SiO_x nanocomposite structures [12, 13]. In such films, silver nanoparticles are mostly isolated either by an oxide layer or by a dielectric matrix, and only individual particles of the system come into contact with each other. The state of the film in which individual particles are on the verge of forming a bound system is called the percolation threshold. In such a system, switching can be associated with various mechanisms of current flow: thermally induced tunneling at low fields, and field-induced tunneling at high fields [14, 32]. On the other hand, the switching effect may be associated with the formation of conductive filaments (CF) in the dielectric layer (in our case $\text{SiO}_2 + a\text{-Si}$) between the silver granules under the action of voltage [12, 13, 32]. The formation

of conductive filaments in the dielectric is due to the interaction of Ag atoms on the surface of nanogranules with broken Si bonds, followed by diffusion and gradual accumulation of Ag atoms in the dielectric [13]. The second mechanism describing the switching effect in this case seems to be predominant, since the studied ion-beam film $\text{Ag}_{80}\text{Si}_{20}$ after switching to a low-resistance state does not return to a high-resistance state when the electric voltage is removed, which indicates structural changes in the film.

4. Conclusions

As a result of comprehensive studies of the morphology, structure and phase composition of the $\text{Ag}_{80}\text{Si}_{20}$ film with a high silver content (80 at.%) obtained by ion beam sputtering, it was found that the film is a nanocomposite material. According to XRD and AFM microscopy, the $\text{Ag}_{80}\text{Si}_{20}$ film is nanogranulated with an average size of silver granules ~15÷30 nm. Some silver nanoparticles are in direct contact, while some Ag nanoparticles are isolated from each other by a shell, which, according to ultra-soft X-ray emission spectroscopy, consists of silicon dioxide SiO_2 and amorphous silicon $a\text{-Si}$. At the same

time, in the surface layer of the $\text{Ag}_{80}\text{Si}_{20}$ film with a depth of 10 nm, silicon is mainly contained in the form of the SiO_2 phase, and only about 10% of silicon atoms are in the amorphous silicon α -Si phase. At the same time, with an increase in the depth of analysis to 35 and 60 nm leads to an increase in the content of α -Si up to 35%. According to USXES data, the phase composition of the $\text{Ag}_{80}\text{Si}_{20}$ ion-beam film is uniform in depth. The nanogranulated structure of the $\text{Ag}_{80}\text{Si}_{20}$ film causes the presence in the test sample of the switching effect from a high-resistance state (880 Ohm) to a low-resistance state (~ 1 Ohm) under the influence of a voltage of ~ 0.2 V. The switching effect in this case may be associated with the formation of conductive filaments of Ag atoms in the dielectric layer (in our case $\text{SiO}_2 + \alpha$ -Si) between the silver granules.

Contribution of the authors

The authors contributed equally to this article.

Conflict of interests

The authors declare that they have no known competing financial interests or personal relationships that could have influenced the work reported in this paper.

References

1. Dzhagan V., Mazur N., Kapush O., ... Yukhymchuk V. Self-organized SERS substrates with efficient analyte enrichment in the hot Spots. *ACS Omega*. 2024;9(4): 4819–4830. <https://doi.org/10.1021/acsomega.3c08393>
2. Ermina A. A., Solodovchenko N. S., Levitskii V. S., ... Zharova Y. A. Plasmonic disordered array of hemispherical AgNPs on $\text{SiO}_2/\text{c-Si}$: their optical and SERS properties. *Materials Science in Semiconductor Processing*. 2024;169: 107861. <https://doi.org/10.1016/j.mssp.2023.107861>
3. Yang Z. W., Meng L. Y., Lin J. S., ... Li J. F. 3D hotspots platform for plasmon enhanced Raman and second harmonic generation spectroscopies and quantitative analysis. *Advanced Optical Materials*. 2019;7: 3–8. <https://doi.org/10.1002/adom.201901010>
4. Morawiec S., Mendes M. J., Priolo F., Crupi I. Plasmonic nanostructures for light trapping in thin-film solar cells. *Materials Science in Semiconductor Processing*. 2019;92: 10–18. <https://doi.org/10.1016/j.mssp.2018.04.035>
5. Atwater H. A., Polman A. Plasmonics for improved photovoltaic devices. *Nature Materials*. 2010;9: 205–213. <https://doi.org/10.1038/nmat2629>
6. Cesca T., Michieli N., Kalinic B., Balasa I. G., Rangel-Rojo R., Reyes-Esqueda J. A., Mattei G. Bidimensional ordered plasmonic nanoarrays for nonlinear optics, nanophotonics and biosensing applications. *Materials Science in Semiconductor Processing*. 2019;92: 2–9. <https://doi.org/10.1016/j.mssp.2018.03.025>
7. Lippitz M., Van Dijk M. A., Orrit M. Third-harmonic generation from single gold nanoparticles. *Nano Letters*. 2005;5: 799–802. <https://doi.org/10.1021/nl0502571>
8. Sato R., Ohnuma M., Oyoshi K., Takeda Y. Experimental investigation of nonlinear optical properties of Ag nanoparticles: Effects of size quantization. *Physical Review B*. 2014;90: 1–6. <https://doi.org/10.1103/PhysRevB.90.125417>
9. Polat D. B., Eryilmaz L., Keles O. Generation of agsi film by magnetron sputtering for use as anodes in lithium ion batteries. *ECS Meeting Abstracts*. 2015;MA2015-01: 514–514. <https://doi.org/10.1149/ma2015-01/2/514>
10. Liu B., Xu G., Jin C., ... Zhou L. The Si/Ag₂Si/Ag particles with the enhanced mechanical contact as anode material for lithium ion batteries. *Materials Letters*. 2020;280: 128536. <https://doi.org/10.1016/j.matlet.2020.128536>
11. Li S., Ma W., Luo B., ... Wang L. High-performance porous silicon/nanosilver anodes from industrial low-grade silicon for lithium-ion batteries. *ACS Applied Materials and Interfaces*. 2020;12: 49080–49089. <https://doi.org/10.1021/acsami.0c14157>
12. Li R., Yang H., Zhang Y., ... Huang P. Physical mechanisms and enhancement of endurance degradation of SiOx:Ag-based volatile memristors. *2023 Silicon Nanoelectronics Workshop (SNW)*. 2023;40: 117–118. <https://doi.org/10.23919/SNW57900.2023.10183918>
13. Ding X., Huang P., Zhao Y., Feng Y., Liu L. Understanding of the volatile and nonvolatile switching in Ag-based memristors. *IEEE Transactions on Electron Devices*. 2022;69: 1034–1040. <https://doi.org/10.1109/TED.2022.3144373>
14. Sarkar D. K., Cloutier F., El Khakani M. A. Electrical switching in sol-gel derived Ag-SiO₂ nanocomposite thin films. *Journal of Applied Physics*. 2005;97: 2–7. <https://doi.org/10.1063/1.1870112>
15. Dias C., Lv H., Picos R., ... Ventura J. Bipolar resistive switching in Si/Ag nanostructures. *Applied Surface Science*. 2017;424: 122–126. <https://doi.org/10.1016/j.apsusc.2017.01.140>
16. Cha J. H., Yang S. Y., Oh J., ... Choi S. Y. Conductive-bridging random-access memories for emerging neuromorphic computing. *Nanoscale*. 2020;12: 14339–14368. <https://doi.org/10.1039/d0nr01671c>
17. Sokolov A. S., Abbas H., Abbas Y., Choi C. Towards engineering in memristors for emerging me-

mory and neuromorphic computing: a review. *Journal of Semiconductors*. 2021;42(1): 013101. <https://doi.org/10.1088/1674-4926/42/1/013101>

18. Raeis-Hosseini N., Lim S., Hwang H., Rho J. Reliable $\text{Ge}_2\text{Sb}_2\text{Te}_5$ -integrated high-density nanoscale conductive bridge random access memory using facile nitrogen-doping strategy. *Advanced Electronic Materials*. 2018;4(11). <https://doi.org/10.1002/aelm.201800360>

19. Cuenya B. R. Synthesis and catalytic properties of metal nanoparticles: Size, shape, support, composition, and oxidation state effects. *Thin Solid Films*. 2010;518: 3127–3150. <https://doi.org/10.1016/j.tsf.2010.01.018>

20. Semenova A.A., Semenov A.P., Goodilin E.A., Semenova I.A. Synthesis of Plasmonic Photonic Crystal SiO_2 -Ag Nanostructures by Ion Beam Deposition of Silver Clusters onto Silica Microspheres. *Bulletin of the Russian Academy of Sciences: Physics*. 2019; 83: 1415–1418. <https://doi.org/10.3103/S1062873819110200>

21. Lunin L.S., Chebotarev S.N., Pashchenko A.S., Bolobanova L.N. Ion beam deposition of photoactive nanolayers for silicon solar cells. *Inorganic Materials*. 2012; 48: 439–444. <https://doi.org/10.1134/S0020168512050111>

22. Saad A. M., Fedotov A. K., Fedotova J. A., ... Sitnikov A. V. Characterization of $(\text{Co}_{0.45}\text{Fe}_{0.45}\text{Zr}_{0.10})_x(\text{Al}_2\text{O}_3)_{1-x}$ nanocomposite films applicable as spintronic materials. *Physica Status Solidi C*. 2006;3: 1283–1290. <https://doi.org/10.1002/pssc.200563111>

23. Svito I., Fedotov A. K., Koltunowicz T. N., Saad A. Hopping of electron transport in granular $\text{Cu}_x(\text{SiO}_2)_{1-x}$ nanocomposite films deposited by ion-beam sputtering. *Journal of Alloys and Compounds*. 2015;615: S371–S374. <https://doi.org/10.1016/j.jallcom.2014.01.136>

24. Agarwal B. K. Soft X-ray spectroscopy. *X-Ray Spectroscopy*. Springer, Berlin, Heidelberg; 1979, p. 311–330 https://doi.org/10.1007/978-3-662-14469-5_7

25. Zimmermann P., Peredkov S., Abdala P. M., ... van Bokhoven J. A. Modern X-ray spectroscopy: XAS and XES in the laboratory. *Coordination Chemistry Reviews*. 2020;423: 213466. <https://doi.org/10.1016/j.ccr.2020.213466>

26. Terekhov V. A., Kashkarov V. M., Manukovskii E. Yu., Schukarev A. V., Domashevskaya E. P. Determination of the phase composition of surface layers of porous silicon by ultrasoft X-ray spectroscopy and X-ray photoelectron spectroscopy techniques. *Journal of Electron Spectroscopy and Related Phenomena*. 2001;114–116: 895–900. [https://doi.org/10.1016/S0368-2048\(00\)00393-5](https://doi.org/10.1016/S0368-2048(00)00393-5)

27. Domashevskaya E. P., Peshkov Y. A., Terekhov V. A., Yurakov Y. A., Barkov K. A. Phase composi-

tion of the buried silicon interlayers in the amorphous multilayer nanostructures $[(\text{Co}_{45}\text{Fe}_{45}\text{Zr}_{10})/\text{a-Si:H}]_{41}$ and $[(\text{Co}_{45}\text{Fe}_{45}\text{Zr}_{10})_{35}(\text{Al}_2\text{O}_3)_{65}/\text{a-Si:H}]_{41}$. *Surface and Interface Analysis*. 2018;50: 1265–1270. <https://doi.org/10.1002/sia.6515>

28. Langford J. I., Wilson A. J. C. Scherrer after sixty years: a survey and some new results in the determination of crystallite size. *Journal of Applied Crystallography*. 1978;11: 102–113. <https://doi.org/10.1107/S0021889878012844>

29. Kovba L. M., Trunov V. K. *X-ray phase analysis*. Moscow: Moscow University Publ.; 1976, 232 p. (In Russ.)

30. Jain R. A review on the development of XRD in ferrite nanoparticles. *Journal of Superconductivity and Novel Magnetism*. 2022;35: 1033–1047. <https://doi.org/10.1007/s10948-022-06213-9>

31. Wiech G., Feldhütter H. O., Šimůnek A. Electronic structure of amorphous SiO_xH alloy films studied by X-ray emission spectroscopy: Si K, Si L, and O K emission bands. *Physical Review B*. 1993;47: 6981–6989. <https://doi.org/10.1103/PhysRevB.47.6981>

32. Nekrashevich S. S., Gritsenko V. A. Electronic structure of silicon dioxide (a review). *Physics of the Solid State*. 2014;56(2): 207–222. <https://doi.org/10.1134/s106378341402022x>

33. Gladskikh I. A., Gushchin M. G., Vartanyan T. A. Resistance switching in Ag, Au, and Cu films at the percolation threshold. *Semiconductors*. 2018;52: 671–674. <https://doi.org/10.1134/S1063782618050093>

34. Vartanyan T. A., Gladskikh I. A., Leonov N. B., Przhibel'skii S. G. Fine structures and switching of electrical conductivity in labyrinth silver films on sapphire. *Physics of the Solid State*. 2014;56: 816–822. <https://doi.org/10.1134/S1063783414040349>

Information about the authors

Konstantin A. Barkov, Cand. Sci. (Phys.-Math.), Head of the Laboratory, Department of Solid State Physics and Nanostructures, Voronezh State University (Voronezh, Russian Federation).

<https://orcid.org/0000-0001-8290-1088>
barkov@phys.vsu.ru

Vladimir A. Terekhov, Dr. Sci. (Phys.-Math.), Full Professor, Department of Solid State Physics and Nanostructures, Voronezh State University (Voronezh, Russian Federation).

<https://orcid.org/0000-0002-0668-4138>
terekhov@phys.vsu.ru

Dmitry N. Nesterov, Cand. Sci. (Phys.-Math.), Assistant Professor, Department of Solid State Physics and Nanostructures, Voronezh State University (Voronezh, Russian Federation).

<https://orcid.org/0000-0002-2462-7153>
nesterov@phys.vsu.ru

Kirill E. Velichko, Process Engineer, Research Institute of Electronic Technology (Voronezh, Russian Federation).

Sergey A. Ivkov, Cand. Sci. (Phys.-Math.), Leading Electronics Engineer, Department of Solid State Physics and Nanostructures, Voronezh State University (Voronezh, Russian Federation).

<https://orcid.org/0000-0003-1658-5579>

ivkov@phys.vsu.ru

Nikita S. Buylov, Cand. Sci. (Phys.-Math.), Assistant Professor, Department of Solid State Physics and Nanostructures, Voronezh State University; Engineer, Research Institute of Electronic Technology (Voronezh, Russian Federation).

<https://orcid.org/0000-0003-1793-4400>

buylov@phys.vsu.ru

Sergey V. Kannykin, Cand. Sci. (Phys.-Math.), Assistant Professor, Department of Materials Science and the Industry of Nanosystems, Voronezh State University; Engineer, Research Institute of Electronic Technology (Voronezh, Russian Federation).

<https://orcid.org/0000-0001-8756-5722>

svkannykin@gmail.com

Igor E. Zanin, Cand. Sci. (Phys.-Math.), Assistant Professor, General Physics Department, Voronezh State University (Voronezh, Russian Federation).

iezan@mail.ru

Boris L. Agapov, Cand. Sci. (Tech.), Centre for Collective Use of Scientific Equipmen, Voronezh State University, Research Institute of Electronic Technology (Voronezh, Russian Federation).

b.agapov2010@yandex.ru

Sergey V. Rodivilov, Leading Process Engineer, Research Institute of Electronic Technology (Voronezh, Russian Federation).

Evgenii S. Kersnovsky, student, Department of Solid State Physics and Nanostructures, Voronezh State University (Voronezh, Russian Federation).

<https://orcid.org/0009-0006-8215-6077>

kersnovsky@phys.vsu.ru

Ivan V. Polshin, student, Department of Solid State Physics and Nanostructures, Voronezh State University (Voronezh, Russian Federation).

<https://orcid.org/0009-0008-7639-6538>

polshin@phys.vsu.ru

Stanislav V. Ryabtsev, Dr. Sci. (Phys.-Math.), Leading Researcher, Joint Scientific and Educational Laboratory “Atomic and Electronic Structure of Functional Materials” of Voronezh State University and the National Research Center “Kurchatov Institute”, Voronezh State University (Voronezh, Russian Federation).

<https://orcid.org/0000-0001-7635-8162>

ryabtsev@phys.vsu.ru

Margarita V. Grechkina, Leading Electronics Engineer, Departments of Semiconductor Physics and Microelectronics, Voronezh State University (Voronezh, Russian Federation).

<https://orcid.org/0000-0002-7873-8625>

grechkina_m@mail.ru

Aleksandr V. Sitnikov, Dr. Sci. (Phys.-Math.), Full Professor, Departments of Solid-State Electronics, Voronezh State Technical University (Voronezh, Russian Federation).

<https://orcid.org/0000-0002-9438-9234>

sitnikov04@mail.ru

Received 09.11.2023; approved after reviewing 05.12.2023; accepted for publication 14.12.2023; published online 01.10.2024.

Translated by Konstantin Barkov



Original articles

Research article

<https://doi.org/10.17308/kcmf.2024.26/12216>

Electrophysical properties of PIN photodiodes of the 2.2–2.6 μm range based on InGa(Al)As/InP heterostructures with a metamorphic buffer layer

E. I. Vasilkova¹✉, E. V. Pirogov¹, K. Yu. Shubina¹, K. O. Voropaev², A. A. Vasil'ev²,
L. Ya. Karachinsky^{1,3}, I. I. Novikov^{1,3}, O. V. Barantsev¹, M. S. Sobolev

¹Alferov University,
8/3 Khlopina st., Saint Petersburg 194021, Russian Federation

²JSC "OKB-Planeta",
13a, room 1n Bolshaya Moskovskaya st., Velikiy Novgorod 173004, Russian Federation

³ITMO University
49, bldg. A Kronverksky pr., Saint Petersburg 197101, Russian Federation

Abstract

Due to a large number of applications in the near and short-wave IR spectrum and a relatively high detectivity, PIN photodiodes based on epitaxial InGa(Al)As/InP heterostructures are of a great scientific interest. The operational spectral range of such photodetectors is up to 2.6 μm . However, to reach such wavelengths it is necessary to synthesize heterostructures with metamorphic buffer layers. In our study, we investigated the current–voltage and capacitance–voltage characteristics of PIN photodiodes based on InGa(Al)As/InP heterostructures with an original metamorphic buffer layer and an $\text{In}_{0.85}\text{Ga}_{0.17}\text{As}$ absorbing layer grown by means of molecular beam epitaxy.

The photodiode chips were formed using standard post-growth processing techniques. The diameter of the photosensitive area of the obtained diodes was 140 μm . The dark currents and the shunt resistance were ~ 300 nA and ~ 25 k Ω at the voltage of -10 mV respectively.

Therefore, the suggested metamorphic buffer layer effectively eliminates threading dislocations in the active area of the heterostructure. The obtained heterostructures with metamorphic buffer layers can be used to produce IR photodetectors for the spectral range of 2.2–2.6 μm .

Keywords: Molecular beam epitaxy, Metamorphic buffer layers, Near IR photodetectors, Current–voltage characteristic, Capacitance–voltage characteristic, Dark currents

Funding: The study was funded by the Ministry of Science and Higher Education of the Russian Federation within the framework of the state assignments No. FSRM-2023-0006 and FSRM-2023-0007 and by the Russian Science Foundation, research project No. 22-79-00146.

For citation: Vasilkova E. I., Pirogov E. V., Shubina K. Yu., Voropaev K. O., Vasil'ev A. A., Karachinsky L. Ya., Novikov I. I., Barantsev O. V., Sobolev M. S. Electrophysical properties of PIN photodiodes of the 2.2–2.6 μm range based on InGa(Al)As/InP heterostructures with a metamorphic buffer layer. *Condensed Matter and Interphases*. 2024;26(3): 417–423. <https://doi.org/10.17308/kcmf.2024.26/12216>

Для цитирования: Василькова Е. И., Пирогов Е. В., Шубина К. Ю., Воропаев К. О., Васильев А. А., Карачинский Л. Я., Новиков И. И., Баранцев О. В., Соболев М. С. Электрофизические характеристики PIN-фотодиодов диапазона 2.2–2.6 мкм на основе гетероструктур InGa(Al)As/InP с метаморфным буферным слоем. *Конденсированные среды и межфазные границы*. 2024;26(3): 417–423. <https://doi.org/10.17308/kcmf.2024.26/12216>

✉ Elena I. Vasilkova, e-mail: elenvasilkov@gmail.com

© Vasilkova E. I., Pirogov E. V., Shubina K. Yu., Voropaev K. O., Vasil'ev A. A., Karachinsky L. Ya., Novikov I. I., Barantsev O. V., Sobolev M. S., 2024



The content is available under Creative Commons Attribution 4.0 License.

1. Introduction

IR photodetectors attract attention due to the specifics of their spectral range, namely the high contrast of short-wave IR radiation in the Earth's atmosphere. They also have numerous applications in the atmospheric window in a range of 1–3 μm , including in satellites, night vision equipment and thermal visors, lidars, fluid and gas spectroscopy, etc. [1]. Therefore, the development of effective near IR photodetectors is a promising area.

At the moment, the most well-studied is the wavelength range of up to 1.7 μm , with the leading position occupied by photodiodes based on $\text{In}_{0.53}\text{Ga}_{0.47}\text{As}/\text{InP}$ lattice-matched heterostructures, which are characterized by lower dark currents and higher mobility of charge carriers as compared to photodiodes based on germanium (Ge). However, the 1.9–2.7 μm spectral range (in between the strong absorption spectra of water vapor) is often more preferable. In this case, analogous to the short-wave range, PIN photodiodes based on heterostructures with active $\text{In}_x\text{Ga}_{1-x}\text{As}$ ($x > 0.53$) layers grown on indium phosphide substrates demonstrate good performance. Their cut-off wavelengths can be up to 2.6 μm [2; 3]. However, during the transition from the lattice-matched heterostructure to the layers enriched with indium, the dark currents of photodiodes grow rapidly by several orders of magnitude, which results in an abrupt drop in their detectivity [4]. Nevertheless, InGa(Al)As nanoheterostructures on InP substrates can compete with HgCdTe and InAsSb materials in the 2.2-2.6 μm spectral region because this technology makes it possible to synthesize perfect crystalline semiconductor structures with highly homogeneous parameters and to use mature post-growth processing techniques to form crystal photodiode. Photodetectors based on $\text{InGa(Al)As}/\text{InP}$ are highly effective at room temperature. Therefore, they require neither active, nor passive cooling, which helps to make the final devices smaller and more attractive commercially.

As compared to photodetectors based on $\text{In}_{0.53}\text{Ga}_{0.47}\text{As}/\text{InP}$ lattice-matched heterostructures, photodetectors based on InGa(Al)As in the 2.2–2.6 μm spectral region are more difficult to produce, because they require very

thick (about 1–2 μm) active layers with a high (up to 83%) concentration of indium. The pseudomorphic epitaxial growth of such layers on InP is impossible due to the strong elastic strain [5]. To grow relatively thick $\text{In}_{0.83}\text{Ga}_{0.17}\text{As}$ layers on InP substrates, it is necessary to artificially match the crystal lattice parameters of the material and the substrate.

The misfit dislocations occurring during the epitaxial growth are extended charged defects of the crystal structure and result from elastic deformations taking place during the growth of layers with different parameters of their crystal lattices. Dislocations always have a negative effect on the properties of active optoelectronic devices, including photodetectors. Specifically, they reduce the breakdown voltage and increase the leakage current within the whole reverse bias range [6]. In the active area of photodiodes, dislocations can act as conductive channels between p -type and n -type regions, i.e. as a p - n junction barrier. Furthermore, dislocations result in a number of traps in the band gap for charge carriers acting as parasitic recombination centers. One solution to this problem involves introducing transitional epitaxial layers of variable compositions between the InP substrate and the active area of InGaAs, i.e. using the so-called metamorphic buffer layer [7]. The main purpose of growing metamorphic structures is to slow down the penetration of dislocations into the buffer layers and to obtain a strain-free active area with a low density of defects in the crystal structure [8–10]. Metamorphic buffer layers prevent the penetration of dislocations into the active areas of photodiodes with an $\text{In}_{0.83}\text{Ga}_{0.17}\text{As}$ absorbing layer, thus reducing the dark currents. Together with shunt resistance and the capacitance of photodiodes, dark currents are critical for the detection and identification of small optical signals with high signal-to-noise ratio.

Therefore, it is important to obtain $\text{InGa(Al)As}/\text{InP}$ heterostructures for PIN photodetectors characterized by a high structural quality and low dark currents and functioning in the spectral region of up to 2.6 μm . To obtain such a heterostructure, we suggested a design for InAlAs metamorphic buffer layers and performed the epitaxial growth of the test samples with an

active area of a high structural quality [11]. In the present study, we investigated the effect of the suggested structure of the metamorphic buffer layer on the electrophysical properties of crystal PIN photodiodes.

2. Experimental

The sample heterostructures with metamorphic buffer layers for PIN photodiodes were grown by means of molecular beam epitaxy on n^+ -InP (100) doped epi-ready substrates using a Riber MBE49 industrial molecular beam epitaxy setup. The heterostructure obtained for PIN photodiodes is demonstrated in fig. 1. It contained a p^+ -In_{0.83}Al_{0.17}As region, a 1500 nm thick n^- -In_{0.83}Ga_{0.17}As layer serving as an IR absorption i-region, a 2 μm thick n^+ -InAlAs graded metamorphic buffer layer of variable composition, and a 100 nm thick In_{0.52}Al_{0.48}As lattice-matched layer. The layers between the substrate and the active InGaAs area were doped with silicon (n^+), and the contact layers were doped with beryllium (p^+). The InGaAs region was doped to the degree of $(0.5-2)\cdot 10^{16} \text{ cm}^{-3}$. The In_xAl_{1-x}As metamorphic buffer layer was formed by linearly increasing the molar fraction of In from 0.52 to 0.86 at a constant temperature of the substrate with three thin inserts [InAs/InAlAs] $\times 3$ every 0.5 μm . At the end of the formation of the graded layer, the structure was annealed at a maximum temperature, and the temperature of the substrate holder was then lowered. The technology of the epitaxial growth of metamorphic buffer heterostructures for PIN photodiodes is detailed in [11].

p^+ -In _{0.83} Ga _{0.17} As	20 nm
p^+ -In _{0.83} Al _{0.17} As	600 nm
n^- -In _{0.83} Ga _{0.17} As	1,5 μm
buffer n^+ -In _x Al _{1-x} As x=0.52->0.86	2 μm
n^+ -In _{0.52} Al _{0.48} As	100 nm
substrate n^+ -InP	

Fig. 1. The heterostructure obtained for PIN photodiodes

Fig. 2 presents the diffraction pattern of the studied sample. The diffraction pattern demonstrates peaks of the InP substrate, the InGaAs layer, and the InAlAs metamorphic buffer with a linear composition gradient. The X-ray diffraction was performed using a DRON-8 diffractometer with a Bartels monochromator and the radiation at the X-ray tube of $\text{CuK}\alpha_1 = 0.15406 \text{ nm}$. The diffraction maximum of the InGaAs layer corresponds to the reference maximum of a completely strain-free layer with a composition of about 83%.

In order to perform electrophysical measurements of the heterostructure by means of double photoresistive mask lift-off photolithography, we formed p^- and n^- type ohmic contacts based on a Ti/Pt/Au metal system and anode-cathode contact pads based on the V/Au metallization. The diameter of the photosensitive area of the diode was 140 μm . An optical microscope image of the obtained crystal photodiodes is presented in fig. 3. The crystals were then studied by means of electrophysical methods using a SUSS MicroTec PM 8 microprobe unit at the temperature of 295 K.

3. Results and discussion

3.1. Current-voltage characteristics

The effectiveness of the suggested design of the metamorphic buffer layer can be assessed based on the dark current-voltage characteristics of the resulting photodiode. The dark current-voltage characteristics of several photodiodes from the middle of the wafer are shown in fig. 4. They were obtained using an Agilent B1500A semiconductor device parameter analyzer in the forward bias range V from -1 to 0.25 V with a 5 mV step. The figure demonstrates strictly asymmetric forward and reverse branches, which is common for diodes. The reverse current branch initially located in the third quadrant was projected to the positive semiplane for the convenience of presentation on a logarithmic scale. The most rapid increase in the dark current is observed at low reverse voltage bias range of up to 100 mV. The reverse branch corresponds to low dark currents: $\sim 10 \text{ uA}$ at reverse voltage bias of 1 V and $\sim 300 \text{ nA}$ at 10 mV respectively.

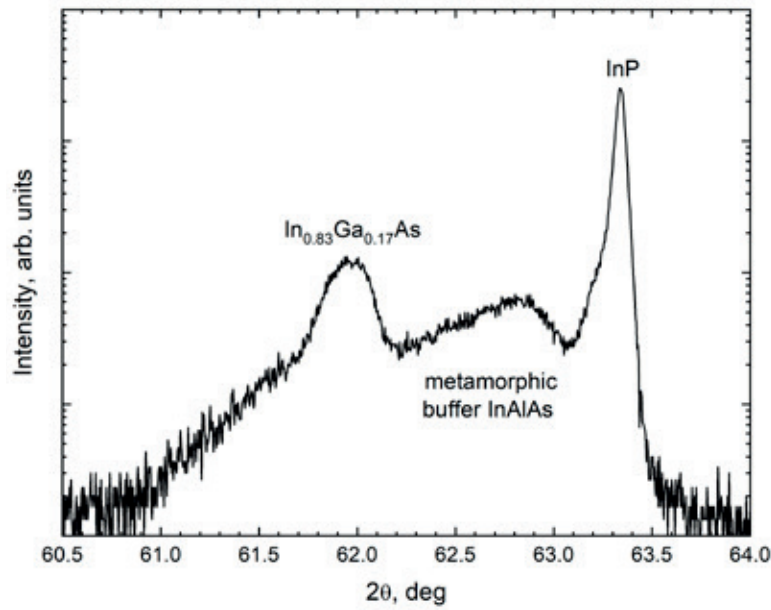


Fig. 2. X-ray diffraction pattern of the heterostructure with regard to the symmetric InP (004) reflection

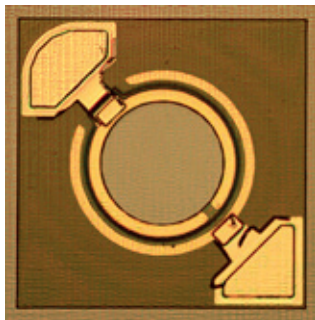


Fig. 3. An image of a PIN photodiode crystal

The shunt resistance of the photodiode is the resistance of the unbiased *p-n* junction. It is usually measured based on the current value at the reverse bias of $10 \text{ mV} < kT/q$ at room temperature $T = 295 \text{ K}$ (where k is the Boltzmann constant, q is the elementary charge) in accordance with the Ohm's law: $R_0 = \frac{dU}{dI}$.

The calculated shunt resistance was on average $\sim 25 \text{ k}\Omega$, which corresponds to the product of $R_0 A \sim 4 \text{ Ohm}\cdot\text{cm}^2$, where A is the junction area of the photodiode.

When the crystal PIN photodiodes are subjected to IR radiation with a wide spectrum and the maximum intensity in the region of $2.5 \text{ }\mu\text{m}$, the current values of the reverse branch grew by about an order of magnitude. This indicated effective formation of electron-

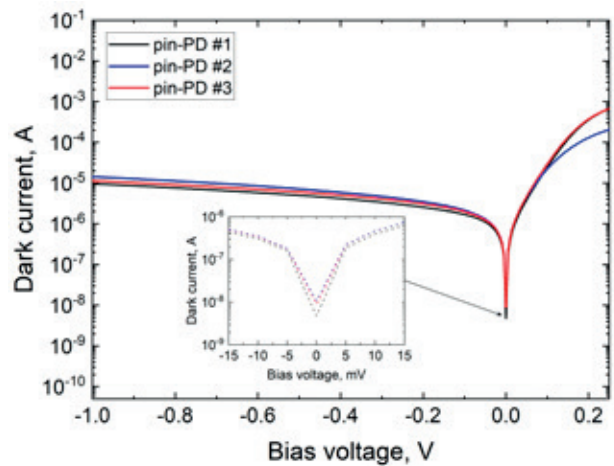


Fig. 4. The dark current-voltage characteristics of crystal PIN photodiodes at 295 K

hole pairs in the *i*-region of the photodiode. Therefore, the obtained heterostructure can be used to produce photodetectors of near IR radiation.

The dark current is an important parameter of photodetectors affecting the signal-to-noise ratio and detectivity. There are several major dark current mechanisms reported for photodiodes: the diffusion current mechanism, the generation-recombination current in the depletion region, and the deep level tunneling mechanisms [3]. Surface leakage at the sidewall of mesa can also contribute to the dark current [12]. For a better understanding of the processes

occurring in photodiodes it is necessary to determine the dominant mechanism based on the dependence of the dark current on the temperature. This is generally an exponential dependence $I_T \sim \exp(-E_a/kT)$. However, the activation energies E_a in the exponent differ depending on the dark current mechanism. For the diffusion current, the activation energy is about the band gap of the semiconductor material E_g , for the generation-recombination current it is about $E_g/2$, and for the deep level tunneling and surface leakage the activation energy is $E_g/4$ [12]. The existing literature focuses on the dominating nature of generation-recombination currents and trap-assisted tunneling [2, 3]. Indeed, at high concentrations of indium, the InGaAs solid solution becomes a narrow-bandgap material. This can be one of the reasons for the increase of the share of the generation-recombination currents as compared to lattice-matched heterostructures. However, a large number of dislocations characteristic of heterostructures with metamorphic buffer layers can result in additional levels in the band gap. Therefore, the contribution to the dark current is of mixed nature. In our study, we observed a four-time decrease in the dark current at the voltage of -10 mV during the thermoelectric cooling of crystal PIN photodiodes by 10 degrees (fig. 5). To refine the dark current mechanism, further research is required in a larger temperature range of up to 77 K.

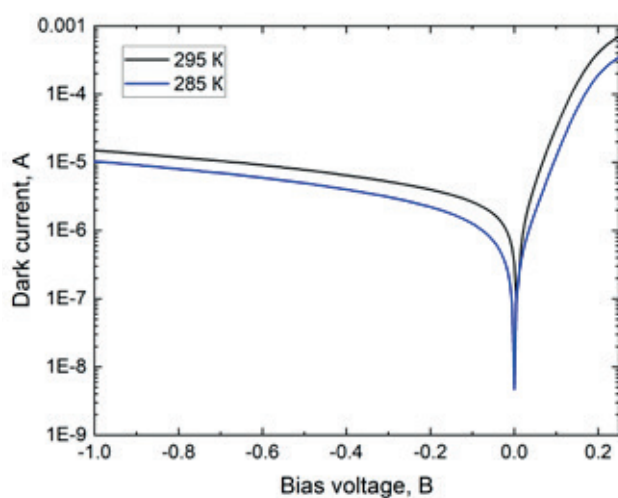


Fig. 5. The dark current-voltage characteristics of a crystal PIN photodiode at various temperatures

3.2. Capacitance–voltage characteristics

Standard capacitance–voltage characteristics of PIN photodiodes were determined by means of microprobe analysis using an Agilent E4980A precision LCR meter at frequencies of 200 kHz and 1 MHz in the reverse bias range from 0 to 3 V. Typical capacitance–voltage characteristics are presented in fig. 6. Fig. 6 demonstrates that capacitance–voltage profile curves are practically identical at different frequencies. The capacitance of bias-free photodiodes was about 14 pF and then decreased following an increase in reverse voltage. In the reverse bias range of up to 2 V curves $1/C^2(V)$ are linear with the slope coefficient practically independent of the frequency of the signal (fig. 7), which can indicate the abrupt nature of the obtained $p-n$ junction [13].

4. Conclusions

In our study, we produced PIN photodiode chips of the near IR spectrum based on InAlAs/In_{0.83}Ga_{0.17}As/InP heterostructures with a metamorphic buffer layer. The measurements of the electrophysical properties of the chips with the sensitivity area of 140 μm gave the following results: the dark current was ~ 300 nA at the reverse bias of 10 mV, the shunt resistance was ~ 25 k Ω , and the shunt capacity was ~ 14 pF. Relatively low dark currents indicate effective resistance to the penetration of dislocations in the active area of the heterostructure, which are the main sources of noise and leakages.

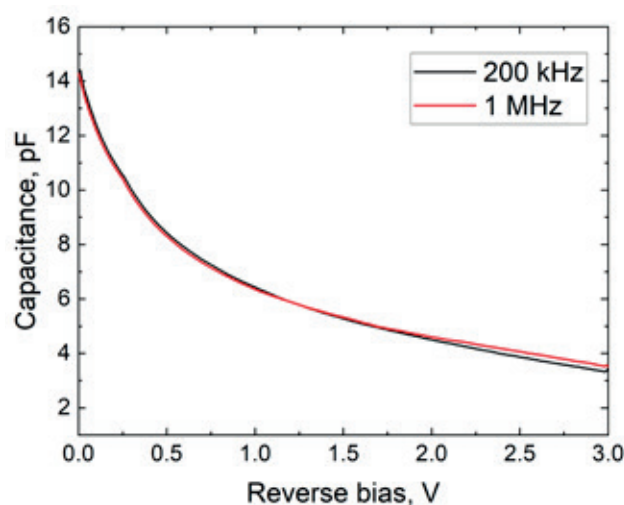


Fig. 6. The capacitance–voltage characteristics of crystal PIN photodiodes at 295 K

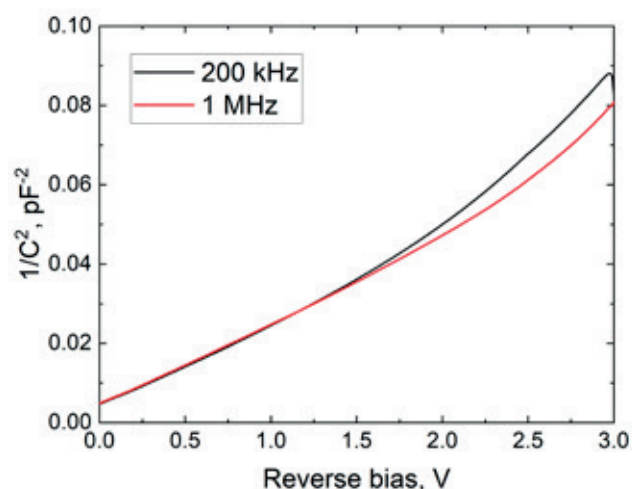


Fig. 7. Dependence of $1/C^2$ on the voltage for crystal PIN photodiodes at 295 K

The results demonstrate that the suggested metamorphic buffer layers of the heterostructure can be effectively used for the production of PIN photodiodes in the spectral range of 2.2–2.6 μm .

Contribution of the authors

The authors contributed equally to this article.

Conflict of interests

The authors declare that they have no known competing financial interests or personal relationships that could have influenced the work reported in this paper.

References

1. Burlakov I. D., Grinchenko L.Y., Dirochka A.I., Zaletaev N. B. Short wavelength infrared InGaAs detectors. *Advances of Applied Physics*. 2014;2(2). (In Russ.). Available at: <https://www.elibrary.ru/item.asp?id=21505376>
2. Chen X. Y., Gu Y., Zhang Y. G., ... Zhu Y. In_{0.83}Ga_{0.17}As photodetectors with different doping concentrations in the absorption layers. *Infrared Physics & Technology*. 2018;89: 381–386. <https://doi.org/10.1016/j.infrared.2018.01.029>
3. Ji X., Liu B., Tang H., ... Yan F. 2.6 μm MBE grown InGaAs detectors with dark current of SRH and TAT. *AIP Advances*. 2014;4(8): 087135. <https://doi.org/10.1063/1.4894142>
4. Rogalski A. Infrared detectors: status and trends. *Progress in Quantum Electronics*. 2003;27(2-3): 59–210. [https://doi.org/10.1016/S0079-6727\(02\)00024-1](https://doi.org/10.1016/S0079-6727(02)00024-1)
5. Gendry M., Drouot V., Santinelli C., Hollinger G. Critical thicknesses of highly strained InGaAs layers grown on InP by molecular beam epitaxy. *Applied*

Physics Letters. 1992;60(18): 2249–2251. <https://doi.org/10.1063/1.107045>

6. Beam E. A., Temkin H., Mahajan S. Influence of dislocation density on IV characteristics of InP photodiodes. *Semiconductor Science and Technology*. 1992;7(1A): A229. <https://doi.org/10.1088/0268-1242/7/1A/044>

7. Tersoff J. Dislocations and strain relief in compositionally graded layers. *Applied Physics Letters*. 1993;62(7): 693–5. <https://doi.org/10.1063/1.108842>

8. Karachinsky L. Y., Kettler T., Novikov I. I., ... Vasil'Ev A. P. Metamorphic 1.5 μm -range quantum dot lasers on a GaAs substrate. *Semiconductor Science and Technology*. 2006;21(5): 691. <https://doi.org/10.1088/0268-1242/21/5/022>

9. Egorov A. Yu., Karachinsky L. Ya., Novikov I. I., Babichev A. V., Berezovskaya T. N., Nevedomskiy V. N. Metamorphic distributed Bragg reflectors for the 1440–1600 nm spectral range: Epitaxy, formation, and regrowth of mesa structures. *Semiconductors*. 2015;49(10): 1388–1392. <https://doi.org/10.1134/S1063782615100073>

10. Egorov A. Yu., Karachinsky L. Ya., Novikov I. I., Babichev A. V., Nevedomskiy V. N., Bugrov V. E. Optical properties of metamorphic GaAs/InAlGaAs/InGaAs heterostructures with InAs/InGaAs quantum wells, emitting light in the 1250–1400-nm spectral range. *Semiconductors*. 2016;50(5): 612–615. <https://doi.org/10.1134/S1063782616050079>

11. Vasilkova E. I., Pirogov E. V., Sobolev M. S., Ubiyovk E. V., Mizerov A.M., Seredin P. V. Molecular beam epitaxy of metamorphic buffer for InGaAs/InP photodetectors with high photosensitivity in the range of 2.2–2.6 μm . *Condensed Matter and Interphases*. 2023;25(1): 20–26. <https://doi.org/10.17308/kcmf.2023.25/10972>

12. Liu Y., Ma Y., Li X., ... Fang J. Surface leakage behaviors of 2.6 μm In_{0.83}Ga_{0.17}As photodetectors as a function of mesa etching depth. *IEEE Journal of Quantum Electronics*. 2020;56(2): 1–6. <https://doi.org/10.1109/JQE.2020.2970745>

13. Sze S. M., Li Y., Ng K. K. *Physics of semiconductor devices*. John Wiley & Sons; 2021. 994 p.

Information about the authors

Elena I. Vasilkova, postgraduate student, Engineer, Alferov University (Saint Petersburg, Russian Federation).

<https://orcid.org/0000-0002-0349-7134>
elenvasilkov@gmail.com

Evgeny V. Pirogov, Researcher, Alferov University (Saint Petersburg, Russian Federation).

<https://orcid.org/0000-0001-7186-3768>
zzzavr@gmail.com

Kseniya Yu. Shubina, Cand. Sci. (Phys.–Math.),
Researcher, Alferov University (Saint Petersburg,
Russian Federation).

<https://orcid.org/0000-0003-1835-1629>

rein.raus.2010@gmail.com

Kirill O. Voropaev, Head of the group, JSC “OKB-
Planeta” (Velikiy Novgorod, Russian Federation).

<https://orcid.org/0000-0002-6159-8902>

kirill.voropaev@novsu.ru

Andrey A. Vasil'ev, Engineer-technologist, JSC
“OKB-Planeta” (Velikiy Novgorod, Russian Federation).

<https://orcid.org/0009-0009-2615-6795>

Wasiliew.andre@yandex.ru

Leonid Ya. Karachinsky, Dr. Sci. (Tech.), Chief
Researcher, Alferov University; Leading Researcher,
ITMO University (Saint Petersburg, Russian
Federation).

<https://orcid.org/0000-0002-5634-8183>

karach@switch.ioffe.ru

Innokenty I. Novikov, Cand. Sci. (Phys.–Math.),
Senior Researcher, Alferov University; Senior
Researcher, ITMO University (Saint Petersburg,
Russian Federation).

<https://orcid.org/0000-0003-1983-0242>

novikov@switch.ioffe.ru

Oleg V. Barantsev, student, Laboratory Assistant,
Alferov University (Saint Petersburg, Russian
Federation).

<https://orcid.org/0009-0001-6873-8488>

ovbarantsev@gmail.com

Maxim S. Sobolev, Cand. Sci. (Phys.–Math.), Head
of the Laboratory, Alferov University (Saint Petersburg,
Russian Federation).

<https://orcid.org/0000-0001-8629-2064>

sobolevsms@gmail.com

*Received 16.11.2023; approved after reviewing
05.12.2023; accepted for publication 06.12.2023;
published online 01.10.2024.*

Translated by Yulia Dymant



Original articles

Research article

<https://doi.org/10.17308/kcmf.2024.26/12217>

Effect of plasmonic Au nanoparticles on IR luminescence of Ag₂S quantum dots

I. G. Grevtseva[✉], O. V. Ovchinnikov, M. S. Smirnov, S. V. Aslanov, A. N. Latyshev, M. S. Astashkina

Voronezh State University,
1 Universitetskaya pl., Voronezh 394018, Russian Federation

Abstract

Luminescent manifestations of the interaction of Ag₂S quantum dots (QDs) with Au nanorods (NRs) depending on the overlap degree of the corresponding luminescence bands and plasmon resonance peaks have been experimentally established. Under spectral resonance conditions, the possibility of controlling the intensity of QDs luminescence by changing the interaction with Au NRs by varying the distance between the components of the plasmon-exciton mixture has been demonstrated. In turn it determines the influence of the near-field of metal nanoparticles on photoprocesses in Ag₂S QDs. The detuning of the spectral resonance due to the change in the Au QDs length leads to the asymmetry of the spectral contour of the Ag₂S QDs luminescence band, which may be due to the manifestation of the Fano effect during plasmon-exciton interaction, taking into account the inhomogeneous broadening of the corresponding bands.

Keywords: Quantum dot, Plasmonic nanoparticles, Plasmon resonance, IR luminescence, Plasmon-exciton interaction

Funding: The study was supported by the grant of the President of the Russian Federation (grant No.MK-3746.2022.1.2).

Acknowledgements: The results of transmission electron microscopy on a Libra 120 microscope were obtained using the equipment of the Centre for Collective Use of Scientific Equipment of Voronezh State University.

For citation: Grevtseva I. G., Ovchinnikov O. V., Smirnov M. S., Aslanov S. V., Astashkina M. S. Effect of plasmonic Au nanoparticles on IR luminescence of Ag₂S quantum dots. *Condensed Matter and Interphases*. 2024;26(3): 424–430. <https://doi.org/10.17308/kcmf.2024.26/12217>

Для цитирования: Гревцева И. Г., Овчинников О. В., Смирнов М. С., Асланов С. В., Асташкина М. С. Влияние плазмонных наночастиц Au на ИК люминесценцию квантовых точек Ag₂S. *Конденсированные среды и межфазные границы*. 2024;26(3): 424–430. <https://doi.org/10.17308/kcmf.2024.26/12217>

✉ Grevtseva Irina Gennadievna, e-mail: grevtseva_ig@inbox.ru

© Grevtseva I. G., Ovchinnikov O. V., Smirnov M. S., Aslanov S. V., Astashkina M. S., 2024



The content is available under Creative Commons Attribution 4.0 License.

1. Introduction

Semiconductor colloidal quantum dots (QDs) are relevant objects of research due to their size-dependent spectral-luminescent properties, which ensure control of the corresponding peaks by varying the size without changing the chemical composition of the nanocrystals [1–9]. Such unique spectral properties of colloidal QDs make them promising materials for a wide range of practical applications in modern photonics, including optoelectronics [1, 2, 7–9], luminescence and biosensors [2, 5, 6], photocatalysis [1–4], and others.

Additional opportunities for controlling the spectral-luminescent properties of QDs are provided by the use of exciton-exciton and plasmon-exciton interaction effects [10–21]. Plasmon-exciton interaction, realized during the association of colloidal QDs with plasmonic nanoparticles, leads to striking effects [12–21]. The physical mechanism of plasmon-exciton effects is associated with the mutual near-field interaction of QDs and NPs, in which the NPs acts as both a source of strong polarization of the environment and a nano-resonator concentrating the field energy [13, 14, 17]. A lot of experimental studies, implemented primarily within the framework of single-object spectroscopy techniques, demonstrate an increase in the intensity of QDs luminescence with a simultaneous decrease in its duration in the presence of plasmonic NPs, which is interpreted as a manifestation of the Purcell effect [12, 13, 18–21]. Depending on the magnitude of the mutual distance between the components of the plasmon-exciton structure and spectral tuning of resonances in the luminescence and extinction spectra of plasmonic NPs, the occurrence of the effect of quantum interference (Fano effect) is probable, as well as the splitting of the luminescence spectra under conditions of strong plasmon-exciton coupling (Rabi splitting) [13, 15–17]. The development of applications related to the use of plasmon-exciton effects in luminescent sensors requires an understanding of the interactions that arise between NPs and QDs, as well as their manifestation in the luminescence of ensembles of QDs [18, 19, 22–24]. The dispersion of QDs in size in the ensemble suggests a noticeable broadening of their luminescence band, as well as offset of the

spectral resonance, which determines the effects of interaction in the resulting spectral properties of plasmon-exciton nanostructures [18, 19, 22–24]. In addition, the necessary conditions for observing the effects of plasmon-exciton interaction (spectral resonance of the extinction peak of NPs and the luminescence band of QDs, the distance between the components) suggest the presence of other, accompanying interaction processes, in particular, non-radiative energy transfer between QDs and NPs [25], as well as photoinduced charge transfer [26, 27]. In this regard, the manifestation of plasmon-exciton interaction effects in the luminescent properties of colloidal ensembles of QDs may differ significantly from the manifestation of these effects for a single emitter.

This study is devoted to the experimental establishment of the influence of Au plasmonic nanorods (NRs) on the IR trap state luminescence of Ag₂S QDs ensembles depending on the degree of overlap of the plasmon resonance peak and luminescence band.

2. Experimental

Synthesis of colloidal Ag₂S QDs was carried out in ethylene glycol. The 2-mercaptopropionic acid (2-MPA) molecules were used as a passivating ligand [28]. The synthesis method involved mixing AgNO₃ precursors and 2-MPA in a molar ratio of 1:2 in 30 ml of ethylene glycol. The control of particle size and position of the luminescence peak within this approach was achieved by exposing a colloidal solution of Ag₂S QDs by radiation with a wavelength of 405 nm (100 mW) for 20 hours. The removal of reaction by-products, colloidal Ag₂S QDs were precipitated by centrifugation and re-dissolution in ethylene glycol.

Plasmonic Au NRs were obtained by aqueous synthesis using cetyltrimethylammonium bromide (CTAB) molecules, which form cylindrical micelles, thereby defining anisotropic conditions for NRs growth [18]. The length of the Au NRs was controlled by adding AgNO₃ to the reaction solution. The changes in the length of the Au NRs allows to control the position of the extinction peak of the longitudinal plasmon resonance of the Au NRs, ensuring spectral resonance with the luminescence band of the Ag₂S QDs.

In the Ag₂S QDs colloidal solution Au NRs were introduced in a concentration ratio $\sim 10^4:1$ pcs. for the formation of plasmon-exciton mixtures. Solutions containing Ag₂S QDs and Au NRs separately in concentrations equivalent to those introduced during the formation of their mixtures served as comparison samples in the study of spectral-luminescent properties of mixtures of Ag₂S QDs and Au NRs.

Structural data of Ag₂S QDs and Au NRs were determined using a Libra 120 transmission electron microscope (TEM) (CarlZeiss, Germany) and a JEOL 2000FX high-resolution TEM (JEOL Ltd., Japan). The absorption properties were studied using a USB2000+ spectrometer (OceanOptics, USA) with a USB-DT radiation source (OceanOptics, USA). Luminescence spectra and luminescence decay of Ag₂S QDs were studied using USB2000+ and TimeHarp~260 system for time correlated photon counting (PicoQuant Germany) with a PMC-100-20 photomultiplier tube (Becker&Hickl Germany) with a time resolution of 0.2 ns. A diode laser LD PLTB450 (Osram, Germany) with a wavelength of 445 nm (200 mW) was used to stimulate the luminescence.

3. Results and discussion

3.1. Structural properties

The analysis of TEM images of Ag₂S ODs showed the formation of individual nanocrystals with an average size of 2.8 ± 0.5 nm with an ensemble dispersion of $\sim 30\%$, which was due to the chosen approach of colloidal synthesis in an aqueous solution (Fig. 1a).

According to TEM images, the formation of Au NRs with average length values of 30 ± 5 nm and 35 ± 5 nm and a diameter of 9 ± 2 nm (Fig. 1b) and Au NRs with an average length of 45 ± 5 nm and a diameter of 9 ± 2 nm was established (Fig. 1c). The dispersion of the Au NRs in the ensemble did not exceed 30% (Fig. 1b, c).

High-resolution TEM data (Fig. 1d) showed cluster of spherical nanoparticles near cylindrical nanoparticles. The interplanar distance of ~ 0.251 nm of spherical nanoparticles corresponded to the crystallographic plane (022) of the monoclinic crystal lattice of Ag₂S, and the interplanar distance of 0.237 nm of cylindrical nanoparticles corresponded to the crystallographic plane (111) of the face-centred cubic crystal lattice of Au (Fig. 2d).

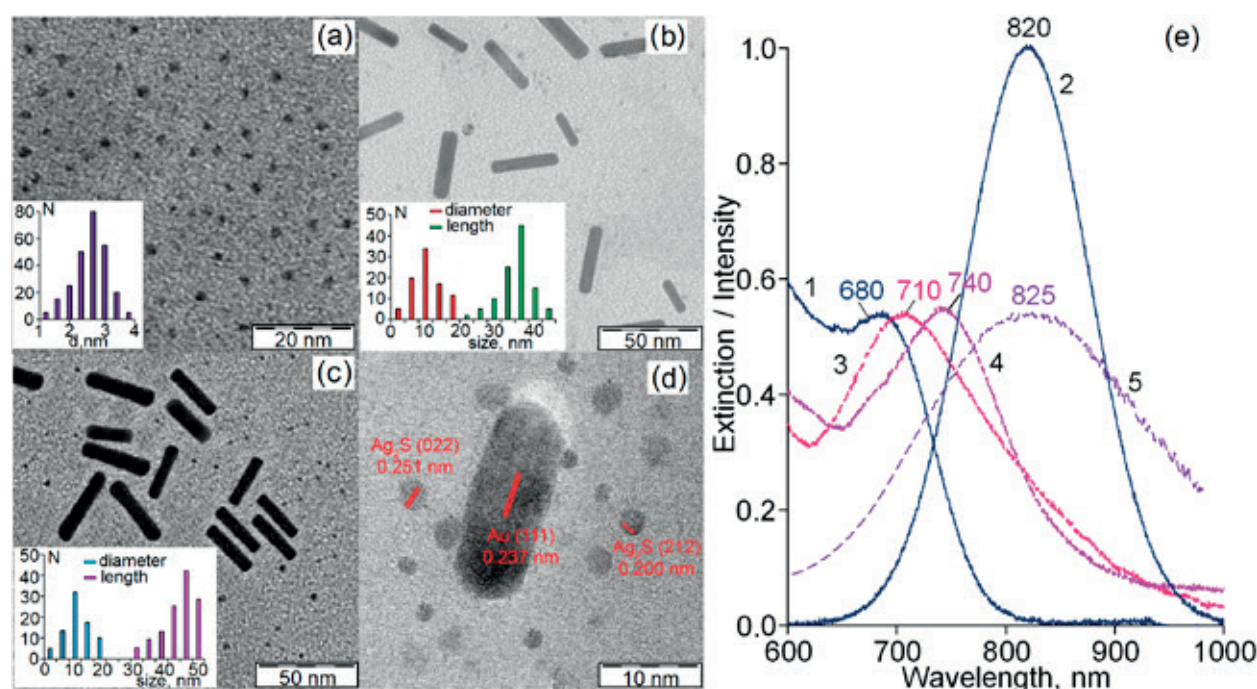


Fig. 1. TEM image of Ag₂S QDs – (a). TEM image of Au NRs with average length of 30 nm and 35 nm – (b). TEM image of Au NRs with average length of 45 nm – (c) High resolution TEM image of Ag₂S QDs and Au NRs – (d). Optical absorption (1) and luminescence (2) spectrum of Ag₂S QDs, extinction spectra of Au NRs with average length of 30 nm (3), 35 nm (4) and 45 nm (5) – (e)

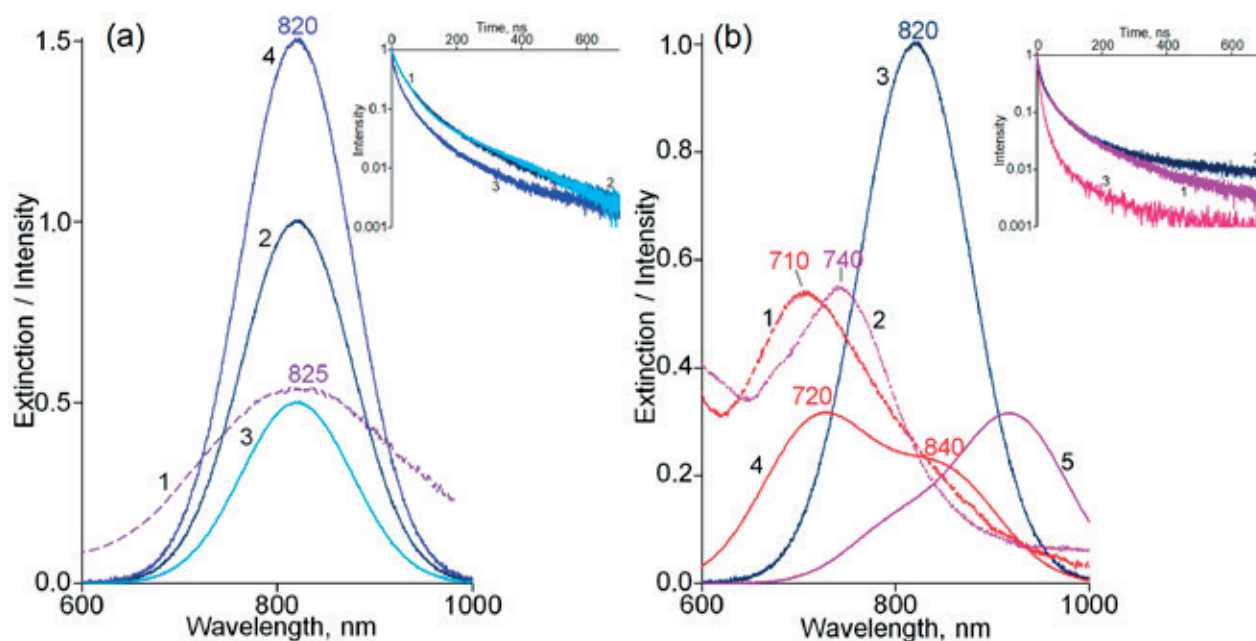


Fig. 2. Extinction spectrum of Au NRs with an average length of 45 nm (1), luminescence spectra of free Ag₂S QDs (2), in the presence of plasmonic Au NRs (3) and in the presence of plasmonic Au NRs and polymer (4) – (a). Extinction spectrum of Au NRs with an average length of 30 nm (1) and 35 nm (2), luminescence spectra of free Ag₂S QDs (3), in the presence of plasmonic Au NRs with an average length of 30 nm (4) and in the presence of plasmonic Au NRs with an average length of 35 nm (5) – (b)

3.2. Spectral-luminescent properties

In UV-Vis absorption spectrum of Ag₂S QDs in the region of 680 nm, a clearly expressed feature, corresponding to the ground exciton transition in the optical absorption of QDs, characteristic of charge carriers with confinement in nanocrystals was observed (Fig. 1e, curve 1). UV-Vis absorption spectrum corresponded to Ag₂S QDs with an average size of 2.7 nm [28], which was in good agreement with the TEM image data (Fig. 1a). The studied colloidal Ag₂S QDs were characterized by luminescence with a peak at 820 nm (Fig. 1e, curve 2). The Stokes shift was 0.31 eV (140 nm). According to the data of study [29], the luminescence of Ag₂S QDs is the result of radiative hole recombination with electrons localized at the levels of structural impurity defects.

The morphology and average length of Au NRs of 30, 35, and 45 nm provided the location of longitudinal plasmon resonance peaks at 710, 740, and 825 nm, respectively (Fig. 1e, curves 3, 4, 5). Thus, Au NRs with an average length of 30 and 35 nm provided a detuning of the spectral resonance of the longitudinal plasmon peak of Au NRs from the luminescence band of Ag₂S QDs at

110 and 80 nm, respectively (Fig. 1e, curves 2, 3, 4). The Au NRs with a length of 45 nm provided significant spectral resonance of the longitudinal mode peak of Au NRs with a luminescence spectrum of Ag₂S QDs (Fig. 1e), curves 2, 5).

The formation of plasmon-exciton structures based on Ag₂S QDs and Au NRs, providing significant spectral overlap of the peak of longitudinal plasmon resonance of NRs and the luminescence band of QDs, led to a decrease in the intensity of the Ag₂S QDs luminescence by 2.5 times (Fig. 2a, curves 1–3) at constant luminescence decay time of Ag₂S QDs (Fig. 2a, inset, curves 1, 2). The observed regularities were usually interpreted as photoinduced charge transfer from Ag₂S QDs to Au NRs [18, 26, 27]. At the same time, the authors of the study [30], for the simple classical model of forced and spontaneous dipole transitions in a two-level system near a metal NPs, showed that a decrease in the of luminescence intensity of emitter while maintaining its lifetime near the surface of the metal NPs can be caused by the high absorption of the NPs wave energy. In this case, an increase in the distance between the components of the plasmon-exciton mixture in some cases leads

to an increase, and in others to a decrease in the luminescence intensity of emitter, which is determined by the mutual orientation of the dipole moment of the transition of the emitter from the ground to the excited state and the field of the metal NPs, which strongly depends on the distance between the components of the mixture [30]. Spatial separation of mixture components by introduction of a polymer into a plasmon-exciton mixture provides an increase in the quantum yield of Ag₂S QDs luminescence from 5 to 7.5% (Fig. 2a, curves 2, 4). A slight increase in the luminescence quantum yield may be due to a significant contribution of the constant luminescence of Ag₂S QDs to the resulting luminescent properties of plasmon-exciton mixtures, free from interaction with Au NRs. The increase of the quantum yield of Ag₂S QDs luminescence in the presence of plasmonic Au NRs was accompanied by reduction of the luminescence decay time from 77 to 58 ns (Fig. 2a, inset, curves 1, 3), which may also indicate the implementation of the Purcell effect in the studied plasmon-exciton mixtures [12, 13, 18–21, 31].

The most interesting regularities were found in the case of plasmon-exciton mixtures, based on Ag₂S QDs and metallic Au NRs with the length of 30 and 35 nm, providing the spectral resonance shift of the NRs extinction from the QDs luminescence band by 80–110 nm (Fig. 2a, curves 1–3). In this case, an asymmetry of the luminescence contour of Ag₂S QDs was observed. This asymmetry was manifested in a decrease in the peak luminescence intensity (820 nm) with a simultaneous increase in intensity at the band edge in the region of 720 nm (Fig. 2a, curve 4) or in the region of 900 nm (Fig. 2a, curve 5) with spectral resonance shift at 110 and 80 nm, respectively. In this case, an increase in the average luminescence decay time from 94 to 115 ns was established at a wavelength of 720 nm (900 nm) (Fig. 2a, inset, curves 1, 2) and decrease in the average luminescence decay time from 94 to 16 ns was revealed at a wavelength of 820 nm (Fig. 2a, inset, curves 1, 3). The observed spectral regularities were a manifestation of exciton-plasmon interaction and can be interpreted as the Fano effect [13, 15–17]. The non-monotonic change of the luminescence spectral contour of Ag₂S

QDs when changing the spectral resonance shift of the plasmonic peak of Au NRs from the Ag₂S QDs luminescence band within 30 nm (Fig. 2b, curves 1, 2, 4, 5) can be caused by dispersion in the size and distances between components in the plasmon-exciton mixture. Thus, the obtained experimental data certainly require a theoretical description for each specific case. The determination of the parameters of the emitters ensemble and plasmonic nanoparticles for the theoretical description of the experimentally observed effects of plasmon-exciton interaction is a complex task, which requires separate and detailed consideration.

4. Conclusions

The study presents experimental data demonstrating the manifestation of plasmon-exciton interaction effects in the luminescent properties of colloidal Ag₂S QDs depending on the degree of overlap of their luminescence band with the plasmon resonance peak of metallic Au NRs. It was established that, under the condition of spectral resonance of the corresponding peaks, control of the luminescence quantum yield is achieved by changing the distance between components of the plasmon-exciton mixture. The spectral resonance shift by 80–110 nm due to a change in the length of the Au NRs leads to a decrease in the luminescence quantum yield of Ag₂S QDs and asymmetry of the luminescence contour of Ag₂S QDs. Such luminescent properties are the result of the implementation of the Fano effect, the spectral manifestation of which is complicated by the influence of the dispersion of QDs in the ensemble and mutual distances of the components.

Author contributions

Grevtseva I. G. – problem statement, methodology development, conducting research, writing and editing text. Ovchinnikov O. V. – scientific supervision, research concept, development of methodology, writing of text, final conclusions. Smirnov M. S. – research concept, research implementation, review writing and editing of the text. Aslanov S. V. – conducting research, review writing. Astashkina M. S. – conducting research, editing of the text.

Conflict of interests

The authors declare that they have no known competing financial interests or personal relationships that could have influenced the work reported in this paper.

References

- Cotta M. A. Quantum dots and their applications: What lies ahead? *ACS Applied Nano Materials*. 2020;3(6): 4920–4924. <https://doi.org/10.1021/acsnm.0c01386>
- Bera D., Qian L., Tseng T. K., Holloway P. H. Quantum dots and their multimodal applications: a review. *Materials*. 2010;3(4): 2260–2345. <https://doi.org/10.3390/ma3042260>
- Reshma V. G., Mohanan P. V. Quantum dots: applications and safety consequences. *Journal of Luminescence*. 2019;205: 287–298. <https://doi.org/10.1016/j.jlumin.2018.09.015>
- Perepelitsa A. S., Aslanov S. V., Ovchinnikov O. V., ... Kondratenko T. S. Photosensitising reactive oxygen species with titanium dioxide nanoparticles decorated with PbS quantum dots. *Condensed Matter and Interphases*. 2023;25(2): 215–224. <https://doi.org/10.17308/kcmf.2023.25/11103>
- Caponetti V., Trzcinski J. W., Cantelli A., ... Montalti M. Self-assembled biocompatible fluorescent nanoparticles for bioimaging. *Frontiers in Chemistry*. 2019;7:168. <https://doi.org/10.3389/fchem.2019.00168>
- Gu Yi-P., Cui R., Zhang Z.-L., Xie Z.-X., Pang D.-W. Ultrasmall near-infrared Ag₂Se quantum dots with tunable fluorescence for in vivo imaging. *American Chemical Society*. 2012;134(1): 79–82. <https://doi.org/10.1021/ja2089553>
- Park Y. S., Roh J., Diroll B. T., Schalle R. D., Klimov V. I. Colloidal quantum dot lasers. *Nature Reviews Materials*. 2021;6(5): 382–401. <https://doi.org/10.1038/s41578-020-00274-9>
- Gurchenko V. S., Mazinov A. S., Smirnov M. S., Grevtseva I. G., Nesterenko L. P., Ovchinnikov O. V. Photoelectric response in sandwich structures based on condensed layers of Ag₂S quantum dots passivated with thioglycolic acid. *Condensed Matter and Interphases*. 2023;25(2): 190–197. <https://doi.org/10.17308/kcmf.2023.25/11100>
- Yin Q., Zhang W., Zhou Y., Wang R., Zhao Z., Liu C. High efficiency luminescence from PbS quantum dots embedded glasses for near-infrared light emitting diodes. *Journal of Luminescence*. 2022;250: 119065. <https://doi.org/10.1016/j.jlumin.2022.119065>
- Ovchinnikov O. V., Smirnov M. S., Kondratenko T. S., ... Perepelitsa A. S. Förster resonance energy transfer in hybrid associates of colloidal Ag₂S quantum dots with thionine molecules. *Journal of Nanoparticle Research*. 2017;19(12): 403. <https://doi.org/10.1007/s11051-017-4093-2>
- Smirnov M. S., Ovchinnikov O. V., Grevtseva I. G., ... Kondratenko T. S. Control of direction of nonradiative resonance energy transfer in hybrid associates of colloidal Ag₂S/TGA QDs with thionine molecules. *Journal of Nanoparticle Research*. 2019;21(4): 67. <https://doi.org/10.1007/s11051-019-4487-4>
- Guo R., Derom S., Väkeväinen A. I., ... Törmä P. Controlling quantum dot emission by plasmonic nanoarrays. *Optics Express*. 2015;23: 28206–28215. <https://doi.org/10.1364/OE.23.028206>
- Luo Y., Zhao J. Plasmon-exciton interaction in colloiddally fabricated metal nanoparticle-quantum emitter nanostructures. *Nano Research*. 2019;12(9): 2164–2171. <https://doi.org/10.1007/s12274-019-2390-z>
- Gupta S. N., Bitton O., Neuman T., ... Haran G. Complex plasmon-exciton dynamics revealed through quantum dot light emission in a nanocavity. *Nature Communications*. 2021;12: 1310. <https://doi.org/10.1038/s41467-021-21539-z>
- He Y., Zhu K.-D. Fano effect and quantum entanglement in hybrid semiconductor quantum dot-metal nanoparticle system. *Sensors*. 2017;17(6): 1445. <https://doi.org/10.3390/s17061445>
- Chen H.-J. Fano resonance induced fast to slow light in a hybrid semiconductor quantum dot and metal nanoparticle system. *Laser Physics Letters*. 2020;17: 025201. <https://doi.org/10.1088/1612-202X/ab60ac>
- Westmoreland D. E., McClelland K. P., Perez K. A., Schwabacher J. C., Zhang Z., Weiss E. A. Properties of quantum dots coupled to plasmons and optical cavities. *The Journal of Chemical Physics*. 2019;151: 210901 <https://doi.org/10.1063/1.5124392>
- Grevtseva I., Ovchinnikov O., Smirnov M., ... Selyukov A. IR luminescence of plexcitonic structures based on Ag₂S/L-Cys quantum dots and Au nanorods. *Optics Express*. 2022;30: 4668–4679. <https://doi.org/10.1364/OE.447200>
- Derepko V. N., Ovchinnikov O. V., Smirnov M. S., ... Turishchev S. Yu. Plasmon-exciton nanostructures, based on CdS quantum dots with exciton and trap state luminescence. *Journal of Luminescence*. 2022;248: 118874. <https://doi.org/10.1016/j.jlumin.2022.118874>
- He R., Meunier M., Dong Zh., Liu X. Interplay of Purcell effect and extraction efficiency in CsPbBr₃ quantum dots coupled to Mie resonators. *Nanoscale*. 2023;15: 1652–1660. <https://doi.org/10.1039/D2NR05945B>
- Borrero Landazabal D., Meza Olivo A., Garay Palmett K., Montiel R. S. Reduction of the fluorescence lifetime of quantum dots in presence of plasmonic nanostructures. *Journal of Physics: Conference Series*.

2019;1159: 012004. <https://doi.org/10.1088/1742-6596/1159/1/012004>

22. Ruiz D., del Rosal B., Acebrón M., ... Juárez B. H. Ag/Ag₂S nanocrystals for high sensitivity near-infrared luminescence nanothermometry. *Advanced Functional Materials*. 2017;27(6): 1604629-1-9. <https://doi.org/10.1002/adfm.201604629>

23. Grevtseva I. G., Chevychelova T. A., Derepko V. N., ... Parshina A. S. Spectral manifestations of the exciton-plasmon interaction of Ag₂S quantum dots with silver and gold nanoparticles. *Condensed Matter and Interphases*. 2021;23(1): 25–31. <https://doi.org/10.17308/kcmf.2021.23/3294>

24. Ovchinnikov O. V., Smirnov M. S., Grevtseva I. G., ... Kondratenko T. S. Luminescent properties of colloidal mixtures of Zn_{0.5}Cd_{0.5}S quantum dots and gold nanoparticles. *Condensed Matter and Interphases*. 2021;23(1): 49–55. <https://doi.org/10.17308/kcmf.2021.23/3302>

25. Oh E., Huston A. L., Shabaev A., ... Medintz I. L. Energy transfer sensitization of luminescent gold nanoclusters: more than just the classical Förster mechanism. *Scientific Reports*. 2016;6: 35538. <https://doi.org/10.1038/srep35538>

26. Kamat P. V., Shanghavi B. Interparticle electron transfer in meta/semiconductor composites. Picosecond dynamics of CdS-capped gold nanoclusters. *The Journal of Physical Chemistry B*. 1997;101: 7675–7679. <https://doi.org/10.1021/jp9709464>

27. Mondal N., Samanta A. Ultrafast charge transfer and trapping dynamics in a colloidal mixture of similarly charged CdTe quantum dots and silver nanoparticles. *The Journal of Physical Chemistry C*. 2016;120: 650–658. <https://doi.org/10.1021/acs.jpcc.5b08630>

28. Ovchinnikov O. V., Aslanov S. V., Smirnov M. S., ... Grevtseva I. G., Perpelitsa A. S. Photostimulated control of luminescence quantum yield for colloidal Ag₂S/2-MPA quantum dots. *RSC Advances*. 2019;9: 37312–37320. <https://doi.org/10.1039/C9RA07047H>

29. Smirnov M. S., Ovchinnikov O. V. IR luminescence mechanism in colloidal Ag₂S quantum dots. *Journal of Luminescence*. 2020;227: 117526. <https://doi.org/10.1016/j.jlumin.2020.117526>

30. Zeinidenov A. K., Ibraev N. Kh., Kucherenko M. G. Effect of silver nanoparticles on electronic transitions in the dye molecules and lasing characteristics of liquid lasers on their basis. *Vestnik*

of the Orenburg State University. 2014;9(170): 96–102. (In Russ.). Available at: <https://elibrary.ru/item.asp?id=23161960>

31. Purcell E. M. Spontaneous emission probabilities at radio frequencies. In: Confined Electrons and Photons. Burstein E., Weisbuch C. (eds). NATO ASI Series. Springer, Boston, MA. 1995. vol. 340. https://doi.org/10.1007/978-1-4615-1963-8_40

Information about the authors

Irina G. Grevtseva, Cand. Sci. (Phys.–Math.), Associate Professor, Department of Optics and Spectroscopy, Voronezh State University (Voronezh, Russian Federation).

<https://orcid.org/0000-0002-1964-1233>
grevtseva_ig@inbox.ru

Oleg V. Ovchinnikov, Dr. Sci. (Phys.–Math.), Full Professor, Dean of the Faculty of Physics, Head of the Department of Optics and Spectroscopy, Voronezh State University (Voronezh, Russian Federation).

<https://orcid.org/0000-0001-6032-9295>
ovchinnikov_o_v@rambler.ru

Mikhail S. Smirnov, Dr. Sci. (Phys.–Math.), Professor, Department of Optics and Spectroscopy, Voronezh State University (Voronezh, Russian Federation).

<https://orcid.org/0000-0001-8765-0986>
smirnov_m_s@mail.ru

Anatoly N. Latyshev, Dr. Sci. (Phys.–Math.), Professor, Department of Optics and Spectroscopy, Voronezh State University (Voronezh, Russian Federation).

<https://orcid.org/0000-0002-7271-0795>
latyshev@phys.vsu.ru

Aslanov Sergey Vladimirovich, Cand. Sci. (Phys.–Math.), Lecturer, Department of Optics and Spectroscopy, Voronezh State University (Voronezh, Russian Federation).

<https://orcid.org/0000-0002-3961-2480>
windmaster7@yandex.ru

Astashkina Marina Sergeevna, postgraduate student, Department of Optics and Spectroscopy, Voronezh State University (Voronezh, Russian Federation).

marina_kush@mail.ru

Received 30.11.2023; approved after reviewing 06.12.2023; accepted for publication 15.12.2023; published online 01.10.2024.

Translated by Valentina Mittova



Original articles

Research article

<https://doi.org/10.17308/kcmf.2024.26/12218>

Formation of hybrid nanostructures based on $Zn_{0.5}Cd_{0.5}S$ quantum dots and silver nanoparticles for nonlinear optical applications in the near ultraviolet

A. I. Zvyagin , T. A. Chevychelova, M. S. Smirnov, O. V. Ovchinnikov, A. N. LatyshevVoronezh State University,
1 Universitetskaya pl., Voronezh 394018, Russian Federation**Abstract**

The goal of this study was to establish optimal conditions for the formation of hybrid nanostructures based on quantum dots and metal nanoparticles with a nonlinear optical response in the near ultraviolet. The relevance of this study is confirmed by the need to create passive devices for controlling the parameters of laser radiation in the presence of semiconductor colloidal quantum dots (QDs) and plasmonic nanoparticles (NPs). Manifestations of interaction in the nonlinear optical response of $Zn_{0.5}Cd_{0.5}S$ QDs and spherical Ag NPs (10 nm) in the field of laser pulses of 10 ns duration at a probing radiation wavelength of 355 nm have been established using the Z-scan method. Manifestations of the formation of hybrid nanostructures have been established using transmission electron microscopy and optical absorption and luminescence spectroscopy. The interaction of colloidal QDs and NPs was manifested as the recombination luminescence quenching of the former with a peak at a wavelength of 450–480 nm. For ensembles of colloidal $Zn_{0.5}Cd_{0.5}S$ QDs with an average size (2.0, 2.2, 2.4 nm), nonlinear refraction (defocusing) of 10 ns laser pulses in the near ultraviolet (355 nm) was established, the coefficient of which increased with increase in QDs. It has been established that during the interaction of $Zn_{0.5}Cd_{0.5}S$ QDs with Ag NPs, the suppression of nonlinear refraction was observed against the background of a twelvefold increase in the nonlinear absorption coefficient. It was concluded that the most probable reason for the observed changes in the nonlinear optical response is the polarizing effect of plasmonic Ag NPs.

Keywords: Nonlinear refraction, Nonlinear absorption, Quantum dot, $Zn_{0.5}Cd_{0.5}S$, Plasmonic nanoparticle, Z-scan**Funding:** The study was supported by the grant of the President of the Russian Federation No. MK-4408.2022.1.2.**Acknowledgements:** the study of structural properties by transmission electron microscopy was carried out using the equipment of the VSU Centre for Collective Use of Scientific Equipment.**For citation:** Zvyagin A. I., Chevychelova T. A., Smirnov M. S., Ovchinnikov O. V., Latyshev A. N. Formation of hybrid nanostructures based on $Zn_{0.5}Cd_{0.5}S$ quantum dots and silver nanoparticles for nonlinear optical applications in the near ultraviolet. *Condensed Matter and Interphases*. 2024;25(3): 431–439. <https://doi.org/10.17308/kcmf.2024.26/12218>**Для цитирования:** Звягин А. И., Чевычелова Т. А., Смирнов М. С., Овчинников О. В., Латышев А. Н. Формирование гибридных наноструктур на основе квантовых точек $Zn_{0.5}Cd_{0.5}S$ и наночастиц серебра для нелинейно-оптических приложений в ближнем ультрафиолете. *Конденсированные среды и межфазные границы*. 2024;25(1): 431–439. <https://doi.org/10.17308/kcmf.2024.26/12218> Andrey I. Zvyagin, e-mail: andzv92@yandex.ru

© Zvyagin A. I., Chevychelova T. A., Smirnov M. S., Ovchinnikov O. V., Latyshev A. N., 2024



The content is available under Creative Commons Attribution 4.0 License.

1. Introduction

The interaction of noble metal NPs and semiconductor colloidal QDs and dye molecules can significantly affect the optical properties of the latter [1, 2]. Recently, in the scientific literature there has been widespread interest in the study of hybrid nanostructures, characterized by the manifestation of plasmon-exciton interaction [3–9]. Such nanosystems are interesting from the point of view of controlling the luminescent, spectral and nonlinear optical properties of components due to the exchange of electronic excitations between QDs and Nps and the Rabi, Fano, and Purcell effects [1, 5, 6, 10–14]. The most attention is paid to the analysis of the manifestations of plasmon-exciton interaction in the spectral and luminescent properties of such nanosystems, while the nonlinear optical response remains practically unstudied, despite the prospect of their active use to control the intensity and phase of laser radiation [4, 5]. Theoretical studies propose models of plasmonic amplification of third-order nonlinear optical processes [15] and demonstrate the possibility of creating nanostructures with ultrafast response and the ability to reduce the size of nonlinear optical components [16]. In addition, there is evidence of a dielectric-metal hybrid system where an enhancement of optical nonlinearities is observed due to the strong coupling between the epsilon-near-zero mode in the indium tin oxide (ITO) nanofilm and the localized surface plasmon in the nanocavity [17]. The study revealed increases in the nonlinear refractive index and nonlinear absorption coefficient by three and two orders of magnitude compared to pure ITO, respectively. Plasmonic interaction is used to enhance such nonlinear processes as second harmonic generation and sum frequency generation [18]. An example of this is the experimental study [19], where the authors demonstrated the possibility of amplifying the output of the second harmonic generation signal of a Ti:Sapphire femtosecond laser on a nanosystem of gold nanoparticles with an average size of 80 nm in the presence of CdS quantum dots with an average size of 3 nm up to 20 times. The ratio of QDs to NPs was 200 to 1.

In addition to inorganic plasmon-exciton nanostructures, nanomaterials based on dyes and plasmonic nanoparticles have recently

been considered promising in nonlinear optics [20]. There are several methods for modifying specified linear and nonlinear optical properties of organic dyes [21, 22]. One of the simplest and most effective methods is formation of the nanostructure with nanoparticles of noble metals. Plasmonic nanoparticles have unique optical characteristics resulting from localized surface plasmon resonances that generate intense electromagnetic fields near the nanoparticle surface and can interact with electronic transitions in nearby molecules such as organic dyes [23, 24]. Various studies have been reported on the modification of the electrical, chemical and optical properties of nanostructures based on organic dyes and metal nanoparticles; there are studies that consider the modification of the nonlinear optical response in such nanosystems [25, 26]. The driving force for these studies is the fact that the nanosystem acquires many unique optical properties compared to its components, since the presence of plasmonic nanoparticles affects the probabilities of optical transitions in organic dyes [27, 28]. The study [29] which demonstrates the enhancement of nonlinear refraction and nonlinear absorption of the organic dye Methyl Orange in the presence of silver and gold nanoparticles in the field of nanosecond pulses of the second harmonic generated by Nd^{3+} :YAG laser should be mentioned. Our study [4] is devoted to the investigation of such effects of the modification of nonlinear absorption of the solution of the Methylene blue dye in the presence of gold nanoparticles coated with a silicon oxide shell, where an increase in reverse saturable absorption in the dye was demonstrated. It should be noted that the number of studies considering the nonlinear optical response in the near ultraviolet range is small; mainly the properties of glasses and various nonlinear crystals are considered.

The goal of this study was to establish optimal conditions for the formation of hybrid nanostructures for nonlinear optical applications in the near ultraviolet. The nonlinear optical properties of $Zn_{0.5}Cd_{0.5}S$ quantum dots passivated with thioglycolic acid (QD $Zn_{0.5}Cd_{0.5}S$ /TGA), with average sizes of 2.0, 2.2 and 2.4 nm in mixtures with silver nanoparticles (Ag NPs) of spherical geometry (10 nm) have been studied using the

Z-scan method. The samples were probed with third harmonic pulses generated by Nd^{3+} :YAG laser (355 nm) with a duration of 10 ns. In our study we used $Zn_{0.5}Cd_{0.5}S$ QDs, interesting because their exciton absorption peak is easily tuned by the synthesis and is located near the wavelength of the probing radiation (355 nm).

2. Experimental

The studied QDs and NPs samples were created using aqueous colloidal synthesis techniques. The $Zn_{0.5}Cd_{0.5}S$ /TGA QDs were synthesized using an aqueous solution of zinc and cadmium nitrates in a ratio of 1 to 1. Then, with constant stirring, an aqueous solution of thioglycolic acid (TGA) was added to the reactor, and the formation of the Zn(Cd)-TGA complex was observed (the solution became cloudy, pH was 2.4). By adjusting the pH to 7 with an aqueous 0.1 M NaOH solution, the solution became transparent. Then an aqueous Na_2S solution, which is a source of sulfur was added. Molar ratios of precursors $v(TGA):n(Zn(NO_3)_2(Cd(NO_3)_2)):n(Na_2S)$ were 2:1:0.5 for quantum dots with an average size of 2.0 nm. The variation in the size of QDs was achieved by increasing the sulfur precursor ratio to 0.6 and 0.7, respectively, for QDs with sizes of 2.2 and 2.4 nm. Reaction products were removed from the QD colloidal solution by centrifugation with the addition of ethanol and re-dissolution in water in the original ratio. We estimated the ratio of Zn to Cd in the obtained QDs as 1 to 1; the provision of the more accurate estimate of the ratio of atoms using X-ray diffraction is a rather labor-intensive task due to the significant broadening of X-ray diffraction peaks from the studied nanocrystals. This has been demonstrated in many studies, including ours [5].

Silver nanoparticles of spherical geometry (Ag NPs) were obtained by the Turkevich method [30]. The method involves the reduction of silver ions Ag^+ from silver nitrate precursor $AgNO_3$ by sodium citrate ($Na_3C_6H_5O_7$). During the reduction process, clusters, and then nanoparticles stabilized by sodium citrate molecules are successively formed. The 20 ml of an aqueous solution of sodium citrate $Na_3C_6H_5O_7$ (4 mM) were added within 5 min into a boiling aqueous solution of silver nitrate $AgNO_3$ (1 mM) with a volume of 20 ml, followed by boiling and stirring for 30 min. The

final solution had yellow color. Molar ratio of precursors in $v(AgNO_3):v(Na_3C_6H_5O_7)$ solution was 1:4. The resulting colloidal solution of silver nanoparticles was purified from reaction products by several cycles of deposition of Ag NPs on the bottom of test tubes during centrifugation and washing with distilled water. For the preparation of mixtures of the studied samples, a solution of Ag NPs was introduced into the QD solution in a ratio of about 1000 QDs to 1 NP.

The size of the studied QDs and NPs was determined by digital image analysis, using a Libra 120 transmission electron microscope (TEM) (CarlZeiss, Germany) with an accelerating voltage of 120 kV. The spectral and luminescent properties of the studied QDs, NPs and their mixtures were studied using USB2000+XR spectrometer (OceanOptics, USA) with a USB-DT radiation source (OceanOptics, USA). The luminescence spectra of $Zn_{0.5}Cd_{0.5}S$ /TGA QDs was recorded under excitation with a 313 nm source (monochromatic mercury lamp radiation). The luminescence decay kinetics of QDs was measured using a TimeHarp~260 module (PicoQuant, Germany). The single photon detector was a PMT PMC-100-20 (Becker&Hickl Germany) with a time resolution of 0.2 ns. The luminescence decay curves were approximated by the theoretical curve using the deconvolution procedure with the experimentally measured instrument response function.

The nonlinear optical properties of the samples were studied using the Z-scan method [31]. The setup and methodology are described in detail in [5].

Probing of the studied samples was carried out with pulsed laser radiation of the third harmonic of YAG: Nd^{3+} laser (LS-2132UTF, LOTIS TII) with a wavelength of 355 nm, a duration of 10 ns and a repetition rate of 1 Hz. The divergence of the laser beam was ensured by a converging spherical quartz lens with a focal length of 300 mm. The beam waist radius was $\sim 30 \mu m$. Samples of colloidal solutions in quartz cuvettes with the thickness of 1 mm were moved along the optical z axis of the collecting lens using a linear translator 8MT50-200BS1-MEn1 (Standa), from minus to plus z values, e.g. from the converging lens to the detector. The energy of the probing laser pulses was controlled by a PM100USB power and energy

meter with an ES111C pyroelectric detector (Thorlabs) and amounted to 1.33 mJ.

3. Results and discussion

Digital analysis of TEM images of the initial components of QDs and NPs and their mixtures (Fig. 1) allows to determine the size and morphology of nanostructures. Thus, separate ensembles of $Zn_{0.5}Cd_{0.5}S$ /TGA QDs were formed (2.0, 2.2, 2.4 nm) with a size dispersion of 20–30% (Fig. 1a-c). Ag NPs with spherical geometry had an average size of 10 nm (Fig. 1d).

In the optical absorption spectra of $Zn_{0.5}Cd_{0.5}S$ /TGA QDs features associated with the most probable exciton transition at wavelengths of 320, 335 and 345 nm for QDs with an average size of 2.0, 2.2 and 2.4 nm (Fig. 2a) were observed. The light extinction spectrum of Ag NPs contained a plasmon resonance peak at a wavelength of 400 nm (Fig. 2a).

The absorption spectra of associates were a summation of the absorption spectra of QDs and the light extinction spectra of NPs (Fig. 2b). This finding indicates the absence of structural changes in the components during the formation of the associate. Luminescence spectra of $Zn_{0.5}Cd_{0.5}S$ /TGA QDs were broad bands with maxima at 450, 473, 480 nm. A significant Stokes shift of 1.1 eV in the maximum of the luminescence band relative to the exciton absorption peak indicated the recombination nature of the luminescence. The situation with a noticeable offset of resonances in the absorption and luminescence of QDs and the light extinction of NPs was considered. A slight overlap of the light extinction spectra of NPs and luminescence of QDs will facilitate the exchange of electronic excitations between the components of QDs and NPs mixtures. Luminescence quenching by QDs by 3–4 times and acceleration of luminescence

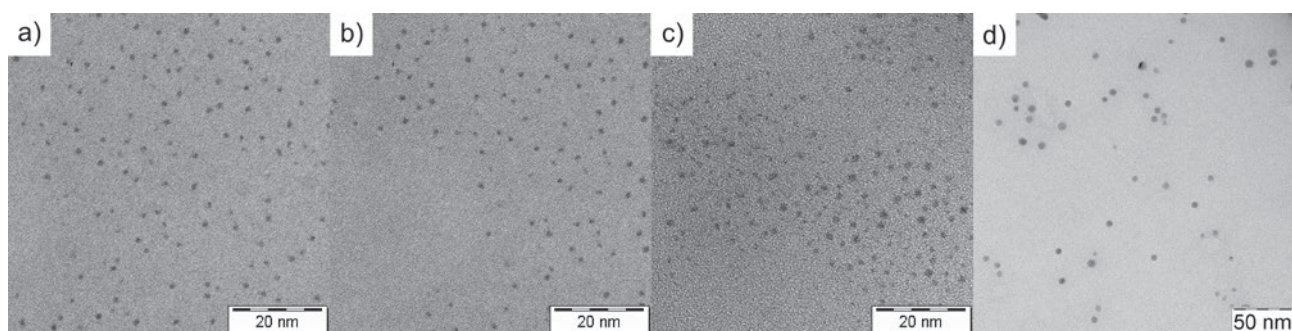


Fig. 1. TEM images of the studied $Zn_{0.5}Cd_{0.5}S$ /TGA QDs samples with an average size of 2.0 nm (a), 2.2 nm (b), 2.4 nm (c) and silver nanoparticles of spherical geometry with an average size of 10 nm (d)

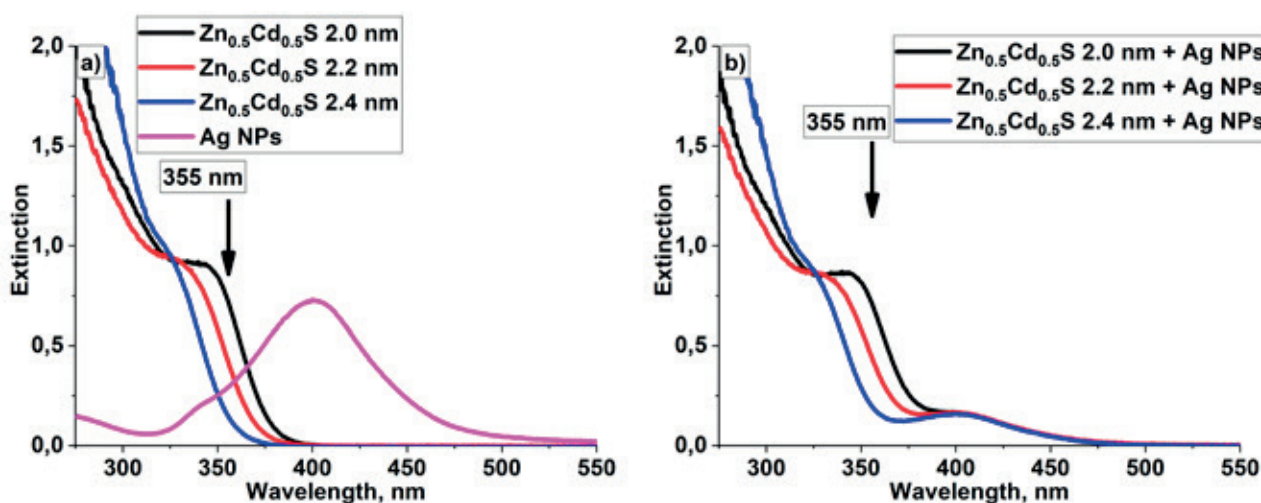


Fig. 2. Light extinction spectra of initial colloidal solutions of synthesized $Zn_{0.5}Cd_{0.5}S$ /TGA QDs, Ag NPs (a) and their mixtures in a ratio of 1000 QDs to 1 NP (b)

decay kinetics by up to 2 times in mixtures with NPs indicated their interaction. Under the existing spectral conditions, two processes of exchange of electronic excitations can occur: nonradiative electronic excitation energy transfer from QDs to NPs and photoinduced charge transfer.

Under conditions of interaction between colloidal QDs $Zn_{0.5}Cd_{0.5}S/TGA$ and AgNPs upon electronic excitation of one of the components, changes in the nonlinear optical response of a colloidal mixture compared to the response of individual components of the mixture. Using the Z-scan method using a scheme with a closed aperture, which allows recording nonlinear absorption and nonlinear refraction (beam divergence), suppression of nonlinear refraction and enhancement of nonlinear absorption were established QDs $Zn_{0.5}Cd_{0.5}S/TGA$ in the presence of Ag NPs (Fig. 3b).

It is noteworthy that Z-scans of $Zn_{0.5}Cd_{0.5}S/TGA$ exhibit profiles characteristic of defocusing laser probe pulses (Fig. 3a) and very weak nonlinear absorption. As the average QDs size increased, an increase in the level of nonlinear refraction was observed. Nonlinear refraction in QDs is realized due to the “band filling” [32, 33], and nonlinear absorption was associated with reverse saturable absorption (RSA), which occurred during transitions involving levels of localized states, including levels of luminescence centers.

In turn, for Ag NPs in Z-scans a dip in the focal plane associated with dynamic scattering

was observed, which was confirmed by the signal on an additional photodiode located at an angle to the optical axis of the converging lens during Z-scanning.

An estimation of nonlinear refractive coefficients (γ) and nonlinear absorption (β) was performed by approximating the experimentally obtained dependences by the expression [34]:

$$T(z) = 1 + \frac{4x}{(x^2 + 9)(x^2 + 1)} \Delta\Phi - \frac{2(x^2 + 3)}{(x^2 + 9)(x^2 + 1)} \Delta\Psi,$$

where $x = z/z_0$, $z_0 = 0.5k(w_0)^2$, $k = 2\pi/\lambda$, w_0 – beam radius in the focal plane, λ – radiation wavelength, $\Delta\Phi = k\gamma I_0 L_{\text{eff}}$ and $\Delta\Psi = \beta I_0 L_{\text{eff}}/2$ – parameters describing the phase shift near the focal point, γ – nonlinear refractive index, β – nonlinear absorption coefficient, I_0 – intensity of laser radiation in the waist, $L_{\text{eff}} = (1 - \exp(-\alpha L))/\alpha$ – the effective thickness of the sample, α – the linear absorption coefficient, L – sample thickness. The values of the nonlinear refraction coefficient equal to $\gamma = -5.9 \cdot 10^{-16} \text{ cm}^2 \text{ W}^{-1}$ (2.0 nm); $\gamma = -7.2 \cdot 10^{-16} \text{ cm}^2 \text{ W}^{-1}$ (2.2 nm), $\gamma = -9.1 \cdot 10^{-16} \text{ cm}^2 \text{ W}^{-1}$ (2.4 nm) were established for $Zn_{0.5}Cd_{0.5}S/TGA$ QDs of various mean sizes. The nonlinear absorption coefficient for all QD samples was no higher than $1.0 \cdot 10^{-11} \text{ cm W}^{-1}$.

The theoretical analysis of the contribution of thermal defocusing into nonlinear refraction was analyzed by analogy with study [35] by solving the heat equation. It was concluded that, under the conditions of our experiments, the time for the

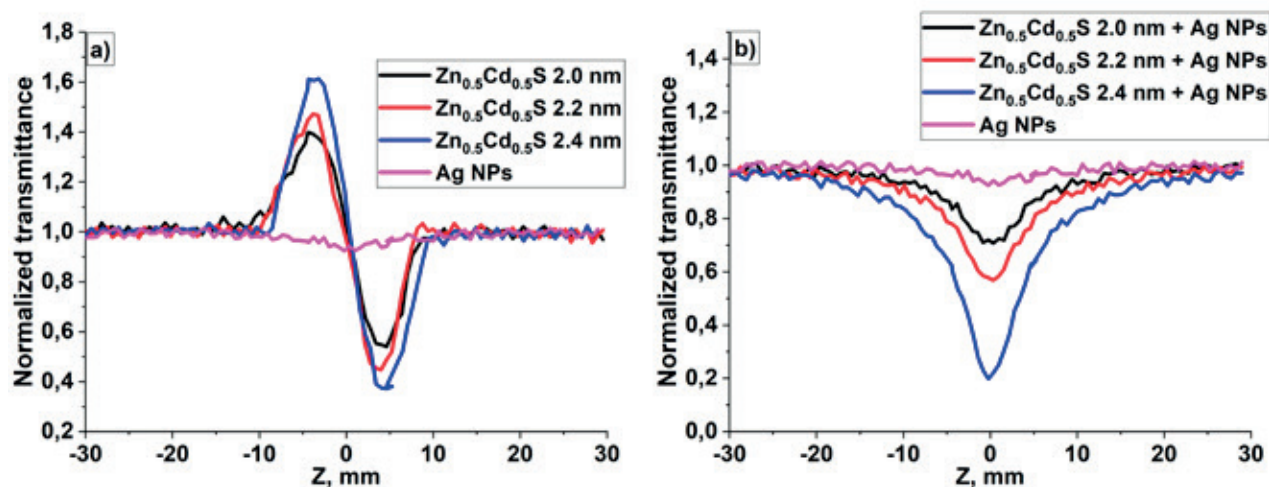


Fig. 3. Z-scans in closed-aperture geometry of the initial components of a $Zn_{0.5}Cd_{0.5}S$ -based hybrid nanostructure and silver nanospheres (a) and their mixtures (b). Z-scans were obtained by probing the studied colloidal solution with laser pulses with a duration of 10 ns at a wavelength of 355 nm and a pulse energy of 1.33 mJ

implementation of a thermal lens in solutions of the studied samples was about ≈ 3.8 ms, which significantly exceeded the laser pulse duration of 10 ns. The low repetition rate of probing pulses of 1 Hz also prevented heat accumulation. An estimate of the nonlinear refractive index of the thermal conductivity equation indicated a value on the order of -10^{-19} cm² W⁻¹, which was two orders of magnitude lower than the value obtained experimentally. Thus, it can be established that thermal refraction does not influence the nonlinear optical response in our samples.

In addition to the calculations obtained above, the distance between the peak and the dip in the Z-scan with a closed aperture was analyzed and it was about 0.6 cm. This distance, according to the data of [36], allows to determine the predominant mechanism for defocusing laser radiation as follows: for a thermal lens the characteristic distance between the peaks in the Z-scan corresponds to the distance $\Delta Z \approx 1.2z_0$ (z_0 – Rayleigh length equal to 0.353 cm for the probe radiation length of 355 nm); for nonlinearities of higher orders, the corresponding distance was equal to $\Delta Z \approx 1.7z_0$. These data were obtained by studying nonlinear refraction in CS₂ in the field of femtosecond pulses. Accordingly, the characteristic distances between the peak and the dip for the thermal nature of defocusing were equal to 0.42 and 0.56 cm for nonlinearities of higher orders. In this case, non-thermal nature of refraction in our experiments can be concluded.

It has been established that the lowest contribution to the nonlinear optical response from dynamic scattering was made by mixtures of QDs and NPs in a concentration ratio of 1000:1. Concentrations were estimated spectroscopically using literature data on molar extinction coefficients. Along with the disappearance of the nonlinear refraction of QDs in mixtures with NPs, an increase in the dip in the Z-scan in the focal plane of the lens, characteristic of nonlinear absorption, was observed, which, based on the analysis of the shape of the dependence of the energy of radiation transmitted through the sample on the energy of the incident radiation, was attributed to RSA. The analysis was performed by mathematical processing of Z-scans by analogy with [37], which allowed to establish

a saturable dependence of the absorption coefficient of the studied samples on the intensity of the incident radiation, characteristic of reverse saturable absorption with the involvement of real QD states, while two-photon absorption was characterized by a linear dependence. With increasing QD size, an increase in the level of reverse saturable absorption was observed. This pattern can be explained by an increase in the number of broken bonds on the QD surface involved in the implementation of RSA with increasing QD volume. This assumption was confirmed by the results of [38], which showed a significant influence of surface broken bonds and defects in CuS quantum dots with an average size of 2–4 nm and 5–11 nm on the reverse saturable absorption. In this study the nonlinear optical response in a field of 100 fs laser pulses at a probe radiation wavelength of 800 nm was investigated. The nonlinear absorption coefficient increased up to 26 times with increase in size of CuS QDs. The study [39] provides experimental data on the effect of surface defects of PbS QDs on the nonlinear absorption and nonlinear refraction coefficients in the field of femtosecond laser pulses at a wavelength of 800 nm. It was shown that as the size of PbS QDs decreased from 4.3 to 1.5 nm, the ratio of the QD surface to volume increased sharply, which made the influence of surface traps even more pronounced and led to a further decrease in the nonlinear response. The authors noted that improved nonlinear optical response can be achieved by creating QDs with fewer defects, which will prevent capture of the charge into trap states and decrease the oscillator strength.

Based on the approximation of Z-scans, the values of the nonlinear absorption coefficient for the studied mixtures of $Zn_{0.5}Cd_{0.5}S$ QDs (2.0 nm) and Ag NPs were established – $\beta = 4.5 \cdot 10^{-11}$ cm W⁻¹; for mixtures of $Zn_{0.5}Cd_{0.5}S$ QDs (2.2 nm) and Ag NPs – $\beta = 6.6 \cdot 10^{-11}$ cm W⁻¹; for mixtures of $Zn_{0.5}Cd_{0.5}S$ QDs (2.4 nm) and Ag NPs – $\beta = 12.3 \cdot 10^{-11}$ cm W⁻¹. Thus, an increase in the nonlinear absorption coefficient of mixtures of QDs and NPs up to 12 times compared to free $Zn_{0.5}Cd_{0.5}S$ /TGA QDs was revealed.

The enhancement of RSA in QDs and NPs mixtures indicated the participation of local states in the formation of nonlinear absorption,

which were most likely determined by broken bonds on the QD surface. Accordingly, optical transitions involving these states in the presence of plasmonic NPs can lead to a change in the probability ratio of two-step optical transitions that determine RSA [40]. In this case, a redistribution of the population of local states of the QD in the field of laser pulses is probable, which can lead to the suppression of the effect of nonlinear refraction caused initially by the “band-filling” effect and a change in the refractive index of the colloidal solution in accordance with the Kramers-Kronig relation [31]. The probabilities of the corresponding transitions can change under the polarizing action of NPs, which affects the nonlinear optical response (an increase in nonlinear optical absorption) regardless of the settings of the optical resonances (luminescence peak and plasmon peak, respectively). At the same time, the observed pattern in nonlinear optical and spectral luminescent properties can also arise during photostimulated charge transfer between the components of QDs and NPs mixtures.

4. Conclusions

Control of the nonlinear optical response of $Zn_{0.5}Cd_{0.5}S$ /TGA QDs associated with Ag NPs of spherical geometry in the radiation field of laser pulses (10 ns) with a wavelength of 355 nm using spectral-luminescent methods and the Z-scanning method has been demonstrated. The predominant mechanism for the implementation of the nonlinear optical response in the studied samples has been established: nonlinear absorption is realized due to reverse saturable absorption, self-focusing was of a non-thermal nature and was associated with the “band filling”. The mixtures of $Zn_{0.5}Cd_{0.5}S$ /TGA QDs and Ag NPs of different mean sizes were characterized by suppression of nonlinear refraction and enhancement of nonlinear absorption by up to 12 times, which can find practical application in the production of passive optical power limiters in the near ultraviolet.

Author contributions

Zvyagin A. I. – conducting scientific research, writing of the article, scientific editing of the text. Chevychelova T. A. – conducting scientific research. Smirnov M. S. – scientific editing of

the text, discussion of the results of the study. Ovchinnikov O. V. – scientific editing of the text, discussion of the results of the study. Latyshev A. N. – scientific editing of the text, discussion of the results of the study.

Conflict of interests

The authors declare that they have no known competing financial interests or personal relationships that could have influenced the work reported in this paper.

References

1. Cao E., Lin W., Sun M., Liang W., Song Yi. Exciton-plasmon coupling interactions: from principle to applications. *Nanophotonics*. 2018;7(1): 145–167. <https://doi.org/10.1515/nanoph-2017-0059>
2. Hu S., Ren Y., Wang Y., ... Tang Y. Surface plasmon resonance enhancement of photoluminescence intensity and bioimaging application of gold nanorod@CdSe/ZnS quantum dots. *Beilstein Journal of Nanotechnology*. 2019;10: 22–31. <https://doi.org/10.3762/bjnano.10.3>
3. Zvyagin A. I., Perepelitsa A. S., Ovchinnikov O. V., Smirnov M. S., Ganeev R. A. Nonlinear optical properties of associates of erythrosine molecules and gold nanoparticles. *Materials Research Express*. 2019;6: 1150c8. <https://doi.org/10.1088/2053-1591/ab4e2a>
4. Ovchinnikov O. V., Smirnov M. S., Chevychelova T. A., Zvyagin A. I., Selyukov A. S. Nonlinear absorption enhancement of Methylene Blue in the presence of Au/SiO₂ core/shell nanoparticles. *Dyes and Pigments*. 2022;197: 109829. <https://doi.org/10.1016/j.dyepig.2021.109829>
5. Zvyagin A. I., Chevychelova T. A., Perepelitsa A. S., Smirnov M. S., Ovchinnikov O. V. Formation of plasmon-exciton nanostructures based on quantum dots and metal nanoparticles with a nonlinear optical response. *Condensed Matter and Interphases*. 2023;25(3): 350–358. <https://doi.org/10.17308/kcmf.2023.25/11258>
6. Davoodi F., Talebi N. Plasmon-exciton interactions in nanometer-thick gold-WSe₂ multilayer structures: implications for photodetectors, sensors, and light-emitting devices. *ACS Applied Nano Materials*. 2021;4(6): 6067–6074. <https://doi.org/10.1021/acsnm.1c00889>
7. Grevtseva I. G., Chevychelova T. A., Derepko V. N., ... Parshina A. S. Spectral manifestations of the exciton-plasmon interaction of Ag₂S quantum dots with silver and gold nanoparticles. *Condensed Matter and Interphases*. 2021;23(1), 25–31. <https://doi.org/10.17308/kcmf.2021.23/3294>
8. Daniel M. C., Astruc D. Gold nanoparticles: assembly, supramolecular chemistry, quantum-size-re-

- lated properties, and applications toward biology, catalysis, and nanotechnology. *Chemical Reviews*. 2004;104(1): 293–346. <https://doi.org/10.1021/cr030698+>
9. Komarala V. K., Rakovich Yu. P., Bradley A. L. Off-resonance surface plasmon enhanced spontaneous emission from CdTe quantum dots. *Applied Physics Letters*. 2006;89 (25): 253118. <https://doi.org/10.1063/1.2422906>
10. Ke L., Katsnelson M. I. Electron correlation effects on exchange interactions and spin excitations in 2D van der Waals materials. *Npj Computational Materials*. 2021;7(4): 1–8. <https://doi.org/10.1038/s41524-020-00469-2>
11. De Vera P., Abril I., Garcia-Molina R. Excitation and ionisation cross-sections in condensed-phase biomaterials by electrons down to very low energy: application to liquid water and genetic building blocks. *Physical Chemistry Chemical Physics*. 2021;23: 5079–5095. <https://doi.org/10.1039/d0cp04951d>
12. Yadav R. K., Aneesh J., Sharma R.,... Adarsh K. V. Designing hybrids of graphene oxide and gold nanoparticles for nonlinear optical response. *Physical Revied Applied*. 2008;9(4): 044043(10). <https://doi.org/10.1103/PhysRevApplied.9.044043>
13. Kholmicheva N., Royo Romero L., Cassidy J., Zamkov M. Prospects and applications of plasmon-exciton interactions in the near-field regime. *Nanophotonics*. 2019;8(4): 613–628. <https://doi.org/10.1515/nanoph-2018-0143>
14. Danilov V. V., Panfutova A. S., Khrebtov A. I., Ambrosini S., Videnichev D. A. Optical limiting as result a of photoinduced electron transfer in hybrid systems with CdSe/ZnS quantum dots, C60, and Perylene. *Optics Letters*. 2012;37(19): 3948–3950. <https://doi.org/10.1364/OL.37.003948>
15. Khurgin J. B., Sun G. Plasmonic enhancement of the third order nonlinear optical phenomena: Figures of merit. *Optics Express*. 2013;21: 27460. <https://doi.org/10.1364/oe.21.027460>
16. Kauranen M., Zayats A. V. Nonlinear plasmonics. *Nature Photonics*. 2012;6: 737–748. <https://doi.org/10.1038/nphoton.2012.244>
17. Zhang F., Xiao X., Lu Y-P., Dong J., Chen Y. Broadband enhancement of optical nonlinearity in a Pplasmonic nanocavity coupled with an epsilon-near-zero film. *The Journal of Physical Chemistry C*. 2023;127: 3726–3732. <https://doi.org/10.1021/acs.jpcc.2c07796>
18. Wang J., Gao M., He Y., Yang Z. Ultrasensitive and ultrafast nonlinear optical characterization of surface plasmons. *APL Materials*. 2022;10: 030701. <https://doi.org/10.1063/5.0083239>
19. Cox J. D., Singh M. R., Von Bilderling C., Bra-gas A. V. A nonlinear switching mechanism in quantum dot and metallic nanoparticle hybrid systems. *Advanced Optical Materials*. 2013;1: 460–467. <https://doi.org/10.1002/adom.201300105>
20. Milanchian K., Tajalli H., Gilani A. G., Zakerhamidi M. S. Nonlinear optical properties of two oxazine dyes in aqueous solution and polyacrylamide hydrogel using single beam Z-scan. *Optical Materials*. 2009;32: 12–17. <https://doi.org/10.1016/j.optmat.2009.05.011>
21. Delaire J. A., Nakatani K. Linear and nonlinear optical properties of photochromic molecules and materials. *Chemical Reviews*. 2000;100: 1817–1846. <https://doi.org/10.1021/cr980078m>
22. Albert I. D. L., Marks T. J., Ratner M. A. Rational design of molecules with large hyperpolarizabilities. Electric field, solvent polarity, and bond length alternation effects on merocyanine dye linear and nonlinear optical properties. *The Journal of Physical Chemistry*. 1996;100: 9714–9725. <https://doi.org/10.1021/jp960860v>
23. Parida M. R., Vijayan C., Rout C. S., Sandeep C. S. S., Philip R. Enhanced optical nonlinearity in β -AgVO₃ nanobelts on decoration with Ag nanoparticles. *Applied Physics Letters*. 2012;100: 121119. <https://doi.org/10.1063/1.3696301>
24. Sreekumar G., Fröbel P., Sreeja S.,... Mukharjee C. Nonlinear absorption and photoluminescence emission in nanocomposite films of Fuch sine Basic dye-polymer system. *Chemical Physics Letters*. 2011;506: 61–65. <https://doi.org/10.1016/j.cplett.2011.02.048>
25. Sengupta D., Das P., Mondal B. Effects of doping, morphology and film-thickness of photo-anode materials for dye sensitized solar cell application – a review. *Renewable & Sustainable Energy Reviews*. 2016;60: 356–376. <https://doi.org/10.1016/j.rser.2016.01.104>
26. Mathew S., Yella A., Gao P., ... Grätzel M. Dye-sensitized solar cells with 13% efficiency achieved through the molecular engineering of porphyrin sensitizers. *Nature Chemistry*. 2014;6: 242–247. <https://doi.org/10.1038/nchem.1861>
27. Tam F., Goodrich G. P., Johnson B. R., Halas N. J. Plasmonic enhancement of molecular fluorescence. *Nano Letters*. 2007;7: 496–501. <https://doi.org/10.1021/nl062901x>
28. Edappadikkunnummal S., Nherakkayyil S. N., Kuttippurath V., Chalil D. M., Desai N., Keloth C. Surface plasmon assisted enhancement in the nonlinear optical properties of phenothiazine by gold nanoparticle. *The Journal of Physical Chemistry C*. 2017;121: 26976–26986. <https://doi.org/10.1021/acs.jpcc.7b06528>
29. Francis J., Purayil N. P., Edappadikkunnummal S., Chandrasekharan K., Sangeeth C. S. S. Impact of photoinduced energy transfer and LSPR of Au and Ag nanoparticles on nonlinear optical response of methyl orange. *Journal of Molecular Liquids*. 2023;390: 123048. <https://doi.org/10.1016/j.molliq.2023.123048>

30. Turkevich J., Stevenson P. C., Hillier J. A study of the nucleation and growth processes in the synthesis of colloidal gold. *Discussions of the Faraday Society*. 1951;11: 55–75. <https://doi.org/10.1039/DF9511100055>
31. Sheik-Bahae M., Hutchings D. C., Hagan D. J., Van Stryland E. W. Dispersion of bound electron nonlinear refraction in solids. *IEEE Journal of Quantum Electronics*. 1991;27: 1296–1309. <https://doi.org/10.1109/3.89946>
32. Chang Q., Gao Y., Liu X., Chang C. Nonlinear properties of water-soluble Ag_2S and PbS quantum dots under picosecond laser pulses. *IOP Conference Series: Earth and Environmental Science*. 2018;186: 012076. <https://doi.org/10.1088/1755-1315/186/4/012076>
33. Yan D., Shi T., Zang Z., Zhao S., Du J., Leng Y. Stable and low-threshold whispering-gallery-mode lasing from modified $CsPbBr_3$ perovskite quantum dots@ SiO_2 sphere. *Chemical Engineering Journal*. 2020;401: 126066. <https://doi.org/10.1016/j.cej.2020.126066>
34. Liu X., Guo S., Wang H., Hou L. Theoretical study on the closed-aperture Z-scan curves in the materials with nonlinear refraction and strong nonlinear absorption. *Optics Communications*. 2001;197(4-6): 431–437. [https://doi.org/10.1016/s0030-4018\(01\)01406-7](https://doi.org/10.1016/s0030-4018(01)01406-7)
35. Zvyagin A. I., Chevychelova T. A., Grevtseva I. G., ... Ganeev R. A. Nonlinear refraction in colloidal silver sulfide quantum dots. *Journal of Russian Laser Research*. 2020;41: 670–80. <https://doi.org/10.1007/s10946-020-09923-4>
36. Falconieri M, Salvetti G. Simultaneous measurement of pure-optical and thermo-optical nonlinearities induced by high-repetition-rate, femtosecond laser pulses: application to CS_2 . *Applied Physics B*. 1999;69: 133. <https://doi.org/10.1007/s003400050785>
37. Zvyagin A. I., Chevychelova T. A., Chirkov K. S., Smirnov M. S., Ovchinnikov O. V. Size dependence of nonlinear optical properties of PbS QDs, passivated with thioglycolic acid. *Optik*. 2023;272, 170276. <https://doi.org/10.1016/j.ijleo.2022.170276>
38. Mary K. A. A., Unnikrishnan N. V., Philip R. Role of surface states and defects in the ultrafast nonlinear optical properties of CuS quantum dots. *APL Materials*. 2014;2: 076104. <https://doi.org/10.1063/1.4886276>
39. Skurlov I. D., Ponomareva E. A., Ismagilov A. O., ... Litvin A. P. Size dependence of the resonant third-order nonlinear refraction of colloidal PbS quantum dots. *Photonics*. 2020;7: 39. <https://doi.org/10.3390/photonics7020039>
40. Rusinov A. P., Kucherenk M. G. Nonlinear absorption of methylene blue solutions in the presence of plasma nanoparticles with various surface charge. *Optics and Spectroscopy*. 2020;128(9): 1492-1499. <https://doi.org/10.1134/S0030400X20090179>

Information about the authors

Andrey I. Zvyagin, Cand. Sci. (Phys.–Math.), Lecturer, Department of Optics and Spectroscopy, Voronezh State University (Voronezh, Russian Federation).

<https://orcid.org/0000-0002-1914-9054>
andzv92@yandex.ru

Tamara A. Chevychelova, Lecturer, Department of Optics and Spectroscopy, Voronezh State University (Voronezh, Russian Federation).

<https://orcid.org/0000-0001-8097-0688>
tamarachevychelova@yandex.ru

Mikhail S. Smirnov, Dr. Sci. (Phys.–Math.), Associate Professor, Professor at the Department of Optics and Spectroscopy, Voronezh State University (Voronezh, Russian Federation).

<https://orcid.org/0000-0001-8765-0986>
smirnov_m_s@mail.ru

Oleg V. Ovchinnikov, Dr. Sci. (Phys.–Math.), Full Professor, Dean of the Faculty of Physics, Head of the Department of Optics and Spectroscopy, Voronezh State University (Voronezh, Russian Federation).

<https://orcid.org/0000-0001-6032-9295>
ovchinnikov_o_v@rambler.ru

Anatoly N. Latyshev, Dr. Sci. (Phys.–Math.), Full Professor, Consulting Professor at the Department of Optics and Spectroscopy, Voronezh State University (Voronezh, Russian Federation).

<https://orcid.org/0000-0002-7271-0795>
latyshev@phys.vsu.ru

Received 05.12.2023; approved after reviewing 12.12.2023; accepted for publication 25.12.2023; published online 01.10.2024.

Translated by Valentina Mittova



Original articles

Research article

<https://doi.org/10.17308/kcmf.2024.26/12219>

Formation of smooth and microporous ZnO-based substrate material

A. M. Ismailov¹✉, A. E. Muslimov²

¹Dagestan State University,
43-a Magomet Gadzhiev st., Makhachkala 367000, Republic of Dagestan, Russian Federation

²National Research Centre “Kurchatov Institute”
1 Akademika Kurchatova pl., Moscow 123182, Russian Federation

Abstract

The paper investigates the influence of the deposition temperature on the morphology and structural-phase composition of the ZnO-based substrate material with a thickness of over 50 μm during the magnetron sputtering of hot ceramic targets.

The study revealed the influence of the deposition temperature on the growth rate, morphology, and structural parameters of the ZnO single crystal precipitate. It was shown that the ZnO deposition rates during the spluttering of hot ceramic targets were ultra-high (up to 1.5 μm/min). The authors propose a method for the formation of both smooth and microporous ZnO-based substrate materials without using template technologies.

The results obtained in the work can be widely used in optoelectronics and nitride technologies.

Keywords: Zinc oxide, Hot target, Magnetron sputtering, Microporous Structure, substrates, Nitride technologies

Funding: This study was supported by Russian Science Foundation (grant No. 24-29-00696).

For citation: Ismailov A. M., Muslimov A. E. Formation of smooth and microporous ZnO-based substrate material *Condensed Matter and Interphases*. 2024;25(3): 440–446. <https://doi.org/10.17308/kcmf.2024.26/12219>

Для цитирования: Исмаилов А. М., Муслимов А. Э. Формирование гладкого и микропористого подложечного материала на основе ZnO. *Конденсированные среды и межфазные границы*. 2024;26(3): 440–446. <https://doi.org/10.17308/kcmf.2024.26/12219>

✉ Ismailov Abubakar Magomedovich, e-mail: egdada@mail.ru

© Ismailov A. M., Muslimov A. E., 2024



The content is available under Creative Commons Attribution 4.0 License.

1. Introduction

Many modern optoelectronic devices, in particular white LEDs, are based on nitride technologies. The main components of white LEDs are blue-light emitting LEDs [1,2] and phosphors that convert blue-light quanta into quanta of lower energy [3, 4]. A typical example of a blue LED is the multi-layer InGaN/GaN heterostructure with an active region based on multiple InGaN quantum wells [5]. Significant disadvantages of such structures reducing the light yield efficiency are background impurities, high density of lattice defects, and mechanical stresses affecting the parameters of the band structure. Structural defects and stresses are associated with discrepancies between the crystallographic parameters of nitride growth structures and sapphire substrates. Also, total internal reflection leading to photon scattering results in a decrease in the efficiency of light-emitting devices. Background impurities are almost impossible to eliminate due to the specific features of the method of organometallic vapor-phase epitaxy, while defects and stresses can be reduced by using “native” substrates for nitride compounds. Currently, widespread use of “native” gallium nitride substrates is not possible due to their high production costs. Therefore, it appears to be promising to use a ZnO-based substrate material (a gallium nitride isostructural material). Despite the minimal discrepancies between the parameters of ZnO and GaN (less than 2% [6]), the production of bulk ZnO single crystals is also expensive, however, ZnO film synthesis technologies are simple and affordable. To use ZnO films as a substrate material, their sufficient thickness should be at least tens of micrometers. Conventional thin-film technologies for gas-phase, magnetron deposition, laser ablation, etc. are characterized by relatively low growth rates and are not designed to produce bulk substrate material.

In this paper, the technology of magnetron sputtering of hot zinc oxide ceramic targets was used to obtain thick ZnO layers, i.e. a ZnO target, thermally insulated from the water-cooled magnetron base, was sputtered. It should be noted that the hot sputtering technology is mainly used for sputtering single-component metal targets [7,8]. In addition, it is known [9] that

oxide or nitride films are formed by sputtering hot metal targets in the corresponding gaseous medium. In this regard, studies dedicated to the sputtering of multicomponent ceramic targets at a high discharge power are very relevant. The main problem is associated with the difficulty of building a model for sputtering of “hot” ceramic targets. In contrast to the cooled target sputtering, cascade sputtering is accompanied by interconnected processes of radiation-enhanced diffusion of atoms, leading to the formation of growths on the surface of the target, and microparticle emissions characteristic of shock-evaporation processes. Due to the inhomogeneity of the gas phase, the study of deposition processes and their dependence on technological parameters (discharge power, pressure of the working gas, and substrate temperature) is important and of scientific novelty. It is challenging to consider all parameters at the same time, so at this stage only the temperature of the substrate was changed. Our first results on the sputtering of hot ZnO ceramic targets were published earlier [10]. Studies showed that at a sufficiently high temperature of the substrate of 900 °C, epitaxial films were formed with an ultra-high rate of about 0.9 $\mu\text{m}/\text{min}$, which is uncommon for thin-film technologies. What is more, the films had a developed micromorphology and characteristic hexagonal microcrystals up to several micrometers in size were isolated on the surface. It should be noted that reducing the deposition temperature is a priority that meets the requirements of energy efficiency. A decrease in the deposition temperature under conditions of high discharge power and, as a result, high inhomogeneity of the ionized gas phase, can lead to radical changes in the growth processes. This work studies the influence of the deposition temperature on the morphology and structural-phase composition of the ZnO-based substrate material with a thickness of more than 50 μm during the magnetron sputtering of hot ceramic targets.

2. Experimental

Chemically and mechanically polished R-plane of a sapphire was used as a substrate. ZnO films were precipitated by magnetron sputtering with a cut-off of the cooling mode as described in [10], under the following conditions:

type I: temperature 750 °C, oxygen atmosphere, pressure 1 Pa, discharge current strength 500 mA, deposition time 35 min; type II: temperature 830 °C, oxygen atmosphere, pressure 1 Pa, discharge current strength 500 mA, deposition time 2 h. Samples obtained at a temperature of 900 °C (type III) were used for comparison [10].

X-ray diffraction (XRD) was used for structural studies of the films. X-ray diffraction patterns were recorded with Bragg-Brentano geometry using an Empyrean diffractometer manufactured by PANalytical (Netherlands). The study involved using copper anode radiation ($\text{CuK}\alpha_2 = 1.54 \text{ \AA}$). Electron microscopic studies of the cross-section of the sample were carried out on a Jeol NEOSCOPE 2 (JCM-6000) scanning electron microscope (SEM).

3. Results and discussion

During the hot ceramic target sputtering, the target is heated, which results in the formation of growths of various morphologies on the target surface. These growths are further destroyed by micro-arcs, as a result of which both ionized components and their microparticles enter the gas phase. The large mass of the microparticles restricts their diffusion activity on the growing surface. In addition, it is necessary to take into consideration that the adsorbed microparticles can melt. The melting point in thin layers is lower, and the Tammann temperature (T_t) can be used as a rough estimate [11]: $T_t \approx (0.3-0.5) T_0$, where $T_0 = 1,975 \text{ °C}$, the melting point of bulk ZnO. The vibration spectrum of the atoms on the crystal surface differs from their bulk spectrum. The oscillation amplitude of atoms located on the surface is always much higher than in bulk. It was established that for a wide class of single crystals of metals and semiconductors, the Debye temperature T_D , at which all vibrational modes in a solid are excited, for the surface phase, decreases to the values of about $0.5 T_D$ [12]. For ZnO, the value of T_D is about 100 °C [13] and at low temperatures, a significant weakening of the elastic harmonic forces in the near-surface layers of ZnO can be expected. Therefore, at the precipitation temperatures of 700–900 °C studied in the work, the processes of precipitate nucleation and growth cardinally depended on the temperature of the substrate.

The thickness of the ZnO film on the *R-plane* of the sapphire measured by SEM was 53.6 μm . The average growth rate of ZnO films was about 1.50 $\mu\text{m}/\text{min}$, which is a high rate comparable to the growth rate of ZnO uniaxial microcrystals (monocrystalline whiskers). The high rate was achieved due to the emission of microparticles from the surface of the hot target and their incorporation in a growing film according to the “liquid-crystal” mechanism [10]. The surface of the ZnO film was rough and morphologically heterogeneous (Fig. 1a) with individual microcrystallites of different shapes.

During the next stage, the ZnO film easily separated from the sapphire substrate. This was facilitated by a significant (more than 10 times) difference in the coefficients of thermal expansion of ZnO and sapphire and a sufficiently large thickness of the ZnO film. According to the SEM data, the lower (reverse) surface of the film (Fig. 1b) adjacent to the surface of the substrate during growth was cardinally different from the upper surface, which was loose. The lower surface was a honeycomb-like structure with linear sizes of its pores of 3–10 μm and a depth of up to 5 μm . The thickness of the pore walls was several micrometers (1–2 μm), which allows characterizing them as microwalls. The pore shape was predominantly trigonal. There were fewer pores of hexagonal shape and they were often compressed along one of the diameters of the hexagon. In addition, the microwalls had a multilayer structure.

The diffraction reflections in the XRD images (Fig. 2a) corresponded to the hexagonal (wurtzite) phase of ZnO (JCPDS card. No 36-1451). The ZnO film on both front and back sides was textured along direction [0001]. The XRD curve recorded on the back of the film had reflections associated with parasitic [103] crystallites. The parameters of the ZnO lattice calculated from the XRD data differed significantly for the two sides of the film. Parameters $d_{001} = 2.61 \text{ \AA}$ and $d_{103} = 1.48 \text{ \AA}$ for the porous part of the film were close to the standard ($d_{001} = 2.60 \text{ \AA}$ and $d_{103} = 1.477 \text{ \AA}$). Taking into consideration the low-intensity asymmetric reflexes on the diffraction pattern of the smooth front side of the film, parameters $d_{001} = 2.56 \text{ \AA}$ and $d_{110} = 1.610 \text{ \AA}$ were calculated, which appeared to be smaller than the standard ($d_{001} = 2.60 \text{ \AA}$ and

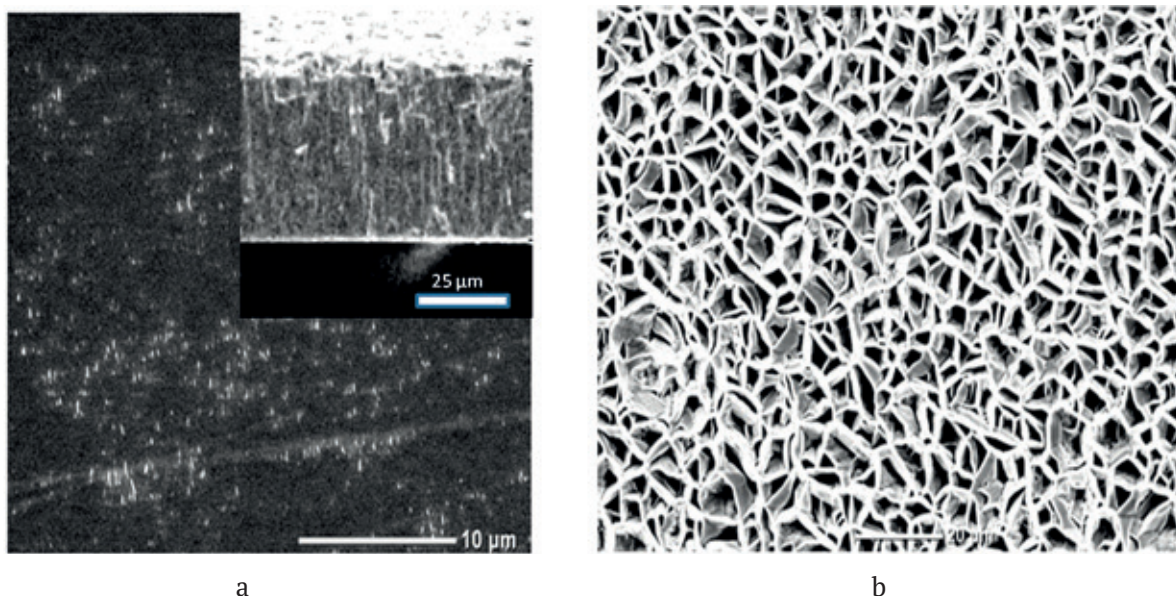


Fig. 1 Electron microscopic images of ZnO type I film: upper (a) and lower (b) surfaces

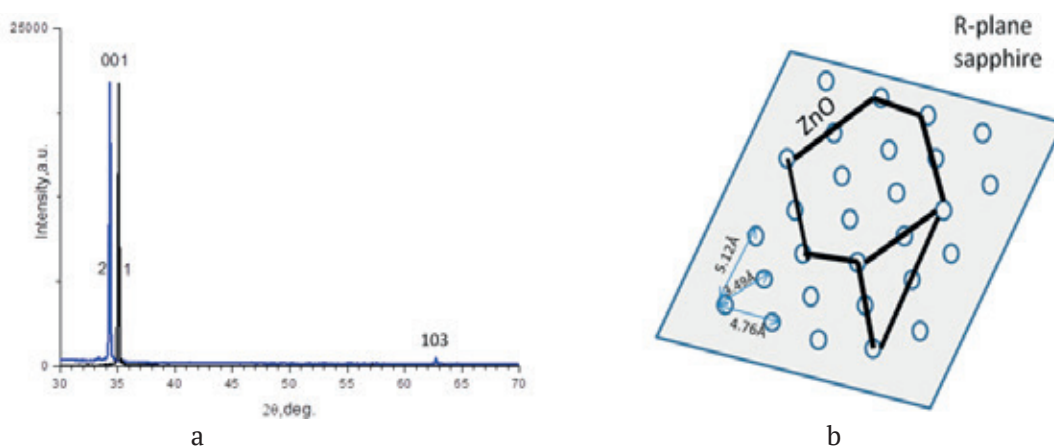


Fig. 2. a – X-ray diffraction patterns recorded from the upper (curve 1) and lower (curve 2) sides of the type I ZnO. b – scheme of the initial ZnO layers growth on the *R*-plane of the sapphire

$d_{110} = 1.6245 \text{ \AA}$). The unit cell volume $V = 45.97 \text{ \AA}^3$ was also smaller than the unit cell volume of the standard $V = 47.58 \text{ \AA}^3$, however, the decrease was mainly due to compression along axis $\langle 0001 \rangle$.

During the epitaxial deposition of ZnO on the *R*-plane of the sapphire, due to the structural and geometric similarity of the lattices, the following epitaxial ratio is usually realized: $A(110)\text{ZnO} \parallel R\text{-sapphire}$, with ZnO axis $[001]$ located in the plane of the sapphire surface [14]. In our case, $[110]$ -oriented ZnO crystallites were absent due to the specific features of hot target sputtering (emission of microparticles) and the peculiarities of nucleation at low diffusion mobility of clusters. The ZnO film was growing along energetically

favorable direction $[001]$. It is known [15] that $[001]$ -textured ZnO films grow quite easily even on non-orienting substrates. Parasitic $[103]$ crystallites of ZnO are usually observed in films growing at high rate [16]. The ZnO hexagonal structure of the wurtzite type had a six-fold symmetry. This was due to the formation of hexagonal and trigonal pores. ZnO clusters deposited on the *R*-plane of the sapphire self-organized along the directions with the highest linear density of atoms and in accordance with the symmetry of the wurtzite structure (Fig. 2b). What is more, the lattice points formed a rectangle (almost a square) with sides of 4.76 and 5.12 Å, which explains the distortions of the

shape of the growing hexagonal and trigonal ZnO structures. Thus the first layer was formed and the subsequent ones were deposited on the previous one, forming a multilayer structure of the pore walls. It should be noted that the lattice parameters complied with the standard. The resulting honeycomb-like microstructure of the film confirmed a predominant emission of clusters from the surface of the overheated ZnO target. Adsorbed atoms and clusters, due to their diffusion activity, formed a continuous precipitate. The self-organization of ZnO microparticles on the sapphire surface must be mostly due to their Coulomb interaction, however, this needs to be studied in more detail.

The situation was different for the front side of the film. A significant compression of the Zn lattice and high stresses combined with the visually orange-brownish coloring of the film indicated a high concentration of structural defects, in particular oxygen vacancies. There was a high likelihood of oxygen deficiency in the clusters emitted by the target. Since a significant compression of the lattice was observed along axis $\langle 0001 \rangle$, it can be assumed that the ultra-high growth rate of ZnO films was due to the layering of oxygen-deficient clusters and the lag in the ordering process. Whereas a small deviation in azimuthal parameter α was associated with the high lateral activity of adatoms and clusters, supported by the high temperature of the substrate, which contributed to the partial filling of oxygen vacancies, interatomic interaction, and ordering.

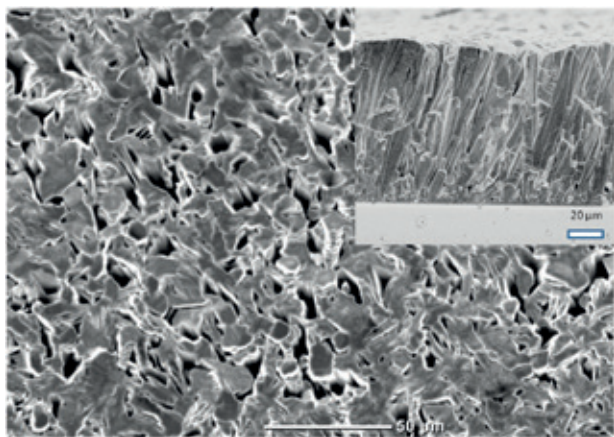


Fig. 3 Electron microscopic images of ZnO type II film

With an increase in the deposition temperature to 830 °C, the growth rate decreased to 0.85 $\mu\text{m}/\text{min}$. According to the SEM data, the thickness of the sample was 102 μm . The film had good adhesion to the substrate and did not peel off. The study of the morphology of the film section confirmed the columnar microstructure characteristic of ZnO synthesized at a high rate. The axis of the columnar microstructure deviated from the normal to the substrate plane, which was obviously associated with the direction of the shortest distance to the source (target). On the surface (Fig. 3) and in the film's bulk, there were penetrating micropores with a diameter of up to 10 μm . The elements of the columnar structure were formed by flat ZnO c -crystallites layered on top of each other. The high intensity of the incoming clusters created conditions in which, as a whole, the normal [17] growth of the ZnO precipitate prevailed. What is more, the formation of faceted flat microcrystals indicated a sufficient temperature for epitaxial deposition. However, there were no direct indicators of cluster melting at the adsorption stage.

According to X-ray diffraction data, a highly textured c -oriented ZnO film was formed during the deposition process. The parameters $d_{001} = 2.61 \text{ \AA}$ of the ZnO type II film were close to the standard ($d_{001} = 2.60 \text{ \AA}$). After the chemical-mechanical polishing, the surface of the ZnO film was smoothed to roughness values below 5 nm (Fig. 4). During the treatment, about 20 μm was stripped. The porosity remained at the level of

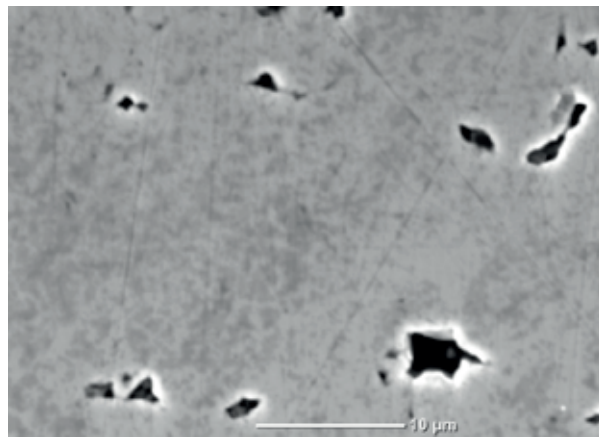


Fig. 4. Electron microscopic image of the surface of the ZnO type II film after chemical-mechanical polishing

10^6 cm^{-1} , which confirms the penetration of pores into the film bulk.

For comparison, the average growth rate of the type III film [10] was about $0.9 \mu\text{m}/\text{min}$. It can be concluded that after the deposition temperature was increased to above $800 \text{ }^\circ\text{C}$, the growth rate practically did not change. At these temperatures, the quality of the ZnO film was significantly improved, and the mechanisms of epitaxial deposition, azimuthal orientation of clusters were triggered. However, at higher temperatures, there were signs of cluster melting. Apparently, the deposited clusters came into thermal equilibrium with the substrate. The formation of hexagonal microparticles indicated that the crystallization mechanism proceeded under equilibrium conditions through the liquid phase of the initial microparticles melting. A decrease in the porosity of films at high deposition temperatures may also be associated with melting processes.

4. Conclusions

The paper investigated the influence of the deposition temperature during the magnetron sputtering of hot ZnO targets on the morphology and structural-phase composition of the ZnO substrate material. The growth rate of the ZnO single crystal precipitate at a precipitation temperature of $830 \text{ }^\circ\text{C}$ was $0.85 \mu\text{m}/\text{min}$. The ZnO precipitate had a columnar microstructure and a developed surface with isolated pores with a density of less than 10^6 cm^{-1} and linear dimensions of up to $10 \mu\text{m}$. After chemical-mechanical polishing, the surface of the ZnO precipitate was smoothed to roughness values below 5 nm and the porosity still remained. With a decrease in the deposition temperature to $750 \text{ }^\circ\text{C}$, the growth rate increased to $1.5 \mu\text{m}/\text{min}$ and the film easily peeled off the sapphire substrate. The upper surface of the film was heterogeneous: a smooth surface had microcrystals of various shapes. The lower surface of the film had a microporous structure with the following parameters: Pores with a size of up to $10 \mu\text{m}$ and multilayer pore walls with a thickness of $1\text{--}2 \mu\text{m}$. All ZnO films were textured along $[001]$. With an increase in the deposition temperature, the epitaxial quality of the films increased.

The paper demonstrated that the ZnO deposition rates during the sputtering of hot ceramic targets were ultra-high (up to

$1.5 \mu\text{m}/\text{min}$). The obtained samples of ZnO films with a thickness of more than $50 \mu\text{m}$ can be used as a substrate material in microelectronics to manufacture light-emitting devices. Microporous films were obtained for the first time without any special surface pretreatment and template technologies. Microporous structures may be used for photonic applications: pores may be filled with various fluorescent fillers. In addition, the ZnO luminescence spectrum has two main bands: a narrow band-edge luminescence in the region of $380\text{--}390 \text{ nm}$ and a relatively wide band of visible luminescence, often characterized by a maximum of $490\text{--}530 \text{ nm}$ in the green range. Provided that pores are filled with a material with luminescence in the blue region, microporous ZnO can be a very promising source of white light.

Contribution of the authors

The authors contributed equally to this article.

Conflict of interests

The authors declare that they have no known competing financial interests or personal relationships that could have influenced the work reported in this paper.

References

1. Nakamura S., Senoh M., Mukai T. P-GaN/N-InGaN/N-GaN double-heterostructure blue-light-emitting diodes. *Japanese Journal of Applied Physics*. 1993;32(2,1A/B): 8–11. <https://doi.org/10.1143/JJAP.32.L8>
2. Nakamura S., Mukai T., Senoh M. Candela-class high-brightness InGaN/AlGaN double-heterostructure blue-light-emitting diodes. *Applied Physics Letters*. 1994;64(13): 1687–1689. <https://doi.org/10.1063/1.111832>
3. Kong X., Qiu Z., Wu L., Lei Y., Chi L. Luminescence properties of green phosphor $\text{Ca}_2\text{Ga}_2(\text{Ge}_{1-x}\text{Si}_x)\text{O}_7:y\%\text{Eu}^{2+}$ and application. *Materials*. 2023;16(10): 3671. <https://doi.org/10.3390/ma16103671>
4. Wang Q., Xie M., Fang M., ... Min X. Synthesis and luminescence properties of a novel green-yellow-emitting phosphor $\text{BiOCl}:\text{Pr}^{3+}$ for blue-light-based w-LEDs. *Molecules*. 2019;24(7): 1296. <https://doi.org/10.3390/molecules24071296>
5. Xu H., Hou X., Chen L., Mei Y., Zhang B. Optical properties of InGaN/GaN QW with the same well-plus-barrier thickness. *Crystals*. 2022;12(1): 114. <https://doi.org/10.3390/cryst12010114>
6. Gu X., Reshchikov M. A., Teke A., ... Nause J. GaN epitaxy on thermally treated c-plane bulk ZnO sub-

strates with O and Zn faces. *Applied Physics Letters*. 2004;84(13): 2268–2270. <https://doi.org/10.1063/1.1690469>

7. Sidelev D. V., Bleykher G. A., Krivobokov V. P., Koishybayeva Z. High-rate magnetron sputtering with hot target. *Surface and Coatings Technology*. 2016;308: 168–173. <https://doi.org/10.1016/j.surfcoat.2016.06.096>

8. Komlev A. A., Minzhulina E. A., Smirnov V. V., Shapovalov V. I. Influence of argon pressure and current density on substrate temperature during magnetron sputtering of hot titanium target. *Applied Physics A*. 2017;124(1): 48. <https://doi.org/10.1007/s00339-017-1458-4>

9. Graillot-Vuilecot R., Anne-Lise T., Lecas T., Cachoncinlle C., Millon E., Caillard A. Hot target magnetron sputtering process: effect of infrared radiation on the deposition of titanium and titanium oxide thin films. *Vacuum*. 2020;181: 109734. <https://doi.org/10.1016/j.vacuum.2020.109734>

10. Ismailov A. M., Nikitenko V. A., Rabadanov M. R., Emiraslanova L. L., Aliev I. S., Rabadanov M. K. Sputtering of a hot ceramic target: experiments with ZnO. *Vacuum*. 2019;168: 108854. <https://doi.org/10.1016/j.vacuum.2019.108854>

11. Tammann G. Die temperatur des beginnsinnerer diffusion in kristallen. *Zeitschrift Fur Anorganische Und Allgemeine Chemie*. 1926;157(1): 321–325. <https://doi.org/10.1002/zaac.19261570123>

12. Kiselev V. F., Kozlov S. N., Zoteev A. V. *Osnovy fiziki poverkhnosti tverdogo tela (Fundamentals of Solid Surface Physics)*. Moscow: MSU Publ., 1999. 294 p. (In Russ.)

13. Abrahams S. C., Bernstein J. L. Remeasurement of the structure of hexagonal ZnO. *Acta Crystallographica*

Section B: Structural Crystallography and Crystal Chemistry. 1969;25(7): 1233–1236. <https://doi.org/10.1107/S0567740869003876>

14. Peng C.-Y., Tian J.-S., Wang W.-L., Ho Y.-T., Chang L. Morphology evolution of a-plane ZnO films on r-plane sapphire with growth by pulsed laser deposition. *Applied Surface Science*. 2013;265: 553. <https://doi.org/10.1016/j.apsusc.2012.11.044>

15. Yang W., Wang F., Guan Z., ... Fu Y. Comparative study of ZnO thin films grown on quartz glass and sapphire (001) substrates by means of magnetron sputtering and high-temperature annealing. *Applied Sciences*. 2019;9: 4509. <https://doi.org/10.3390/app9214509>

16. Taabouche A., Bouabellou A., Kermiche F., ... Amara S. *Advances in Materials Physics and Chemistry*. 2013;3: 209. <https://doi.org/10.4236/ampc.2013.34031>

17. Kozhevnikov I. V., Buzmakov A. V., Siewert F., ... Sinn H. *Journal of Synchrotron Radiation*. 2016;23(1): 78–90. <https://doi.org/10.1107/s160057751502202x>

Information about the authors

Arsen E. Muslimov, Dr. Sci. (Phys.–Math.), Research Fellow, Federal Research Institute “Crystallography and Photonics” of the Russian Academy of Sciences (Moscow, Russian Federation).

<https://orcid.org/0000-0002-0524-7606>
amuslimov@mail.ru

Abubakar M. Ismailov, Cand. Sci. (Phys.–Math.), Associate Professor at the Department of Physical Electronics, Dagestan State University (Makhachkala, Russian Federation).

<https://orcid.org/0000-0001-6834-0560>
egdada@mail.ru

Received 02.12.2023; approved after reviewing 02.02.2024; accepted for publication 15.02.2024; published online 01.10.2024.

Translated by Irina Charychanskaya



Original articles

Research article

<https://doi.org/10.17308/kcmf.2024.26/12220>**Influence of the nature of the organic acid salt on the current-voltage characteristics and electrochemical impedance spectra of anion-exchange membranes**T. V. Karpenko[✉], V. V. Shramenko, N. V. SheldeshovKuban State University,
149 Stavropol st., Krasnodar 350040, Russian Federation**Abstract**

To improve the processes of obtaining and isolating organic acids from solutions, it is necessary to understand the processes occurring on heterogeneous and homogeneous anion-exchange membranes in contact with solutions of salts of organic acids when electric current flows through the membrane system.

The purpose of this paper was to study the effect of sodium salts of acetic, malonic, and citric acids on the current-voltage characteristics (CVC) and electrochemical impedance (ECI) spectra of heterogeneous and homogeneous anion-exchange membranes.

Heterogeneous Ralex AMH (Mega, Czech Republic) and homogeneous Lancytom® AHT (LANRAN, China) membranes in contact with 0.1 mol-eq/L solutions of neutral and acidic sodium salts of acetic, malonic and citric acids were studied. In solutions of neutral salts, the current-voltage characteristics of both membranes have a traditional form typical for mineral salt solutions, with the exception of the homogeneous Lancytom® AHT membrane in a sodium malonate solution. In the latter case and in solutions of acidic salts of these acids CVC of both membranes are nonlinear at currents less than the limiting. This is caused by proton transfer reactions between water molecules and carboxyl groups of acid anions or acid molecules and, as a result, the rate constant of dissociation of water molecules in solutions of organic acidic salts increased by many orders of magnitude. By the appearance of additional semicircles in the spectra, ECI frequency spectra allow identifying the occurrence of new processes in the membrane system when an electric current flows through it.

In most cases, the results of impedance measurements of the studied systems are consistent with the results of voltammetry, although the protonation-deprotonation processes in solution with the participation of organic acid anions are not reflected in the frequency spectra of a heterogeneous membrane. This feature may have been caused by a greater intensity of electroconvection near the surface of heterogeneous anion-exchange membranes as compared to homogeneous anion-exchange membranes.

Keywords: Anion-exchange membrane, Voltammetry, Impedance measurement, Organic acid, Protonation-deprotonation reaction

Funding: The study was supported by the Russian Science Foundation grant No. 23-23-00660, <https://rscf.ru/project/23-23-00660/>

For citation: Karpenko T. V., Shramenko V. V., Sheldeshov N. V. Influence of the nature of the organic acid salt on the current-voltage characteristics and electrochemical impedance spectra of anion-exchange membranes. *Condensed Matter and Interphases*. 2024;26(3): 447–455. <https://doi.org/10.17308/kcmf.2024.26/12220>

Для цитирования: Карпенко Т. В., Шраменко В. В., Шельдешов Н. В. Влияние природы соли органической кислоты на вольтамперные характеристики и спектры электрохимического импеданса анионообменных мембран. *Конденсированные среды и межфазные границы*. 2024;26(3): 447–455. <https://doi.org/10.17308/kcmf.2024.26/12220>

✉ Tatiana V. Karpenko, e-mail: tany1328@mail.ru

© Karpenko T. V., Shramenko V. V., Sheldeshov N. V., 2024



The content is available under Creative Commons Attribution 4.0 License.

1. Introduction

In recent years, cation and anion-exchange membranes have been widely used in membrane technologies for the production of organic acids [1, 2, 3, 4, 5, 6]. In fermentation solutions, these acids are mainly found in the form of neutral salts. Before obtaining organic acids using electrodialysis with bipolar membranes, their neutral salts are concentrated by traditional electrodialysis. In this case, acid anions are transferred from the fermentation solution to the concentration chamber through anion-exchange membranes. Anion-exchange membranes are used at the stage of obtaining organic acids from their salts [7] without the preliminary concentration of the salts in order to isolate organic acid anions from mixtures with mineral salts [8,9] and separate mixtures of organic acids [10].

There are a lot of studies focusing on the transfer of organic acids through anion-exchange membranes, as well as their electrochemical characteristics in solutions of these acids [11–21]. The transfer of individual acids through anion-exchange membranes [11, 12] and the formation of a limiting state in a system with an anion-exchange membrane [13, 14] in contact with an organic acid solution were studied. In addition, the sorption and diffusion characteristics, electrical conductivity of anion-exchange membranes in organic acid solutions [15], and the effect of solution pH on the selectivity [16] of an anion-exchange membrane in relation to organic acids were studied.

Most organic acids are polybasic. When converting their neutral salts into acids using electrodialysis with bipolar membranes, as well as in electrodialyzers for the separation and purification of organic acids, a mixture of acidic salts of these acids is formed in the electrodialyser chambers during the intermediate stages of the process. Chemical protonation-deprotonation reactions with the participation of acidic salts of organic acids that occur in diffusion layers near anion-exchange membranes [17–21] also affect the electrochemical characteristics of membranes and require additional research. Most of these studies are devoted to systems with homogeneous anion-exchange membranes, although heterogeneous anion-exchange

membranes can also be used for processing solutions that contain salts of organic acids. The study of such membrane systems is required for expanding the area of application of membrane technologies for the production of organic acids and their isolation from mixtures.

Voltammetry and electrochemical impedance spectroscopy are the main methods used to study the processes occurring in membrane systems that contain salts of organic acids. These methods allow obtaining information on the processes occurring in systems with anion-exchange membranes depending on the density of the electric current flowing through the studied membrane.

Thus, the purpose of this work was to study the influence of the nature of the organic acid salts – acetic, malonic, and citric – on the current-voltage characteristics and electrochemical impedance spectra of heterogeneous and homogeneous anion-exchange membranes.

2. Experimental

The heterogeneous Ralex AMH (Mega, Czech Republic) [22] and homogeneous Lancyтом® AHT (LANRAN, China) [23] membranes were used as the studied anion-exchange membranes. The Ralex AMH membrane contain strongly basic quaternary ammonium groups and are reinforced with polyethersulphone. The thickness of the membrane in the swollen state is about 700 μm , it was stable in acids and alkalis in the pH range 0–10. The Lancyтом® AHT membrane is stable in concentrated solutions of acids and alkalis in the pH range 0–14 and it is also thermostable. It retains its properties at temperatures below 60 $^{\circ}\text{C}$. The thickness of the membrane in the swollen state is 220 μm .

To determine the value of the limiting electrodiffusion current on Ralex AMH and Lancyтом® AHT anion-exchange membranes in solutions of organic acid salts and to study the mechanisms of processes occurring on the studied membranes in various current modes, we measured the galvanodynamic current-voltage characteristics of the membranes and the frequency spectra of the electrochemical impedance. During the measurements, the membranes were in contact with 0.1 mol-eq/l solutions of neutral and acidic sodium salts of acetic, malonic, and citric acids.

The study was conducted in an electrochemical cell formed by the studied anion-exchange membrane (Ralex AMH or Lancyotom® AHT) and Ralex CMH cation-exchange membranes placed on both sides of it (Fig. 1).

The working area of the studied anion-exchange membrane was 0.60 cm². The linear velocity of solutions in each chamber was 0.06 cm/s. Standard silver chloride electrodes connected to capillaries on either side of the studied membrane were used for measurements.

Measurements of the current-voltage characteristics of the studied anion-exchange membranes were conducted in galvanodynamic mode at a scan rate of $2 \cdot 10^{-5}$ A/s and a temperature of 25 ± 1 °C using an AUTOLAB 100N potentiostat-galvanostat.

The limiting current densities according to CVC were found using the method of tangents to the ohmic section of CVC and the subsequent section at the inflection point of the curve [24].

The electrochemical impedance spectra of the membranes were measured after establishing a steady state at a temperature of 25 ± 1 °C using an AUTOLAB-100N potentiostat-galvanostat with an FRA32M impedance measurement module. The measurements were performed in the frequency range from 0.1 Hz to 1 MHz, distributed evenly on a logarithmic scale. The amplitude of the measuring alternating current did not exceed 50 mV.

3. Results and discussion

The current-voltage characteristics of the heterogeneous Ralex AMH anion-exchange membrane in solutions of neutral salts of acetic,

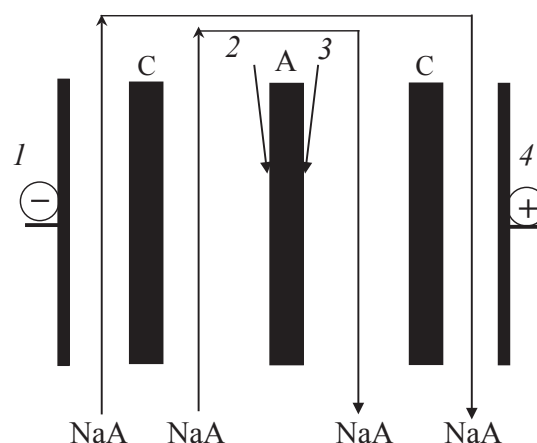


Fig. 1. Scheme of an electrochemical cell for measuring current-voltage characteristics and frequency spectra of the electrochemical impedance of the anion-exchange membranes under study in solutions of salts of acetic, malonic and citric acids. A is the anion exchange membrane under study; C is the Ralex CMH auxiliary cation exchange membranes; 1 and 4 are electrodes polarizing the membrane under study with direct and alternating current; 2 and 3 are standard silver chloride electrodes for measuring the potential difference on the membrane

malonic, and citric acids have a traditional form with a well-defined limiting current section (Fig. 2). The current-voltage characteristics of the homogeneous anion-exchange membrane Lancyotom® AHT have a traditional form only in solutions of neutral salts of acetic and citric acids (Fig. 3a, 3c). In a solution of sodium malonate (neutral salt), the section of the underlimiting current is nonlinear (Fig. 3b). Similar nonlinear sections at currents lower than the limiting ones have the current-voltage characteristics of both

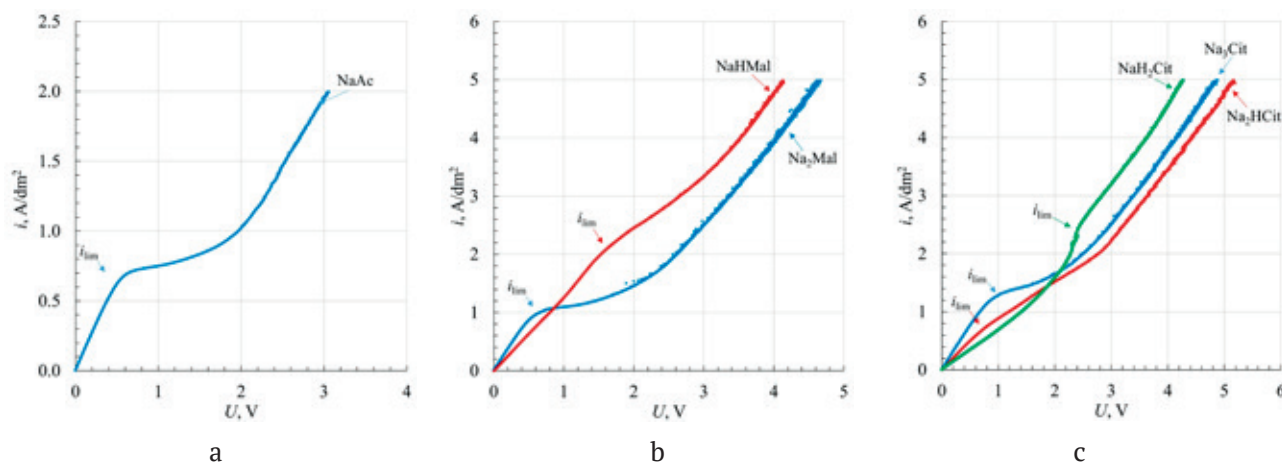


Fig. 2. Current-voltage characteristics of the Ralex AMH anion exchange membrane in 0.1 mol-eq/L solutions of acetic (a), malonic (b) and citric acid (c) salts

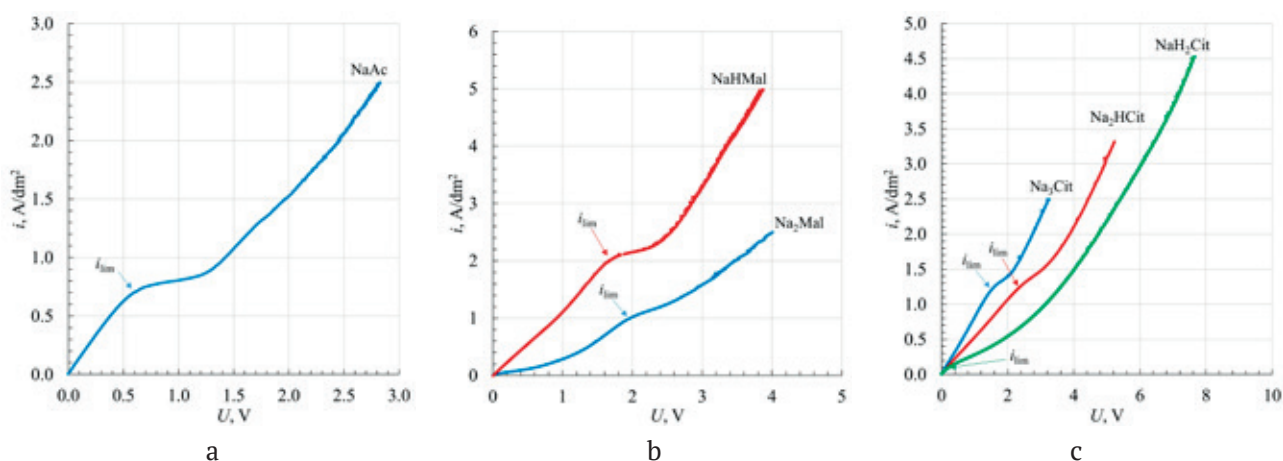


Fig. 3. Current-voltage characteristics of the Lancytom® AHT anion exchange membrane in 0.1 mol-eq/L solutions of acetic (a), malonic (b) and citric acid (c) salts

membranes in solutions of acidic salts of malonic and citric acids (Fig. 2b, 2c and 3b, 3c). These features can be explained by the occurrence of protonation-deprotonation reactions in solution with the participation of anions of acidic salts [18, 19, 21]. These reactions have the same mechanism as the one that was first proposed for the “membrane – solution” system [25]. An increase in the rate of dissociation of water molecules by many orders of magnitude in such systems is explained in [25] by the occurrence of proton

transfer reactions between water molecules and ionogenic groups of compounds that are found in solutions or ionogenic groups of membranes. As for acetic, malonic, and citric acids, as well as their salts in aqueous solutions, the mechanism of dissociation of water molecules corresponds to equations (1)–(12) (Tables 1–3).

Reaction equilibrium constants $K_1 - K_{12}$ were taken from [26], rate constants of reverse reactions (k_{-1} and k_{-12}) were taken from [27, 28]. Analysis of these equations showed that the limiting stages

Table 1. Proton transfer reactions in acetic acid solution

Proton transfer reactions	Reaction equilibrium constants	Reactions rate constants	
$\text{HAc} + \text{H}_2\text{O} \xrightleftharpoons[k_{-1}]{k_1} \text{Ac}^- + \text{H}_3\text{O}^+$	$K_1 = 1.74 \cdot 10^{-5} \text{ mol/L}$	$k_1 = 8.7 \cdot 10^5 \text{ s}^{-1}$	(1)
		$k_{-1} = 5 \cdot 10^{10} \text{ L/(mol s)}$	
$\text{Ac}^- + \text{H}_2\text{O} \xrightleftharpoons[k_{-2}]{k_2} \text{HAc} + \text{OH}^-$	$K_2 = 5.75 \cdot 10^{-10} \text{ mol/L}$	$k_2 = 5.75 \text{ s}^{-1}$	(2)
		$k_{-2} = 1 \cdot 10^{10} \text{ L/(mol s)}$	

Table 2. Proton transfer reactions in malonic acid solution

Proton transfer reactions	Reaction equilibrium constants	Reactions rate constants	
The first stage of dissociation			
$\text{H}_2\text{Mal} + \text{H}_2\text{O} \xrightleftharpoons[k_{-3}]{k_3} \text{HMal}^- + \text{H}_3\text{O}^+$	$K_3 = 1.479 \cdot 10^{-3} \text{ mol/L}$	$k_3 = 7.39 \cdot 10^7 \text{ s}^{-1}$	(3)
		$k_{-3} = 5 \cdot 10^{10} \text{ L/(mol s)}$	
$\text{HMal}^- + \text{H}_2\text{O} \xrightleftharpoons[k_{-4}]{k_4} \text{H}_2\text{Mal} + \text{OH}^-$	$K_4 = 6.761 \cdot 10^{-12} \text{ mol/L}$	$k_4 = 0.0676 \text{ s}^{-1}$	(4)
		$k_{-4} = 1 \cdot 10^{10} \text{ L/(mol s)}$	
The second stage of dissociation			
$\text{HMal}^- + \text{H}_2\text{O} \xrightleftharpoons[k_{-5}]{k_5} \text{Mal}^{2-} + \text{H}_3\text{O}^+$	$K_5 = 2.042 \cdot 10^{-6} \text{ mol/L}$	$k_5 = 1.02 \cdot 10^5 \text{ s}^{-1}$	(5)
		$k_{-5} = 5 \cdot 10^{10} \text{ L/(mol s)}$	
$\text{Mal}^{2-} + \text{H}_2\text{O} \xrightleftharpoons[k_{-6}]{k_6} \text{HMal}^- + \text{OH}^-$	$K_6 = 4.90 \cdot 10^{-9} \text{ mol/L}$	$k_6 = 49.0 \text{ s}^{-1}$	(6)
		$k_{-6} = 1 \cdot 10^{10} \text{ L/(mol s)}$	

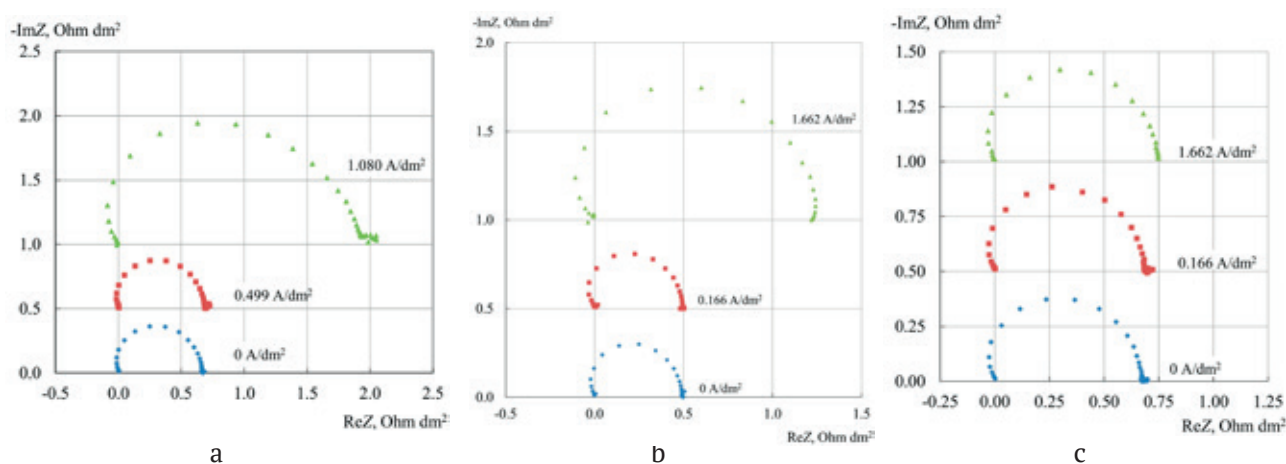
Table 3. Proton transfer reactions in citric acid solution

Proton transfer reactions	Reaction equilibrium constants	Reactions rate constants	
The first stage of dissociation			
$\text{H}_3\text{Cit} + \text{H}_2\text{O} \xrightleftharpoons[k_{-7}]{k_7} \text{H}_2\text{Cit}^- + \text{H}_3\text{O}^+$	$K_7 = 7.413 \cdot 10^{-4} \text{ mol/L}$	$k_7 = 3.71 \cdot 10^7 \text{ s}^{-1}$ $k_{-7} = 5 \cdot 10^{10} \text{ L/(mol s)}$	(7)
$\text{H}_2\text{Cit}^- + \text{H}_2\text{O} \xrightleftharpoons[k_{-8}]{k_8} \text{H}_3\text{Cit} + \text{OH}^-$	$K_8 = 1.349 \cdot 10^{-11} \text{ mol/L}$	$k_8 = 0.135 \text{ s}^{-1}$ $k_{-8} = 1 \cdot 10^{10} \text{ L/(mol s)}$	(8)
The second stage of dissociation			
$\text{H}_2\text{Cit}^- + \text{H}_2\text{O} \xrightleftharpoons[k_{-9}]{k_9} \text{HCit}^{2-} + \text{H}_3\text{O}^+$	$K_9 = 1.738 \cdot 10^{-5} \text{ mol/L}$	$k_9 = 8.69 \cdot 10^5 \text{ s}^{-1}$ $k_{-9} = 5 \cdot 10^{10} \text{ L/(mol s)}$	(9)
$\text{HCit}^{2-} + \text{H}_2\text{O} \xrightleftharpoons[k_{-10}]{k_{10}} \text{H}_2\text{Cit}^- + \text{OH}^-$	$K_{10} = 5.751 \cdot 10^{-10} \text{ mol/L}$	$k_{10} = 5.75 \text{ s}^{-1}$ $k_{-10} = 1 \cdot 10^{10} \text{ L/(mol s)}$	(10)
The third stage of dissociation			
$\text{HCit}^{2-} + \text{H}_2\text{O} \xrightleftharpoons[k_{-11}]{k_{11}} \text{Cit}^{3-} + \text{H}_3\text{O}^+$	$K_{11} = 4.074 \cdot 10^{-7} \text{ mol/L}$	$k_{11} = 2.04 \cdot 10^4 \text{ s}^{-1}$ $k_{-11} = 5 \cdot 10^{10} \text{ L/(mol s)}$	(11)
$\text{Cit}^{3-} + \text{H}_2\text{O} \xrightleftharpoons[k_{-12}]{k_{12}} \text{HCit}^{2-} + \text{OH}^-$	$K_{12} = 2.45 \cdot 10^{-8} \text{ mol/L}$	$k_{12} = 245 \text{ s}^{-1}$ $k_{-12} = 1 \cdot 10^{10} \text{ L/(mol s)}$	(12)

of the reaction of dissociation of water molecules with the participation of anions of acetic, malonic, and citric acids were the reactions (2), (4), (6), (8), (10), and (12) with corresponding rate constants of 5.75 s^{-1} , 0.0676 s^{-1} , 49.0 s^{-1} , 0.135 s^{-1} , 5.75 s^{-1} , and 245 s^{-1} . These constants are many orders of magnitude greater than the rate constant of dissociation of water molecules in pure water that is equal to $2.5 \cdot 10^{-5} \text{ s}^{-1}$. As a result, the reaction rate of dissociation of water molecules in the diffusion layers of membrane systems significantly exceeded

the rate of water dissociation in pure water. Naturally, in an accurate calculation of the rate of water dissociation in the studied systems not only the rate constants, but also the concentrations of anions and acid molecules must be taken into account.

At currents exceeding the limiting current in membrane systems, the dissociation reaction of water molecules occurred on the surface of anion-exchange membranes at a high rate. This leads to an increase in the voltage on the membrane, and


Fig. 4. Frequency spectra of electrochemical impedance Ralex AMH anion exchange membrane in 0.1 mol-eq/L solutions of NaAc (a), Na_2Mal (b) and NaHMal (c)

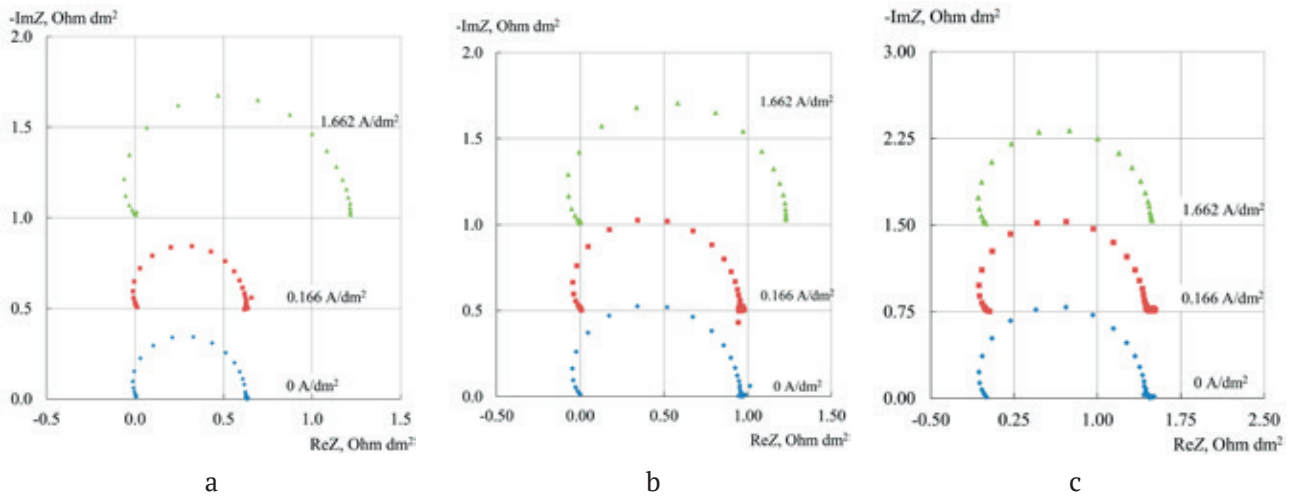


Fig. 5. Frequency spectra of electrochemical impedance Ralex AMH anion exchange membrane in 0.1 mol-eq/L solutions of Na_3Cit (a), Na_2HCit (b) и NaH_2Cit (c)

the contributions from reactions involving acid anions occurring in the solution adjacent to the membrane become undetectable on the current-voltage characteristic.

Despite the fact that at currents lower than the limiting ones, protonation-deprotonation

reactions with the participation of anions of organic acids occurred in the “Ralex AMH – acidic salt solution” system, this was not reflected in the frequency spectra of the impedance of the heterogeneous Ralex AMH membrane (Fig. 4, 5). There is only one distorted semicircle in the

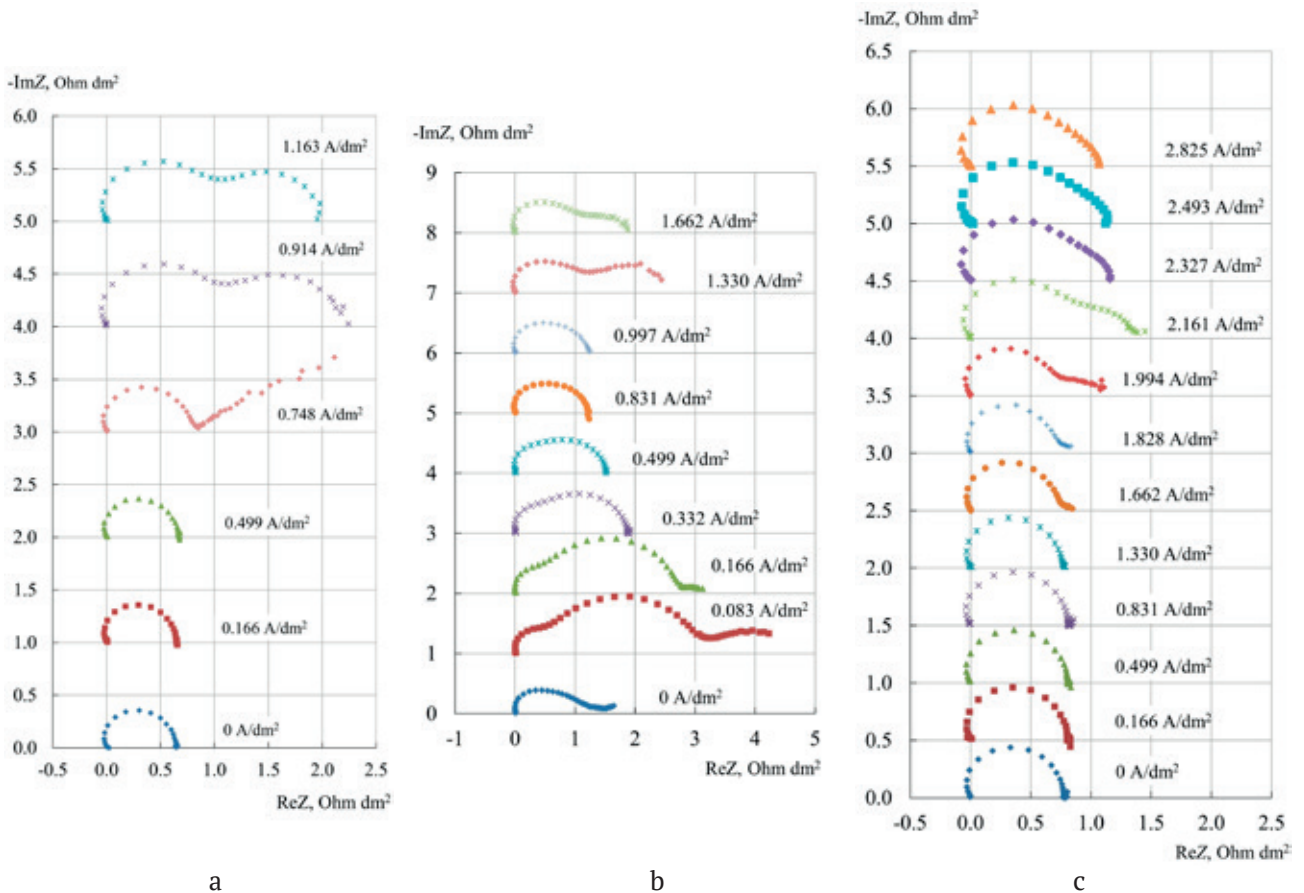


Fig. 6. Frequency spectra of electrochemical impedance Lancyтом® AHT anion exchange membrane in 0.1 mol-eq/L solutions of NaAc (a), Na_2Mal (b) and NaHMal (c)

frequency range 0.1 Hz – 1 MHz. The appearance of additional semicircles in the system with the homogeneous Lancytom® AHT membrane (Fig. 6, 7) in similar cases can be caused by more intense electroconvection that occurs on the surface of the heterogeneous anion-exchange membrane when electric current flows through it [29, p. 240].

In the region of underlimiting current densities on the surface of the Lancytom® AHT membrane in Na_2Mal solutions, the processes of protonation-deprotonation of organic acid anions occurred causing the appearance of an additional semicircle in the low-frequency part of the impedance spectrum (Fig. 6b). This process was weakly expressed in Na_2HCit and NaH_2Cit solutions in this current range (Fig. 7b, 7c).

4. Conclusions

Current-voltage characteristics of Ralex AMH and Lancytom® AHT anion-exchange membranes in solutions of neutral salts of acetic, malonic, and

citric acids have a traditional appearance, with the exception of the “Lancytom® AHT membrane – sodium malonate” system. The reason for the nonlinearity of the underlimiting current section in the latter system was not clear, so this system requires further research. The nonlinear appearance of sections of current-voltage curves at currents lower than the limiting was caused by the occurrence of proton transfer reactions between water molecules and carboxyl groups of acid anions, or acid molecules. This resulted in an increase by many orders of magnitude in the rate constant for the dissociation of water molecules in solutions of salts of organic acids. By the appearance of additional semicircles in the spectra, ECI frequency spectra allow identifying the occurrence of new processes in the membrane system when an electric current flows through it. In most cases, the results of impedance measurements of the studied systems are consistent with the results of voltammetry,

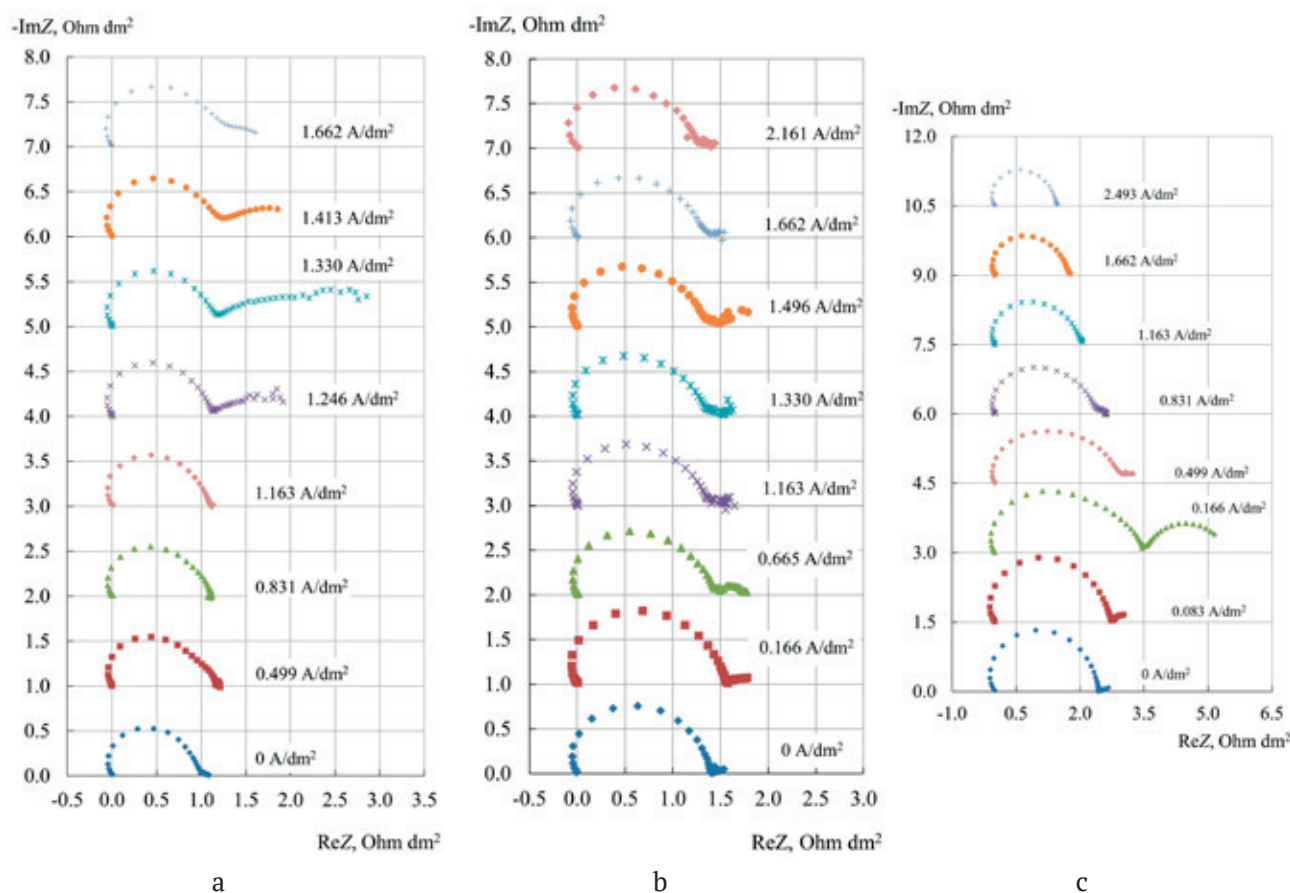


Fig. 7. Frequency spectra of electrochemical impedance Lancytom® AHT anion exchange membrane in 0.1 mol-eq/L solutions of Na_3Cit (a), Na_2HCit (b) и NaH_2Cit (c)

although the protonation-deprotonation processes in solution with the participation of organic acid anions are not reflected in the frequency spectra of a heterogeneous membrane. This feature may have been caused by a greater intensity of electroconvection near the surface of heterogeneous anion-exchange membranes as compared to homogeneous anion-exchange membranes. Measuring ion fluxes and effective transport numbers of ion through anion-exchange membranes may be able to provide additional information about the processes of ion transfer through these membranes in systems containing salts of organic acids.

Author contributions

All authors made an equivalent contribution to the preparation of the publication.

Conflict of interests

The authors declare that they have no known competing financial interests or personal relationships that could have influenced the work reported in this paper.

References

1. Kemperman A. J. B. *Handbook bipolar membrane technology*. Enschede: Twente University Press (TUP). 2000. 275 p. Available at: <https://research.utwente.nl/en/publications/handbook-bipolar-membrane-technology>
2. Hoek E. M. V., Tarabara V. V. (eds). *Encyclopedia of membrane science and technology*. Vol. 3. Hoboken, NJ: Wiley; 2013. 2328 p. <https://doi.org/10.1002/9781118522318>
3. Tanaka Y. *Ion exchange membranes. Fundamentals and applications, 2nd Edition*. Amsterdam: Elsevier Science; 2015. 522 p. <https://doi.org/10.1016/b978-0-444-63319-4.00002-x>
4. Jiang C., Wang Y., Xu T. Membranes for the recovery of organic acids from fermentation broths. *Membrane Technologies for Biorefining*. 2016: 135–161. <https://doi.org/10.1016/B978-0-08-100451-7.00006-2>
5. Ran J., Wu L., He Y., ... Xu T. Ion exchange membranes: New developments and applications. *Journal of Membrane Science*. 2017;522: 267–291. <https://doi.org/10.1016/j.memsci.2016.09.033>
6. Karaffa L., Ch. P. Kubicek Ch. P. Production of organic acids by fungi. In: *Encyclopedia of Mycology*. Óscar Zaragoza, Arturo Casadevall (eds.). Elsevier; 2021. pp. 406–419. <https://doi.org/10.1016/B978-0-12-809633-8.21066-2>
7. Szczygiełda M., Prochaska K. Effective separation of bio-based alpha-ketoglutaric acid from post-fermentation broth using bipolar membrane electrodialysis (EDBM) and fouling analysis. *Biochemical Engineering Journal*. 2021;166: 107883. <https://doi.org/10.1016/j.bej.2020.107883>
8. Melnikov S. S., Nosova E. N., Melnikova E. D., Zabolotsky V. I. Reactive separation of inorganic and organic ions in electrodialysis with bilayer membranes. *Separation and Purification Technology*. 2021;268: 118561. <https://doi.org/10.1016/j.seppur.2021.118561>
9. Mandal P., Mondal R., Goel P., Bhuvanesh E., Chatterjee U., Chattopadhyay S. Selective recovery of carboxylic acid through PVDF blended anion exchange membranes using electrodialysis. *Separation and Purification Technology*. 2022;292: 121069. <https://doi.org/10.1016/j.seppur.2022.121069>
10. Karpenko T. V., Kovalev N. V., Kirillova K. R., ... Zabolotsky V. I. Competing transport of malonic and acetic acids across commercial and modified RALEX AMH anion-exchange membranes. *Membranes and Membrane Technologies*. 2022;4: 118–126. <https://doi.org/10.1134/S2517751622020056>
11. Kotov V. V., Isaev N. I., Shaposhnik V. A. Transfer of weak electrolytes through ion-exchange membranes*. *Russian Journal of Physical Chemistry A*. 1972;46: 539–540. (In Russ.) Available at: <https://elibrary.ru/item.asp?id=28901705>
12. Reshetnikova A. K., Rozhkova M. V., Kotov V. V., Akimenko I. B. Transfer of dicarboxylic acids across ion-exchange membranes. *Electrochemistry*. 1996;32(2): 180–183. Available at: <https://elibrary.ru/item.asp?id=13247836>
13. Vasil'eva V. I., Reshetnikova A. K. Diffusion boundary layers in transport of aliphatic acids in electromembrane systems. *Russian Journal of Electrochemistry*. 2002;38: 965–971. <https://doi.org/10.1023/A:1020284826862>
14. Vasil'eva V. I., Grigorchuk O. V., Shaposhnik V. A. Limiting current density in electromembrane systems with weak electrolytes. *Desalination*. 2006;192(1–3): 401–407. <https://doi.org/10.1016/j.desal.2005.07.044>
15. Kozaderova O. A. Sorption, diffusion characteristics and electrical conductivity of anion-exchange membranes in solutions of lactic acid and sodium chloride. *Sorbtsionnye i Khromatograficheskie Protssy*. 2023;23(4): 539–546. (In Russ., abstract in Eng.). <https://doi.org/10.17308/sorpchrom.2023.23/11563>
16. Chandra A., Tadimetri J. G. D., Bhuvanesh E., Pathiwada D., Chattopadhyay S. Switching selectivity of carboxylic acids and associated physico-chemical changes with pH during electrodialysis of ternary mixtures. *Separation and Purification Technology*. 2018;193: 327–344. <https://doi.org/10.1016/j.seppur.2017.10.048>

17. Martí-Calatayud M. C., Evdochenko E., Bär J., García-Gabaldón M., Wessling M., Pérez-Herranz V. Tracking homogeneous reactions during electro dialysis of organic acids via EIS. *Journal of Membrane Science*. 2020;595: 117592. <https://doi.org/10.1016/j.memsci.2019.117592>
18. Pismenskaya N. D., Rybalkina O. A., Kozmai A. E., Tsygurina K. A., Melnikova E. D., Nikonenko V. V. Generation of H⁺ and OH⁻ ions in anion-exchange membrane/ampholyte-containing solution systems: A study using electrochemical impedance spectroscopy. *Journal of Membrane Science*. 2020;601: 117920. <https://doi.org/10.1016/j.memsci.2020.117920>
19. Rybalkina O. A., Sharafan M. V., Nikonenko V. V., Pismenskaya N. D. Two mechanisms of H⁺/OH⁻ ion generation in anion-exchange membrane systems with polybasic acid salt solutions. *Journal of Membrane Science*. 2022;651: 120449. <https://doi.org/10.1016/j.memsci.2022.120449>
20. Chandra A., Bhuvanesh E., Chattopadhyay S. A critical analysis on ion transport of organic acid mixture through an anion-exchange membrane during electro dialysis. *Chemical Engineering Research and Design*. 2022;178: 13–24. <https://doi.org/10.1016/j.cherd.2021.11.035>
21. Gorobchenko A. D., Mareev S. A., Rybalkina O. A., Tsygurina K. A., Nikonenko V. V., Pismenskaya N. D. How do proton-transfer reactions affect current-voltage characteristics of anion-exchange membranes in salt solutions of a polybasic acid? Modeling and experiment. *Journal of Membrane Science*. 2023;683: 121786. <https://doi.org/10.1016/j.memsci.2023.121786>
22. MEGA Group; RALEX[®] electro separation membranes. Available at: <https://www.mega.cz/membranes>
23. Acid/Alkali resistance Anion IEM-LANCYTOM[®] IEM-Bipolar-ED-RED-LiOH-LANRAN. Available at: http://lanran.com.cn/?list_8/102.html
24. Zabolotskii V. I., Shel'deshov N. V., Sharafan M. V. Electric mass transfer of sodium chloride through cation-exchange membrane MK-40: A rotating membrane disk study. *Electrochemistry*. 2006; 42(12): 1345–1351. <https://doi.org/10.1134/s1023193506120123>
25. Simons R. Electric field effects on proton transfer between ionizable groups and water in ion exchange membranes. *Electrochimica Acta*. 1984;29: 151–158. [https://doi.org/10.1016/0013-4686\(84\)87040-1](https://doi.org/10.1016/0013-4686(84)87040-1)
26. Lurie Yu. Yu. *Handbook of analytical chemistry**. Moscow: Khimiya Publ.; 1989. 448 p. (In Russ.)
27. Eigen M. Proton transfer, acid-base catalysis, and enzymatic hydrolysis. Part I: Elementary processes. *Angewandte Chemie International Edition in English*. 1964;3(1): 1–19. <https://doi.org/10.1002/anie.196400011>
28. Fersht A. *Enzyme structure and mechanism*. San Francisco: W.H. Freeman; 1977. 371 p.
29. Nikonenko V. V., Vasil'eva V. I., Akberova E. M., ... Pourcelly G. Competition between diffusion and electroconvection at an ion-selective surface in intensive current regimes. *Advances in Colloid and Interface Science*. 2016;235: 233–246. <https://doi.org/10.1016/j.cis.2016.06.014>

*Translated by author of the article

Information about the authors

Karpenko Tatyana V., Young Researcher at the Scientific Research Department of Kuban State University (Krasnodar, Russian Federation). <https://orcid.org/0000-0002-5840-7984>
tany1328@mail.ru

Shramenko Vladislava V., Laboratory Assistant at the Scientific Research Department of Kuban State University (Krasnodar, Russian Federation).
vladislava.19991211@gmail.com

Sheldeshov Nikolay Viktorovich, Dr. Sci. (Chem.), Professor at the Department of Physical Chemistry, Kuban State University (Krasnodar, Russian Federation).

<https://orcid.org/0000-0003-0577-6265>
sheld_nv@mail.ru

Received 14.11.2023; approved after reviewing 06.12.2023; accepted for publication 11.12.2023; published online 01.10.2024.

Translated by Marina Strepetova



Condensed Matter and Interphases

Kondensirovannye Sredy i Mezhfaznye Granitsy
<https://journals.vsu.ru/kcmf/>

Original articles

Research article

<https://doi.org/10.17308/kcmf.2024.26/12221>

Synthesis of nanoscale nickel (II) ferrite and a study of its catalytic and sorption activities towards methyl orange

A. A. Meshcheryakova^{1✉}, E. V. Tomina^{1,2}, S. A. Titov¹, Nguyen Anh Tien³, A. I. Dmitrenkov²

¹Voronezh State University,
1 Universitetskaya pl., Voronezh 394018, Russian Federation

²Voronezh State University of Forestry and Technologies named after G. F. Morozov
8 Timiryazeva st., Voronezh 394087, Russian Federation

³Ho Chi Minh City University of Education,
280. An Duong Vuong st., District 4, District 5, Ho Chi Minh City, Vietnam

Abstract

Nanoscale magnetic spinel ferrites are attracting an increased attention as functional materials for catalysis and sorption. Such catalysts and sorbents are advantageous due to their chemical stability in aggressive media, their thermal stability, a large area of specific surface, and high saturation magnetization, which allows using them to create magnetically controlled functional materials. This article presents the results of the synthesis of nickel (II) ferrite nanopowder, its characterization, and a study of its catalytic and sorption activities towards methyl orange dye.

X-ray diffraction (XRD), transmission electron microscopy (TEM), and scanning electron microscopy (SEM) were used to characterize nanocrystalline NiFe₂O₄ synthesized by citrate combustion. The nickel spinel was tested as a catalyst of Fenton-like reaction of oxidative degradation of methyl orange under UV irradiation of $\lambda = 270$ nm. The study involved differentiation of oxidation during dye sorption on a NiFe₂O₄ nanoscale catalyst. The oxidative degradation of the pollutant under ultraviolet irradiation in the presence of a catalyst was satisfactorily described by a pseudo-first-order model, the rate constant of the reaction was 0.0191 min⁻¹. The degree of methyl orange destruction reached 99% 150 minutes after the beginning of the reaction. A parallel experiment without the addition of hydrogen peroxide to the dye solution allowed assessing the sorption capacity of nanoscale nickel (II) ferrite. After 150 minutes, the concentration of the dye decreased by 7.5% due to its sorption, the equilibrium sorption capacity of NiFe₂O₄ was low (0.132 mg/g). This indicates that the methyl orange solution decolorizes mainly due to its catalytic oxidative degradation according to the Fenton reaction.

This allows considering nanoscale nickel ferrite as a promising material for wastewater treatment by deep oxidation of organic pollutants.

Keywords: Nickel ferrite, Nanopowder, Photocatalysis, Fenton reaction

Funding: The study was supported by Russian Science Foundation grant No. 23-23-00122, <https://rscf.ru/project/23-23-00122/>

Acknowledgements: The research results were partially obtained using the equipment of the Center for Collective Use of Scientific Equipment of Voronezh State University. URL: <http://ckp.vsu.ru>.

For citation: Meshcheryakova A. A., Tomina E. V., Titov S. A., Nguyen A. T., Dmitrenkov A. I. Synthesis of nanoscale nickel (II) ferrite and a study of its catalytic and sorption activities towards methyl orange. *Condensed Matter and Interphases*. 2024;26(3): 456–463. <https://doi.org/10.17308/kcmf.2024.26/12221>

Для цитирования: Мещерякова А. А., Томина Е. В., Титов С. А., Нгуен А. Т., Дмитренко А. И. Синтез, исследование каталитической и сорбционной активности наноразмерного феррита никеля (II) в отношении метилового оранжевого. *Конденсированные среды и межфазные границы*. 2024;26(3): 456–463. <https://doi.org/10.17308/kcmf.2024.26/12221>

✉ Anna A. Meshcheryakova, e-mail: anna-meshcheryakova@internet.ru

© Meshcheryakova A. A., Tomina E. V., Titov S. A., Vo Kuang Mai, Nguen An' T'en, Dmitrenkov A. I., 2024



The content is available under Creative Commons Attribution 4.0 License.

Introduction

In recent years, there has been a growth of interest in nanoscale spinel ferrites as multifunctional materials. Using nanoscale spinels (NiFe_2O_4 where $\text{Me} = \text{Zn, Ni, Mg, Co, Mn}$) as catalysts and sorbents is advantageous due to their chemical stability in acid media, thermal stability, a highly developed surface, and high saturation magnetization [1, 2]. The magnetic properties of ferrites allow using them to create magnetically controlled functional materials, primarily catalysts and sorbents.

Currently, spinel ferrite-based catalysts have a wide range of applications, such as oxidative dehydration of hydrocarbons, decomposition of alcohols, and purification of exhaust gases generated by cars [3–6].

Spinel ferrites [7,8] and ferrite-based nanocomposites [9–11] are used in a number of technologies for wastewater treatment from pollutants: dyes, antibiotics, phenol derivatives, etc.

Nanoscale catalysts and sorbents should not only have high activity due to their developed surface with a large number of active sites, but also be products of energy-efficient and resource-saving technologies in order to economically justify their industrial implementation. For large-scale practical use of ferrites, it is necessary to distinguish simple, reproducible, and economical methods of their synthesis among the many known methods of synthesis [12–16]. These methods should allow regulating the characteristics of nanoscale spinel ferrites and obtaining samples with a large number of active sites for catalysis and sorption and magnetic properties necessary and sufficient to control the external magnetic field.

The purpose of this study was to synthesize nanoscale nickel (II) ferrite, a soft magnetic material with a reverse spinel structure, by citrate combustion and to test it as a catalyst for a Fenton-like reaction of oxidative degradation of the methyl orange dye.

Experimental

NiFe_2O_4 synthesis was carried out by citrate combustion according to [17]. Phase composition was determined by X-ray diffractometry (Empyrean BV diffractometer with Cu anode ($\lambda = 1.54060 \text{ nm}$)). The scanning was performed

within a range of angles $2\theta = 10\text{--}80^\circ$ with a step of 0.0200. The JCPDC database [18] was used to identify the phases (card 54-0964) [18]. The size and morphology of particles were determined by transmission electron microscopy (TEM, CarlZeiss Libra-120 transmission electron microscope). SEM image of the sample and quantitative elemental analysis was performed on a JSM-6380LV JEOL scanning electron microscope with an INCA 250 microanalysis system.

The catalytic activity of nanoscale nickel (II) ferrite was studied in a model reaction of methyl orange (MO) oxidation by hydrogen peroxide. To do this, we prepared a solution containing 0.0100 mg/ml of methyl orange and 10 wt. % of hydrogen peroxide. pH of the solution, which was 4.5, was maintained by an acetate buffer. Then, 0.2500 g of catalyst was added to a series of solution samples with a volume of 15.00 ml. Control measurements of the concentrations of MO solutions without a catalyst were performed in the same manner.

The experiment was conducted under ultraviolet irradiation with $\lambda = 270 \text{ nm}$ (LightBest UV lamp, 25 W). The MO concentration was determined using photocolometry (KFK-3-01 photocolometer). The analytical wavelength for MO was 364 nm. The degree of degradation was calculated by formula (1):

$$W = \frac{C_0 - C_t}{C_0} \cdot 100 \%, \quad (1)$$

where W is the degree of degradation %, C_0 is the concentration of the dye at the initial moment of time, and C_t is the concentration of the dye at the present moment of time.

To differentiate the catalytic oxidation and sorption of the dye on a nanoscale NiFe_2O_4 catalyst, we performed an experiment using the above-described method in the darkness without adding H_2O_2 oxidant to the solutions. In this case, oxidative degradation of MO was not performed, while decolorization of the solution was only determined by the sorption of the pollutant on ferrite. The duration of static sorption was 2 hours. The sorption capacity of nickel ferrite (II) was determined using equation (2):

$$A = \frac{(C_0 - C) \cdot V}{m}, \quad (2)$$

where C_0 is the initial concentration of the solution of the organic dye, mol/l; C is the concentration of the organic dye after a certain time after the beginning of the reaction, mol/l; V is the volume of the adsorbate solution, l; m is the weight of ferrite, g.

Results and discussion

Reflexes in the diffraction patterns of the nanopowder synthesized by citrate combustion (Fig. 1) referred to the target phase of $NiFe_2O_4$ (JCPDC 54-0964). We also identified a single low-intensity reflex of Fe_2O_3 iron oxide, however, it did not seem critical due to the potential catalytic activity of the Fe^{3+} ion.

The average size of coherent scattering regions (CSRs) of $NiFe_2O_4$ particles calculated using the Debye–Scherrer formula [19] was 31 ± 2 nm.

TEM (Fig. 2.) showed that the shape of $NiFe_2O_4$ particles was close to spherical. There

were individual coarse particles with a size of 90–100 nm, however, the predominant particle size fraction was in the range of 21–50 nm. According to TEM data, the average size of $NiFe_2O_4$ particles was 38 ± 3 nm. According to XRD, the calculated CSR values generally correlated with the TEM results.

The average values of the weight and atomic percentages of the Ni, Fe, and O elements according to the data of energy dispersion analysis (Table 1) correlate with the expected chemical composition of the synthesized samples. The presence of residual carbon on the energy dispersive spectrum (Fig. 3) indicated the probable accumulation of solid x-ray amorphous products of gel degradation in the pores of the nanopowder without complete oxidation of the combustion products.

The surface of nickel (II) ferrite was characterized by a “coral-like” structure,

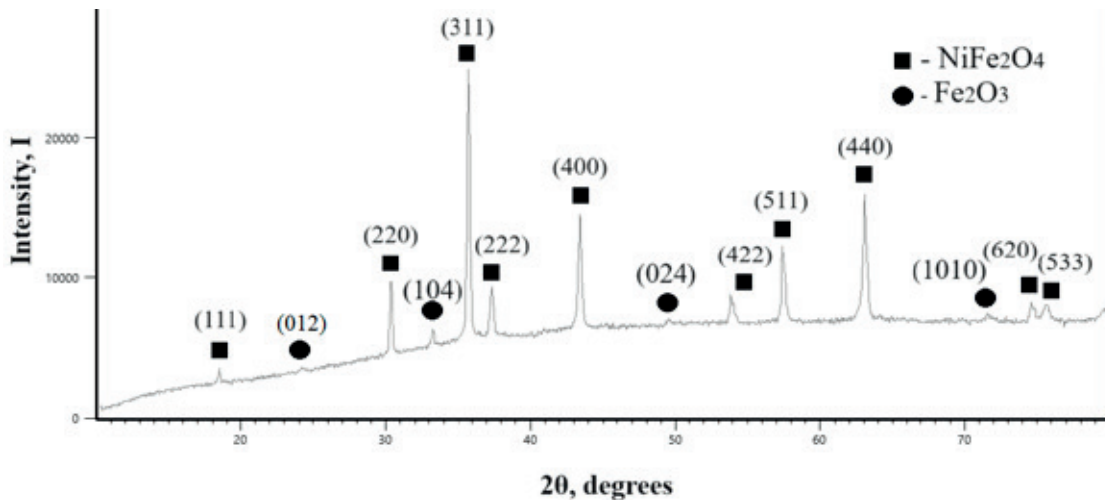


Fig. 1. Diffraction pattern of $NiFe_2O_4$ nanopowder

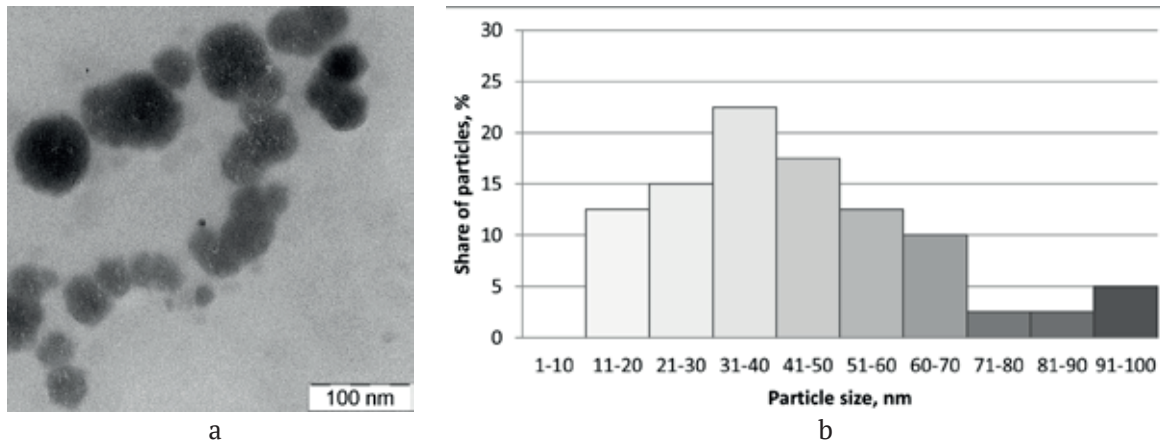


Fig. 2. TEM image (a) and histogram of $NiFe_2O_4$ particle size distribution (b)

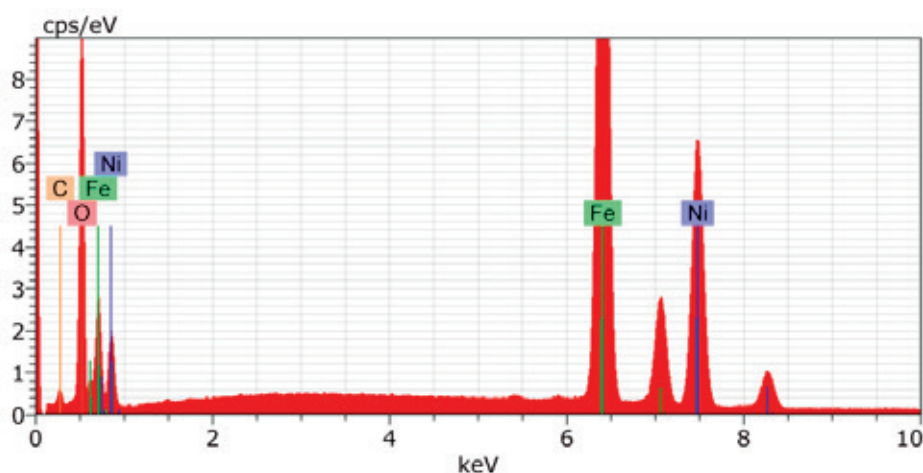


Fig. 3. Energy dispersive spectrum of NiFe_2O_4

Table 1. Results of energy dispersion analysis of ferrite

Element	Weight %	Atomic %
O	30.50	55.05
Fe	40.19	20.78
Ni	24.21	11.91
C	5.10	12.26

crystallites had a pronounced agglomeration (Fig. 4). TEM data allows assuming that NiFe_2O_4 agglomerates up to $20\ \mu\text{m}$ in size were formed by nanoparticles below $100\ \text{nm}$ in size. In the SEM image, equiaxial small particles with pronounced crystallinity clearly differentiated.

The rather high porosity of spinel is explained by the release of gaseous products of the polymer gel combustion, primarily carbon oxides CO and CO_2 , which is a distinctive feature of nanoscale powders synthesized by citrate combustion [20].

It was experimentally established that nickel spinel nanopowder synthesized by citrate combustion is an effective heterogeneous catalyst for the hydrogen peroxide decomposition by a Fenton-like reaction. Oxidative degradation of MO under the influence of UV irradiation in the presence of the NiFe_2O_4 catalyst proceeded more intensely than in its absence (Fig. 5). Therefore, the concentration of the dye during catalytic oxidation 2.5 hours after the beginning of the reaction decreased by 17 times. In the absence of a catalyst, after 2.5 hours of the reaction, the concentration of MO decreased only by 2 times.

The degree of degradation of the methylene orange dye without catalyst in visible light

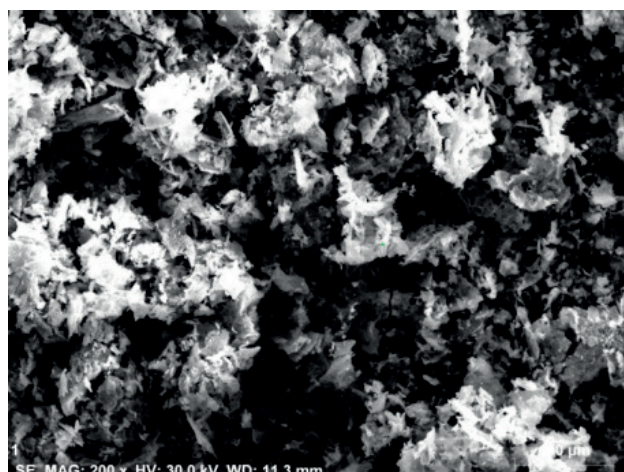


Fig. 4. SEM image of NiFe_2O_4 nanopowder

2.5 hours after the beginning of the reaction was 50%. In the presence of nickel (II) ferrite under UV irradiation of the reaction mixture, the degree of degradation of MO increased to 99%.

The shape of kinetic curves of the oxidative degradation of the dye corresponded to the pseudo-first order of the reaction. The rate constant was evaluated by linearization of the kinetic dependences in logarithmic coordinates (Fig. 6). The rate constant of oxidative degradation of MO under UV irradiation in the presence of NiFe_2O_4 was $0.0191\ \text{min}^{-1}$. The rate constant in the absence of a catalyst with natural lighting was almost an order of magnitude lower ($0.0044\ \text{min}^{-1}$).

The process without the H_2O_2 oxidant revealed a small sorption capacity of nickel spinel towards MO, the concentration of the dye decreased by

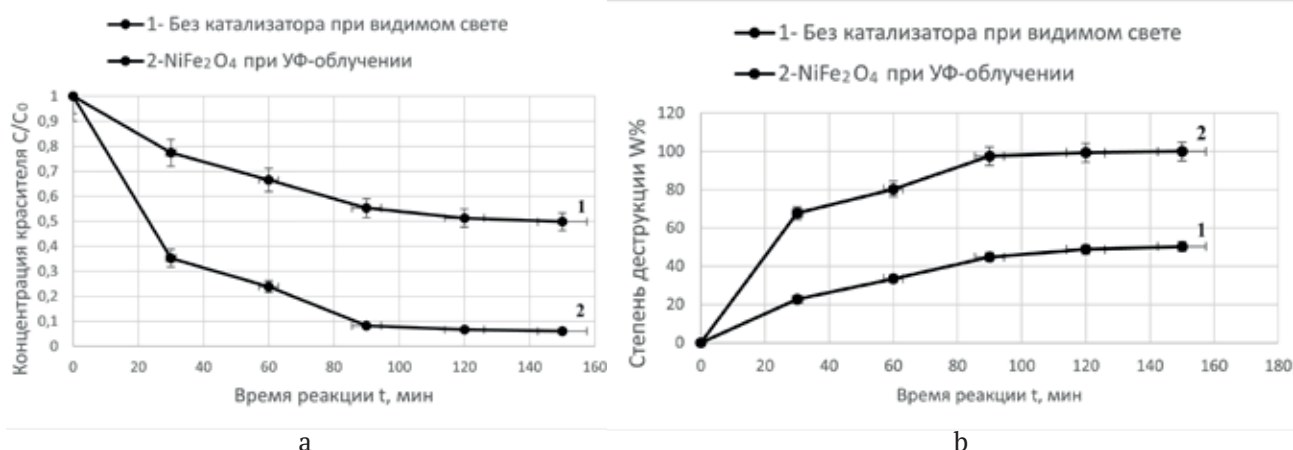


Fig. 5. Change in the concentration (a) and degree of degradation (b) of the MO dye without catalyst (1) and in the presence of NiFe₂O₄ under UV irradiation (2)

7.5% 2.5 hours after the beginning of the reaction (Fig. 7).

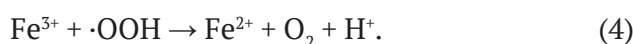
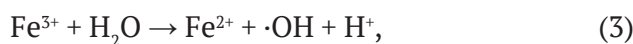
The sorption capacity of NiFe₂O₄ reached its maximum value of 0.132 mg/g in 120 min (Fig. 7, insert), which indicates a slight contribution of sorption to the overall process of decolorization of the MO solution in the presence of a nanoscale NiFe₂O₄ catalyst.

The structure of the mixed spinel, characteristic of nickel (II) ferrite means that Fe³⁺ ions distribute in octahedral and tetrahedral voids. The catalytic activity of spinel ferrites in Fenton processes is due to the formation of active oxidants with their participation during the decomposition of hydrogen peroxide. According to [21], the formation of ·OH hydroxyl radicals is associated with the activity of Fe²⁺ ions, whereas Fe³⁺ ions are mainly responsible for the formation of ·OOH radicals. The oxidation state

for octahedral ions of Fe³⁺ changes to +2 due to lattice oxygen [22]. Fe³⁺ ions in the tetrahedral position exhibit electron-withdrawing properties (reaction 1) and contribute to the formation of active sites of the Fenton-like reaction of Fe²⁺, on which the decomposition of hydrogen peroxide is accompanied by the formation of hydroxyl radicals (reaction 2):



UV irradiation induces regeneration of Fe²⁺ accompanied by the formation of hydroxyl radicals and molecular oxygen (reactions 3, 4):



The oxidizing radicals oxidize the dye molecule according to equation (5):

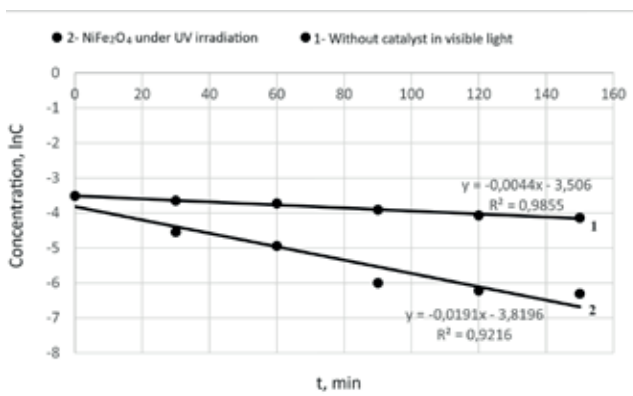


Fig. 6. Kinetic curves of MO oxidation by hydrogen peroxide in lnC - t coordinates without catalyst (1) and in the presence of NiFe₂O₄ catalyst (2)

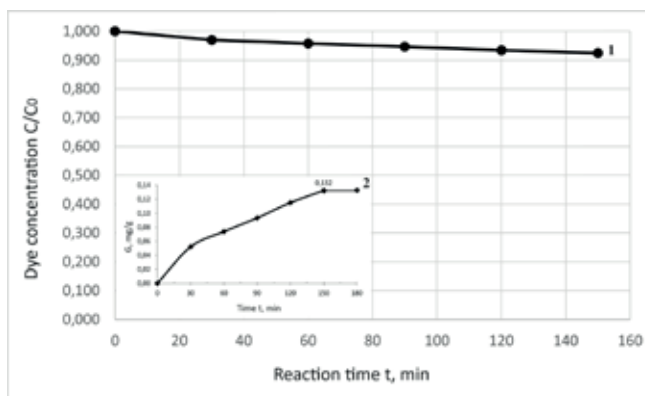
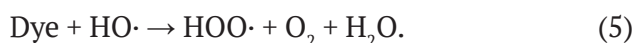


Fig. 7. MO sorption curves in the presence of NiFe₂O₄ (1) and sample sorption capacity (2)



Previously, under similar conditions we established a rate constant of 0.0354 min^{-1} for nanoscale CoFe_2O_4 with a reverse spinel structure as a catalyst of Fenton-like reaction of methyl orange oxidation [23]. Probably, the $\text{Co}^{2+}/\text{Co}^{3+}$ pair in the spinel lattice increases the catalytic activity of cobalt ferrite as compared to NiFe_2O_4 due to accelerated electron transfer. Co^{2+} cobalt ions are located in the center of the oxygen octahedra, and electrons of oxygen ions can easily participate in the oxidation of H_2O_2 accompanied by the formation of hydroxyl radicals and the change of the oxidation state of cobalt to +3. The probability of participation of nickel ions due to the predominant oxidation state of +2 in such a process is much lower, however, in [24], X-ray photoelectron spectroscopy was used to confirm the presence of Ni^{3+} ions in nickel spinel after ozone treatment of oxalic acid. However, it should be emphasized that the value of the rate constant of MO oxidation in the presence of NiFe_2O_4 exceeded the value for the oxidative degradation of MO under similar conditions when nanoscale normal spinel ZnFe_2O_4 was present as a catalyst (0.010 min^{-1}), where A cation also had one oxidation state +2 despite a sufficiently high specific surface area of the catalyst ($453.1 \text{ m}^2/\text{g}$) [25]. This is consistent with the data in [24] about poor capability of ZnFe_2O_4 to transfer electrons when A cation changes to the Zn^{3+} state.

Conclusions

Citrate combustion was used to synthesize a nanoscale nickel ferrite with a spinel structure (XRD data) with an average particle size of $38 \pm 3 \text{ nm}$ (TEM data). It was established that nanodispersed NiFe_2O_4 had high catalytic activity in the Fenton-like reaction of methyl orange dye oxidation. Under optimized conditions and effective control of parameters, including contact time, solution pH, and catalyst dose and under additional UV irradiation, over 99% of the pollutant was removed. The oxidative degradation of the dye without catalyst was 50%. The rate constant of oxidative degradation of MO under UV irradiation in the presence of nickel (II) ferrite was 0.0191 min^{-1} , while in the absence of a catalyst and in natural lighting it was 0.0044 min^{-1} . The sorption capacity of

NiFe_2O_4 reached its maximum value of 0.132 mg/g 120 min after the beginning of the reaction, which means that the contribution of sorption to the decolorization of the MO solution is insignificant.

Author contributions

All authors made an equivalent contribution to the preparation of the publication.

Conflict of interests

The authors declare that they have no known competing financial interests or personal relationships that could have influenced the work reported in this paper.

References

- Gagan K. B., Sumit B., Mahavir S., Khalid M. B. *Ferrites and multiferroics fundamentals to applications: fundamentals to applications*. Springer Singapore; 2021. 213 p. <https://doi.org/10.1007/978-981-16-7454-9>
- Sharma S. K. (ed). *Spinel nano ferrites. Synthesis, properties and applications*. Springer Cham; 2021. 475 p. <https://doi.org/10.1007/978-3-030-79960-1>
- Winiarska K., Klimkiewicz R., Tylus W., ... Szczygieł I. Study of the catalytic activity and surface properties of manganese-zinc ferrite prepared from used batteries. *Journal of Chemistry*. 2019;201: 1–14. <https://doi.org/10.1155/2019/5430904>
- Ramazania A., Fardood S. T., Hosseinzadeha Z., ... Jooc S. W. Green synthesis of magnetic copper ferrite nanoparticles using tragacanth gum as a biotemplate and their catalytic activity for the oxidation of alcohols. *Iranian Journal of Catalysis*. 2017;7(3): 181–185.
- Taghavi Fardood S., Ramazani A., Golfar Z., Joo S. W. Green synthesis of $\alpha\text{-Fe}_2\text{O}_3$ (hematite) nanoparticles using tragacanth gel. *Quarterly Journal of Applied Chemical Research*. 2017;11(3): 19–27.
- Thomas J., Thomas N., Girgsdies F., Beherns M., Huang X., Sudheesh V. D. Synthesis of cobalt ferrite nanoparticles by constant pH co-precipitation and their high catalytic activity in CO oxidation. *New Journal of Chemistry*. 2017;41: 7356–736. <https://doi.org/10.1039/C7NJ00558J>
- Zelenskaya E. A., Chernyshev V. M., Shabelskaya N. P., Sulima S. I., Sulima E. V., Semchenko V. V., ... Vlasenko A. I. Study of catalytic activity of oxides of transition elements in the reaction of hydrogen peroxide decomposition. *Fundamentalnye issledovaniya = Fundamental studies*. 2016;4: 261–265. (In Russ).
- Artemyanov A. P., Zemsikova L. A., Ivanov V. V. Catalytic liquid-phase oxidation of phenol in water media using carbon fiber (iron, iron oxide) catalyst. *Izvestia vysshikh uchebnykh zavedenii Khimiya Khimicheskaya Tekhnologiya = News of higher education institutions. Series: Chemistry and Chemical Technology*.

2017;60(8): 88–95. (In Russ). <https://doi.org/10.6060/tcct.2017608.5582>

9. Ding C., Zhao H., Zhu X., Liu X. Preparation of cotton linters' aerogel-based C/NiFe₂O₄ photocatalyst for efficient degradation of methylene blue. *Nanomaterials*. 2022;12(12): 2021. <https://doi.org/10.3390/nano12122021>

10. Goma H., Abd El-Monaem E. M., Eltaweil A. S., Omer A. M. Efficient removal of noxious methylene blue and crystal violet dyes at neutral conditions by reusable montmorillonite/NiFe₂O₄@amine-functionalized chitosan composite. *Scientific Reports*. 2022;15;12(1): 15499. <https://doi.org/10.1038/s41598-022-19570-1>

11. Tomina E., Novikova L., Kotova A., ... Alekhina Y. ZnFe₂O₄/zeolite nanocomposites for sorption extraction of Cu²⁺ from aqueous medium. *Applied Chem*. 2023;(3):452–476. <https://doi.org/10.3390/applied-chem3040029>

12. Rashidi S., Ataie A. One-step synthesis of CoFe₂O₄ nano-particles by mechanical alloying. *Advanced Materials Research*. 2014;829: 747–751. <https://doi.org/10.4028/www.scientific.net/amr.829.747>

13. Srinivasa Rao K., Ranga Nayakulu S. V., Chaitanya Varma M., Choudary G. S. V. R. K., Rao K. H. Controlled phase evolution and the occurrence of single domain Co_xFe_{2-x}O₄ nanoparticles synthesized by PVA assisted sol-gel method. *Journal of Magnetism and Magnetic Materials*. 2018;451(1): 602–608. <https://doi.org/10.1016/j.jmmm.2017.11.069>

14. Manikandan A., Sridhar R., Arul Antony S., Ramakrishna S. A simple aloe vera plant-extracted microwave and conventional combustion synthesis: morphological, optical, magnetic and catalytic properties of CoFe₂O₄ nanostructures. *Journal of Molecular Structure*. 2014;1076: 188–200. <https://doi.org/10.1016/j.molstruc.2014.07.054>

15. Petrova E., Kotsikau D., Pankov V., Fahmi A. Influence of synthesis methods on structural and magnetic characteristics of Mg–Zn-ferrite nanopowders. *Journal of Magnetism and Magnetic Materials*. 2019;473: 85–91. <https://doi.org/10.1016/j.jmmm.2018.09.128>

16. Mittova I. Ya., Tomina E. V., Lavrushina S. S. *Nanomaterials: synthesis of nanocrystalline powders and production of compact nanocrystalline materials**. Textbook for universities. Voronezh: Publisher: IPC VSU Publ.; 2007. (In Russ.)

17. Meshcheryakova A. A., Tomina E. V., Titov S. A. Study of the sorption and catalytic properties of nickel ferrite with respect to 2,4-dinitrophenol. *High Energy Chemistry*. 2023;57: 342–345. <https://doi.org/10.1134/S0018143923080180>

18. JCPDC PCPDFWIN: A Windows Retrieval/Display program for Accessing the ICDD PDF – 2 Data base. International Centre for Diffraction Data, 1997.

19. Brandon D., Kaplan U. *Microstructure of materials. Research and control methods*. West Sussex: John Wiley & Sons Ltd; 1999, p. 384.

20. Tomina E. V., Kurkin N. A., Konkina D. A. ZnFe₂O₄ nanoscale catalyst for wastewater treatment from dyes by oxidative degradation. *Ecology and Industry of Russia*. 2022;26(5): 17–21. (In Russ). <https://doi.org/10.18412/1816-0395-2022-5-17-21>.

21. Maldonado A. C. M., Winkler E. L., Raineri M., ... Lima E. Free-radical formation by the peroxidase-like catalytic activity of MFe₂O₄ (M = Fe, Ni, and Mn) nanoparticles. *The Journal of Physical Chemistry C*. 2019;123(33): 20617–20627. <https://doi.org/10.1021/acs.jpcc.9b05371>

22. Tatarchuk T., Shyichuk A., Trawczyńska I., ... Gargula R. Spinel cobalt(II) ferrite-chromites as catalysts for H₂O₂ decomposition: synthesis, morphology, cation distribution and antistructure model of active centers formation. *Ceramics International*. 2020;46(17): 27517–27530. <https://doi.org/10.1016/j.ceramint.2020.07.243>

23. Kurkin N. A., Volkov A. S., Doroshenko A. V., Gudkova N. A., Tomina E. V. *Actual problems of theory and practice of heterogeneous catalysts and adsorbents: Proceedings of the VII All-Russian scientific conference**. Kazan; 2023. pp. 248–249. (In Russ.)

24. Zhang F., Wu C., Kaiyi W., Zhou H., ... Wei S. Ozonation of aqueous phenol catalyzed by biochar produced from sludge obtained in the treatment of coking wastewater. *Journal of Environmental Management*. 2017;547: 60–68. <https://doi.org/10.1016/j.jenvman.2018.07.038>

25. Shabelskaya N. P., Egorova M. A., Vasileva E. V., Polozhentsev O. E. Photocatalytic properties of nanosized zinc ferrite and zinc chromite. *Advances in Natural Sciences: Nanoscience and Nanotechnology*. 2021;12(1): 015004. <https://doi.org/10.1088/2043-6254/abde3b>

*Translated by author of the article

Information about the authors

Anna A. Meshcheryakova, postgraduate student at the Department of Materials Science and Industry of Nanosystems, Voronezh State University, (Voronezh, Russian Federation).

<https://orcid.org/0000-0003-4899-609X>

anna-meshcheryakova@internet.ru

Elena V. Tomina, Dr. Sci. (Chem.), Head of the Department of Chemistry, Voronezh State University of Forestry and Technologies named after G. F. Morozov (Voronezh, Russian Federation).

<https://orcid.org/0000-0002-5222-0756>

tomina-e-v@yandex.ru

Anh Tien Nguyen, PhD (Chem.), Associate Professor, Head of the Inorganic Chemistry Department, Ho Chi Minh City University of Education Vietnam (Ho Chi Minh City, Vietnam).

<https://orcid.org/0000-0003-3919-8571>

tienna@hcmue.edu.vn

Alexander I. Dmitrenkov, Cand. Sci. (Tech.), Associate Professor, Voronezh State Forestry University named after G. F. Morozov (Voronezh, Russian Federation).

<https://orcid.org/0000-0001-9296-1762>

dmitrenkov2109@mail.ru

Received 26.03.2024; approved after reviewing 22.04.2024; accepted for publication 15.05.2024; published online 01.10.2024.

Translated by Irina Charychanskaya



Original articles

Research article

<https://doi.org/10.17308/kcmf.2024.26/12277>

Features of the local activation of aluminum in the presence of bicarbonate ions

T. A. Minakova¹✉, S. A. Kaluzhina², E. N. Aksyonova²

¹Air Force Military Educational and Scientific Centre “Zhukovsky and Gagarin Air Force Academy”,
54a Starykh Bol'shevikov ul., Voronezh 394064, Russian Federation

²Voronezh State University,
1 Universitetskaya pl., Voronezh 394018, Russian Federation

Abstract

The purpose of the article is to study the effect of bicarbonate ions on the local activation of aluminum at a temperature of 25 °C.

The features of local activation of aluminum in the presence of bicarbonate ions ($2 \cdot 10^{-4}$ – $4 \cdot 10^{-3}$ M) were studied using the methods of voltammetry, chronoamperometry, optical and scanning electron microscopy, and X-ray spectral microanalysis.

As a result, we established the range of sodium bicarbonate concentrations, in which there is local activation of aluminum; obtained experimental data on the dependence of the main quantitative characteristics of the process (potential of pitting formation, potential of local activation, and induction period) on the concentration of sodium bicarbonate. Formal kinetic approach was used to propose a mechanism for the local activation of aluminum in hydrocarbonate media.

Keywords: Sodium bicarbonate, Aluminum, Local activation, Passivation, Voltammetry, Chronoamperometry, Scanning electron microscopy

For citation: Minakova T. A., Kaluzhina S. A., Aksenova E. N. Features of the local activation of aluminum in the presence of bicarbonate ions. *Condensed Matter and Interphases*. 2024;26(3): 464–473. <https://doi.org/10.17308/kcmf.2024.26/12277>

Для цитирования: Минакова Т. А., Калужина С. А., Аксёнова Е. Н. Особенности локальной активации алюминия в присутствии гидрокарбонат-ионов. *Конденсированные среды и межфазные границы*. 2024;26(3): 464–473. <https://doi.org/10.17308/kcmf.2024.26/12277>

✉ Tatyana A. Minakova, e-mail: tatiana_bor_vrn@mail.ru

© Minakova T. A., Kaluzhina S. A., Aksenova E. N., 2024

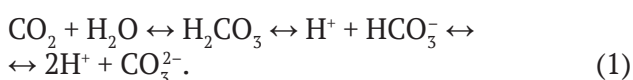


1. Introduction

Hydrogen carbonates mainly enter surface waters as a result of natural processes of chemical weathering and dissolution of carbonate rocks or aluminosilicates, as well as with waste water from chemical, silicate, and soda industry enterprises. Bicarbonate ions are one of the main anions present in natural water which is supplied to water and heat supply systems. The equipment of these systems can be made of various metals and alloys, including aluminum, copper, steel, etc. [1–5].

According to previous studies [6, 7], copper and iron are prone to passivation and localized damage depending on the salt content in the hydrocarbonate solution. For example, in [8, 9], it was found that passive layers formed in diluted electrolytes ($C(\text{CNaHCO}_3) \leq 0.08 \text{ M}$) have low protective characteristics, and HCO_3^- ions act as pitting corrosion activators and cause metal depassivation if local activation potentials exceed the corrosion potential. With an increase in the concentration of HCO_3^- ions, the protective properties of the oxide film in relation to pitting formation (PF) increase, which is due to the stabilization of the passive film on copper and iron under the action of malachite or basic iron carbonate formed under these conditions, respectively. In contrast to the anodic behavior of copper and iron in dilute solutions, they have a wide region of passivity (up to the potential of oxygen release) in more concentrated solutions ($C(\text{NaHCO}_3) = 0.1 \text{ M}$). Scanning electron microscopy (SEM) in this case does not record any pitting (PT) on the above-mentioned metals after their anodic oxidation [10].

Another approach was proposed in [11, 12]. According to it, PF on copper is not associated with the special properties of HCO_3^- ions, which have a weak activating ability, but is determined by the increasing value of pH of solutions in concentrated media, which leads to a deeper passive state of the metal. The effect of pH is also manifested in the change in the ratio of CO_2 , H_2CO_3 , HCO_3^- , and CO_3^{2-} . Under equilibrium conditions, there is a balance between all four forms [3, 4, 13]:



At pH = 4.3, water contains practically only CO_2 . With an increase in pH, the HCO_3^- content increases, at pH = 8.35 only HCO_3^- ions are present in water, and at pH ~ 12, there are only CO_3^{2-} ions [13].

It is known [14–22] that aluminum and its alloys can be in a passive state, however, they can undergo local activation (LA) in the presence of chloride, sulfate, nitrate, and other ions. Yet, there is hardly any information about the behavior of aluminum and its alloys in the presence of bicarbonate ions. Papers [23–24] describe studies on the effect of temperature on aluminum LA in NaHCO_3 solutions. It was also shown that at concentrations of 10^{-5} – 10^{-4} M and $5 \cdot 10^{-5}$ – 10^{-1} M of NaHCO_3 , aluminum is in a passive state, while at concentrations between $2 \cdot 10^{-4}$ and $4 \cdot 10^{-3} \text{ M}$, there is LA in NaHCO_3 . Controversial behavior of aluminum [23–24], as well as different views [6–12] on the role of pH of bicarbonate solutions and HCO_3^- ions in the LA processes on metals with low salt content in the solution means that there is a need for a more detailed study in a wide range of potentials, clarification of the concentration boundaries of LA and its kinetic parameters, and determination of the mechanism of the process of aluminum LA in bicarbonate media. Therefore, the purpose of the article is to study the effect of bicarbonate ions on the local activation of aluminum at a temperature of 25 °C.

2. Experimental

Experiments were carried out on a stationary aluminum (Al 99.99%) electrode in aqueous solutions of sodium bicarbonate within the concentration range from $2 \cdot 10^{-4}$ to $4 \cdot 10^{-3} \text{ M}$, which were prepared from a chemically pure reagent and distilled water and which were kept for a day. The pH control of the studied solutions (PH-107 pH meter with an accuracy of 0.1) showed a change in the pH value from 6.5 to 7.7 with an increase in the salt content of the electrolytes.

Prior to each experiment, the aluminum surface was polished with sandpaper with a decreasing grain radius, polished with filter paper, degreased with ethanol, and washed with distilled water.

The electrolytic cell was a glass three-electrode cell with unseparated cathode and anode spaces and free access of air. The working (aluminum) and auxiliary platinum electrodes

and a salt bridge tube were fixed in the cell lid. A silver chloride electrode ($E = 0.20$ V) was used as the reference electrode. It was located in the salt bridge, which was filled with a working solution at room temperature and had a Haber-Luggin capillary at its end. All potentials were further recalculated relative to the standard hydrogen electrode [25–28].

The anodic behavior of aluminum in the corresponding NaHCO_3 solutions was studied at room temperature on an IPC-Compact potentiostat using Equivalent Circuits Solver software (Ver 1.2) (accuracy ± 0.002 V).

Linear sweep voltammetry was chosen as the main electrochemical method of the study. To use it, at the beginning of each experiment, the electrode was placed in the working solution and kept in it for 10 minutes. Then, the anodic polarization curve (APC) of the steady-state potential was taken (scanning rate of $v_p = 0.15$ V/min). The electrode potential was shifted sequentially to the region of positive values up to $E = +1.00$ V. For quantitative evaluation of the stage of the PT initiation, we used the potential of pitting formation (E_{PF}), i.e. the critical value of the potential, more positive values of which are associated with the activating effect of anions. The approximate E_{PF} was determined by the potential corresponding to the sharp increase in the anodic current on the APC [29–31].

Additional studies were carried out by chronoamperometry, within which the shape of kinetic $I - \tau$ curves at fixed potential values were used to draw conclusions about the state of the studied metal: whether it was being actively dissolved, passivated, or exposed to LA. Importantly, the quantitative characteristic of LA was the LA potential (E_{LA}), which corresponded to the potential associated with the formation of the first metastable PT, the further development or repassivation of which was determined by a number of factors: the conditions of the experiment, the nature of the metal and the activator, the temperature, and the rate of PT formation. To obtain chronoamperograms, the surface of the electrode was treated as described above prior to each experiment. Then, the electrode was kept in the working solution for 10 min. After that, the sample was anodically

polarized at different potential values around E_{LA} . After that, the change in the current over time was recorded for 10 minutes every 10 seconds. The obtained chronoamperometric data were compared with visual (microscopic) observations [32–34].

The combination of voltammetric and chronoamperometric methods was necessary in this case, since, as a rule, E_{LA} and E_{PF} did not agree with each other, and usually $E_{\text{LA}} < E_{\text{PO}}$.

When studying the stage of PT initiation, the concept of the induction period of PF or LA (τ_{ind}) is often used [33, 35], which, depending on the accepted theory of metal passivity, is understood as the time required for the penetration of the activator ion through the oxide film (film theory), or for successful competitive adsorption between the passivator and the activator in favor of the latter (adsorption theory) [28, 35]. The τ_{ind} value depends not only on the nature of the metal, the composition of the solution, the type of activator, its concentration, pH, the presence of foreign substances, and temperature, but also on the potential of the electrode. This indicates [32, 33, 35] that the τ_{ind} value can be interpreted as a characteristic proportional to the reaction rate responsible for the appearance of PT. The τ_{ind} value was determined according to the following procedure. After mechanical treatment of the electrode surface and immersing it for 10 minutes in the solution, the sample was exposed to anodic polarization in the solution at a potential corresponding to the potential of stable LA. The start time of the electrode activation, τ_{ind} , was recorded, which corresponded to the start of fluctuations of the anodic current or its sharp increase [31, 36].

Electrochemical measurements were supplemented with visual control of the state of the working surface of the electrode before and after each experiment (voltammetry, chronoamperometry) using MBS-2 (at magnification of $\times 7$) and MIM-7 (at magnification of $\times 500$) microscopes. The intensity of aluminum LA in the working solutions was determined by the shape, diameter, and depth of the PT and its concentration on the surface. The depth of the PT was established by the method of double focusing using the micrometric screw of the MIM-7 microscope. The method involved

alternate focusing of the optical system on the inner surface of the PT and on the smooth surface of the metal [37]. The diameter was determined using the eyepiece reticle of the MIM-7 microscope. The destruction of the metal surface was photographed with a digital camera. The surface morphology of the working electrode was determined by the SEM method. For this, the analyzed sample was placed in a cuvette in the working chamber of the JSM-6510 LV scanning electron microscope and then the corresponding micrographs were taken.

The elemental composition of the products formed during the electrochemical studies was determined using X-ray spectral microanalysis on the BRUKER 129 eV energy dispersive attachment to the JSM-6510 LV scanning electron microscope.

3. Results and discussion

Electrochemical studies of the aluminum behavior in bicarbonate solutions allowed establishing the region of metal LA corresponding to the concentration range of $2 \cdot 10^{-4}$ – $4 \cdot 10^{-3}$ M. Beyond this range, aluminum remained in a passive state [23–24]. The results of the study showed that the LA region is characterized by both a change in the shape of the anodic polarization curves (Fig. 1) and nonmonotonic dependencies of the main quantitative characteristics of the LA process (E_{PF} , E_{LA} , and τ_{ind}) on the concentration of bicarbonate ions.

In the range from $2 \cdot 10^{-4}$ M to $4 \cdot 10^{-3}$ M, E_{PF} on the APC varied from 0.165 V (in a solution of $2 \cdot 10^{-4}$ M NaHCO_3) to 0.766 V (in a solution of $4 \cdot 10^{-3}$ M NaHCO_3) (Table 1). Moreover, after APC was taken, localized damage was observed on the surface of aluminum, i.e. PT, the diameter (d) and height (h) of which decreased with an increase in the concentration of HCO_3^- ions (Table 1).

Breakdown of metal passivity in the studied systems was also confirmed by characteristic fluctuations on the corresponding chronoamperograms taken at E_{LA} (Fig. 2).

According to the chronoamperograms, pitting damage on the surface of aluminum at E_{LA} did not occur immediately, but only after some τ_{ind} (Fig. 2), the value of which increased considerably with an increase in the concentration of NaHCO_3 from $2 \cdot 10^{-5}$ to $4 \cdot 10^{-3}$ M. The opposite effect was observed in solutions of $2 \cdot 10^{-4}$ – $2 \cdot 10^{-3}$ M NaHCO_3 , where the value of τ_{ind} decreased with an increase in salt content.

What is more, E_{LA} was first gradually shifted to the negative region from 0.180 V (at $2 \cdot 10^{-4}$ M NaHCO_3) to -0.020 V (at $2 \cdot 10^{-3}$ M NaHCO_3), and then it began to increase sharply to 0.600 V (at $4 \cdot 10^{-3}$ M NaHCO_3) (Table 1).

For a more detailed study of the morphology of the aluminum surface, an additional study was carried out using the SEM and PCM methods. The latter was used to determine the quantitative

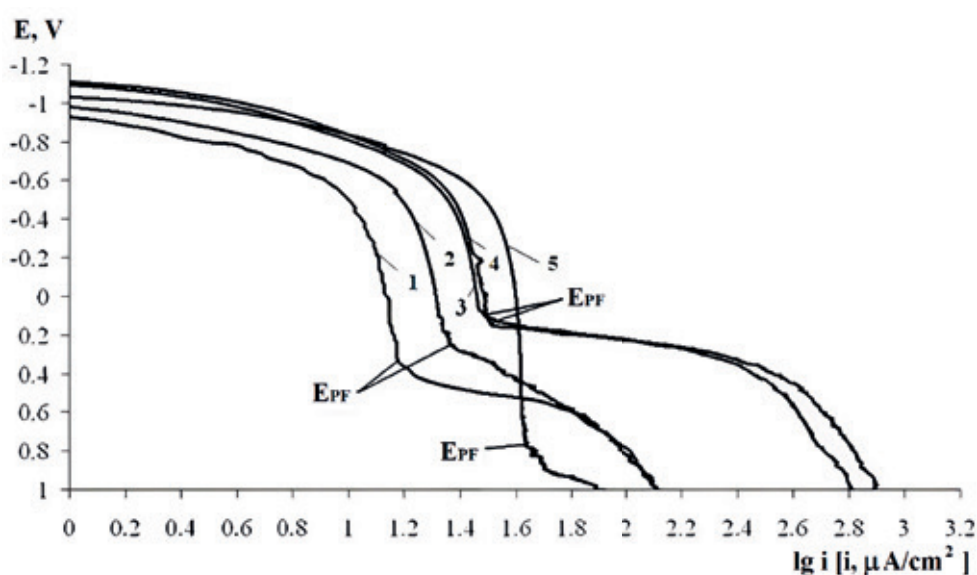


Fig. 1 APC for aluminum in NaHCO_3 solution with concentrations of $5 \cdot 10^{-4}$ (1), $1 \cdot 10^{-3}$ (2), $2 \cdot 10^{-3}$ (3), $3 \cdot 10^{-3}$ (4), $4 \cdot 10^{-3}$ (5) M ($v_p = 0.15$ V/min, $T = 25 \pm 2^\circ$ C)

Table 1. Quantitative characteristics of the process of aluminum LA in NaHCO₃ solutions

The concentration of NaHCO ₃ , M	pH before/pH after the experiment	E_{PP} , V	E_{LA} , V	τ_{ind} , s	Depth h , μm	Diameter d , μm
$2 \cdot 10^{-4}$	6.5/6.5	0.165	0.180	155	6	10
$5 \cdot 10^{-4}$	6.8/6.8	0.340	0.080	40	6	10
$1 \cdot 10^{-3}$	7.2/7.2	0.260	0.060	53	6	10
$2 \cdot 10^{-3}$	7.4/7.4	0.0830	-0.020	32	<3	5
$3 \cdot 10^{-3}$	7.4/7.4	0.150	-0.020	202	<3	5
$4 \cdot 10^{-3}$	7.7/7.7	0.766	0.600	228	<3	5

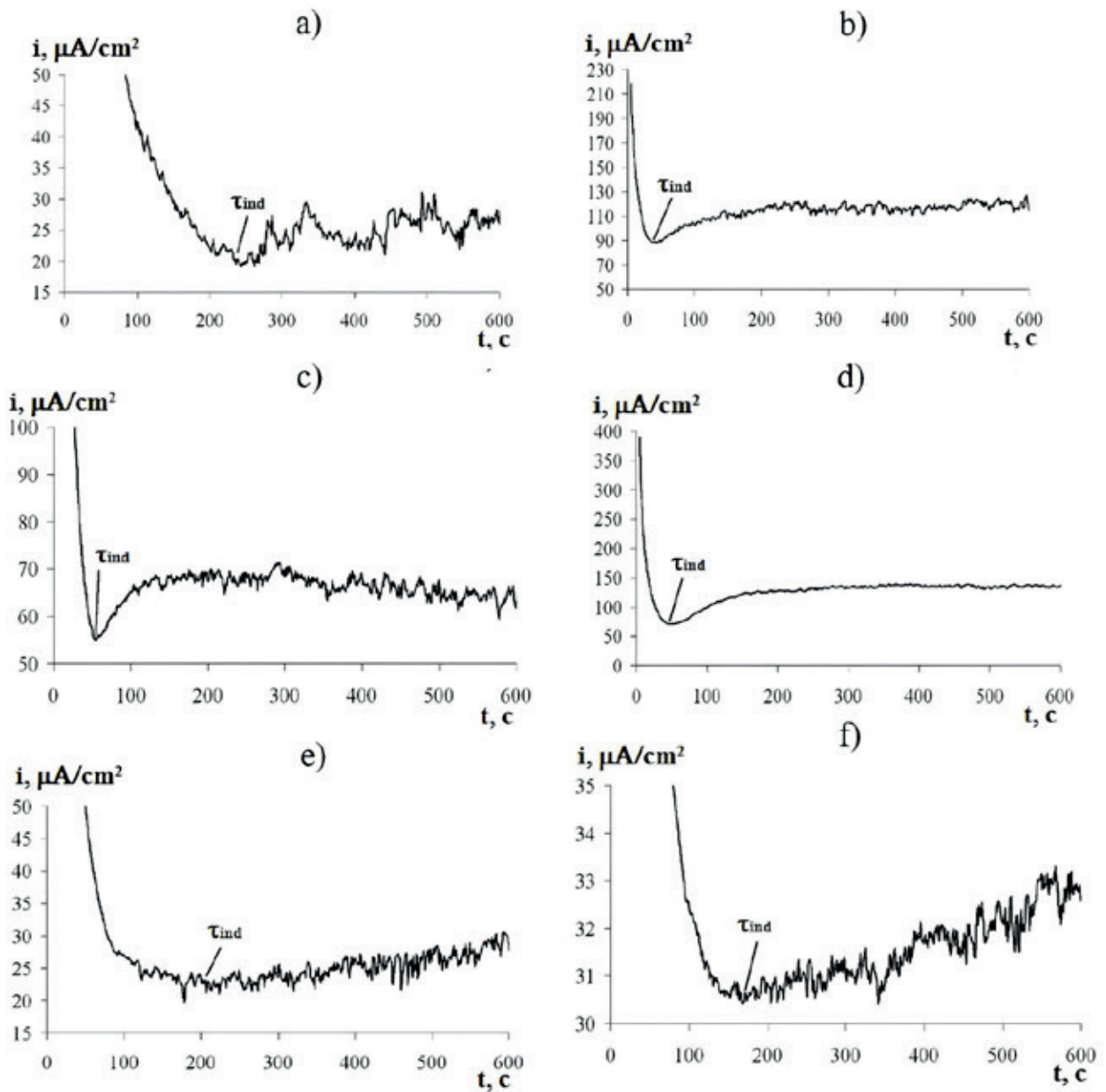
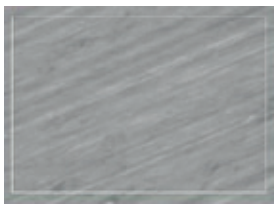


Fig. 2 Chronoamperograms for aluminum in NaHCO₃ solution at: a) $C = 2 \cdot 10^{-4}$ M and $E = 0.18$ V; b) $C = 5 \cdot 10^{-4}$ M and $E = 0.08$ V; c) $C = 1 \cdot 10^{-3}$ M and $E = 0.06$ V; d) $C = 2 \cdot 10^{-3}$ M and $E = -0.02$ V; e) $C = 3 \cdot 10^{-3}$ M and $E = -0.02$ V; f) $C = 4 \cdot 10^{-3}$ M and $E = 0.60$ V

content of chemical elements present in the film on the metal surface before (Table 2) and after (Tables 3 and 4) the electrochemical experiments. After that, comparative studies of the PT region (Tables 3a and 4a) and the metal surface without localized damage (Tables 3b and 4b) were carried out.

Table 2. Elemental composition of the film (in the selected region) on the surface of aluminum before voltammetric studies at 25 °C and their quantitative ratio

X-ray structural microanalysis		Surface micrography (SEM)
Element	Weight %	
Al	70.38	
O	7.20	
Si	14.17	
C	8.25	

According to the data obtained before the electrochemical experiments, the following elements were present on the aluminum surface: Al, O, Si, and C (Table 2). After the APC was taken, the following elements were found on the aluminum surface in the solutions of $1 \cdot 10^{-3}$ M and $4 \cdot 10^{-3}$ M NaHCO_3 : Al, O, C, Na, Si, and Mg (the weight percentage of the corresponding element given in Tables 3–4 corresponded to the location of the selected band on the metal). The ratio of the weight percentage of Al and O elements related to the thickness of the film formed on the metal surface was of particular interest [6, 18, 26]. For example, the total film thickness after voltammetric studies (Tables 3b and 4b) was almost 2 times greater as compared to the original surface (Table 2).

Following the formal kinetic approach [21, 22], to assess the control stage of the PF process, the LA region was divided into two regions ($n_1 = 0.60$ ($C_{\text{NaHCO}_3} = 2 \cdot 10^{-4} - 2 \cdot 10^{-3}$ M) and $n_2 = -2.94$

Table 3. Elemental composition of the film (in the selected region) on the surface of aluminum after voltammetric studies in a solution of $1 \cdot 10^{-3}$ M of NaHCO_3 (in PT (a) and in the film on the surface (b)) at 25 °C, and their quantitative ratio

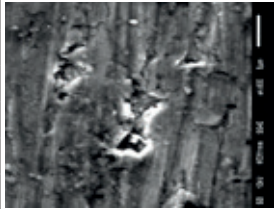
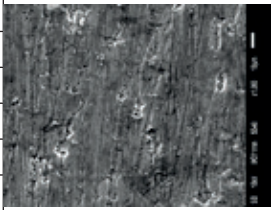
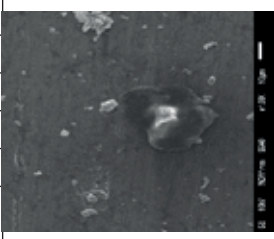
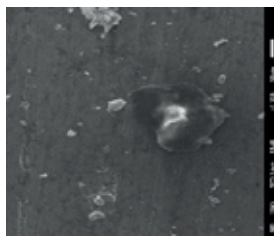
X-ray structural microanalysis		Surface micrography (SEM)	X-ray structural microanalysis		Surface micrography (SEM)
Element	Weight %		Element	Weight %	
a) In the PT			b) In the surface film		
Na	0.53		Na	0.30	
Al	82.43		Al	75.52	
C	7.06		C	7.62	
O	8.92		O	15.33	
Si	0.67		Si	0.94	
Mg	0.39		Mg	0.29	

Table 4. Elemental composition of the film (in the selected region) on the surface of aluminum after voltammetric studies in a solution of $4 \cdot 10^{-3}$ M of NaHCO_3 (in PT (a) and in the film on the surface (b)) at 25 °C, and their quantitative ratio

X-ray structural microanalysis		Surface micrography (SEM)	X-ray structural microanalysis		Surface micrography (SEM)
Element	Weight %		Element	Weight %	
a) In the PT			b) In the surface film		
Na	0.29		Na	0.09	
Al	39.32		Al	79.88	
C	47.81		C	4.81	
O	11.45		O	14.23	
Si	0.68		Si	0.99	
Mg	0.45		Mg	0.99	

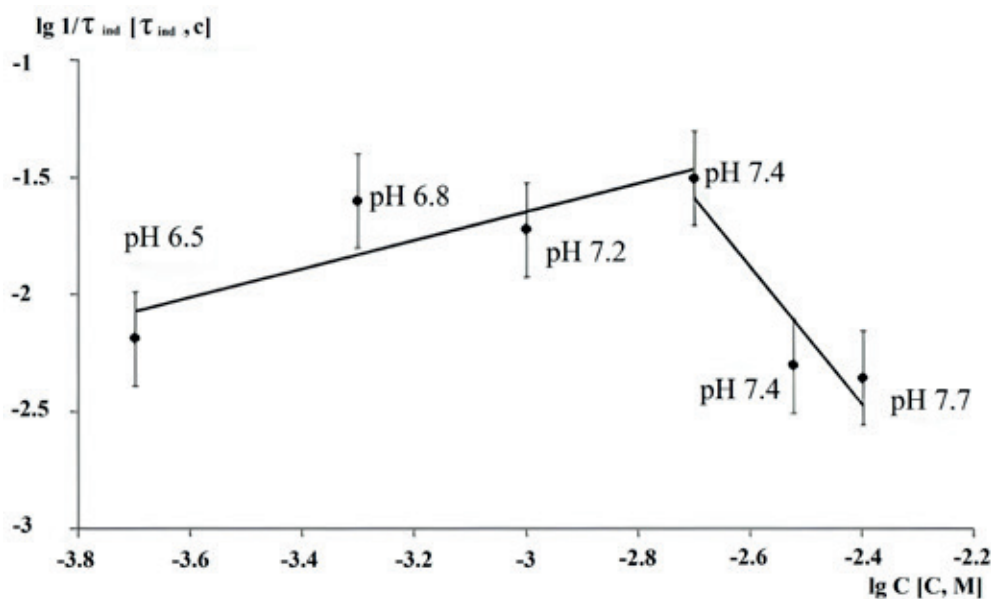


Fig. 3 Influence of NaHCO_3 concentration and pH on the rate of the process of aluminum LA ($C_{\text{NaHCO}_3} = 2 \cdot 10^{-4}$ – $4 \cdot 10^{-3}$ M, $T = 25 \pm 2$ °C)

($C_{\text{NaHCO}_3} = 2 \cdot 10^{-3}$ – $4 \cdot 10^{-3}$ M)), at the boundary of which the PF mechanism probably changed (Fig. 3). In this case, the value of n is the apparent kinetic order of the reaction for the aggressive ion, and $1/\tau_{\text{ind}}$ is the rate of PT initiation [13, 33, 35]:

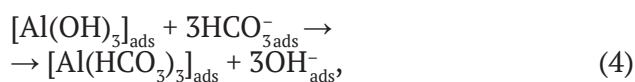
$$n_{\text{HCO}_3^-} = d \lg(1/\tau_{\text{ind}}) / d \lg C_{\text{HCO}_3^-} \quad (2)$$

The fractional reaction orders obtained during the studied process (Fig. 3) were associated with the accuracy of determining the induction period. The type of adsorption isotherm of ions involved in the PF and PT repassivation processes or the proportion of the actual surface of the localized damage on aluminum were mainly not taken into consideration.

It was shown that with an increase in the concentration of NaHCO_3 , the rate of PT initiation ($1/\tau_{\text{ind}}$) first increased (n_1) and then decreased (n_2) (Fig. 3).

In accordance with previous studies, in particular conducted within the adsorption theory and the model of nucleophilic substitution model [22, 35, 38–41], we proposed the following mechanism for the observed phenomenon.

In the range of NaHCO_3 concentrations from $2 \cdot 10^{-4}$ to $2 \cdot 10^{-3}$ M (pH = 6.5–7.4) and $n_1 = 0.60$, the passivating film has low protective characteristics, and HCO_3^- ions act as activators of pitting corrosion and cause aluminum depassivation as follows:

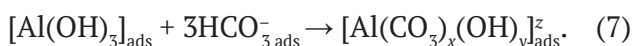


Since the apparent kinetic order of the process for HCO_3^- ion is $n = 0.60$ (i.e. close to an integer value of 1) (Fig. 3), the limiting stage of the process is most likely the association of the $[\text{Al}(\text{OH})_3]_{\text{ads}}$ complex with bicarbonate ions (4).

The formed compounds $[\text{Al}(\text{HCO}_3)_3]_{\text{ads}}$ are unstable, since they are formed by a weak base and a weak acid and probably further decompose and pass into the bulk electrolyte (5). This mechanism is confirmed by the formation of open PT on aluminum in this LA region, which is clearly visible in the SEM photographs (Table 3a). PCM method, which was also used, allowed to establish that the ratio of the weight percentage of Al and O elements in the PT corresponded to the original surface (Tables 2 and 3a).

With an increase in the concentration of HCO_3^- ions from $2 \cdot 10^{-3}$ to $4 \cdot 10^{-3}$ M (pH = 7.4–7.7) and $n_2 = -2.94$, the protective properties of the oxide film in relation to the PF increased, the LA process was inhibited, and the PT diameter and depth decreased (Table 1), which was explained by the stabilization of the passive film on aluminum as follows:





SEM photographs were used to prove the proposed mechanism (Table 4a). They clearly showed that in the second LA region PT formed under a “cap” of an insoluble compound. Moreover, according to the PCM data, PT (Table 4a) had a high (in comparison with the initial surface (Table 2)) content of O and C elements and low content of Al. In accordance with previous studies [42], for example, dawsonite $\text{NaAlCO}_3(\text{OH})_2$ can be classified as such insoluble salt (8). However, more research is needed to establish the exact formula of the chemical compound formed on the surface of aluminum.

4. Conclusions

A set of independent physicochemical methods were used to determine the concentration boundaries of the area of localized destruction of aluminum in bicarbonate media ($2 \cdot 10^{-4}$ – $4 \cdot 10^{-3}$ M NaHCO_3), to obtain systematic experimental data on the dependence of the main quantitative characteristics of the LA process (E_{pf} , E_{LA} , and τ_{ind}) on the concentration of sodium bicarbonate. It was shown that HCO_3^- ions can exhibit a dual nature, causing both activation and inhibition of the LA process depending on the concentration of bicarbonate ions. During the study, in accordance with the formal kinetic approach, to assess the control stage of the pitting formation process, the LA region was divided into two regions: $2 \cdot 10^{-4}$ – $2 \cdot 10^{-3}$ M and $2 \cdot 10^{-3}$ – $4 \cdot 10^{-3}$ M of NaHCO_3 concentrations with the reaction order $n_1 = 0.60$ ($C_{\text{NaHCO}_3} = 2 \cdot 10^{-4}$ – $2 \cdot 10^{-3}$ M) and $n_2 = -2.94$ ($C_{\text{NaHCO}_3} = 2 \cdot 10^{-3}$ – $4 \cdot 10^{-3}$ M), respectively. The adsorption theory and the model of nucleophilic substitution were used to propose the mechanisms of aluminum LA in hydrocarbonate media. The limiting stage of the process in the first LA region is the stage of association of the $[\text{Al}(\text{OH})_3]_{\text{ads}}$ complex with bicarbonate-ions. In the second LA region, an insoluble compound of complex composition is formed (the general formula of which is probably $[\text{Al}(\text{CO}_3)_x(\text{OH})_y]_{\text{ads}}^z$) in a shape of a “cap” over the pitting. It was shown that the mechanism of the process of aluminum LA changes at a concentration of $2 \cdot 10^{-3}$ M of NaHCO_3 , which is associated with a change in the solubility and nature of the compounds forming the protective film. Further research should be aimed

at studying the adsorption of bicarbonate ions on passive metal and should take into consideration the type of its isotherms.

Contribution of the authors

T. A. Minakova: text writing, study of literature, development of methodology, and final conclusions. S. A. Kaluzhina: scientific supervision, research concept, text editing, E. N. Aksyonova: conducting research.

Conflict of interests

The authors declare that they have no known competing financial interests or personal relationships that could have influenced the work reported in this paper.

References

- Balaban-Irmenin Yu. V., Fokina N. G., Petrova S. Yu. Protection against internal corrosion of water heating network pipelines*. *Energy saving and water treatment*. 2009;62(6): 1–4. (In Russ.). Available at: <https://elibrary.ru/item.asp?edn=kzdbnh>
- Mass concentration of hydrocarbonates and alkalinity of natural waters*. Guidance document RD 52.24.493-2020. Ministry of Natural Resources and Environment of the Russian Federation. Federal Service for Hydrometeorology and Environmental Monitoring (Roshydromet) Rostov-on-Don. 2020. (In Russ.)
- Akolzin P. A. *Local corrosion of metal in heat power equipment*. Moscow: Energoatomizdat Publ.; 1992. 272 p. (In Russ.)
- Tödt F., Althoff F. C. *Korrosion und Korrosionsschutz*. Berlin, Boston: De Gruyter; 1961. <https://doi.org/10.1515/9783111508436>
- Balaban-Irmenin Yu. V. Protection against internal corrosion of water heating network pipelines. Moscow: Heat Supply News Publ.; 2013. 288 p. (In Russ.)
- Kaluzhina S. A., Sieber I. V. Copper passivity and its breakdown in sodium bicarbonate solutions: A scanning electron microscopy and x-ray photoelectron and auger spectroscopy study. *Russian Journal of Electrochemistry*. 2006;42(12): 1352–1357. <https://doi.org/10.1134/S1023193506120135>
- Nafikova N. G., Kaluzhina S. A., Sanina M. Y. Specificity of the passive state of iron in slightly alkaline aqueous media with different anionic composition. *Condensed Matter and Interphases*. 2017;19(3): 376–383. <https://doi.org/10.17308/kcmf.2017.19/214>
- Skrypnikova E. A., Kaluzhina S. A. Effect of hydrodynamic conditions on copper pitting corrosion

inhibition in hydrocarbonate-chloride solutions by benzotriazole. *International Journal of Corrosion and Scale Inhibition*. 2015;4(2): 139–145. <https://doi.org/10.17675/2305-6894-2015-4-1-139-145>

9. Thomas J. G. N., Tiller A. K. Formation and breakdown of surface films on copper in sodium hydrogen carbonate and sodium chloride solutions. I. Effect of anion concentrations. *British Corrosion Journal*. 1972;11(7): 256–262.

10. Skrypnikova E. A., Kaluzhina S. A. Inhibition of copper local depassivation in alkaline media with oxygen-containing anions. *International Journal of Corrosion and Scale Inhibition*. 2017;2(6): 142–150. <https://doi.org/10.17675/2305-6894-2017-6-2-4>

11. Ushakova E. Yu., Tutukina N. M., Marshakov I. K. The copper pitting corrosion and a mechanism of its initiation in carbonate-bicarbonate solutions. *Protection of Metals*. 1991; 27(6): 934–939. Available at: <https://elibrary.ru/item.asp?id=12713135>

12. Ushakova E. Yu., Tutukina N. M., Marshakov I. K. A mechanism of pitting development on copper in carbonate-bicarbonate solutions. 1991; 27(6): 940–944. Available at: <https://elibrary.ru/item.asp?id=12712488>

13. *Corrosion resistance of chemical production equipment*. Corrosion under the action of heat carriers, coolants and other working bodies* / A. M. Sukhotin, V. M. Berenblit (eds.). Leningrad: Khimiya Publ.; 1988. 360 p. (In Russ.)

14. Minakova T. A., Kaluzhina S. A. Peculiarities of the anodic behavior of aluminum in environments with different pH in the presence of sodium chloride and glycine*. *Proceedings of Voronezh State University. Series: Chemistry. Biology. Pharmacy*. 2012;12(2): 49–54. (In Russ., abstract in Eng.). Available at: <https://www.elibrary.ru/item.asp?id=18358962>

15. Borisenkova T. A., Kaluzhina S. A. The nature of aluminum distraction at neutral mediums with different anion composition. *Condensed Matter and Interphase*. 2009;11(2): 106–110. (In Russ., abstract in Eng.). Available at: <https://www.elibrary.ru/item.asp?edn=kxfppl>

16. Borisenkova T. A., Kaluzhina S. A. The passivation and local activation of aluminum at water solutions under action of inorganic and organic additives. *Condensed Matter and Interphase*. 2011;13(2): 132–136. (In Russ., abstract in Eng.). Available at: <https://www.elibrary.ru/item.asp?id=16445515>

17. Minakova T. A. *Passivation and local anodic activation of aluminum in environments of different composition at elevated temperatures**. Cand. chem. sci. diss. Abstr. Voronezh: 2013. 18 p. Available at: <https://viewer.rsl.ru/ru/rsl01005535132?page=1&rotate=0&theme=white>

18. Kaluzhina S. A., Minakova T. A. *Passivation and local activation of aluminum**. Saarbrücken: Lambert

Academic Publ.; 2015. 141 p. (In Russ.). Available at: <https://www.elibrary.ru/item.asp?edn=wecplf>

19. Satarayev D. A., Akhmetova A. N., Dresvyannikov A. F., Petrova E. V. Electrochemical behavior of aluminum in sodium chloride solutions in the presence of zirconium (IV), magnesium (II) and lanthanum (III) ions. (In Russ., abstract in Eng.). *Bulletin of the Technological University*. 2023;26(10): 96–100. https://doi.org/10.55421/1998-7072_2023_26_10_96

20. Dresvyannikov A. F., Ivshin Y. V., Chong P. T., Khairullina A. I. Features of the anodic behavior of a combined titanium-aluminum electrode and the physicochemical properties of the products of its dissolution. *Protection of Metals and Physical Chemistry of Surfaces*. 2022;58(1): 90–98. <https://doi.org/10.1134/S2070205122010075>

21. Kaesche H. *Die Korrosion der Metalle*. Berlin: Springer-Verlag; 1979. 388 p.

22. Sinyavskiy V. S. Development of concepts of pitting corrosion and stress corrosion of aluminum alloys*. In: *Physical Chemistry: Collection of reports of the Karpov Scientific Research Institute, June 5-9, 2000, Moscow*. Moscow: NIITEKHM Publ.; 2000. pp. 86–98. (In Russ.)

23. Kaluzhina S. A., Aksenova E. N., Minakova T. A. Effect of hydrocarbonate ions on the anodic behavior of aluminum at different temperatures*. *Protection of Metals and Physical Chemistry of Surfaces*. 2016;5(1): 1–6. (In Russ.). Available at: <https://www.elibrary.ru/item.asp?edn=vxcilj>

24. Minakova T. A., Kaluzhina S. A., Aksenova E. N. Features of local activation of aluminum in the presence of hydrocarbonate ions*. In: *Electrochemistry and corrosion of metals and alloys: Collection of materials of the All-Russian conference with international participation; Dedicated to the 110th anniversary of the birth of A. Ya. Shatalov, the 95th anniversary of the birth of I. K. Marshakov, October 4–5, 2023, Voronezh*. Voronezh: Publishing House of Voronezh State University; 2023. pp. 101–103. (In Russ.). Available at: <https://www.elibrary.ru/item.asp?edn=rswppw>

25. Shatalov A. Ya. *Practical training in physical chemistry**. Moscow: Vysshaya Shkola Publ.; 1975. 284 p. (In Russ.)

26. Skripnikova E. A. *Inhibition of local activation of copper in alkaline media at elevated temperatures**. Cand. chem. sci. diss. Abstr. Tambov: 2009. 24 p. Available at: https://new-dissert.ru/_avtoreferats/01004592734.pdf

27. Khomutov N. E. *Electromotive forces, electrode potentials and chemical equilibria**. Moscow: Khimiya Publ; 1971. 116 p. (In Russ.)

28. Gorokhovskaya V. I. *Practical training in electrochemical methods**. Moscow: Vysshaya Shkola Publ.; 1983. 191 p. (In Russ.)

29. Kozin L. F. *Electrodeposition and dissolution of multivalent metals**. Kyiv: Naukova Dumka Publ.; 1989. 462 p. (In Russ.)
30. Rachev H. *Handbook of corrosion**. Moscow: Mir Publ.; 1982. 517 p. (In Russ.)
31. Plambeck J. A. *Electroanalytical chemistry: Basic principles and applications*. N.Y.: John Wiley & Sons, Inc.; 1982. 426 p.
32. Revie R. W. *Uhlig's corrosion handbook*. Hoboken: John Wiley & Sons Limited; 2011. 1285 p.
33. Freiman L. I. Stability and kinetics of pitting development*. In: *Results of Science and Technology. Corrosion and Corrosion Protection*. 1985;11(1): 3–71. (In Russ.)
34. Rosenfeld I. L. *Corrosion and protection of metals*. Moscow: Metallurgiya Publ.; 1969. 448 p. (In Russ.)
35. Kuznetsov Yu. I., Lukyanchikov O. A., Andreev N. N. On the role of the anion nature in the initial stages of metal depassivation in neutral aqueous media*. *Russian Journal of Electrochemistry*. 1985;21(12): 1690–1693. (In Russ.)
36. Kolotyrtkin Ya. M., Alekseev Yu. V. On the mechanism of self-regulation of the process of dissolution (corrosion) of a passive metal in aqueous solutions*. *Russian Journal of Electrochemistry*. 1995;31(1): 5–10. (In Russ.)
37. Zhuk N. P. *Course in the theory of corrosion and protection of metals**. Moscow: Metallurgiya Publ.; 1976. 472 p. (In Russ.)
38. Skorcheletti V. V. *Theoretical electrochemistry**. Leningrad: Khimiya Publ.; 1963. 305 p. (In Russ.)
39. Kuznetsov Yu. I., Luk'yanchikov O. A. Initiation and inhibition of pitting on nickel in neutral solutions. *Protection of Metals*. 1988;24(2): 241–248. Available at: <https://www.elibrary.ru/item.asp?id=30955179>
40. Kuznetsov Yu. I., Valuev I. A. On the role of anions in the kinetics of pitting on iron in aqueous solutions. *Russian Journal of Electrochemistry*. 1984;20(3): 424–427. (In Russ.)
41. Kuznetsov Yu. I. Role of the complexation concept in the present views on the initiation and inhibition of metal pitting. *Protection of Metals*. 2001;37(5): 434–439. <https://doi.org/10.1023/A:1012362029520>
42. Stepanov S. I., Aung M. M., Aung H. Ye., Boyarintsev A. V. Chemical aspects of scandium carbonate leaching from red muds. *Proceedings of the Voronezh State University of Engineering Technologies*. 2018;80(4): 349–355. (In Russ.). <https://doi.org/10.20914/2310-1202-2018-4-349-355>

* Translated by author of the article

Information about the authors

Tatyana A. Minakova, Cand. Sci. (Chem.), Associate Professor, Department of Physics and Chemistry, Military Educational-Research Centre of the Air Force “Air Force Academy named after Professor N. E. Zhukovsky and Yu. A. Gagarin” (Voronezh, Russian Federation).

<https://orcid.org/0009-0001-8486-0029>
tatyana_bor_vrn@mail.ru

Svetlana A. Kaluzhina, Dr. Sci. (Chem.), Professor, Department of Physical Chemistry, Voronezh State University (Voronezh, Russian Federation).

<https://orcid.org/0009-0003-4722-1898>
svetlana.kaluzhina@gmail.com

Evgeniya N. Aksyonova, Master of Physical Chemistry Department, Voronezh State University (Voronezh, Russian Federation).

<https://orcid.org/0009-0006-7648-922X>
tatyana_bor_vrn@mail.ru

Received 05.12.2023; approved after reviewing 12.12.2023; accepted for publication 25.12.2023; published online 01.10.2024.

Translated by Irina Charychanskaya



Condensed Matter and Interphases

Kondensirovannye Sredy i Mezhfaznye Granitsy
<https://journals.vsu.ru/kcmf/>

Original articles

Research article

<https://doi.org/10.17308/kcmf.2024.26/12222>

The effect of the chemical compositions of palladium alloys on their hydrogen permeability

N. B. Morozova^{1,2}✉, A. I. Dontsov^{1,2}, D. A. Pogorelova¹, T. V. Dubovitskaya²

¹Voronezh State University,
1 Universitetskaya pl., Voronezh 394018, Russian Federation

²Baikova Institute of Metallurgy and Materials Science Russian Academy of Sciences,
49 Leninsky pr., Moscow 119334, Russian Federation

Abstract

The purpose of the article is to identify the effect of the alloying element in palladium alloys on their parameters of hydrogen permeability.

Cyclic voltammetry and anodic-cathodic chronoamperometry were used to study the electrochemical behavior of cold-rolled alloys of Pd-5Pb, Pd-6Ru, and Pd-7Y systems (wt. %) in the processes of atomic hydrogen injection and extraction in a deaerated aqueous solution of 0.1 M H₂SO₄.

The study identified the role of lead, ruthenium, and yttrium in the processes of atomic hydrogen injection and ionization. Voltammetry and chronoamperometry data indicate a higher ionization rate for the Pd-6Ru alloy. The parameters of hydrogen permeability calculated from the cathodic current drops show that the hydrogen permeability of alloys varies in the series: Pd-6Ru > Pd-7Y > Pd-5Pb. The effective constant of the injection rate coincides for all alloys within the measurement error, whereas the effective constant of the extraction rate of atomic hydrogen is higher for Pd-5Pb. The marginal solubility of ruthenium in the Pd-6Ru alloy contributes to the passivation of grain boundaries in the alloy with excess ruthenium. As a result, there is preferential movement of hydrogen solely along the grain body. This results in higher hydrogen permeability.

Keywords: palladium, Pd-7Y, Pd-5Pb, Pd-6Ru alloys, hydrogen permeability, atomic hydrogen, phase-boundary transition, membrane separation

Funding: This study was supported by the Russian Science Foundation as part of the project No. 23-19-00767.

For citation: Morozova N. B., Dontsov A. I., Pogorelova D. A., Dubovitskaya T. V. The effect of the chemical compositions of palladium alloys on their hydrogen permeability. *Condensed Matter and Interphases*. 2024;26(3): 474–482. <https://doi.org/10.17308/kcmf.2024.26/12222>

Для цитирования: Морозова Н. Б., Донцов А. И., Погорелова Д. А., Дубовицкая Т. В. Роль химического состава сплавов палладия в их водородопроницаемости. *Конденсированные среды и межфазные границы*. 2024;26(3): 474–482. <https://doi.org/10.17308/kcmf.2024.26/12222>

✉ Morozova Natalya Borisovna, e-mail: mnb@chem.vsu.ru

© Morozova N. B., Dontsov A. I., Pogorelova D. A., Dubovitskaya T. V., 2024



The content is available under Creative Commons Attribution 4.0 License.

1. Introduction

Hydrogen is now seen as a key component of clean energy production, i.e. a 21st century energy solution and a post-oil era fuel. It is expected to mitigate the threat of global warming, while ensuring the sustainable and environmentally friendly energy production. Hydrogen can be produced by various methods, such as water-gas transition, fossil fuel reforming, and water electrolysis [1–3]. However, hydrogen produced by these methods normally contains gaseous impurities that need to be further separated. Membrane separation is viewed as a promising technology for the production of high-purity hydrogen due to its efficiency, energy conservation, ease of operation, and environmental friendliness [4–6].

Palladium has high selectivity to hydrogen and permeability, plasticity, and high chemical compatibility [7, 8]. Its alloys are widely used as membrane materials in hydrogen separation technologies, which reduces its production expenses [9]. The composition of the alloy has a significant impact on its permeability to hydrogen. Metal membranes can contain metals and alloys with a number of elemental components that limit the diffusion of the H atom through the alloy membrane [10, 11]. What is more, the high cost of palladium is a major limitation for its application in industry. Therefore, alternative alloy membranes with higher hydrogen permeability, lower cost, and richer resources than Pd alloy membranes are needed.

Doping palladium with such chemical elements as Pb, Ru, Cu, Y, and Ag can increase the service life of the membrane [12–14]. In addition, even small amounts of some metals lead to increased hardness, durability, and corrosion resistance and facilitate the H sorption and desorption processes.

Fusion of Pd and Ru is a promising method for producing Pd-metal alloy membranes with satisfactory characteristics and durability [15]. The mechanical, physical, electrical, kinetic, and thermodynamic properties of the PdRu system have been studied for a long time [16].

The Pd-Ru system exhibits limited solubility over the entire range of compositions and temperatures. The solubility of Ru in Pd increases

with an increase in temperature and reaches its maximum value at the peritectic temperature for a sample containing 21% of Ru. In [17], it was reported that the hardness of the Pd–Ru alloy membrane is 80% higher than that of pure palladium, while its permeability to hydrogen is very close to pure palladium in the range of 4.5–10 wt. % Ru. Consequently, Pd-Ru alloys with a homogeneous structure and an arbitrary metal ratio are of high interest for fundamental research projects and commercial design of materials [18].

Pd-Y alloy membranes can be used for the purification of H from impurities. Many papers [19–21] have shown that these alloys have a higher diffusion permeability than pure palladium. Adding just 1.68 at. % of Y increases hydrogen permeability at 300 °C by about 80% as compared to pure Pd, while the addition of ~ 8 at. % of Y increases permeability by more than 5 times [22]. The Pd-8Y membrane exhibits the maximum permeability observed over the measured temperature range of 25 to 460 °C. However, according to [21], when palladium is doped with yttrium, the Pd₇Y phase is formed, which reduces the solubility and diffusion of hydrogen. Therefore, it is most advisable to use alloys with a low atomic fraction $X_Y \leq 0.06$.

The Pd-Pb alloy is promising due to its high hydrogen permeability. Additions of lead considerably harden palladium with a slight reduction in plasticity and increase hydrogen permeability. The maximum solubility of lead in palladium is achieved at a eutectic temperature (1,470 K) and is 20 wt. % [23]. The maximum hydrogen permeability is characteristic of the alloy with 8 at. % of Pb [24].

This study was conducted on palladium alloys with yttrium, lead, and ruthenium. The purpose of the work was to identify the role of the alloying element in palladium alloys on the parameters of hydrogen permeability.

2. Experimental

This study was conducted on Pd-5Pb (95 wt. % of Pd and 5 wt. % of Pb), Pd-6Ru (94 wt. % of Pd and 6 wt. % of Ru), and Pd-7Y (93 wt. % of Pd and 7 wt. % of Y) alloys. All studied alloys were substitutional solid solutions with an FCC lattice. To obtain foil, the given alloys were subjected to cold rolling followed by annealing at 950 °C for

3 hours and then rolling on a four-high rolling mill in 10 passes with intermediate vacuum annealing at 900 °C for 30–90 min. The thickness of the studied samples was: $L(\text{Pd-5Pb}) = 46 \mu\text{m}$, $L(\text{Pd-6Ru}) = 30 \mu\text{m}$, and $L(\text{Pd-7Y}) = 50 \mu\text{m}$. The thickness was measured with an MCC 25 electron micrometer.

The geometric characteristics of the studied alloy surfaces were determined by atomic force microscopy (AFM) with a Solver P47PRO atomic force microscope in a semi-contact (intermittent-contact) scanning mode*.

The working solution in which the studies were conducted was a deaerated solution of 0.1 M H_2SO_4 (extra pure) prepared in bidistilled water. To deaerate the working solution, chemically pure argon was passed through the cell for 30 minutes.

When preparing the electrode for the experiment, the foil surface was cleaned, i.e. degreased with chemically pure ethanol and washed with distilled water. Then, a conductive graphite glue was used to deposit the foil on the graphite electrode. The area of the foil had been measured and did not exceed 0.5 cm². Each sample was used for one cycle of the experiment, which involved quadruple potential cycling and obtaining a series of chronoamperograms for different hydrogenation time from 1 to 10 s. After one cycle, the sample was replaced.

Electrochemical measurements were conducted in a glass three-electrode cell at a temperature of 25 °C using a copper sulfate reference electrode (0.311 V). Platinated platinum Pt(Pt) was used as an auxiliary electrode. Spectrally pure graphite electrode was used as a working electrode onto which thin samples of metal foil were deposited with a conductive graphite glue.

The measurements were taken using a computer-aided IPC-Compact potentiostat. All potentials were recalculated relative to a standard hydrogen electrode and the current values were given per single unit of the visible surface.

The studied electrode was placed in an electrochemical cell filled with a working solution, kept for 500 seconds at a pretreatment potential E_{pp} (for surface cleaning), the value of which was 0.3 V.

* The research was carried out using the equipment of the Center for Collective Use of Scientific Equipment of Voronezh State University.

The cyclic voltammograms were obtained at a potential scan rate of 5 mV/s, starting from E_{pp} to the cathodic region until the appearance of a noticeable cathodic current of hydrogen reduction ($E = -0.14 \text{ V}$). Then, the potential sweep was switched to the anodic region until oxygen was released (up to $E = 1.5 \text{ V}$). Cycling was carried out 4 times in the same potential range for electrochemical cleaning of the electrode surface and its standardization.

Chronoamperograms were recorded immediately after the voltammograms were obtained. During the first step, the electrode surface was standardized for 500 s at the potential E_{pp} . Step 2 involved injecting atomic hydrogen at a hydrogenation potential of -0.14 V. During each cycle of obtaining chronoamperograms, the hydrogenation time was changed from 1 to 10 s. During the third step, atomic hydrogen was extracted from the alloy at the peak ionization potential. The ionization potential was determined from the data of the previous voltammograms, i.e. the fourth cycle, and could change when the foil sample was replaced.

3. Results and discussion

3.1. Examination of the foil surface relief

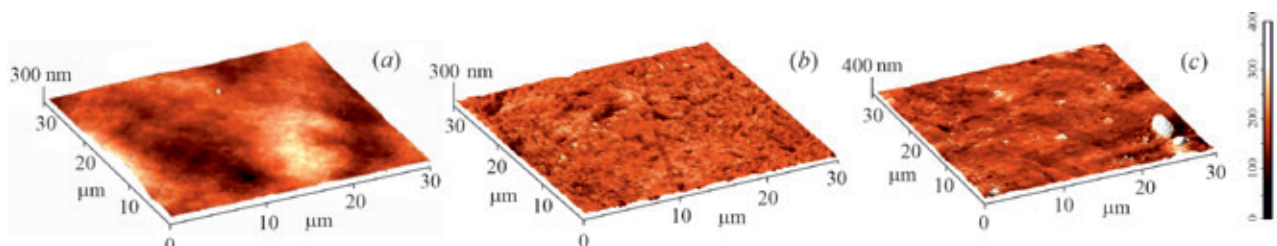
Characteristics of Pd and its alloys and roughness according to the results of AFM studies are given in Table 1.

The analysis of the data in Table 1 showed that the surface roughness of all studied alloys was almost the same (Fig. 1) and there was little difference between the parameters of their crystal lattices. The main difference in the nature of the second component was connected with their electronic structure. Ruthenium and yttrium are *d*-metals that exhibit good solubility in relation to hydrogen. However, Pb is a *p*-metal, for which this property is not characteristic. Therefore, it can be assumed that the Pd-Pb alloy may exhibit lower hydrogen permeability as compared to Pd-Ru and Pd-Y.

The limited solubility of ruthenium in palladium [25] caused a release of excess Ru along the boundaries of the crystal lattice of the studied alloy. This led to the passivation of the intercrystalline space, which prevented the movement of atomic hydrogen along the boundaries in the alloy [26]. As established in

Table 1. Characteristics of palladium and its alloys

$\omega(X)$, wt. %	Pd	PdX		
		5Pb	6Ru	7Y
Electronic configuration	[Kr] $4d^{10}5s^0$	[Xe] $4f^1 5d^1 6s^2 6p^2$	[Kr] $4d^5 5s^1$	[Kr] $4d^1 5s^2$
Atomic radius r , pm	137	175	134	178
Lattice parameter [23], nm	0.3890	0.3908	0.3879	0.3875
Roughness, nm ($30 \times 30 \mu\text{m}^2$)	–	34 ± 5	33 ± 5	32 ± 5


Fig. 1. AFM micrographs of the surface of the Pd5Pb (a), Pd6Ru (b), and Pd7Y (c) alloys

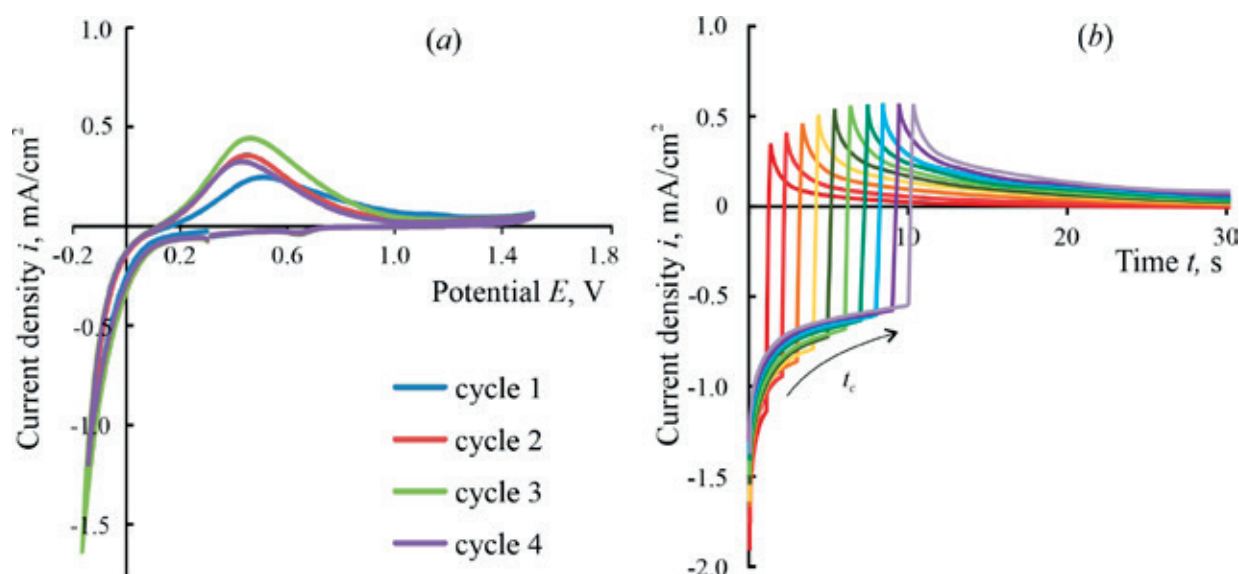
[27], the flow of atomic hydrogen through the crystallite body is dominant and it induces the appearance of various structural defects.

3.2. Electrochemical research

Cyclic voltammograms obtained for all studied alloys were similar. For Pd-6Ru and Pd-5Pb alloys, at a potential of about 0.5 V from the first cycle of voltammograms, there was a clearly expressed anodic peak related to the ionization of atomic hydrogen (Fig. 2a, 3a). At a potential of about 0.7 V, there was a small peak corresponding to the reduction of palladium oxide. The PdO was

formed on the anodic branch of the curve in the range of potentials from 1.2 to 1.3 V and could be observed in the form of a subtle current peak. This fact is confirmed by previous studies [28], as well as the constant position and height of the PdO reduction peak for all studied alloys.

Together with Pd oxidation at a potential of about 1.2 V, there was a pronounced anodic peak for the Pd-7Y alloy, which decreased during the transition from cycle 1 to cycle 4 (Fig. 4a). We explained this peak by the electrooxidation of annealing artifacts of organic substances used during rolling of the alloy to produce foil.


Fig. 2. Cyclic voltamperograms (a) and chronoamperograms (b) of the Pd-5Pb foil in 0.1 M H_2SO_4

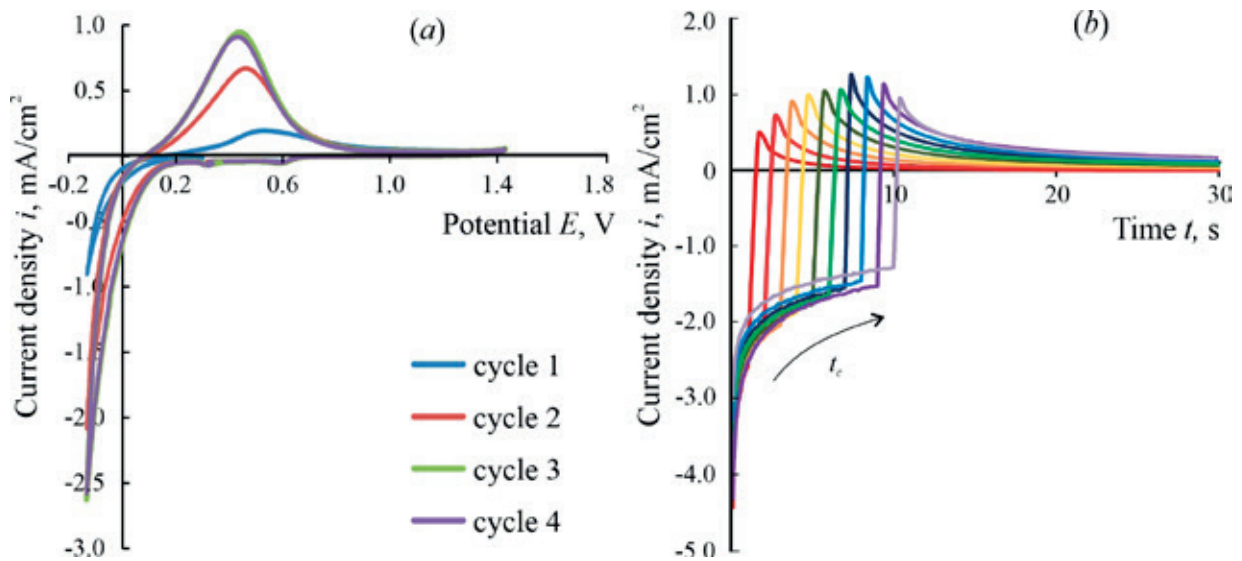


Fig. 3. Cyclic voltamperograms (a) and chronoamperograms (b) of Pd-6Ru foil in 0.1 M H₂SO₄ of the studied sample

Interestingly, during the first cycle of the Pd-7Y voltammogram, there was no peak of hydrogen ionization, however, it developed gradually during further cycling of the potential. This occurred simultaneously with the disappearance of the electrooxidation peak. Most likely, this was due to blocking of active adsorption centers that prevented the interaction of atomic hydrogen with the alloy surface.

The height of the peak of hydrogen ionization on Pd-5Pb and Pd-7Y alloys reached 0.5 V, while on Pd-6Ru alloy it was almost twice as high. Quadruple potential cycling contributed to the

cleaning of the alloy surface, which resulted in the growth of peak of atomic hydrogen ionization [29].

Cathodic i, t -curves for all alloys were characterized by a sharp decline (Fig. 2b-4b). With an increase in the hydrogenation time from 1 to 10 s, there was a decrease in cathodic chronoamperograms. The maximums of the cathodic curves corresponding to the zero degree of surface covering decreased by 1.5 times with an increase in t_c , and this applied to all alloys. The injection rate of atomic hydrogen, which is characterized by the cathodic current, was lower for the Pd-5Pb alloy than for other alloys.

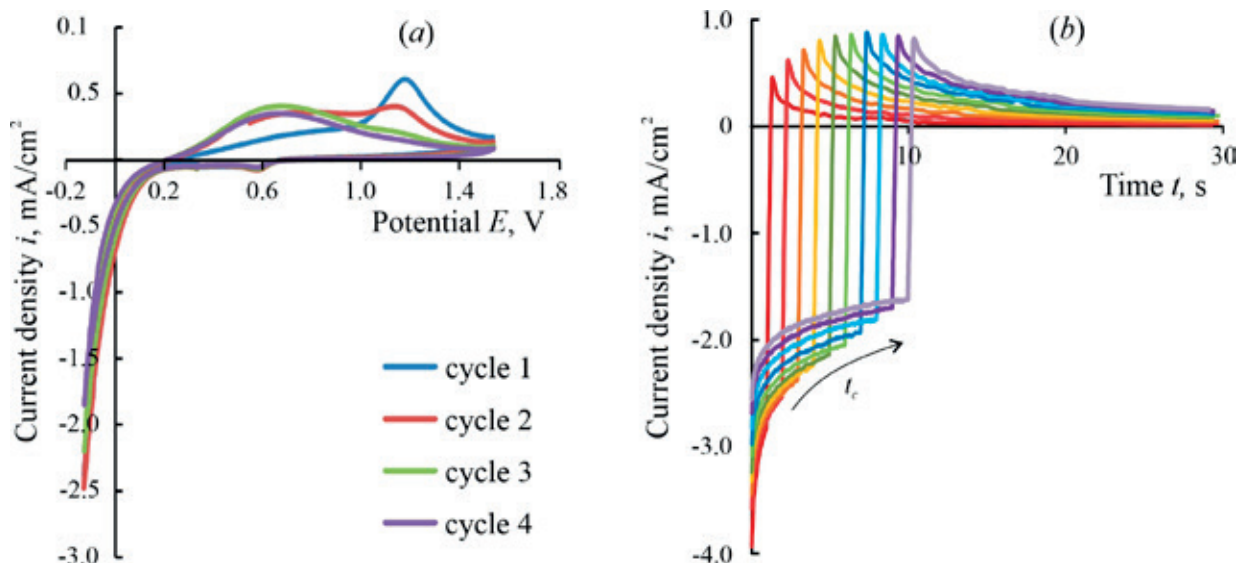


Fig. 4. Cyclic voltamperograms (a) and chronoamperograms (b) of Pd-7Y foil in 0.1 M H₂SO₄ of the studied sample

The anodic chronoamperograms corresponding to H extraction was increasing with an increase in hydrogenation time during the first few seconds and then the value remained almost constant. For the Pd-6Ru alloy, the value of the injection rate was higher (Fig. 3b). The nature of the decline of the anodic i_c -curves was similar for all alloys. This fact can be used as a proof that the kinetics of the injection-extraction processes of atomic hydrogen are invariable.

3.3. Calculating the parameters of hydrogen permeability

The nature of the second component in the processes of atomic hydrogen injection and extraction can be conveniently identified when comparing the parameters of their hydrogen permeability. A mathematical model describing the injection and extraction of atomic hydrogen in alloys of semi-infinite thickness ($L > 10 \mu\text{m}$) was used to calculate these parameters [30].

According to the theoretical modeling of the process of injecting atomic hydrogen for compact electrodes, the total cathodic current drop at the initial stage ($t \leq 3 \text{ s}$) can be described by equation (1):

$$i_c(t) = i_c(0) - F\bar{k} \left[c_{\text{H}}^s(\eta_c) - c_{\text{H}}^e \right] \frac{2\bar{k}t^{1/2}}{\pi^{1/2}D_{\text{H}}^{1/2}} =$$

$$= i_c(0) - \left[i_c(0) - i_c^\infty \right] \frac{2\bar{k}}{\pi^{1/2}D_{\text{H}}^{1/2}} t^{1/2}, \quad (1)$$

where $i_c(0)$ and i_c^∞ are the initial and stationary cathodic current of the chronoamperograms, respectively; \bar{k} is the effective constant of the extraction rate of atomic hydrogen; and D_{H} is the diffusion coefficient of H in the metallic phase.

At the time of the cathodic chronoamperogram $t > 4 \text{ s}$, the limiting stage from the phase boundary transition is passed to the stage of solid-phase diffusion of hydrogen in the alloy and can be described by the equation:

$$i_c(t) = i_c^\infty + \frac{FK_D}{\pi^{1/2}} t^{-1/2}. \quad (2)$$

Based on (2), it is possible to find the hydrogen permeability coefficient, K_D , which includes the solid-phase diffusion coefficient of H and the change in the concentration of hydrogen in the foil relative to its equilibrium value $\Delta c_{\text{H}} = c_{\text{H}}^s(\eta_c) - c_{\text{H}}^e$:

$$K_D = \Delta c_{\text{H}} \cdot D_{\text{H}}^{1/2}. \quad (3)$$

The analysis of the cathodic current drops corresponding to the hydrogenation time of 10 s allowed obtaining hydrogen permeability coefficient K_D , the effective constants of the injection and extraction rates of atomic hydrogen \bar{k} , and \bar{k} , respectively, and the effective constant of phase boundary equilibrium $K = \bar{k} / \bar{k}$. Also, the concentration of atomic hydrogen in the Δc_{H} alloy was estimated from (3) under the assumption that the alloys are enriched with palladium and there is little difference between diffusion coefficients of atomic hydrogen in them and pure Pd.

The obtained values of the hydrogenation parameters obtained from the cathodic current drops are given in Table 2.

The hydrogen permeability K_D and, as a consequence, the concentration of atomic hydrogen in the Δc_{H} alloy increased in the Pb→Y→Ru series. The large values of the confidence intervals for all obtained parameters can be explained by the fact that different foil sections of the same alloy were studied, which could differ slightly in their structure and roughness.

The values of the effective constants of injection \bar{k} and extraction rates \bar{k} differ slightly and coincide within the limits of experimental error. However, the atomic hydrogen transition through the solution/alloy interphase was facilitated for Pd-6Ru alloy and inhibited for Pd-7Y alloy. What is more, the transition of

Table 2. Parameters of hydrogen permeability of the studied alloys, calculated from the cathodic current decays of chronoamperograms

Alloy	i_c^0 , mA/cm ²	i_c^∞ , mA/cm ²	$K_D \cdot 10^8$, mol/(cm ² ·s ^{1/2})	$K \cdot 10^{-4}$, cm ⁻¹	\bar{k} , s ⁻¹	$\bar{k} \cdot 10^4$, cm/s	$\Delta c_{\text{H}} \cdot 10^5$, mol/cm ³
Pd-5Pb	1.79±0.20	0.65±0.38	1.51±0.61	1.92±0.77	8.33±1.16	4.52±1.23	2.75±1.11
Pd-7Y	2.31±0.44	1.23±0.15	1.74±0.65	2.22±0.83	7.85±3.07	3.55±0.25	3.17±1.18
Pd-6Ru	2.43±0.23	1.12±0.31	2.08±0.46	3.32±1.73	9.60±2.78	3.63±0.89	3.80±0.83

atomic hydrogen from the alloy to the surface phase was easier for Pd-5Pb. The nature of the change in the phase boundary exchange constant was similar to that of the hydrogen permeability coefficient.

In previous research [31], it was established that the parameters of hydrogen permeability obtained from cathodic current drops are more informative and exclude the possibility of dilatation of the crystal lattice or hydrogen capture in octahedral and tetrahedral voids of the alloy [27, 32].

To sum up the obtained results, it can be concluded that the best hydrogen permeability is characteristic of the Pd-6Ru alloy as evidenced by the maximum values of the diffusion parameters K_D and Δc_H . This is probably due to similar values of the Pd and Ru atomic radii and the electronic structure that contributes to the dissolution of atomic hydrogen. There is little dependency of the kinetic parameters of injection and extraction on the chemical nature of the second component. For the Pd-7Y alloy, the formation of the intermetallic compound of Pd₇Y contributes to a decrease in hydrogen permeability [21]. In the case of Pd-5Pb alloy, the lowest hydrogen permeability values are most likely due to the electronic structure of lead, which is a *p*-element and has a filled 5*d*-sublevel. Also, fusion of Pd and Pb can be accompanied by the transition of *d*-electrons from the electronic sublevel of palladium to the *p*-sublevel of lead. The values of hydrogen permeability for the studied alloys obtained by other methods [33–35] are consistent in order and sequence of changes in values. However, an accurate comparison is impossible due to the different conditions of the experiments.

4. Conclusions

1. Palladium-based alloys with ruthenium, yttrium, and lead with nearly the same quantitative compositions have similar electrochemical behavior. The highest ionization rate of atomic hydrogen is characteristic of the Pd-6Ru alloy. Whereas surface contamination by annealing artefacts of organic substances used during rolling is most evident in the Pd-7Y alloy where a strong adhesion of organic substances to the surface of the alloy might take place. The data of cathodic and anodic chronoamperograms

generally confirm the voltammetric behavior of the studied alloys.

2. The hydrogen permeability parameters calculated from the cathodic current drops show that the hydrogen permeability ($\text{mol}/(\text{cm}^2 \cdot \text{s}^{1/2})$) of alloys varies in the series: Pd-6Ru ($2.08 \cdot 10^{-8}$) > Pd-7Y ($1.74 \cdot 10^{-8}$) > Pd-5Pb ($1.51 \cdot 10^{-8}$).

3. The effective constants of the injection rate for all alloys coincide within the measurement error, and the effective constants of the extraction rate (cm/s) vary in the series: Pd-5Pb ($4.52 \cdot 10^{-4}$) > Pd-6Ru ($3.63 \cdot 10^{-4}$) \approx Pd-7Y ($3.55 \cdot 10^{-4}$). Therefore, the extraction rate of atomic hydrogen is determined by the nature of the alloying element. The mechanism of atomic hydrogen penetration through the interface into the metal phase is the same for all alloys.

4. The marginal solubility of ruthenium in the Pd-6Ru alloy contributes to the passivation of grain boundaries in the alloy with excess ruthenium. As a result, there is preferential movement of hydrogen solely along the grain body. This results in higher hydrogen permeability.

Contribution of the authors

The authors contributed equally to this article.

Conflict of interests

The authors declare that they have no known competing financial interests or personal relationships that could have influenced the work reported in this paper.

References

1. Chen W. H., Chen C. Y. Water gas shift reaction for hydrogen production and carbon dioxide capture: A review. *Applied Energy*. 2020;258: 114078. <https://doi.org/10.1016/j.apenergy.2019.114078>
2. Fan L., Li C., Aravind P., Cai W., Han M., Brandon N. Methane reforming in solid oxide fuel cells: challenges and strategies. *Journal of Power Sources*. 2022;538: 231573. <https://doi.org/10.1016/j.jpowsour.2022.231573>
3. Shafiev D. R., Trapeznikov A. N., Hokhonov A. A., ... Subcheva E. N. Methods for obtaining hydrogen on an industrial scale. Comparative analysis. *Uspehi v himii i himicheskoj tehnologii*. 2020;34(12): 53–57. (In Russ.). Available at: <https://elibrary.ru/item.asp?id=44712152>
4. Ockwig N. W., Nenoff T. M. Membranes for hydrogen separation. *Chemical Reviews*. 2007;107(10): 4078–4110. <https://doi.org/10.1021/cr0501792>

5. Shahbaz M., Al-Ansar T., Aslam M., ... McKay G. A state of the art review on biomass processing and conversion technologies to produce hydrogen and its recovery via membrane separation. *International Journal of Hydrogen Energy*. 2020;45(30): 15166–15195. <https://doi.org/10.1016/j.ijhydene.2020.04.009>
6. Lin Y. M., Liu S. L., Chuang C. H., Chu Y. T. Effect of incipient removal hydrogen through palladium membrane on the conversion of methane steam reforming experimental and modelling. *Catalysis Today*. 2003;82(1-4): 127–139. [https://doi.org/10.1016/S0920-5861\(03\)00212-8](https://doi.org/10.1016/S0920-5861(03)00212-8)
7. Rahimpour M. R., Samimi F., Babapoor A., Tohidian T., Mohebi S. Palladium membranes applications in reaction systems for hydrogen separation and purification: A review. *Chemical Engineering and Processing: Process Intensification*. 2017;121(1): 24–49. <https://doi.org/10.1016/j.cep.2017.07.021>
8. Tovbin Yu. K., Votyakov E. V. Effect of interstitial hydrogen on the properties of palladium membranes. *Russian Journal of Physical Chemistry A*. 2001;75(4): 640–645. Available at: <https://elibrary.ru/item.asp?id=13382490>
9. Roshan N., Gorbunov S., Chistov E., Karelin F., Kuterbekov K., Abseitov Ye. Palladium-based membranes for separation of high-purity hydrogen. *Perspektivnye Materialy*. 2020;6: 47–57. <https://doi.org/10.30791/1028-978X-2020-6-47-57> (In Russ.)
10. Magnone E., Shin M. C., Lee J. I., Park J. H. Relationship between hydrogen permeability and the physical-chemical characteristics of metal alloy membranes. *Journal of Membrane Science*. 2023;674: 121513. <https://doi.org/10.1016/j.memsci.2023.121513>
11. Livshits A. I. The hydrogen transport through the metal alloy membranes with a spatial variation of the alloy composition: Potential diffusion and enhanced permeation. *International Journal of Hydrogen Energy*. 2017;42(18): 13111–13119. <https://doi.org/10.1016/j.ijhydene.2017.04.016>
12. Burhanov G. S., Gorina N. B., Kolchugina N. B., Roshan N. R., Slovetsky D. I., Chistov E. M. Palladium-based alloy membranes for separation of high purity hydrogen from hydrogen-containing gas mixtures. *Platinum Metals Review*. 2011;55(1): 3–12. <https://doi.org/10.1595/147106711X540346>
13. Avdyuhina V. M., Burhanov G. S., Nazmutdinov A. Z., Roshan N. R. Hydrogen and vacancy induced structural and phase transformations in Pd-Ru alloy foils. *Perspektivnye Materialy*. 2011;11: 68–72. (In Russ.). Available at: <https://www.elibrary.ru/item.asp?id=17561288>
14. Pogorelova D. A., Morozova N. B., Vvedenskii A. V. The influence of ruthenium, yttrium and lead on the hydrogen permeability of palladium-based alloys*. *Elektrokhimiya i korrozija metallov i splavov: Proc. All-Rus. Conf., 4-5 October 2023, Voronezh: VSU Publ.; 2023. p. 47-79. (In Russ.)*
15. Hubkowska K., Koss U., Lukaszewski M., Czerwinski A. Hydrogen electroadsorption into Pd-rich Pd-Ru alloys. *Journal of Electroanalytical Chemistry*. 2013;704: 10–18. <https://doi.org/10.1016/j.jelechem.2013.06.004>
16. Ryi S. K., Li A., Lim C. J., Grace J. R. Novel non-alloy Ru/Pd composite membrane fabricated by electroless plating for hydrogen separation. *International Journal of Hydrogen Energy*. 2011;36(15): 9335–9340. <https://doi.org/10.1016/j.ijhydene.2010.06.014>
17. Gade S. K., Keeling M. K., Davidson A. P., Hatlevik O., Way J. D. Palladium–ruthenium membranes for hydrogen separation fabricated by electroless co-deposition. *International Journal of Hydrogen Energy*. 2009;34(15): 6484–6491. <https://doi.org/10.1016/j.ijhydene.2009.06.037>
18. Liu J., Bellini S., deNooijer N. C. A., ... Caravella A. Hydrogen permeation and stability in ultra-thin Pd-Ru supported membranes. *International Journal of Hydrogen Energy*. 2020;45(12): 7455–7467. <https://doi.org/10.1016/j.ijhydene.2019.03.212>
19. Hughes D. T., Harris I. R. Hydrogen diffusion membranes based on some palladium-rare earth solid solution alloys. *Zeitschrift für Physikalische Chemie*. 1979;117(117): 185–193. <https://doi.org/10.1524/zpch.1979.117.117.185>
20. Hughes D. T., Evans J., Harris I. R. The influence of order on hydrogen diffusion in the solid solution alloys Pd-5.75at.%Ce and Pd-8at.%Y. *Journal of the Less-Common Metals*. 1980;74(2): 255–262. [https://doi.org/10.1016/0022-5088\(80\)90160-5](https://doi.org/10.1016/0022-5088(80)90160-5)
21. Wang D., Flanagan T. B., Shanahan K. Diffusion of H through Pd–Y alloy membranes. *Journal of Membrane Science*. 2016;499: 452–461. <https://doi.org/10.1016/j.memsci.2015.10.020>
22. Wileman R. C. J., Doyle M., Harris I. R. A Comparison of the permeability, solubility, and diffusion characteristics of H and D in a palladium–8% yttrium and palladium–25% silver solid solution alloy. *Zeitschrift für Physikalische Chemie*. 1989;164: 797–802. https://doi.org/10.1524/zpch.1989.164.part_1.0797
23. *Phase diagrams of binary metal systems*. Handbook in 3 volumes / N. N. Lyakishev (eds.). Moscow: Izd-vo Mashinostroenie Publ., 1996. 872 p. (In Russ.)*
24. Morozova N. B., Dontsov A. I., Fedoseeva A. I., Vvedensky A. V. Hydrogen permeability of Pd-Pb foils of various compositions. *Condensed Matter and Interphases*. 2023;24(1): 85–94. <https://doi.org/10.17308/kcmf.2023.25/10977>
25. Hu Z., Li H., Zhao W., Zhou W., Hu S. Microstructure determination of PdRu immiscible alloys based on electron-pair distribution function and local elemental segregation. *Cell Reports Physical*

Science. 2023;4(12): 101713. <https://doi.org/10.1016/j.xcrp.2023.101713>

26. Ievlev V. M., Burkhanov G. S., Maksimenko A. A., ... Roshan N. R. Structure and properties of Pd-Ru membrane alloy foil produced in the process of magnetron sputtering. *Inorganic Materials: Applied Research*. 2014; 5(4): 303–306. <https://doi.org/10.1134/S2075113314040248>

27. Gabrielli C., Grand P. P., Lasia A., Perrot H. Investigation of hydrogen adsorption-absorbition into thin palladium films. I. Theory. *Journal of The Electrochemical Society*. 2004;151(11): A1925–A1936. <https://doi.org/10.1149/1.1797033>

28. Gabrielli C., Grand P. P., Lasia A., Perrot H. Investigation of hydrogen adsorption-absorbition into thin palladium films. II. Cyclic voltammetry. *Journal of The Electrochemical Society*. 2004;151(11): A1937–A1942. <https://doi.org/10.1149/1.1797035>

29. Fedoseeva A. I., Morozova N. B., Dontsov A. I., Kozaderov O. A., Vvedensky A. V. Cold-rolled binary palladium alloys with copper and ruthenium: injection and extraction of atomic hydrogen. *Russian Journal of Electrochemistry*. 2022;58(9). 812–822. <https://doi.org/10.1134/s1023193522090051>

30. Morozova N. B., Vvedensky A. V., Beredina I. P. The phase-boundary exchange and the non-steady-state diffusion of atomic hydrogen in Cu-Pd and Ag-Pd alloys. Part I. Analysis of the model. *Protection of Metals and Physical Chemistry of Surfaces*. 2014;50(6): 699–704. <https://doi.org/10.1134/S2070205114060136>

31. Morozova N. B., Vvedensky A. V., Beredina I. P. Phase boundary exchange and nonstationary diffusion of atomic hydrogen in Cu-Pd and Ag-Pd alloys II experimental data. *Protection of Metals and Physical Chemistry of Surfaces*. 2015;51(1): 72–80. <https://doi.org/10.1134/S2070205115010098>

32. Kuznetsov V. V., Khaldeev G. V., Kichigin V. I. *Hydrogenation of metals in electrolytes*. Moscow: Mashinostroenie Publ.; 1993. 244 p. (In Russ.)

33. Didenko L. P., Sementsova L. A., Chizhov P. E., Babak V. N., Savchenko V. I. Separation performance of foils from Pd–In(6%)–Ru(0.5%), Pd–Ru(6%), and Pd–Ru(10%) alloys and influence of CO₂, CH₄, and water vapor on the H₂ flow rate through the test membranes. *Russian Chemical Bulletin*. 2017;65(8): 1997–2003. <https://doi.org/10.1007/s11172-016-1543-4>

34. Wang X., Feng X., Yang L., ... Luo W. Highly efficient and direct recovery of low-pressure hydrogen isotopes from tritium extraction gas by PdY alloy membrane permeator. *Fusion Engineering and Design*. 2024;202: 114348. <https://doi.org/10.1016/j.fusengdes.2024.114348>

35. Ievlev V. M., Dontsov A. I., Novikov V. I., ... Burkhanov G. S. Composite membranes based on Pd-Cu and Pd-Pb solid solutions. *Metally*. 2018;5: 70–74. Available at: <https://www.elibrary.ru/item.asp?id=36740359> (In Russ.)

* Translated by author of the article

Information about the authors

Natalia B. Morozova, Cand. Sci. (Chem.), Associate Professor, Department of Physical Chemistry, Voronezh State University (Voronezh, Russian Federation); Senior Researcher, Baikova Institute of Metallurgy and Materials Science Russian Academy of Sciences (Moscow, Russian Federation).

<https://orcid.org/0000-0003-4011-6510>
mnb@chem.vsu.ru

Alexey I. Dontsov, Cand. Sci. (Phys.–Math.), Associate Professor, Department of Materials Science and Industry of Nanosystems, Voronezh State University (Voronezh, Russian Federation); Senior Researcher, Baikova Institute of Metallurgy and Materials Science Russian Academy of Sciences (Moscow, Russian Federation).

<https://orcid.org/0000-0002-3645-1626>
dontalex@mail.ru

Daria A. Pogorelova, 2nd year master's student of the Department of Physical Chemistry, Voronezh state University (Voronezh, Russian Federation).

<https://orcid.org/0009-0002-0488-5080>
pogorelova.d@mail.ru

Tatyana V. Dubovitskaya, Cand. Sci. (Pedagogical), Senior Researcher, Baikova Institute of Metallurgy and Materials Science Russian Academy of Sciences (Moscow, Russian Federation).

<https://orcid.org/0000-0003-2201-705X>
d.t.v.n.a@mail.ru

Received 15.03.2024; approved after reviewing 17.06.2024; accepted for publication 15.07.2024; published online 01.10.2024.

Translated by Irina Charychanskaya



Original articles

Research article

<https://doi.org/10.17308/kcmf.2024.26/12223>

Mechanical properties and catalytic activity of the Cu-36Pd (at. %) alloy foil surface after cleaning

N. B. Morozova^{1,2}, A. I. Dontsov^{1,2}✉, T. N. Khmelevskaya¹

¹Baykova Institute of Metallurgy and Materials Science of the Russian Academy of Sciences, 49 Leninsky pr., Moscow 119991, Russian Federation

²Voronezh State University, 1 Universitetskaya pl., Voronezh 394018, Russian Federation

Abstract

The purpose of the study was to evaluate the effect of mechanical treatment and ion sputtering on hydrogen sorption and the mechanical properties of the surface of the membrane foil of the Pd-Cu solid solution system obtained by rolling.

The efficiency of mechanical and ion beam treatment in cleaning of the surface of membrane foil of the Pd-Cu solid solution system obtained by rolling was assessed using cyclic voltammetry, Auger electron spectroscopy and atomic force microscopy.

It was established that ion beam treatment (Ar⁺) and mechanical treatment reproduce the elemental composition of the surface, corresponding to the original composition of the solid solution, and forms a developed relief. The change in the asymmetry of the relief roughness after ion-beam treatment indicates the formation of microcracks on the foil surface, which reduce hardness and plasticity. Ion-beam surface treatment also contributes to the cleaning of the surface from rolling artefacts, which leads to a twofold increase in the ionization rate of atomic hydrogen, compared to a sample subjected to mechanical treatment.

Keywords: Cu-36Pd (at. %) solid solution, thin foil, surface cleaning, voltammetry, atomic force microscopy, nanoindentation

Funding: The study was supported by the Russian Science Foundation grant No. 23-19-00767 (<https://rscf.ru/project/23-19-007671/>)

For citation: Morozova N. B., Dontsov A. I., Khmelevskaya T. N. Mechanical properties and catalytic activity of the Cu-36Pd (at. %) alloy foil surface after cleaning. *Condensed Matter and Interphases*. 2024;26(3): 483–489. <https://doi.org/10.17308/kcmf.2024.26/12223>

Для цитирования: Морозова Н. Б., Донцов А. И., Хмелевская Т. Н. Механические свойства и каталитическая активность поверхности фольги сплава Cu-36Pd (ат. %) после очистки. *Конденсированные среды и межфазные границы*. 2024;26(3): 483–489. <https://doi.org/10.17308/kcmf.2024.26/12223>

✉ Alexey I. Dontsov, e-mail: DontAlex@mail.ru

© Morozova N. B., Dontsov A. I., Khmelevskaya T. N., 2024



1. Introduction

Solid solutions of the Pd-Cu system in a wide range of concentrations may form an ordering with the formation of a CsCl-type structure (β -phase) [1]. Interest in these solid solutions has been ongoing for several decades due to the limited information on the mechanism of ordering processes (α (FCC) \rightarrow β) and disordering ($\beta \rightarrow \alpha$), on the substructure of the β -phase, including possible manifestations of deviations from the equiatomic composition, including in its properties. In terms of practical application the interest is due to the peculiarity of the properties: multiple changes in electrical conductivity during $\alpha \leftrightarrow \beta$ transformations [2]; the high mechanical characteristics of foil with the β -phase structure [3, 4], its advantage in hydrogen permeability in comparison with the α -phase, with pure and doped palladium (the activation energy of hydrogen diffusion in the β -phase is significantly lower) [5]. Therefore, the ordered solid solution foil is promising in the production of effective membranes for deep hydrogen purification, since it provides possibility of a multiple increase in productivity without the reduction with hydrogen, typical for samples made of pure and doped palladium. The low activation energy of hydrogen diffusion in an ordered structure allows the operation of the membrane at a temperature before the start of disordering.

Due to the stage-by-stage nature of the overall mass transfer process, along with the elemental composition, structure and substructure of the foil, it is necessary to take into account the state of the surface (elemental composition, morphology), which may be due to the manufacturing process (rolling, variants of ion sputtering of a target of the corresponding composition [6], galvanizing [7]). Thus, the cleaning of these membrane foil surfaces is an urgent task.

The aim of the study was to evaluate the influence of mechanical treatment and ion sputtering on hydrogen sorption and the mechanical properties of the surface of the membrane foil of the Pd-Cu solid solution system obtained by rolling.

2. Experimental

The rolling process was carried out according to the scheme described in [8], rolling from

2 mm was carried out sequentially up to a thickness of 100 μm . An ingot of Cu-36Pd (at. %), corresponding to the maximum temperature of the existence of the β -phase (about 550 $^{\circ}\text{C}$), which ensured the formation of a single-phase structure was produced for rolling.

The original foil had a two-phase nanocrystalline structure (α - and β -phases [9]). For the ordering of the atomic structure (β -phase) the original foil was heated to 800 $^{\circ}\text{C}$ in a vacuum followed by rapid cooling to room temperature. The diffraction pattern in Fig.1 shows the structure of the foil, heat-treated to 800 $^{\circ}\text{C}$ and cooled to room temperature. As can be seen, the β -phase with an average size of the coherent scattering region of more than 1 μm was restored.

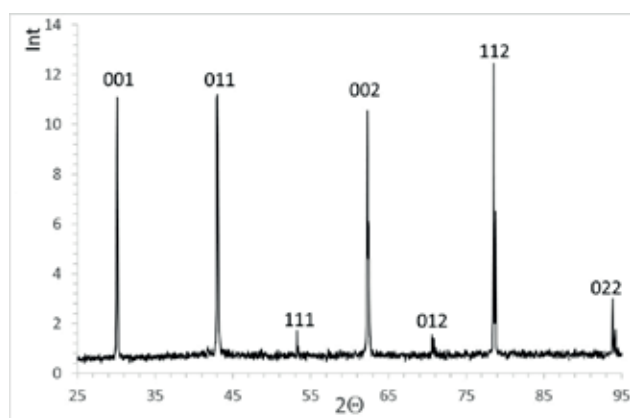


Fig. 1. X-ray diffraction pattern of the foil sample after heating at 800 $^{\circ}\text{C}$ and cooling to room temperature

The phase composition was controlled using X-ray diffractometry* (RD, ARL X'TRA). The elemental composition of the sample surface was assessed using Auger electron spectroscopy (DESA-100 analyser), and quantitative analysis was performed using yield coefficients [10]. The surface morphology of the original foil and after its surface treatment was studied using atomic force microscopy (AFM, Solver Pro EC). The results of the following cleaning options were compared: 1 – mechanical treatment (MT) of the surface by successive use of sandpaper (grain size 2500), aqueous suspension of MgO and ethanol; 2 – ion beam treatment (IBT) for 180 min in an Ar environment (10^{-1} Pa) with an energy of about 50 eV, the initial vacuum is 10^{-3} Pa, to ensure uniform etching, the substrate with the foil was rotated at a speed of 1 rad/s.

* VSU Centre for the Collective Use of Scientific Equipment.

The mechanical properties of the foil surface were studied using the nanoindentation method on a Nano Hardness Tester (maximum load 20 mN, loading and unloading rate 20 mN/min).

The efficiency of foil treatment was assessed using cyclic voltammetry [11, 12] based on the degree of sensitivity to potential cycling, manifested as a local increase in current in the range of 0.1–

0.5 V (at a potential scanning rate of 5 mV/s), corresponding to hydrogen ionization [13], and the complex sorption parameter (K_p , mol/cm² s^{1/2}) [14]. Since the samples had the thickness higher than 10 μm, atomic hydrogen did not pass through the foil during the experiment. It was not possible to determine the diffusion coefficient (D) of atomic hydrogen for the used model.

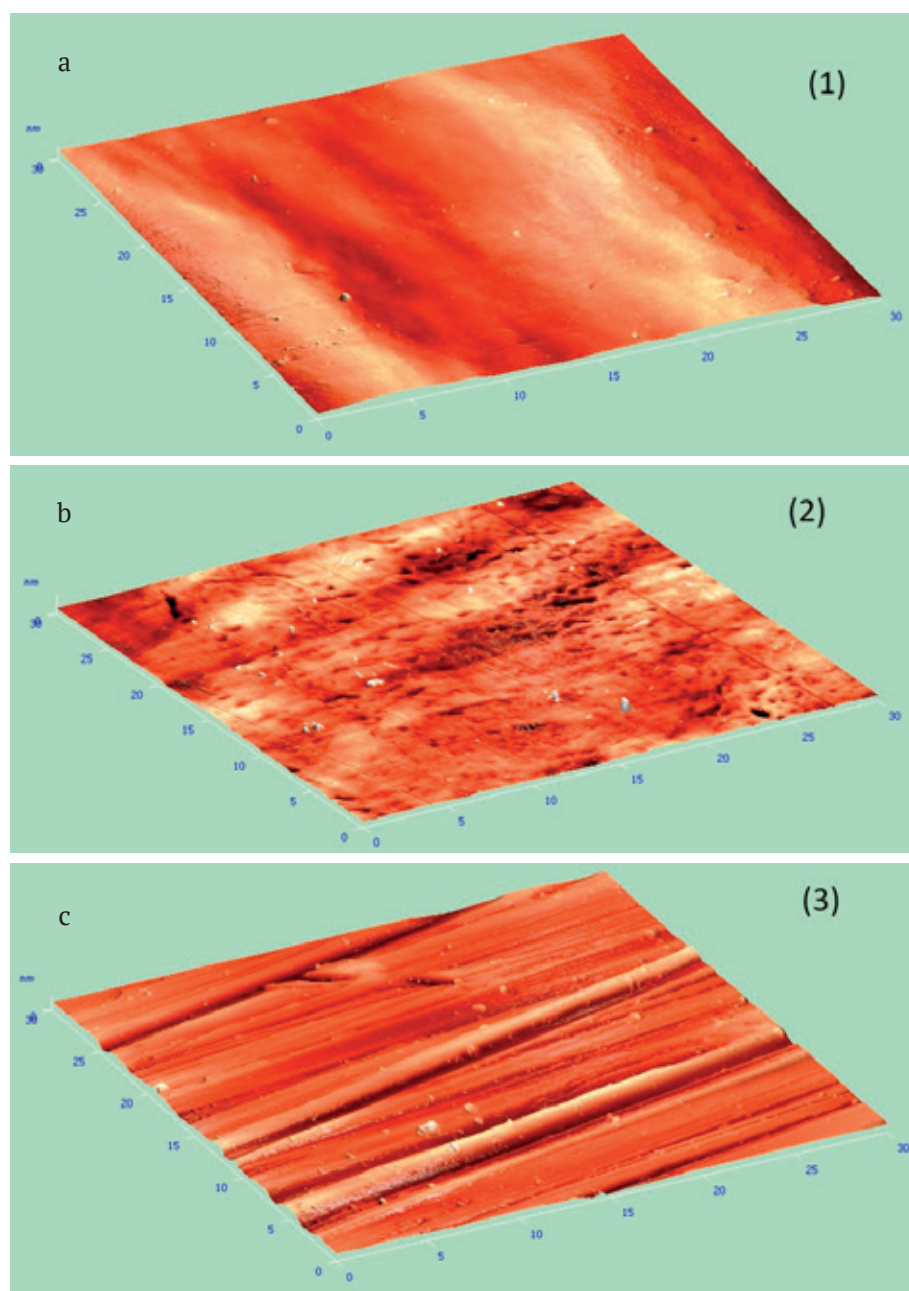


Fig. 2. AFM image of the surface areas of annealed foil (a), after ILD (b) and after mechanical treatment (c)

3. Results and discussion

AFM images of the surface of an annealed sample (a), after ion beam treatment (b) and after mechanical treatment are shown in Fig. 2. The results of image processing are presented in Table 1. After IBT, the height of the surface relief increased by 1.5 times. The type of surface roughness changes with hills ($S_{sk} > 0$) on the depressions ($S_{sk} < 0$) [15], which may indicate selective etching of the foil surface and the formation of pores and microcracks.

The surface relief (Fig. 2c) reflects traces of deformation as a result of the process of mechanical treatment of the surface with abrasive materials: the relief height and roughness increased by 2 times, the type of surface roughness did not change.

Figure 3 shows the distribution profile of elements along the depth of the surface layer, constructed using Auger electron spectroscopy data. Elemental composition of the unclean surface: sulphur - 17 at. %, carbon - 44 at. %, nitrogen - 8 at. %, oxygen - 11 at. %, palladium - 20 at. %. Transitions corresponding to copper atoms were not detected, which can be explained by the presence of rolling artefacts on the foil surface and a low electron yield coefficient of copper in comparison with the detected elements. At a depth of 300–500 nm, rolling artefacts almost completely disappeared, and the elemental composition corresponded to the original composition of the alloy.

The elemental composition of the foil surface after IBT and mechanical treatment is shown in Fig. 3(2) and 3(3), respectively. At the initial stage of etching, the concentration atoms was ~ 45 at. %, which was comparable to the concentration for an unclean surface. At a depth of more than 50 nm, the impurity concentration was ~ 5 at. %. This finding indicates that impurity elements were sorbed in the surface layer of the foil from the atmosphere, and not as a result of the rolling process.

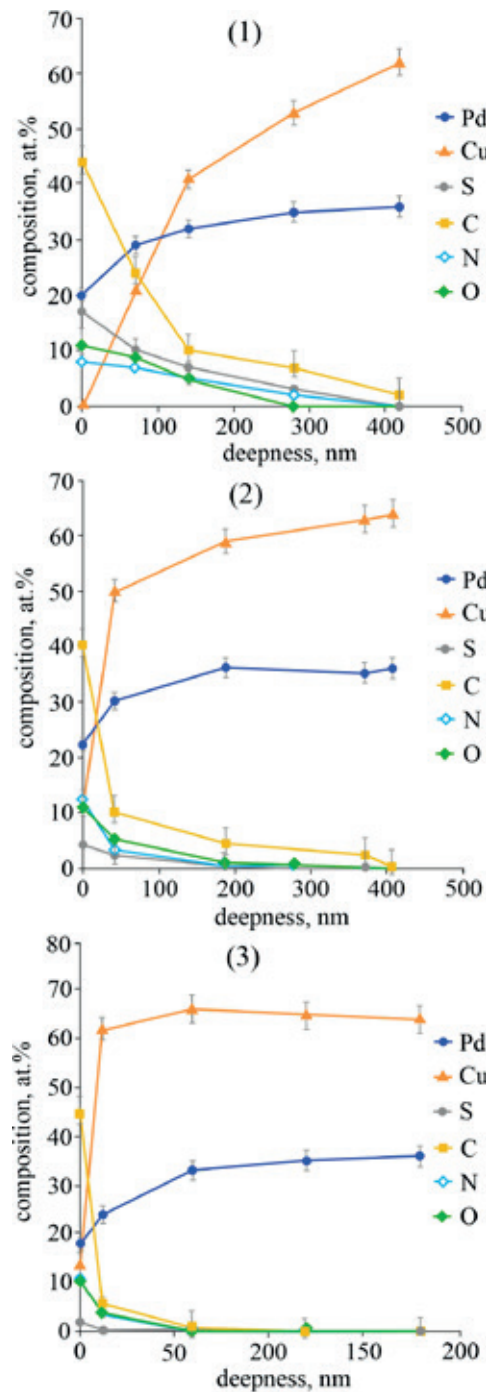


Fig. 3. Profiles of element distribution by depth of the near-surface layer (1) of annealed foil, (2) after ILD and (3) after mechanical treatment

Table 1. Surface roughness parameters

Sample	Параметры шероховатости поверхности			
	Maximum height, S_y (nm)	Average height, S_z (nm)	Roughness, S_a (nm)	Roughness asymmetry, S_{sk}
Without treatment	294	161	26	0.17
After treatment <1>	458	227	10	-0.67
After treatment <2>	583	290	41	0.27

An assessment of the hardness and plasticity of the surface of the uncleaned foil (1), after IBT (2) and MT (3) was performed based on P - h diagrams (Fig. 4): $Hv = 325 \pm 10$ MPa and $h = 54 \pm 1\%$, $Hv = 240 \pm 10$ and $h = 44 \pm 1\%$, $Hv = 268 \pm 10$ MPa, $h = 44 \pm 1\%$ respectively. The presence of bends on the loading and unloading branches of curve (2) indicated a high concentration of microcracks caused by the selective etching of the foil surface with argon ions, which is confirmed by AFM data (see Table 1).

The decrease in hardness and plasticity is explained by the increase in the number of defects on the surface of the cleaned foil compared to the annealed one.

The voltammograms of an annealed sample (1) and the sample after mechanical treatment (2) are shown in Fig. 5. The untreated surface was virtually insensitive to potential cycling, as evidenced by the height (about 0.2 mA/cm^2) of the local maximum in the potential range of 0.3 – 0.5 V, characterizing the ionization process of atomic hydrogen. Hydrogen sorption constant (K_D) was equal to $2.44 \cdot 10^{-9} \text{ mol cm}^{-2} \cdot \text{s}^{-1/2}$.

The effect of mechanical surface treatment was expressed through an increase in the ionization peak, the height of which exceeded 0.7 mA/cm^2 (Fig. 2). This indicates an increase in the hydrogen ionization rate by 3.5 times compared to the untreated sample and an increase in K_D to $5.48 \cdot 10^{-9} \text{ mol cm}^{-2} \cdot \text{s}^{-1/2}$.

Ion beam surface treatment also helped to clean the surface from rolling artefacts (Fig. 6),

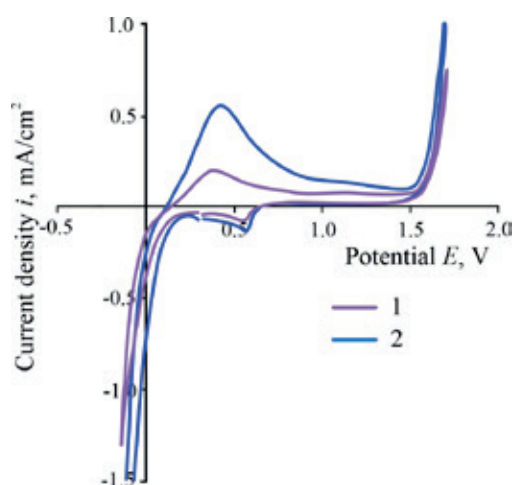


Fig. 5. Cyclic voltammograms obtained on an annealed sample (1) and a sample after mechanical treatment (2). (4 cycles of voltammograms are shown)

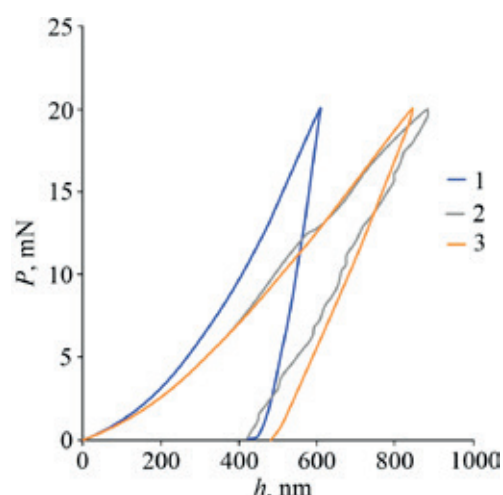


Fig. 4. Load diagram (P) - nanoindenter penetration depth (h) for $100 \mu\text{m}$ thick foil samples after rolling and annealing (1), after IBT (2), after MT (3)

which led to an increase in the ionization peak to 1.4 mA/cm^2 , i.e. to a twofold increase in speed, compared to a sample subjected to mechanical treatment (K_D to $7.14 \cdot 10^{-9} \text{ mol cm}^{-2} \cdot \text{s}^{-1/2}$). This was not only due to the unblocking of sorption centres during the IBT process, but also due to an increase in surface area caused by the formation of microcracks.

A quantitative assessment of hydrogen permeability was carried out using a mathematical model of images of semi-infinite thickness, describing injection (\bar{k}) and extraction (\bar{k}) of atomic hydrogen.

The extraction rate constant increased by 2 times when using ion beam treatment and was $\sim 8.0 \cdot 10^{-4} \text{ cm/s}$, which can be explained by

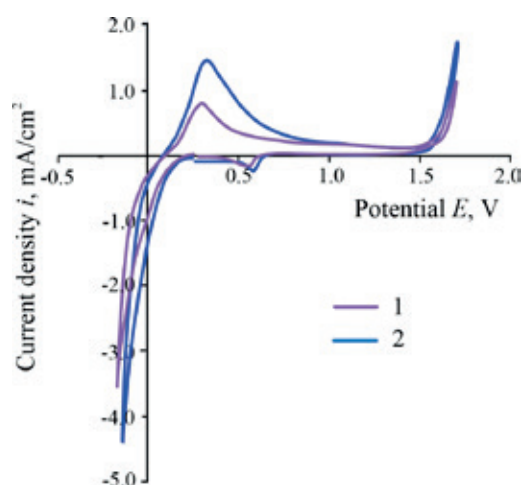


Fig. 6. Cyclic voltammograms obtained on a sample after mechanical treatment (1) and after ILD (2). (4 cycles of voltammograms are shown)

significant changes in the surface structure of the foil after the treatment.

Thus, as a result of IBT, the surface was completely freed from rolling artefacts, relief was developed, microcracks were formed and, accordingly, the effective surface area was increased.

Out of the two studied options for cleaning the surface of foil obtained by rolling, both options were effective. However, such treatment leads to the formation of microcracks on the surface of the foil, which significantly reduced its hardness and plasticity.

4. Conclusions

1. Ion beam treatment (Ar⁺) and mechanical treatment reproduce the elemental composition of the surface corresponding to the original composition of the solid solution and form a developed relief.

2. The change in the asymmetry of the relief roughness after IBT indicates the formation of microcracks on the foil surface, which reduce hardness and plasticity.

3. Ion-beam surface treatment also helps to clean the surface from rolling artefacts, leading to a twofold increase in the ionization rate of atomic hydrogen compared to a sample subjected to mechanical treatment.

Contribution of the authors

The authors contributed equally to this article.

Conflict of interests

The authors declare that they have no known competing financial interests or personal relationships that could have influenced the work reported in this paper.

References

1. Subramanian P. R., Laughlin D. E. Cu-Pd (Copper-Palladium). *Journal of Phase Equilibria* 1991;12: 231–243. <https://doi.org/10.1007/bf02645723>
2. Senchenko A. A., Zelenin L. P., Sachkov I. N., Bashkatov A. N., Kotov A. P., Geld P. V. Measurement of temperature phase state on electrical resistive alloys Pd, Cu and Pd, Cu, In*. *Fizika metallov i metallovedenie*. 1989;67(V.1): 122–128. (In Russ.)
3. Telegin A. B., Syutkin N. N., Shashkov O. D. Structure and mechanical properties of ordered copper-palladium alloy*. *Fizika metallov i metallovedenie*. 1981;52(V.Z): 627–633. (In Russ.)

4. Golikova N. N., Laptevskij A. S., Syutkina V. I. Electrical and mechanical properties of ordered alloys based on palladium - copper with a B2 superstructure. *Fizika metallov i metallovedeniya*. 1996;82(3): 150–160. (In Russ.). Available at: <https://www.elibrary.ru/item.asp?id=14934742>

5. *Hydrogen in metals*. (Topics in applied physics; v. 28–29). Includes bibliographical references and indexes. Contents: v. 1. Basic properties. v. 2. Application-oriented properties. 1. Metals-Hydrogen content. 1. Alefeld G., 1933, 11. Ve1kl, J., 1936-TH690.H97. <https://doi.org/10.1002/bbpc.19800840221>

6. Ievlev V. M., Dontsov A. I., Novikov V. I., ... Burkhanov G. S. Composite membranes based on Pd-Cu and Pd-Pb solid solutions. *Russian Metallurgy (Metally)*. 2018;9: 854–858. <https://doi.org/10.1134/S0036029518090070>

7. Alique D., Imperatore M., Sanz R., Calles J. A., Baschetti M. G. Hydrogen permeation in composite Pd-membranes prepared by conventional electroless plating and electroless pore-plating alternatives over ceramic and metallic supports. *International Journal of Hydrogen Energy*. 2016;41: 19430–19438. <https://doi.org/10.1016/j.ijhydene.2016.06.128>

8. Mironova E. Y., Yaroslavtsev A. B., Dontsov A. I., Morozova N. B., Gorbunov S. V., Ievlev V. M. Lamp processing of the surface of PdCu membrane foil: hydrogen permeability and membrane catalysis. *Inorganic Materials*. 2021;57(8): 781–789. <https://doi.org/10.1134/S0020168521080057>

9. *Phase diagrams of binary metal systems. A Handbook, in 3 volumes: Vol. 2*. Lyakishev N. P. (ed.). Moscow: Mashinostroenie Publ.; 1997. 1024 p. (In Russ)

10. Davis L. E., MacDonald N. C., Palmberg P. W., Rich G. E., Weber R. E. (eds.), *Handbook of Auger Electron Spectroscopy*. Physical Electronics Industries, Inc., 1976.

11. Uluc A.V., Moa J. M. C., Terryn H., Böttger A. J. Hydrogen sorption and desorption related properties of Pd-alloys determined by cyclic voltammetry. *Journal of Electroanalytical Chemistry*. 2014;734(1): 53–60. <https://doi.org/10.1016/j.jelechem.2014.09.021>

12. Iwaoka H., Ide T., Arita M., Horita Z. Mechanical property and hydrogen permeability of ultrafine-grained Pd-Ag alloy processed by high-pressure torsion. *International Journal of Hydrogen Energy*. 2017;42(38): 24176–24182. <https://doi.org/10.1016/j.ijhydene.2017.07.235>

13. Fedoseeva A. I., Morozova N. B., Dontsov A. I., Kozaderova O. A., and Vvedensky A. V. Cold-rolled binary palladium alloys with copper and ruthenium: injection and extraction of atomic hydrogen. *Russian Journal of Electrochemistry*. 2022;58(9): 812–822. <https://doi.org/10.1134/S1023193522090051>

14. Morozova N. B., Vvedensky A. V., Beredina I. P. The phase-boundary exchange and the non-steady-state diffusion of atomic hydrogen in Cu-Pd and Ag-Pd alloys. I. Model analysis. *Protection of Metals and Physical Chemistry of Surfaces*. 2014;50(6): 699–704. <https://doi.org/10.1134/S2070205114060136>

15. Kurth S., Kenan C., Daniel M., Lars W., Seume J. R. Systematic roughness variation to model the influence of skewness on wall bounded flows. *Journal of the Global Power and Propulsion Society*. 2023;7: 177–187. <https://doi.org/10.33737/jgpps/163089>

** Translated by author of the article*

Information about the authors

Natalia B. Morozova, Cand. Sci. (Chem.), Associate Professor, Department of Physical Chemistry, Voronezh State University (Voronezh, Russian Federation); Senior Researcher, A. A. Baikov Institute of Metallurgy and Materials Science Russian Academy of Sciences (Moscow, Russian Federation).

<https://orcid.org/0000-0003-4011-6510>

mnb@chem.vsu.ru

Alexey I. Dontsov, Cand. Sci. (Phys.–Math.), Associate Professor, Department of Materials Science and Industry of Nanosystems, Voronezh State University (Voronezh, Russian Federation); Senior Researcher, A. A. Baikov Institute of Metallurgy and Materials Science Russian Academy of Sciences (Moscow, Russian Federation).

<https://orcid.org/0000-0002-3645-1626>

dontalex@mail.ru

Tatyana N. Khmelevskaya, Cand. Sci. (Chem.), Researcher, A. A. Baikov Institute of Metallurgy and Materials Science of the Russian Academy of Sciences (Moscow, Russian Federation).

tatiana_ilinova@mail.ru

Received 08.09.2023; approved after reviewing 28.09.2023; accepted for publication 20.11.2023; published online 01.10.2024.

Translated by Valentina Mittova



Condensed Matter and Interphases

Kondensirovannyye Sredy i Mezhfaznye Granitsy
<https://journals.vsu.ru/kcmf/>

Original articles

Research article

<https://doi.org/10.17308/kcmf.2024.26/12224>

Photoluminescence of GaPNAs/GaP(N) superlattices and bulk GaPN layers on GaP substrates

E. V. Nikitina^{1,2}, M. S. Sobolev², E. V. Pirogov², I. S. Makhov³, A. M. Nadtochiy³, E. I. Vasilkova^{2✉}, N. V. Kryzhanovskaya³

¹Ioffe Institute,
26 Polytechnicheskaya st., St. Petersburg 194021, Russian Federation

²Alferov University,
8/3 Khlopina st., St. Petersburg 194021, Russian Federation

³HSE University Saint Petersburg,
16 Soyuz Pechatnikov st., St. Petersburg 194100, Russian Federation

Abstract

The addition of a few percent of nitrogen to GaP or GaPAs allows obtaining GaPNAs solid solutions that are lattice-matched to the silicon substrate over a wide range of band gaps, which makes it possible to obtain optoelectronic silicon integrated circuits. However, materials with a small fraction of nitrogen are understudied due to the difficulty in epitaxial growth of quaternary solid solutions with three materials of group V. The purpose of the study was the investigation of the influence of the substrate temperature during the epitaxial growth of dilute nitride materials (GaPN solid solution and GaPNAs/GaP(N) superlattices) on their optical properties, as well as the influence of the growth temperature and superlattice design on the bandgap of the resulting material.

It was shown that there is an optimal growth temperature for samples: at temperatures below the optimal, non-radiative recombination at defects predominates, and at a temperature higher than the optimal one, the solid solution of the GaPN layer material decomposes into components with a larger and smaller fraction of nitrogen. Studies were also carried out on the decay of photoluminescence intensity over time in the studied structures at room temperature, which allowed us to evaluate the influence of growth parameters and structure design on the lifetime of nonequilibrium charge carriers. The best lifetime for structures with superlattices was obtained for the GaPNAs/GaPN superlattice and amounted to ~0.2 ns.

As a result, the optimal growth temperatures were determined for bulk GaPN layers and for GaPNAs/GaP(N) superlattices, which leads to an increase in the PL intensity and lifetime of the carrier.

Keywords: GaPN(As), Superlattices, Photoluminescence

Funding: The study was supported by the Russian Science Foundation No. 23-79-00032 (<https://rscf.ru/project/23-79-00032/>). The optical properties of the samples were analyzed on a unique setup “Complex optoelectronic unit of the National Research University Higher School of Economics - St. Petersburg”.

For citation: Nikitina E. V., Sobolev M. S., Pirogov E. V., Makhov I. S., Nadtochiy A. M., Vasilkova E. I., Kryzhanovskaya N. V. Photoluminescence of GaPNAs/GaP(N) superlattices and bulk GaPN layers on GaP substrates. *Condensed Matter and Interphases*. 2024;26(3): 490–495. <https://doi.org/10.17308/kcmf.2024.26/12224>

Для цитирования: Никитина Е. В., Соболев М. С., Пирогов Е. В., Махов И. С., Надточий А. М., Василькова Е. И., Крыжановская Н. В. Фотолюминесценция сверхрешеток GaPNAs/GaP(N) и объемных слоев GaPN на подложках GaP. *Конденсированные среды и межфазные границы*. 2024;26(3): 490–495. <https://doi.org/10.17308/kcmf.2024.26/12224>

✉ Elena I. Vasilkova, e-mail: elenvasilkov@gmail.com

© Nikitina E. V., Sobolev M. S., Pirogov E. V., Makhov I. S., Nadtochiy A. M., Vasilkova E. I., Kryzhanovskaya N. V., 2024



The content is available under Creative Commons Attribution 4.0 License.

1. Introduction

Now, silicon is the main material of electronics, integrated circuit technology, and solar energy. On the other hand, multi-junction solar converters based on AIII BV materials are the most efficiently used in solar energy, their efficiency for concentrated solar radiation exceeds 47% [1]. The use of a silicon substrate for a multi-junction solar converter based on AIII BV materials as upper stages impairs significant mismatch between silicon lattice and the main AIII BV materials. Among all binary AIII BV materials, GaP has the lowest lattice mismatch with Si [1] ($\sim 0.37\%$ at room temperature [2]). Under normal conditions, GaP is an indirect-bandgap material, which to a certain extent limits its use in optoelectronics, photonics, and photovoltaics [3]. In recent decades, much attention has been paid to the study of chemical compounds of gallium phosphide with nitrogen and arsenic [4, 5], which is associated with the unusual properties of these materials, as well as their great potential for various applications in optoelectronics and photonics. It was found [6] that when a small amount of nitrogen ($\sim 0.5\%$) is added to GaP, the band structure of the material becomes a direct bandgap, and the band gap energy decreases. The advantages of GaPN over GaP also include an improved ability to integrate with Si, since the lattice constant of this material with the addition of nitrogen decreases and can be closer to the lattice constant of silicon [7], which allows the growth of high-quality layers. It was shown in [8] that the additional introduction of arsenic allows one to obtain GaPNAs solid solutions, which are consistent in lattice parameter with Si in a wide range of band gap values (from 1.5 to 2.0 eV). Theoretically, it was shown [9] that the potentially achievable efficiency values of triple-junction solar cells based on lattice-matched GaPNAs (2 eV)/GaPNAs (1.5 eV)/Si heterostructures are 44.5% at AM 1.5D.

However, despite the advantages of dilute nitrides, the addition of nitrogen to the layers leads to the emergence of deep centers of non-radiative recombination, which leads to the need for further improvement of technology and the search for new approaches to the creation of materials based on GaPNAs solid solutions, lattice-matched with silicon, suitable for device applications. One

possible solution is to use a superlattice instead of a bulk material. It was shown in [10] that the use of a short-period GaAsSb/GaAsN superlattice led to an improvement in the crystalline and optical qualities of the material compared to the GaAsSbN solid solution.

In this study we investigated the effect of the substrate temperature during the epitaxial growth of structures with a bulk GaPN layer on the intensity of photoluminescence (PL) spectra, and also studied structures with GaPNAs/GaP and GaPNAs/GaPN superlattices grown by molecular beam epitaxy with a nitrogen plasma source at GaP substrates. We also carried out studies of the decay of photoluminescence intensity over time in the studied structures at room temperature, which allowed us to evaluate the influence of growth parameters and structure design on the lifetime of nonequilibrium charge carriers.

2. Experimental

The epitaxial structures studied were produced by molecular beam epitaxy with a nitrogen plasma source on GaP(100) substrates.

To study the effect of substrate temperature during epitaxial growth on the optical properties of the GaPN material, samples N1, N2, and N3 were prepared. In these samples, a GaP buffer layer with a thickness of 100 nm was grown on a GaP(100) substrate, then a GaPN layer with a thickness of 200 nm was grown with a nitrogen mole fraction of about 0.01 at substrate temperatures of 490, 470, and 505 °C, respectively, after which the structure was completed with a GaP layer with the thickness of 20 nm.

We also produced samples containing 12 periods of a superlattice consisting of GaPNAs/GaP layers in a GaP matrix (samples N4 and N5) and GaPNAs/GaPN in a GaPN matrix (samples N6 and N7) with thicknesses of 7 nm with a nitrogen mole fraction of about 0.01. The mole fraction of arsenic in the superlattice of samples N4 and N5 was 0.1 and 0.17, respectively, and the growth temperature was 510 °C. The mole fraction of arsenic in the superlattice of samples N6 and N7 was 0.2, and the growth temperature of the superlattice was 520 and 490 °C, respectively (the parameters of the studied samples are shown in Table 1).

These structures were studied by photoluminescence (PL) in the spectral range

Table 1. Growth parameters and obtained characteristics of samples

Material of light emitting area	Layer GaPN			Superlattice GaPNAs/GaP		Superlattice GaPNAs/GaPN	
	N 1	N 2	N 3	N 4	N 5	N 6	N 7
Sample							
As mole fraction	–	–	–	0.1	0.17	0.2	0.2
Epitaxial growth temperature, °C	490	470	505	510	510	520	490
α	1.8–1	1.8–1	1	1.15	1.1	1.2	1.6
$\tau_{1/e}$, ps	81	65	99	69	65	200	82

from 500 to 800 nm at room temperature. The structures were pumped by a He-Cd laser (wavelength 325 nm, continuous mode). When studying the evolution of the PL spectra of samples from the pump optical power, the latter was varied in the range of 0.05 – 3 mW using a neutral gradient filter installed in the path of the laser beam. The laser beam was focused using a lens at a normal angle of incidence, and the PL signal was collected using the same lens. To detect the PL signal passed through the AndorSolis monochromator (the grating contained 1200 lines/mm, the blaze angle was 500 nm), a silicon CCD matrix (Andor) was used.

The PL study with the time resolution was carried by the up-conversion method using a FOG-100-DX-IR device for differential fluorescence kinetics measurements in the visible range. Laser pulses with a duration of 120 fs, a frequency of 80 MHz, and a wavelength of 780 nm, generated by a tunable titanium-sapphire laser CoherentMira 900D with a maximum average power of 1.5 W were used for gating and pumping samples. The gating of the optical PL signal occurred due to its up-conversion with the laser pulse (i.e., the addition of photon energies) on a nonlinear BBO crystal (β -BaB₂O₄ or β -barium borate), which allowed us to obtain a time resolution of ~0.2 ps. To excite the PL of the samples, the pulse energy of a titanium-sapphire laser was doubled using a nonlinear BBO crystal. The optical up-conversion signal was detected in a continuous mode by a synchronous detection method using a monochromator and a photomultiplier.

3. Results and discussion

The PL spectra of heterostructures with a GaPN layer (N1, N2, and N3) at room temperature are shown in Fig. 1a. The composition of the ternary and quaternary solid solutions was

determined by X-ray diffraction analysis. The rocking curves for the symmetric reflection (004) of gallium phosphide for samples N1, N2, and N3 showed that the composition of the GaPN layer for the samples was the same and corresponded to a nitrogen mole fraction of about 0.01. The PL intensity increases sharply with increasing temperature of epitaxial growth of the GaPN layer and differed by more than 10 times from the sample with a growth temperature of 470 °C to sample N3 with a growth temperature of 505 °C. A further increase in the substrate temperature during epitaxial growth of the bulk GaPN layer led to the decomposition of the solid solution of the GaPN layer material into components with a larger and smaller fraction of nitrogen and a sharp decrease in the PL intensity.

The dependence of the PL intensity of structures with a bulk GaPN layer on the pump optical power density for three samples is shown in Fig. 1b. For sample N3 this dependence is well described by the dependence $IPL = \eta I \alpha$, where IPL – integrated PL intensity, I – the power density of the exciting laser, η – the coefficient. In sample N3, the α index was almost equal to unity over the entire range of studied powers, which indicated that the main recombination mechanism was radiative recombination. The dependence for samples N1 and N2 had two pronounced sections. In the region of low powers, the dependence had an exponent close to 2, which was associated with a significant contribution of nonradiative transitions. An increase in the power led to the linear behavior of the dependence, which was associated with saturation of nonradiative recombination in GaPN layers.

A mole fraction of nitrogen of 0.01 in the GaPN solid solution was not sufficient to obtain a lattice-matched material with silicon. An increase in the mole fraction of nitrogen in a GaPN

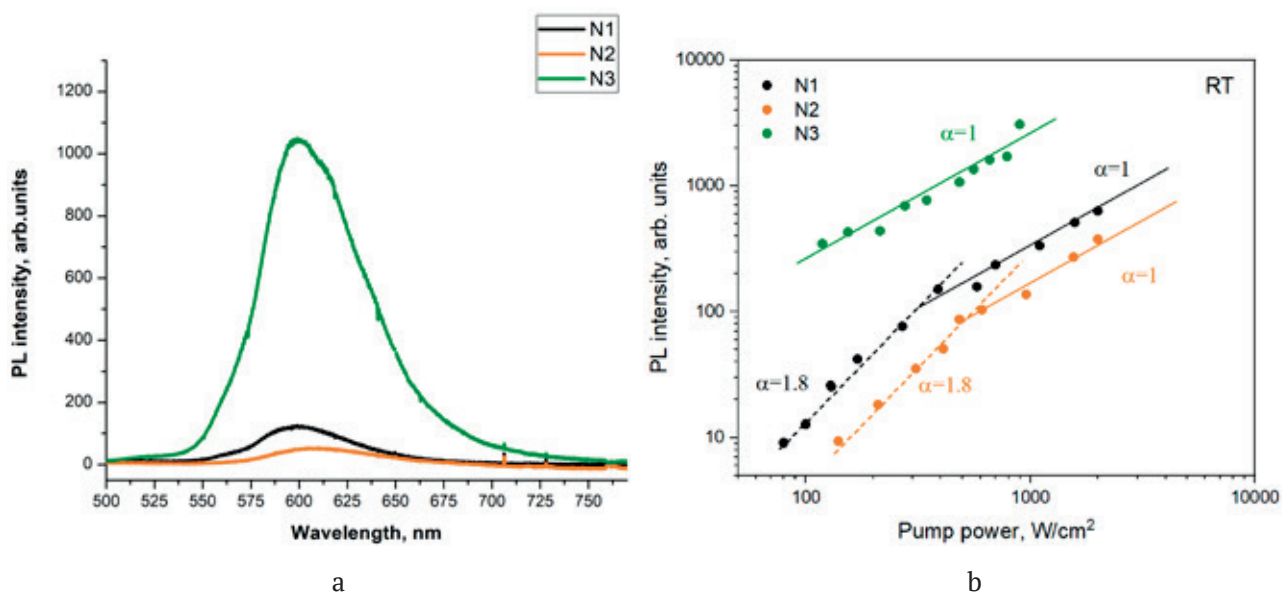


Fig. 1. PL spectra of structures with a bulk GaPN layer on a GaP substrate, obtained at room temperature at a pump optical power density of 800 W/cm²(a); dependence of the integrated PL intensity on the pump optical power density (b)

layer led to a sharp decrease in the PL intensity [11], which indicated an increasing density of nonradiative recombination centers and the impossibility of using this material as an active part of photoelectric converters.

One possible solution to this problem is the use of nanoscale superlattices. The photoluminescence spectra of samples with GaPNAs/GaP (samples N4 and N5) and GaPNAs/GaPN (samples

N6 and N7) superlattices at room temperature are shown in Fig. 2. The PL spectra of samples with superlattices showed a shift of the PL wave to longer wavelengths compared to samples with a bulk GaPN layer and an increase in the peak PL intensity. As we mentioned above, samples N4 and N5 with GaPNAs/GaP superlattices were grown under the same growth conditions with arsenic mole fractions of 0.1 and 0.17,

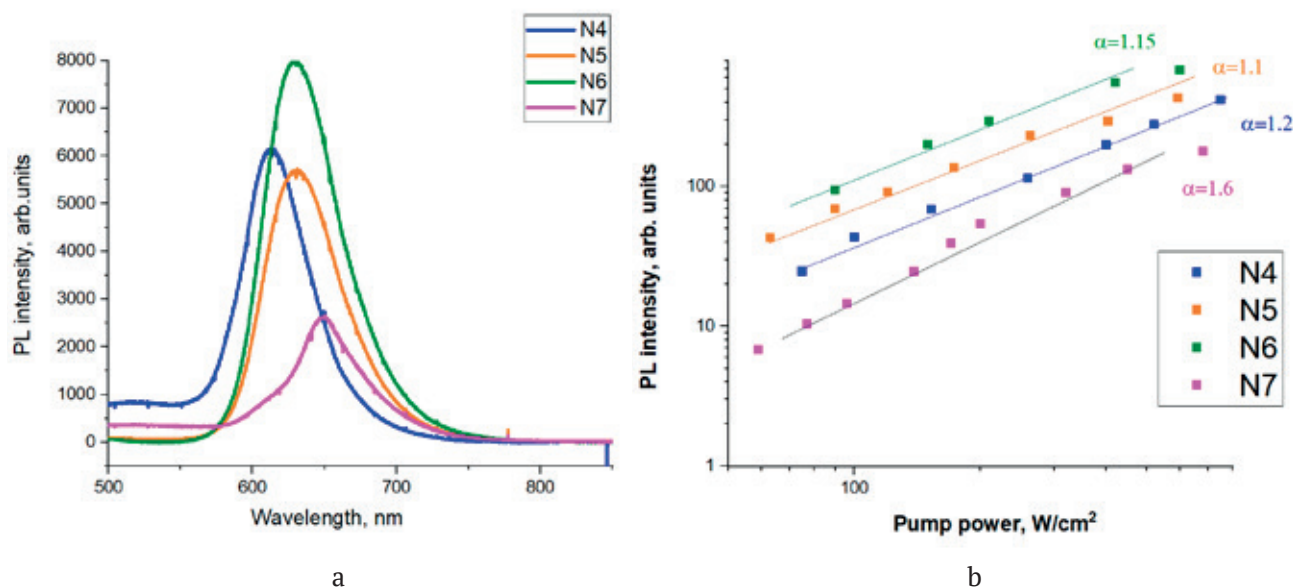


Fig. 2. PL spectra of structures with GaPNAs/GaP (samples N4 and N5) and GaPNAs/GaPN (samples N6 and N7) superlattices on a GaP substrate at room temperature with a pump optical power density of 600 W/cm²(A); dependence of the integrated PL intensity on the pump optical power density at room temperature (b)

respectively. With an increase in the mole fraction of arsenic in the superlattice, the PL intensity remained almost unchanged, and the wavelength of the maximum intensity of the PL band shifted from 615 to 630 nm. A further shift of the PL wave to longer wavelengths is possible when using GaPNAs/GaPN superlattices. Samples N6 and N7 with GaPNAs/GaPN superlattices were grown at the same arsenic and nitrogen flows (arsenic mole fraction 0.2, nitrogen mole fraction 0.01), but had different growth temperatures of the active region – 520 and 490 °C, respectively. The wavelength corresponding to the peak of the PL band of sample N6 coincided with the wavelength for sample N5 and is 630 nm, which indicated the re-evaporation of arsenic from the surface at elevated temperatures during epitaxial growth. A decrease in the growth temperature led to a significant increase in the wavelength of the PL peak intensity up to 650 nm, which indicated a greater incorporation of arsenic and nitrogen into the epitaxial layers, while the PL intensity decreased by approximately 3 times compared to a similar superlattice grown at 520 °C.

The dependence of the PL intensity of structures with GaPNAs/GaP and GaPNAs/GaPN superlattices at room temperature on the pump optical power density are shown in Fig. 2b. The comparison of the slopes of the dependences allowed us to estimate the contribution of nonradiative recombination and the defectiveness of the structures. It can be seen that for samples N4, N5, and N6 the dependence was well described by the relation $IPL = \eta I \alpha$ with the α index was almost equal to unity (1.1–1.2), which indicated that the main recombination mechanism is radiative recombination. In sample N7 with a GaPNAs/GaPN superlattice, recombination at defects predominated ($\alpha = 1.6$).

It was shown in [9] that the operating efficiency of multi-junction GaPNAs/Si solar cells is also strongly influenced by such an important material parameter as the lifetime of minority charge carriers. Therefore, we carried out studies of the photoluminescence kinetics of structures with a bulk GaPN layer and GaPNAs/GaP superlattices and GaPNAs/GaPN at room temperature. The dependence of the PL intensity decay on time for the light wavelength corresponding to the PL intensity peak is shown in Fig. 3.

Thus, the structures demonstrated a time evolution of the PL intensity that slightly deviated from a monoexponential decay. We estimated the characteristic times of decline in PL intensity based on $1/e$ level. The structures showed a similar PL decay time of about 100 ps, except sample N6. Sample N3 showed the longest lifetime among all the studied samples with a GaPN layer ~ 0.1 ns. The best lifetime for structures with superlattices was obtained for the GaPNAs/GaPN superlattice for sample N6 and amounted to ~ 0.2 ns.

The main parameters of the studied samples and the main obtained characteristics are shown in Table 1.

4. Conclusions

In this study the effect of epitaxial growth temperature on the optical properties of the GaPN material was investigated. It was shown that increasing the temperature up to 505 °C for bulk GaPN layers and 520 °C for GaPNAs/GaP(N) superlattices leads to a significant decrease in nonradiative recombination at defects, which leads to an increase in PL intensity and carrier lifetime. The use of GaPNAs/GaP and GaPNAs/GaPN superlattices allows changing the emission wavelength up to 650 nm.

Contribution of the authors

The authors contributed equally to this article.

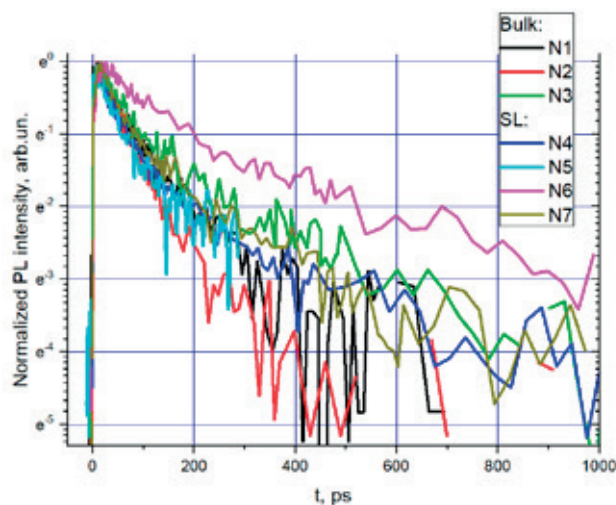


Fig. 3. Dependence of the decay of normalized PL intensity on time, obtained at room temperature

Conflict of interests

The authors declare that they have no known competing financial interests or personal relationships that could have influenced the work reported in this paper.

References

- Green M. A., Dunlop E. D., Siefert G., ... Hao X. Solar cell efficiency tables (Version 61) *Progress in Photovoltaics: Research and Applications*. 2023;31: 3–16. <https://doi.org/10.1002/pip.3646>
- Ang Zhou. *Analyse structurales de pseudo-substrats GaP/Si et d'hétérostructures CIGS/GaP/Si pour des applications photovoltaïques*. Matériaux. INSA de Rennes, 2019. Français. Available at: <https://theses.hal.science/tel-02924619/document>
- Greil J., Assali S., Isono Y., ... Haverkort J. E. M. Optical properties of strained wurtzite gallium phosphide nanowires. *Nano Letters*. 2016;16(6): 3703–3709. <https://doi.org/10.1021/acs.nanolett.6b01038>
- Kunert B., Volz K., Koch J., Stolz W. Direct-band-gap Ga(NAsP)-material system pseudomorphically grown on GaP substrate. *Applied Physics Letters*. 2006;88: 182108. <https://doi.org/10.1063/1.2200758>
- Ilahi S., Almosni S., Chouchane F., ... Cornet C. Optical absorption and thermal conductivity of GaAsPN absorbers grown on GaP in view of their use in multijunction solar cells. *Solar Energy Materials and Solar Cells*. 2015;141: 291. <https://doi.org/10.1016/j.solmat.2015.06.003>
- Shan W., Walukiewicz W., Yu K. M., ... Tu C. W. Nature of the fundamental band gap in GaN_xP_{1-x} alloys. *Applied Physics Letters*. 2000;76: 3251. <https://doi.org/10.1063/1.126597>
- Furukawa Y., Yonezu H., Morisaki Y., Moon S.-Y., Ishiji S., Wakahara A. Monolithic implementation of elemental devices for optoelectronic integrated circuit in lattice-matched Si/III–V–N alloy layers. *Japanese Journal of Applied Physics*. 2006;45(9L): L920. <https://doi.org/10.1143/jjap.45.L920>
- Geisz J. F., Friedman D. J. III–N–V semiconductors for solar photovoltaic applications. *Semiconductor Science and Technology*. 2002;17(8): 769–777. <https://doi.org/10.1088/0268-1242/17/8/305>
- Kudryashov D. A., Gudovskikh A. S., Nikitina E. V., Egorov A. Yu. Design of multijunction GaPNAs/Si heterostructure solar cells by computer simulation. *Semiconductors*. 2014;48(3): 381–386. <https://doi.org/10.1134/s1063782614030154>
- Gonzalo A., Utrilla A. D., Reyes D. F., ... Ulloa J. M. Strain-balanced type-II superlattices for efficient multi-junction solar cells. *Scientific Reports*. 2017;7: 4012. <https://doi.org/10.1038/s41598-017-04321-4>
- Henini M. *Dilute nitride semiconductors*. Elsevier; 2005. <https://doi.org/10.1016/B978-0-08-044502-1.X5000-8>

Information about the authors

Ekaterina V. Nikitina, Cand. Sci. (Phys.–Math.), Lead Researcher, Alferov University (Saint Petersburg, Russian Federation).

<https://orcid.org/0000-0002-6800-9218>

mail.nikitina@mail.ru

Maxim S. Sobolev, Cand. Sci. (Phys.–Math.), Head of the Laboratory, Alferov University (Saint Petersburg, Russian Federation).

<https://orcid.org/0000-0001-8629-2064>

sobolevsms@gmail.com

Evgeny V. Pirogov, Researcher, Alferov University (Saint Petersburg, Russian Federation).

<https://orcid.org/0000-0001-7186-3768>

zzzavr@gmail.com

Ivan S. Makhov, Cand. Sci. (Phys.–Math.), Research Fellow, HSE University (Saint Petersburg, Russian Federation).

<https://orcid.org/0000-0003-4527-1958>

imahov@hse.ru

Alexey M. Nadtochiy, Cand. Sci. (Phys.–Math.), Leading Researcher, HSE University (Saint Petersburg, Russian Federation).

<https://orcid.org/0000-0003-0982-907X>

anadtochiy@hse.ru

Elena I. Vasilkova, postgraduate student, Engineer, Alferov University (Saint Petersburg, Russian Federation).

<https://orcid.org/0000-0002-0349-7134>

elenvasilkov@gmail.com

Natalia V. Kryzhanovskaya, Dr. Sci. (Phys.–Math.), Head of the Laboratory, HSE University (Saint Petersburg, Russian Federation).

<https://orcid.org/0000-0002-4945-9803>

nkryzhanovskaya@hse.ru

Received 20.11.2023; approved after reviewing 30.11.2023 accepted for publication 08.12.2023; published online 01.10.2024.

Translated by Valentina Mittova

**Original articles**

Research article

<https://doi.org/10.17308/kcmf.2024.26/12225>**A molecular dynamics simulation of the release of desloratadine from alloys containing polyvinylpyrrolidone**Yu. A. Polkovnikova[✉], M. Belal, A. I. SlivkinVoronezh State University,
1 Universitetskaya pl., Voronezh 394018, Russian Federation**Abstract**

Computer modeling is currently a promising technique used in pharmaceutical technologies to develop drug compositions. Molecular dynamics has provided space and time resolutions unavailable during experiments and thus has greatly extended the capabilities of chemistry and some other areas. Molecular dynamics stimulations are very important for the development of solid drug dispersions. The purpose of this study is to simulate the molecular dynamics of the release of desloratadine from alloys containing polyvinylpyrrolidone-10000 into the dissolution medium.

The release of desloratadine from alloys containing polyvinylpyrrolidone-10000 was simulated by the method of molecular dynamics (Gromacs 2023 program, Amber 99 force field). The study involved calculating van der Waals energies of interaction between desloratadine and PVP and desloratadine and water and the proportion of desloratadine molecules that lost their bonds with PVP. The desloratadine molecule was considered released into water provided that it did not bind either to the polymer or water.

It was found that the degree of desloratadine release from PVP into the aqueous medium was the highest at a ratio of 1:1 (24.56±2.08%), and the lowest at ratios of 1:2 and 1:5 (8.27±1.79 and 8.65±0.98%, respectively). At a ratio of 1:1, the average energy of interaction between desloratadine with PVP per one molecule of desloratadine was the highest (−36.13±0.62 kJ/mol) when the energy of interaction between desloratadine and water was low (−52.03±0.82 kJ/mol), which indicates that desloratadine involvement in the solvation and desorption processes was the highest at this ratio. The average energy of interaction between desloratadine and the polymer was the lowest at a ratio of 1:5 (−52.03±0.82 kJ/mol) when the energy of interaction between desloratadine and water was −44.45±1.60 kJ/mol. This fact indicates a low intensity of the desorption and solvation processes at this ratio.

Keywords: release, desloratadine, polyvinylpyrrolidone, molecular dynamics**Funding:** The study was supported by Russian Science Foundation grant No. 24-25-20015, <https://rscf.ru/project/24-25-20015/>**For citation:** Polkovnikova Yu. A., Belal M., Slivkin A. I. A molecular dynamics simulation of the release of desloratadine from alloys containing polyvinylpyrrolidone. *Condensed Matter and Interphases*. 2024;26(3): 496–503. <https://doi.org/10.17308/kcmf.2024.26/12225>**Для цитирования:** Полковникова Ю. А., Белал М., Сливкин А. И. Моделирование процесса высвобождения дезлоратадина из сплавов с поливинилпирролидоном методом молекулярной динамики. *Конденсированные среды и межфазные границы*. 2024;26(3): 496–503. <https://doi.org/10.17308/kcmf.2024.26/12225>✉ Yulia A. Polkovnikova, e-mail: juli-polk@mail.ru

© Polkovnikova Yu. A., Belal M., Slivkin A. I., 2024



The content is available under Creative Commons Attribution 4.0 License.

1. Introduction

Currently, a large percentage of medicines on the pharmaceutical market (~ 40%) and medicines under development (~ 90%) are poorly soluble in water [1,2]. Substances poorly soluble in water include desloratadine, which has proven safe and effective non-sedative antihistamine activity that is useful for allergic rhinitis, allergic asthma, and urticaria [3, 4]. Several studies have attempted to improve desloratadine solubility by the formation of a complex inclusion of desloratadine with β -cyclodextrin in a solution [5].

The solubility and dissolution rate of medicines poorly soluble in water can be increased with solid dispersions [6, 7]. Solid dispersions with amorphous carriers usually exhibit higher solubility and dissolution rates due to the high energy of the amorphous phase of the medicine [8–10]. Among amorphous polymer carriers widely used in solid dispersion technologies are polyvinylpyrrolidone (PVP), polyvinylpyrrolidone vinyl acetate, and hydroxypropylmethylcellulose [11–13]. An analysis of scientific literature did not reveal information on the use of PVP as carrier polymers to prepare solid dispersions with desloratadine in order to increase its solubility in water during the development of semi-solid formulations.

The preparation and study of solid dispersions with PVP, including by the method of molecular dynamics, is a promising area of pharmaceutical technology. Molecular dynamics has significantly extended the capabilities of chemistry and some other areas by providing space and time resolutions unavailable during experiments [14]. Molecular modeling allows calculating the physical properties of the medicine/excipient without conducting costly experiments. Molecular modeling, which is important for optimizing formulations and predicting drug release profiles, can provide information about interactions between medicines and excipients, including their complexation. The understanding of these interactions allows researchers to develop optimal filler compositions to increase drug stability and bioavailability [15–17].

The purpose of the study is to simulate the molecular dynamics of the release of desloratadine from alloys containing polyvinylpyrrolidone-10000 (desloratadine

ratio: PEG-6000 1:1, 1:2, 1:5 by weight) into the dissolution medium.

2. Experimental

The release of desloratadine from alloys containing PVP-10000 was simulated by the method of molecular dynamics (Gromacs 2023 program [16,18], Amber 99 force field [19]). Desloratadine molecules and spatial structures of monomers were built in the HyperChem program [20]. The assembly of polymer chains and parametrization of the force field for the molecules of the components in the simulated systems was completed using the ParmEd program [21].

The simulated system included PVP molecules (Fig. 1) with a length of 90 monomers with a molar mass of 10.005 kDa (PVP), desloratadine molecules in the form of a cation, and Cl ions (Fig. 2).

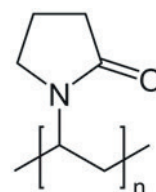


Fig. 1. Structure of the PVP molecule

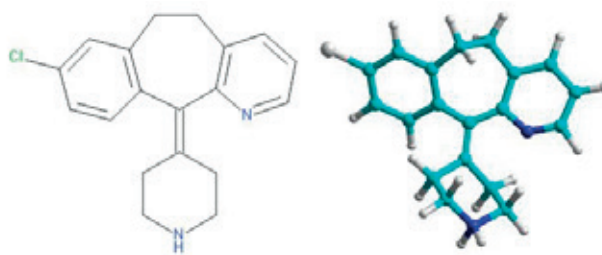


Fig. 2. Chemical structure and spatial structure of the desloratadine molecule

Models of desloratadine alloys containing PVP were built to study the release of desloratadine. Alloy models were prepared by a molecular dynamics simulation of desloratadine and PVP mixtures using periodic boundary conditions along all coordinate axes [16, 22–25]. The geometries of the systems were preliminarily optimized by the gradient method. Further, the molecular dynamics of desloratadine and PVP mixtures was simulated using thermostating (Berendsen thermostat) and barostatting (Berendsen barostat, 1 atm.) [13, 23] with a step of 2 fs for 25 ns.

The study involved calculating van der Waals energies of interaction between desloratadine and PVP and desloratadine and water and the proportion of desloratadine molecules that lost their bonds with PVP. The desloratadine molecule was considered released into water provided that it did not bind either to the polymer or water.

3. Results and discussion

The molecular compositions of the simulated systems are given in Table 1.

The desloratadine alloy with PEG-6000 was prepared with the ratios of 1:1, 1:2, and 1:5 by weight, since these ratios are the most widely used in the solid dispersion technology [11,12].

During the simulation, there was partial diffusion of desloratadine and PVP into water (Table 2). At a ratio of desloratadine and PVP of 1:1, some of the desloratadine molecules lost their bonds with the polymer and clustered, and some of the PVP molecules passed into the dissolution medium.

The graph (Fig. 3) shows that the van der Waals energies of interaction between desloratadine,

the polymer, and the solvent stabilized 20 ns after the beginning of the simulation.

Fig. 4 shows a graph of the dependence of the proportion of desloratadine molecules not bound to the polymer over time. During the first 5 ns of the simulation, over 30% of desloratadine molecules released into the aqueous medium.

The simulation of the release of desloratadine from PVP into water at a ratio of desloratadine to the carrier of 1:2 was accompanied by the formation of clusters and a partial transition of polymer molecules into the solvent (Table 3). During the molecular dynamics simulation, some of the desloratadine molecules released into the aqueous medium, and others retained their bonds with PVP and interacted with water which penetrated into the alloy.

The average energy of the van der Waals interaction between desloratadine and PVP was close to the average energy of the van der Waals interaction between desloratadine and water (Fig. 5).

Fig. 6 provides information on the number of desloratadine molecules not bound to PVP in

Table 1. Amounts of molecules of components of simulated systems

Substance	Desloratadine-PVP 1:1	Desloratadine-PVP 1:2	Desloratadine-PVP 1:5
Desloratadine cation	321	160	64
Cl ⁻ ion	321	160	64
PVP	10	10	10
Water	20264	20064	20960

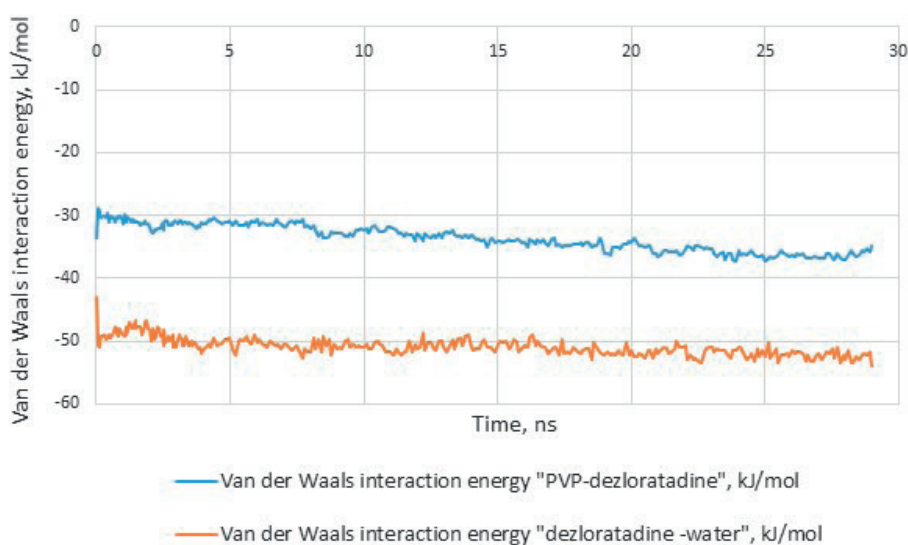


Fig. 3. Energy of van der Waals interaction of desloratadine with PVP and with water (desloratadine: PVP 1:1)

Table 2. Molecular dynamics simulation of the release of desloratadine from a 1:1 PVP alloy by mass into water

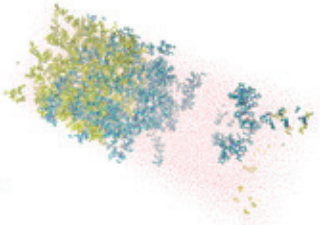
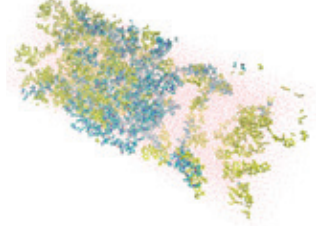
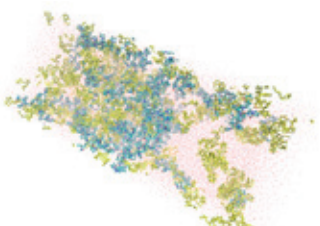
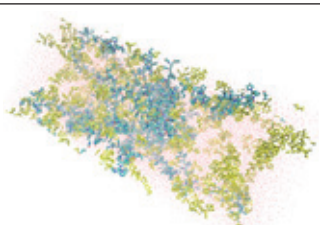
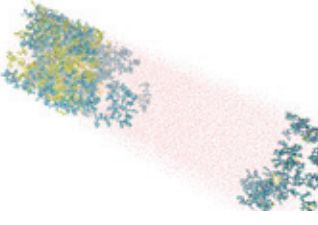
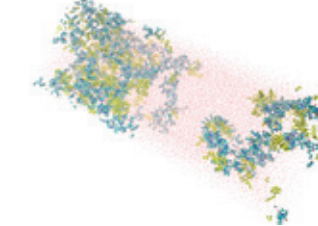
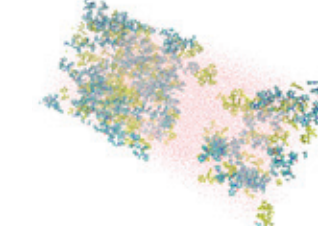
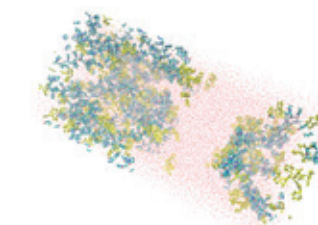
Time, ns	Structure
0	
9	
19	
29	

Table 3. Molecular dynamics simulation of the release of desloratadine from a 1:2 PVP alloy by mass into water

Time, ns	Structure
0	
9	
19	
29	

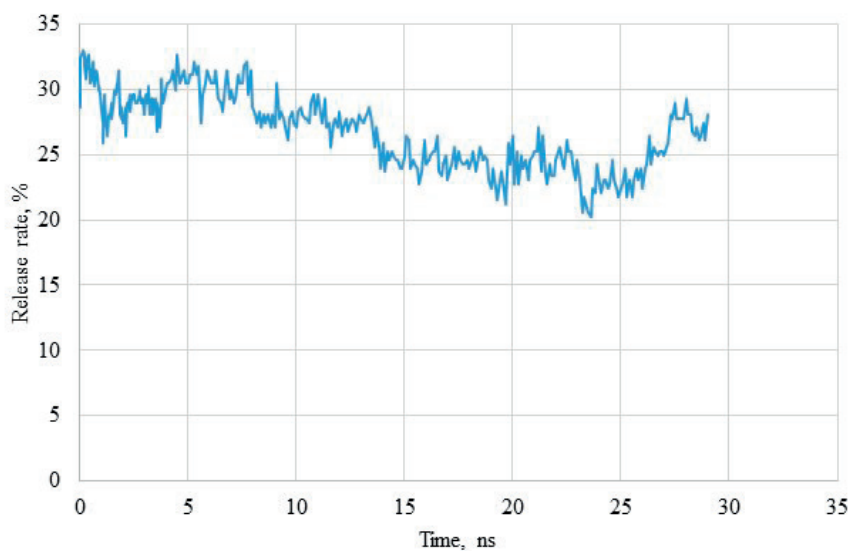


Fig. 4. Release rate of desloratadine (desloratadine: PVP 1:1)

water at a ratio of desloratadine to PVP of 1:2 by weight. It was found that during the first 25 ns of simulation, more than 12% of desloratadine molecules were released into the aqueous medium.

During the simulation of the release of desloratadine from PVP into water at a ratio of desloratadine to carrier of 1:5, a small number of individual desloratadine molecules were released from the polymer into the aqueous medium (Table 4).

The energy of the van der Waals interaction between desloratadine and PVP at a ratio of 1:5 stabilized 20 ns after the beginning of the simulation (Fig. 7).

Fig. 8 shows a graph of the dependence of the proportion of desloratadine molecules not bound

to the polymer over time. During the first 25 ns of the simulation, over 10 % of desloratadine molecules were released into the aqueous medium.

The average values for the parameters of the release of desloratadine from the studied PVP complexes are shown in Table 5. According to the results of the molecular dynamics simulation, it was found that the highest degree of desloratadine release from PVP into aqueous medium was achieved at a ratio of 1:1 ($24.56 \pm 2.08\%$), and the lowest at ratios of 1:2 and 1:5 ($8.27 \pm 1.79\%$ and $8.65 \pm 0.98\%$, respectively). The average energy of interaction between desloratadine and the polymer was the lowest at a ratio of 1:5 (-52.03 ± 0.82 kJ/mol), and the energy of

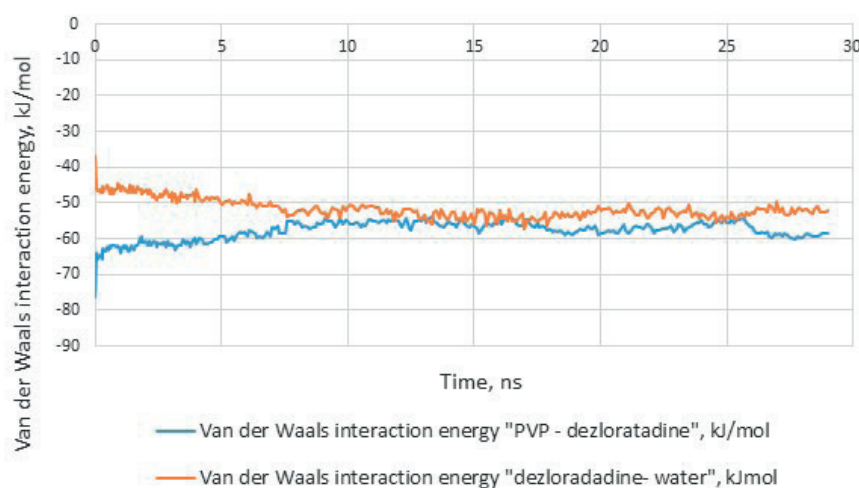


Fig. 5. Energy of van der Waals interaction of desloratadine with PVP and with water (desloratadine: PVP 1:2)

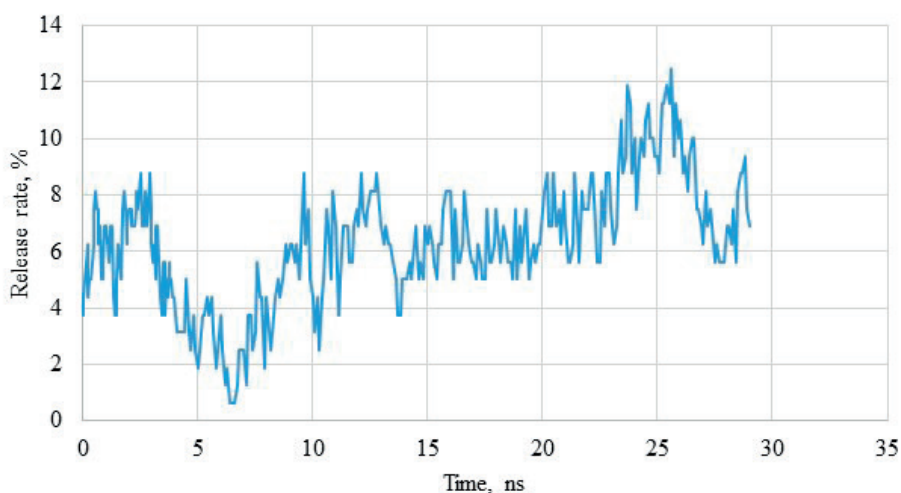
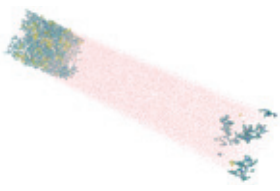
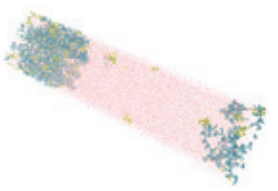
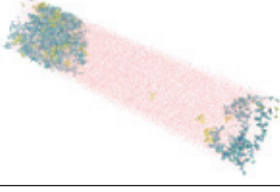
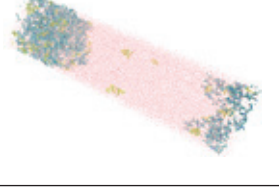


Fig. 6. Release rate of desloratadine (desloratadine: PVP 1:2)

Table 4. Molecular dynamics simulation of the release of desloratadine from a 1:5 PVP alloy by mass into water

Time, ns	Structure	Time, ns	Structure
0		19	
9		29	

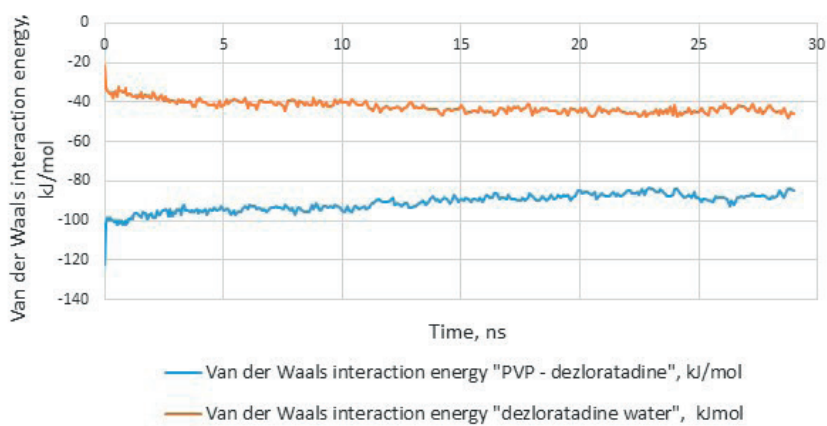


Fig. 7. Energy of van der Waals interaction of desloratadine with PVP and with water (desloratadine: PVP 1:5)

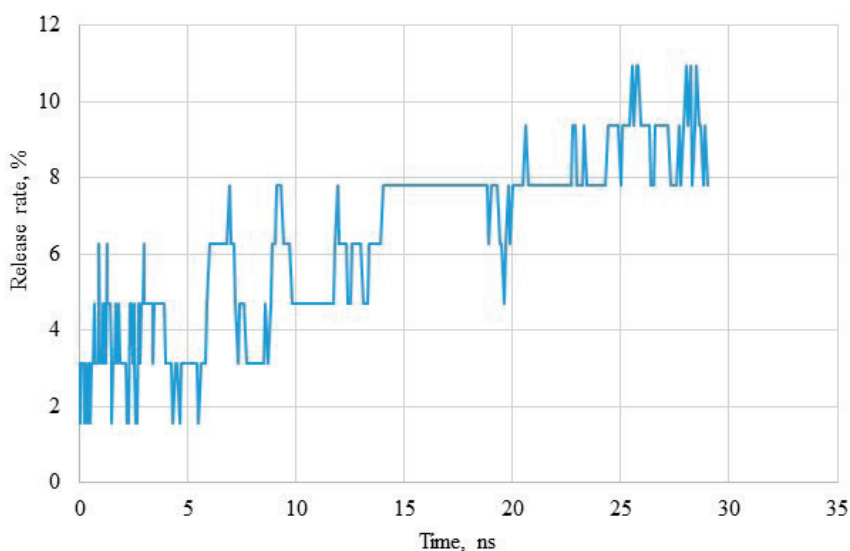


Fig. 8. Release rate of desloratadine (desloratadine: PVP 1:5)

Table 5. Average values of parameters for the release of desloratadine from the studied complexes with PVP

System	Average energy of van der Waals interaction of desloratadine with a polymer, kJ/mol	Average energy of van der Waals interaction of desloratadine with solvent, kJ/mol	Average release rate, %
Desloratadine-PVP 1:1	-36.13±0.62	-52.03±0.82	24.56±2.08
Desloratadine-PVP 1:2	-57.26±1.59	-52.63±1.14	8.27±1.79
Desloratadine-PVP 1:5	-87.07±1.86	-44.45±1.60	8.65±0.98

interaction between desloratadine and water was -44.45 ± 1.60 kJ/mol, which indicates a low intensity of the desorption and solvation processes at this ratio.

4. Conclusions

The conducted study of the release of desloratadine from PVP alloys by the method of molecular dynamics showed that the highest degree of desloratadine release from PVP into the aqueous medium was achieved at a ratio of 1:1, and the lowest at ratios of 1:2 and 1:5. At a ratio of 1:1, the average energy of interaction between desloratadine and PVP per one molecule of desloratadine was the highest (-36.13 ± 0.62 kJ/mol) when the energy of interaction between desloratadine and water was low (-52.03 ± 0.82 kJ/mol), which indicates that desloratadine involvement in the solvation and desorption processes was the highest at this ratio.

Contribution of the authors

The authors contributed equally to this article.

Conflict of interests

The authors declare that they have no known competing financial interests or personal relationships that could have influenced the work reported in this paper.

References

1. Babu N. J., Nangia A. Solubility advantage of amorphous drugs and pharmaceutical cocrystals. *Crystal Growth & Design*. 2011;11: 2662–2679. <https://doi.org/10.1021/cg200492w>
2. Benet L. Z., Broccatelli F., Oprea T. I. BDDCS applied to over 900 drugs. *The AAPS Journal*. 2011;13: 519–547. <https://doi.org/10.1208/s12248-011-9290-9>
3. Popović G., Čakar M., Agbaba D. Acid-base equilibria and solubility of loratadine and desloratadine in water and micellar media. *Journal of Pharmaceutical and Biomedical Analysis*. 2009;49: 42–47. <https://doi.org/10.1016/j.jpba.2008.09.043>
4. DuBuske L. M. Review of desloratadine for the treatment of allergic rhinitis, chronic idiopathic urticaria and allergic inflammatory disorders. *Expert Opinion on Pharmacotherapy*. 2005;6: 2511–2523. <https://doi.org/10.1517/14656566.6.14.2511>
5. Ali S. M., Upadhyay S. K., Maheshwari A. NMR spectroscopic study of the inclusion complex of desloratadine with β -cyclodextrin in solution. *Journal of Inclusion Phenomena and Macrocyclic Chemistry*. 2007;59: 351–355. <https://doi.org/10.1007/s10847-007-9335-y>
6. Ku M. S. Use of the biopharmaceutical classification system in early drug development. *The AAPS Journal*. 2008;10: 208–212. <https://doi.org/10.1208/s12248-008-9020-0>
7. Jatwani S., Rana A. C., Singh G., Aggarwal G. An overview on solubility enhancement techniques for poorly soluble drugs and solid dispersion as an eminent strategic approach. *ChemInform*. 2013;44(13). <https://doi.org/10.1002/chin.201313244>
8. Di L., Fish P. V., Mano T. Bridging solubility between drug discovery and development. *Drug Discovery Today*. 2012;17: 486–495. <https://doi.org/10.1016/j.drudis.2011.11.007>
9. Polkovnikova Yu. A. Study of the release of vinpocetine from solid dispersions with polyvinylpyrrolidone. *Russian Journal of Biopharmaceuticals*. 2021;13(4): 29–32. (In Russ.). <https://doi.org/10.30906/2073-8099-2021-13-4-3-6>
10. Nair A. R., Lakshman Y. D., Anand V. S. K., Sree K. S. N., Bhat K., Dengale S. J. Overview of extensively employed polymeric carriers in solid dispersion technology. *AAPS PharmSciTech*. 2020;21(8): 309. <https://doi.org/10.1208/s12249-020-01849-z>
11. Krasnyuk (Jr.) I. I., Belyatskaya A. V., Krasnyuk I. I., ... Odintsova E. B. Prospects for using solid polyvinylpyrrolidone dispersions in medicine and pharmacy. *Pharmacy*. 2016;6: 7–11. (In Russ.). Available at: <https://www.elibrary.ru/item.asp?id=26603689>
12. Belyatskaya A. V., Krasnyuk (Jr.) I. I., Elagina A. O., ... Kannieva D.R. The study of the solubility of furazolidone from solid dispersions with

polyvinylpyrrolidone. *Moscow University Chemistry Bulletin*. 2020;61(1): 52–56. (In Russ.). Available at: <https://www.chem.msu.ru/rus/vmgu/201/52.pdf>

13. Polkovnikova Yu. A. Simulation of the release process of vinpocetine from an alloy with β -cyclodextrin. *Russian Journal of Biopharmaceuticals*. 2022;14(6): 16–20. (In Russ.). <https://doi.org/10.30906/2073-8099-2022-14-6-16-20>

14. Eastman P., Swails J., Chodera J. D., Pande V. S. OpenMM 7: Rapid development of high performance algorithms for molecular dynamics. *PLoS Computational Biology*. 2017;13: 1–17. <https://doi.org/10.1371/journal.pcbi.1005659>

15. Walden D. M., Bunday Y., Jagarapu A., Antontsev V., Chakravarty K., Varshney J. Molecular simulation and statistical learning methods toward predicting drug-polymer amorphous solid dispersion miscibility, stability, and formulation design. *Molecules*. 2021;26(1): 182. <https://doi.org/10.3390/molecules26010182>

16. Polkovnikova Yu. A., Glushko A. A., Slivkin A. I. Molecular dynamics modeling of the release of aminophenylbutyric acid from sodium alginate. *Vestnik of the Smolensk State Medical Academy*. 2023;22(3): 152–157. (In Russ.). <https://doi.org/10.37903/vsgma.2023.3.20>

17. Chan T., Ouyang D. Investigating the molecular dissolution process of binary solid dispersions by molecular dynamics simulations. *Asian Journal of Pharmaceutical Sciences*. 2018;13(3): 248–254. <https://doi.org/10.1016/j.ajps.2017.07.011>

18. Abraham M. J., Murtola T., Schulz R., ... Lindahl E. GROMACS: High performance molecular simulations through multi-level parallelism from laptops to supercomputers. *SoftwareX*. 2015;1–2: 19–25. <https://doi.org/10.1016/j.softx.2015.06.001>

19. Sorin E. J., Pande V. S. Exploring the helix-coil transition via all-atom equilibrium ensemble simulations. *Biophysical Journal*. 2005;88(4): 2472–2493. <https://doi.org/10.1529/biophysj.104.051938>

20. Teppen J. B. HyperChem, release 2: molecular modeling for the personal computer. *Journal of Chemical Information and Computer Sciences*. 1992;32: 757–759. <https://doi.org/10.1021/ci00010a025>

21. Shirts M. R., Klein C., Swails J. M., ... Zhong E. D. Lessons learned from comparing molecular dynamics engines on the SAMPL5 dataset. *Journal of Computer-Aided Molecular Design*. 2017;31: 147–161. <https://doi.org/10.1007/s10822-016-9977-1>

22. Bekker H. E., Dijkstra J., Renardus M. K. R., Berendsen H. J. C. An efficient, box shape independent non-bonded force and virial algorithm for molecular dynamics. *Molecular Simulation*. 1995;14: 137–152. <https://doi.org/10.1080/08927029508022012>

23. Berendsen H. J. C., Postma J. P. M., van Gunsteren W. F., Di Nola A., Haak J. R. Molecular dynamics with coupling to an external bath. *The Journal of Chemical Physics*. 1984;81(8): 3684–3690. <https://doi.org/10.1063/1.448118>

24. Braga C., Travis K. P. A configurational temperature Nosé-Hoover thermostat. *The Journal of Chemical Physics*. 2005;123(13): 134101. <https://doi.org/10.1063/1.2013227>

25. Parrinello M., Rahman A. Polymorphic transitions in single crystals: A new molecular dynamics method. *Journal of Applied Physics*. 1981;52: 7182–7190. <https://doi.org/10.1063/1.328693>

26. Polkovnikova Yu. A., Slivkin A. I., Glushko A. A. Simulation of the molecular dynamics of the release of gamma-aminobutyric acid from gelatin. *Bulletin of Voronezh State University. Series: Chemistry. Biology. Pharmacy*. 2023;2: 110–116. Available at: <https://www.elibrary.ru/item.asp?id=54070189>

Information about the authors

Yulia A. Polkovnikova, Dr. Sci. (Pharmacy), Associate Professor, Associate Professor at the Department of Pharmaceutical Technology and Pharmaceutical Chemistry, Faculty of Pharmacy, Voronezh State University (Voronezh, Russian Federation).

<https://orcid.org/0000-0003-0123-9526>
juli-polk@mail.ru

Mohamed Belal, resident Faculty of Pharmacy, Voronezh State University (Voronezh, Russian Federation).

<https://orcid.org/0009-0004-7830-8942>
m.blal1996@gmail.com

Alexey I. Slivkin, Dr. Sci. (Pharmacy), Professor, Head of the Department of Pharmaceutical Chemistry and Pharmaceutical Technology, Faculty of Pharmacy, Voronezh State University (Voronezh, Russian Federation).

<https://orcid.org/0000-0001-6934-0837>
slivkin@pharm.vsu.ru

Received 15.04.2024; approved after reviewing 06.06.2024; accepted for publication 17.06.2024; published online 01.10.2024.

Translated by Irina Charychanskaya



Condensed Matter and Interphases

Kondensirovannye Sredy i Mezhfaznye Granitsy
<https://journals.vsu.ru/kcmf/>

Original articles

Research article

<https://doi.org/10.17308/kcmf.2024.26/12226>

Preparation and properties of conversion phosphate-containing coatings on magnesium alloys doped with rare earth elements

A. V. Pospelov¹✉, A. A. Kasach², A. R. Tsyganov¹, I. I. Kurilo¹

¹Belarusian State Technological University, Department of Physical, Colloid, and Analytical Chemistry, 13a Sverdlova ul., Minsk 220006, Republic of Belarus

²Belarusian State Technological University, Department of Chemistry, Technology of Electrochemical Production and Electronic Engineering Materials, 13a Sverdlova ul., Minsk 220006, Republic of Belarus

Abstract

The purpose of our study was to synthesize and analyze the structure, qualitative and quantitative composition, and protective properties of phosphate-containing conversion coatings on WE43, ZRE1, and QE22 magnesium alloys doped with rare earth elements in the Hank's Balanced Salt Solution.

Scanning electron microscopy, energy dispersive X-ray analysis, and X-ray phase analysis methods were used to study the morphology, microstructure, the elemental and phase compositions of QE22, ZRE1, and WE43 magnesium alloys doped with rare earth elements, as well as conversion coatings formed on their surface during phosphating. Linear voltammetry and electrochemical impedance spectroscopy were used to study the kinetic properties of corrosion of the analyzed samples in the Hank's Balanced Salt Solution (pH = 7.4) imitating the human body environment before and after phosphating.

The study showed that the phosphating of magnesium alloys doped with rare earth elements results in the formation of low-soluble fine-grained coatings with a pronounced crystal structure and a thickness from 16 to 21 μm. The obtained conversion coatings are characterized by the following elemental composition: Ca ≈ 40 wt.%; P ≈ 15 wt.%; and O ≈ 35 wt.%. The crystal structure of phosphate-containing coatings is presented by the brushite phase (CaHPO₄·2H₂O).

The electrochemical studies of the corrosion behavior of magnesium alloys in the model Hank's Balanced Salt Solution (pH = 7.4) demonstrated that the corrosion current density decreases in the sequence QE22, ZRE1, WE43 and is i_{corr} , A/cm²: 5.2·10⁻⁵; 2.5·10⁻⁵; 2.0·10⁻⁵. The obtained conversion coatings based on brushite reduce the corrosion rate of QE22, ZRE1, and WE43 magnesium alloys by 15.2, 7.8, and 6.3 times, respectively.

Keywords: Magnesium, Rare earth elements, Conversion coating, Brushite, Corrosion

Funding: The study was funded by the Ministry of Education of the Republic of Belarus as part of the State Research Program “Mechanics, metallurgy, and diagnostics in machinery construction” (2021–2023), subprogram “Electroplating”, order No. 4.08: “Obtaining implant materials based on titanium alloys and biodegradable magnesium alloys with enhanced anticorrosive and biocidal properties” (state registration No. 20212333).

Acknowledgements: studies using scanning electron microscopy were carried out using the equipment of the Centre for Physico-Chemical Research Methods of the Belarusian State Technological University.

For citation: Pospelau A. V., Kasach A. A., Tsyganov A. R., Kurilo I. I. Preparation and properties of conversion phosphate-containing coatings on magnesium alloys doped with rare earth elements. *Condensed Matter and Interphases*. 2024;26(3): 504–517. <https://doi.org/10.17308/kcmf.2024.26/12226>

Для цитирования: Пospelov A.В., Касач А.А., Цыганов А.Р., Курило И.И. Получение и свойства конверсионных фосфатсодержащих покрытий на легированных редкоземельными элементами сплавах магния. *Конденсированные среды и межфазные границы*. 2024; 26(3): 504–517. <https://doi.org/10.17308/kcmf.2024.26/12226>

✉ Andrei V. Pospelau, e-mail: andrei29088@mail.ru

© Pospelau A. V., Kasach A. A., Tsyganov A. R., Kurilo I. I., 2024



The content is available under Creative Commons Attribution 4.0 License.

1. Introduction

Lately, a lot of attention has been paid to biodegradable magnesium alloys in medical applications [1,2]. Construction materials based on magnesium and its alloys have low density, which is close to the density of human bones, and are compatible with the human body [3]. Magnesium is an active metal, so its corrosion in aqueous environments is accompanied by the release of large amounts of hydrogen. Due to abrupt and inhomogeneous corrosion in living organisms, magnesium has limited applications in the production of orthopedic implants. To enhance the mechanical properties and corrosion resistance, magnesium is alloyed with other metals (Zn, Al, Mn, Nd, Ce, Y, Ca, etc.) [4,5]. However, at higher concentrations of alloying additives, especially Al, Zn, and rare earth elements (REE), the corrosion resistance and biocompatibility of magnesium alloys can decrease, and the corrosion products can become more toxic [6–8].

Various physical (laser treatment, magnetron sputtering, intensive plastic deformation) [12–14], chemical (conversion coatings) [15–20], and electrochemical (plasma electrolytic oxidation, electrophoretic deposition) [21–25] methods of surface treatment, as well as biopolymer based coatings [9–11] are used to increase the corrosion resistance and biocompatibility of magnesium alloys. These methods include chemical deposition of conversion coatings, which is the easiest and the most available method that can be used for the treatment of items with complex geometry. Chemical treatment allows obtaining conversion coatings based on magnesium fluorides [16, 17, 26], zinc phosphates [27, 28], strontium [18], magnesium [28, 29], and calcium [15, 28, 30–32].

Obtaining conversion coatings based on magnesium fluorides is environmentally hazardous, because it involves using 20–40% solution of HF, whose vapors cause irritation of the respiratory system, eyes, and skin. In terms of the environment and economy, the most practical method of obtaining conversion coatings is based on phosphates of bioactive materials (Ca, Mg, Zn). Materials based on dicalcium phosphate-dihydrate corresponding to the crystal structure of brushite, are not toxic, have a high biocompatibility, demonstrate osteoconductive

properties, and can be integrated into the bone matrix during bone remodeling, which facilitates the osseointegration of implants [33, 34]. The protective properties of conversion coatings based on $\text{CaHPO}_4 \cdot 2\text{H}_2\text{O}$ depend on the microstructure and porosity. Conversion coatings with the highest density and anticorrosive properties are formed, when the pH of the phosphating agent is ≈ 2.8 – 3.5 and the temperature is 37 – 70 °C [15, 35–38]. The synthesis and the protective properties of this type of conversion coatings are well-studied for pure magnesium [15,38] and alloys based on Mg-Al-Zn (AZ series) [28, 30–32, 35–37]. These coatings can reduce the corrosion rate of magnesium alloys doped with aluminum and zinc in model biological environments by 62 times [28]. It is known, however, that aluminum has adverse effect on neurons [39] and osteoblasts [40], and is associated with dementia and Alzheimer's disease [39]. Magnesium alloys containing rare earth elements (REE) are of a significant interest for basic and applied research aimed at synthesizing biodegradable materials. These alloys have good strength and biocompatibility. Modification of the surface of these alloys with brushite based conversion coatings increases their corrosion resistance in the human body and reduces cytotoxicity of the surface of implants.

The purpose of our study was to synthesize and analyze the structure, qualitative and quantitative composition, and protective properties of phosphate-containing conversion coatings on WE43, ZRE1, and QE22 magnesium alloys doped with rare earth elements in the Hank's Balanced Salt Solution.

2. Experimental

In our experiments we used samples of QE22, ZRE1, and WE43 magnesium alloys whose nominal compositions are presented in Table 1.

The samples were cut into $30 \times 20 \times 5$ mm³ pieces, which were then polished with sandpaper (P1000 and P2000) in 96% ethanol.

To obtain phosphate-containing conversion coatings, we used a solution with the following composition, mol/dm³: $\text{Ca}(\text{NO}_3)_2$ – 0.2; H_3PO_4 – 0.3. The pH of the solution was raised to 3.0 ± 0.1 by adding 3 M of a NaOH solution. The coatings were deposited for 60 minutes at a temperature of 70 ± 2 °C.

Table 1. Elemental composition of the studied magnesium alloys

Content in alloy, wt.%							
Alloy ZRE1							
Zn	P3Э	Zr	Si	Cu	Mn	Ni	Mg
2.7	3.18	0.53	0.01	0.01	0.2	0.001	balance
Alloy QE22							
Ag	Nd	Zr	Cu	Ni	Mg		
2.0–3.0	1.7–2.5	0.4–1.0	0.1	0.01	balance		
Alloy WE43							
Y	Nd	P3Э	Zr	Mg			
3.7	3.2	0.96	0.51	balance			

The morphology and microstructure of the surface of the obtained coatings were studied using a JSM-5610 LV scanning electron microscope (Jeol), with an EDX JED-2201 energy-dispersive X-ray spectrometer (Jeol Ltd.). The phase composition of the analyzed samples was determined using a D8 Advance X-ray diffractometer (Bruker AXS). The cathode material was Cu ($K\alpha$ -1.5406 Å). The diffraction patterns were recorded in the range of 2θ from 5 to 80° with the scanning step of 0.05 °/s. The phases were identified using Match software based on the location and the relative intensity of the registered peaks using the COD (Crystallography Open Database) reference base.

The corrosion behavior of the samples of magnesium alloys was studied in the Hank's Balanced Salt Solution of the following composition, g/dm³: NaCl – 8; KCl – 0.2; CaCl₂ – 0.14; MgSO₄·7H₂O – 0.1; MgCl₂·7H₂O – 0.10; Na₂HPO₄·2H₂O – 0.06; KH₂PO₄ – 0.06; NaHCO₃ – 0.35; pH – 7.4.

The electrochemical studies were carried out using an Autolab PGSTAT 302N potentiostat/galvanostat with an FRA 32N impedance spectroscopy unit in a three-electrode cell with the working electrode placed on the side. The geometric area of the working electrode was 1 cm². The reference electrode was a saturated silver chloride, the counter electrode was a platinum electrode. The stationary potential was established over 30 min. The potentiodynamic polarization curves were registered in the potential range from –200 mV to +200 mV with regard to the stationary potential at a linear potential sweep rate of 1 mV/s. The impedance spectra were measured at a stationary potential

in the frequency range from 10⁵ to 10^{–2} Hz. The stabilization of the stationary potential took 30 min. The analysis of the spectra, the selection of the equivalent circuit, and the calculation of the parameters and their elements were performed using ZView. All electrochemical studies were carried out at least three times.

3. Results and discussion

Fig. 1 presents SEM images of the surface of magnesium alloys without (Fig. 1a–c) and with (Fig. 1d–f) conversion coatings. The structures of QE22 (Fig. 1a), ZRE1 (Fig. 1b), and WE43 (Fig. 1c) alloys include regions characteristic for intermetallic particles. Table 2 presents the results of the EDX point analysis of the surface of the initial samples. They demonstrate that the QE22 alloy consists of a magnesium matrix and intermetallic particles enriched in neodymium (27.3 wt.%), silver (8.5 wt.%), and an insignificant amount of zirconium (0.4 wt.%). The intermetallic particles of the ZRE1 alloy contain mainly zinc (19.1 wt.%) and cerium (9.9 wt.%). The magnesium matrix of the WE43 alloy contains up to 5.6 wt.% of neodymium, whose presence can be accounted for by the thermal treatment of the alloy during the preparation process. As compared to other alloys, WE43 is characterized by smaller intermetallic particles whose width and length vary from 10 to 70 μm. The intermetallic particles of this alloy contain ≈ 20 wt.% of neodymium, ≈ 4.5 wt.% of yttrium, ≈ 1 wt.% of praseodymium, and ≈ 0.5 wt.% of cerium (Table 2).

The chemical treatment of the samples of magnesium alloys results in the formation of granular and rough coatings on their surface

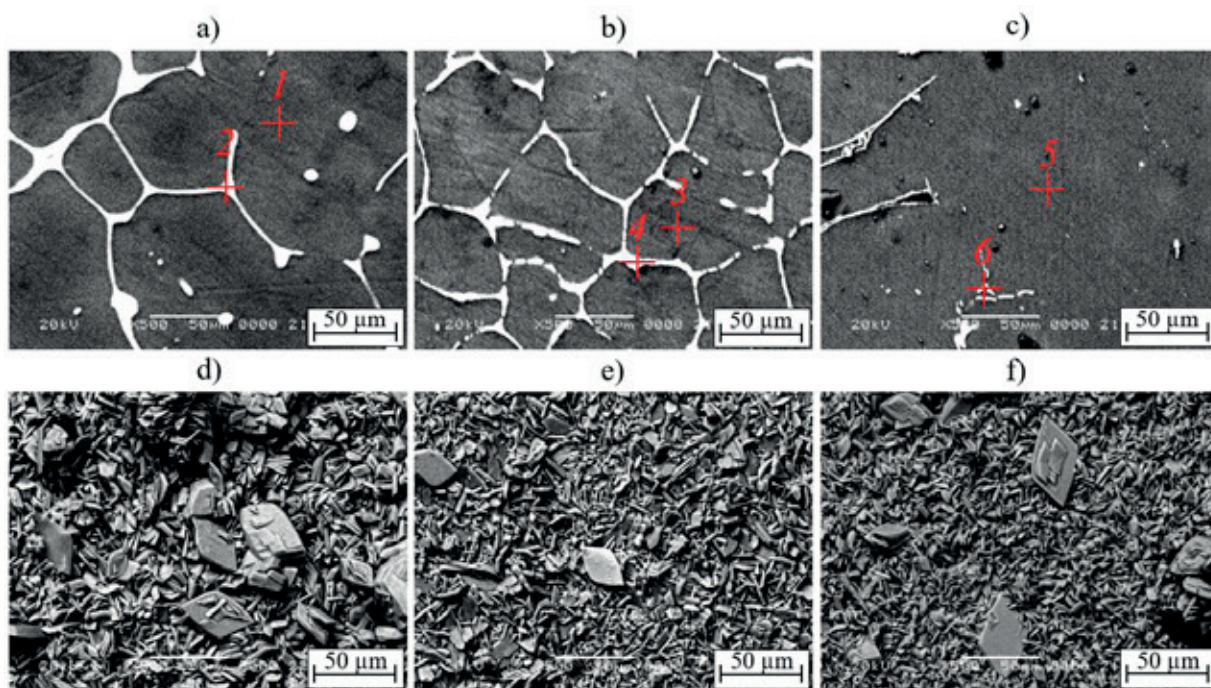


Fig. 1. SEM images of the surface of magnesium alloys without (Fig. 1a–c) and with (Fig. 1d–f) conversion coatings. Alloy: a, d – QE22; b, e – ZRE1; c, f – WE43

Table 2. Results of the point elemental analysis of the initial magnesium alloy samples (the analyzed regions are denoted in Fig. 1)

Number point	Content, wt.%								
	Mg	Zr	Ag	Nd	Zn	Pr	Ce	La	Y
1	100.0	–	–	–	–	–	–	–	–
2	63.8	0.4	8.5	27.3	–	–	–	–	–
3	100.0	–	–	–	–	–	–	–	–
4	63.1	1.3	–	1.8	19.1	0.8	9.9	4.1	–
5	94.4	–	–	5.6	–	–	–	–	–
6	71.4	–	–	21.1	–	1.3	0.6	–	4.6

(Fig. 1e–f). The obtained data demonstrates that conversion coatings on the QE22 alloy have the most inhomogeneous structure (Fig. 1e). This can be explained by the presence of silver, which has a low reactivity.

The obtained conversion coatings consist mainly of calcium, phosphorus, and oxygen, which indicates the formation of phosphate-containing films. Table 3 presents the results of the EDX analysis of the surface of the samples with conversion coatings.

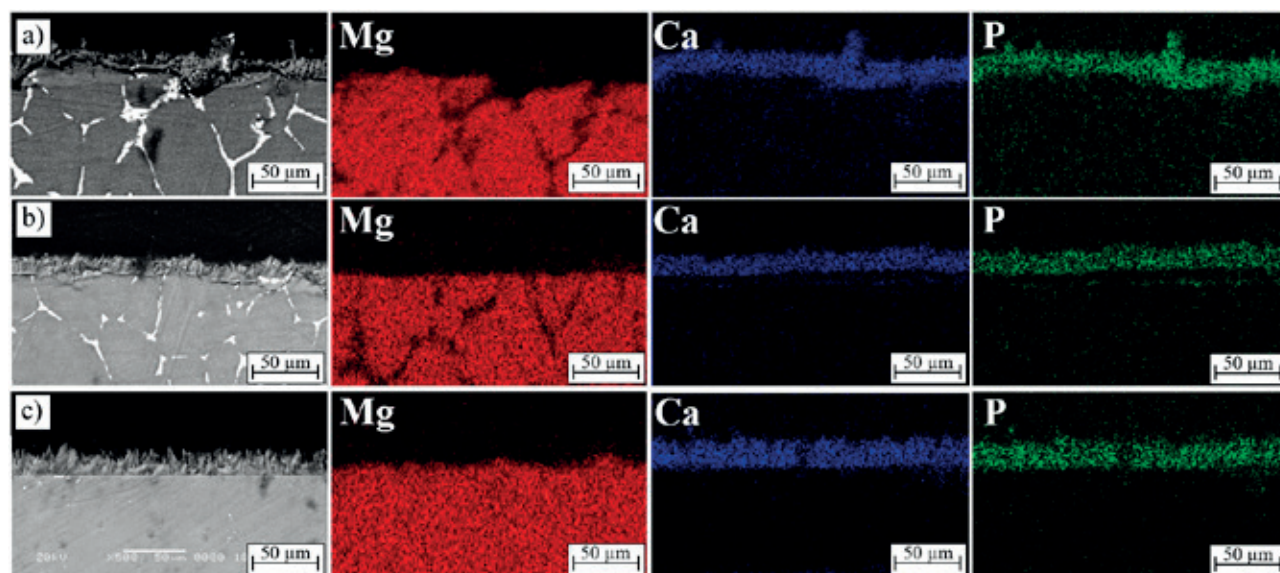
Fig. 2 demonstrates the SEM images and elemental mapping of sections of the studied samples after phosphate conversion coating. They show that the thickness of the conversion coatings on the surface of the studied alloys varies

from 16 to 21 μm. The coatings consist of calcium and phosphorus.

The coating on the surface of the QE22 alloy is more inhomogeneous and has microcracks (Fig. 2a). The formation of an inhomogeneous coating with a large number of defects (microcracks) on the surface of QE22 can be explained by the presence of intermetallic particles with a high concentration of silver of up to 8.5 wt.% (Table 2). The increased defectiveness of the obtained coating can be explained by the fact that silver, as compared to magnesium, has a significantly higher standard electrode potential and is chemically stable in acidic environments without oxidizers (including in H₃PO₄ solutions). Therefore, during the formation of conversion

Table 3. Elemental composition of the phosphated magnesium alloys

Alloy	Content, wt.%								
	O	P	Ca	Y	Zn	Zr	La	Ce	Nd
QE22	35.3	15.5	45.1	–	–	4.1	–	–	–
ZRE1	38.3	15.1	40.8	–	1.3	2.4	0.9	1.2	–
WE43	36.4	13.8	40.9	1.5	–	4.0	1.4	0.9	1.1

**Fig. 2.** SEM images and elemental mapping of sections of the studied samples after phosphate conversion coating. Alloy: a – QE22; b – ZRE1; c – WE43

coatings, regions with high concentrations of silver act as cathodes. The reduction of the depolarizer (hydrogen) takes place on their surface. Magnesium ionization takes place in the regions adjacent to silver-containing intermetallic particles.

An increased rate of the local dissolution of the magnesium matrix around the cathode particles (phase $Mg_{12}Nd_2Ag$) and the resulting intensification of hydrogen evolution on intermetallic particles lead to the formation of loose phosphate-containing coatings with a significant number of structural defects (Fig. 2a). The formed conversion coatings limit contacts between the corrosive environment and the metal substrate thus reducing the corrosion rate of the QE22 alloy. However, the presence of defects around the cathode intermetallic particles results in underfilm corrosion and delamination of the coating.

Using X-ray diffraction, we determined the phase composition of the studied samples

(Fig. 3). Rare earth elements are known to have low solubility in magnesium. Therefore, their crystallization is accompanied by the formation of separate phases, which enhance the strength characteristics of the alloy [41, 42]. According to the obtained data (Fig. 3a, b), $Mg_{12}Nd_2Ag$ and $(Mg, Zn)_{12}$ intermetallic particles are formed in the compositions of QE22 and ZRE1 alloys respectively, which agrees well with the literature data [41, 42]. The diffraction patterns of the WE43 alloy did not show any intense peaks characteristic for $Mg_{12}Nd$ and $Mg_{12}Nd_2Y$. The diffraction peaks of the α -Mg phase for WE43 (Fig. 3c) are shifted towards smaller angles 2θ as compared to the diffraction peaks of α -Mg for QE22 and ZRE1. This shift indicates an increase in the interplanar distance due to the inclusion of Nd atoms in the crystal lattice of magnesium and the formation of a solid substitution solution, which is confirmed by the results of the EDX analysis.

The diffraction patterns of all the studied alloys with conversion coatings demonstrated

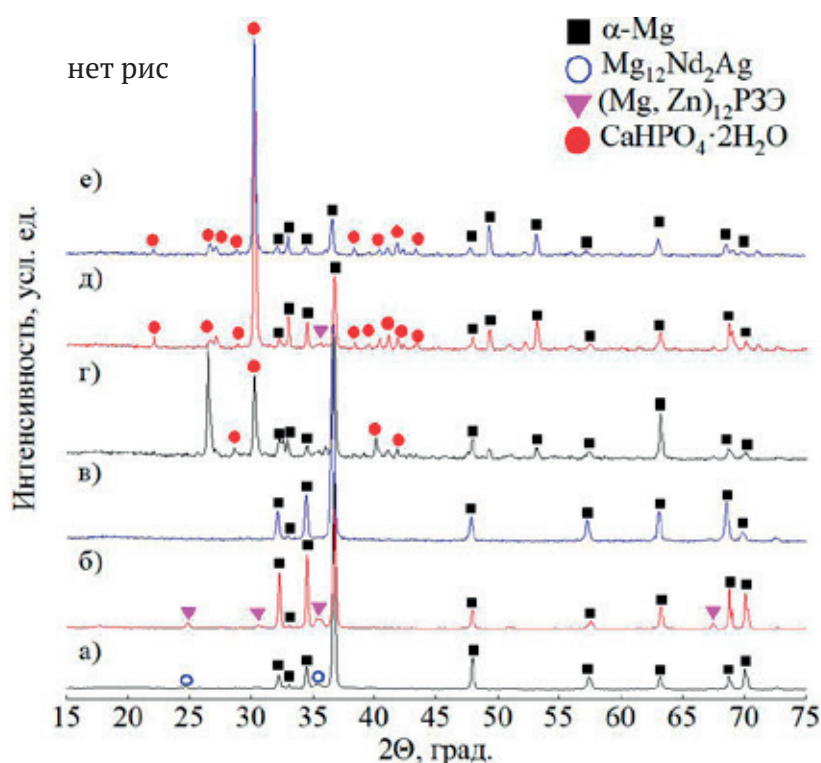
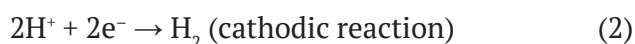


Fig. 3. Diffraction patterns of the surface of magnesium alloys without (Fig. 1a–c) and with (Fig. 1d–f) conversion coatings. Alloy: a, d – QE22; b, e – ZRE1; c, f – WE43

peaks corresponding to the $\text{CaHPO}_4 \cdot 2\text{H}_2\text{O}$ phase (Fig. 3d–f).

The formation of dicalcium phosphate dihydrate during the preparation of conversion coatings can be explained by the following. When magnesium alloy samples are put into the phosphating agent with a slightly acidic pH, intensive dissolution of magnesium is observed, which is accompanied by the release of hydrogen and a local increase in the pH on the electrode/electrolyte interface:



Local alkalization of the electrolyte contacting the surface of magnesium alloys facilitates the formation of a surface layer consisting mainly of $\text{CaHPO}_4 \cdot 2\text{H}_2\text{O}$, according to the following reaction:

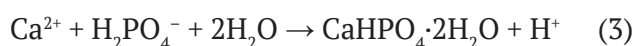


Fig. 4 shows the potentiodynamic polarization curves of the magnesium alloy samples in Hank's Balanced Salt Solution, and Table 4 presents the electrochemical parameters of corrosion of the

studied alloys calculated based on the results of electrochemical polarization. The anodic polarization curve (PC) of QE22 in the potential range from -1.3 to -1.2 V demonstrates a linear region which corresponds to active dissolution of the alloy. The anodic polarization curves of ZRE1 and WE43 in the potential ranges of -1.35 – (-1.30) V and -1.4 – (-1.35) V respectively demonstrate an active-passive region whose presence might indicate the formation of a dense layer of corrosion products. The abrupt change in the angular coefficient b_a of the anodic PC observed when the potential shifted further towards positive values, can be explained by the breakdown of the formed oxide-hydroxide layer and the beginning of active dissolution of the alloy. Regardless of the composition of magnesium alloys, the cathodic PCs have practically the same slope angle, and the cathodic coefficient $|b_c|$ varies in the range from 0.25 to 0.27 V. This indicates that cathodic processes accompanying the corrosion of the studied alloys are of the same type.

According to the obtained results, QE22 (corrosion current density $5.2 \cdot 10^{-5}$ A/cm²)

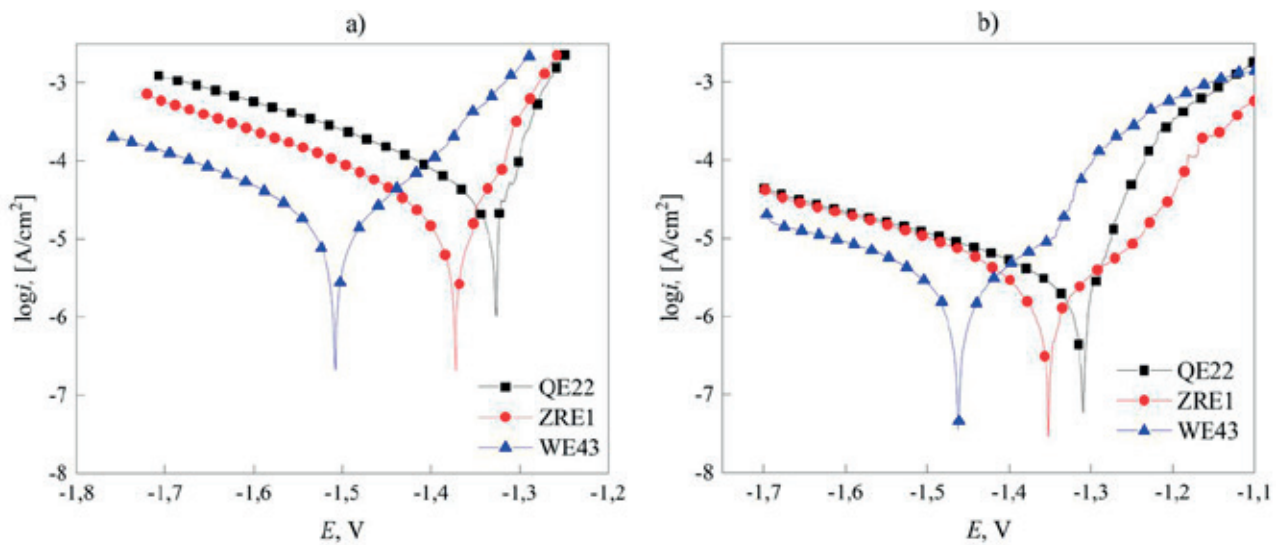


Fig. 4. Polarization curves of magnesium alloys without (a) and with (b) conversion coatings.

Table 4. Electrochemical parameters of corrosion of the magnesium alloy samples

Sample	$ b_k , V$	$ a_k , V$	$ b_a , V$	$ a_a , V$	$i_{\text{corr}}, A/cm^2$
Initial alloy samples					
QE22	0.27	2.46	0.09	0.95	$5.2 \cdot 10^{-5}$
ZRE1	0.25	2.51	0.07	1.01	$2.5 \cdot 10^{-5}$
WE43	0.27	2.70	0.10	0.97	$2.0 \cdot 10^{-5}$
Conversion coated alloys					
QE22	0.33	3.14	0.07	0.99	$3.4 \cdot 10^{-6}$
ZRE1	0.36	3.29	0.17	0.41	$3.3 \cdot 10^{-6}$
WE43	0.35	3.38	0.17	0.52	$3.2 \cdot 10^{-6}$

demonstrated the lowest corrosion resistance in Hank's Balanced Salt Solution. The WE43 alloy has a 2.6 and 1.25 times lower corrosion resistance than QE22 and ZRE1 respectively.

Conversion coatings reduce the corrosion rate of QE22, ZRE1, and WE43 by 15.2, 7.8, and 6.3 times respectively. The anodic PCs of ZRE1 and WE43 demonstrate a significant growth of the active-passive region and an increase in the angular coefficient b_a , which indicated the inhibition of anodic processes. Despite similar corrosion current densities of the studied alloys with conversion coatings, the kinetics of the anodic process of QE22 in Hank's Balanced Salt Solution differs significantly from those of ZRE1 and WE43. The slope angle of the anodic PC of QE22 after phosphating remains practically unchanged, which can indicate a low protective ability of the formed conversion coating.

The method of electrochemical impedance

spectroscopy was used for a more detailed study of the corrosion processes in the studied samples in Hank's Balanced Salt Solution. The impedance spectra of the magnesium samples presented as Nyquist diagrams demonstrate three time constants: capacitive semicircles in the region of high and low frequencies and an inductive loop in the region of low frequencies (Fig. 5). The capacitive semicircle in the region of high frequencies characterizes the charge transfer through the layer of corrosion products, and the capacitive semicircle in the region of low frequencies reflects the relaxation mass transfer processes in the solid phase as well as the charge transfer resistance in the double electric layer. The low-frequency inductive response indicates active ionization of the electrode.

Conversion coatings based on $\text{CaHPO}_4 \cdot 2\text{H}_2\text{O}$ increase the values of the impedance modulus of the studied alloys, which is demonstrated by

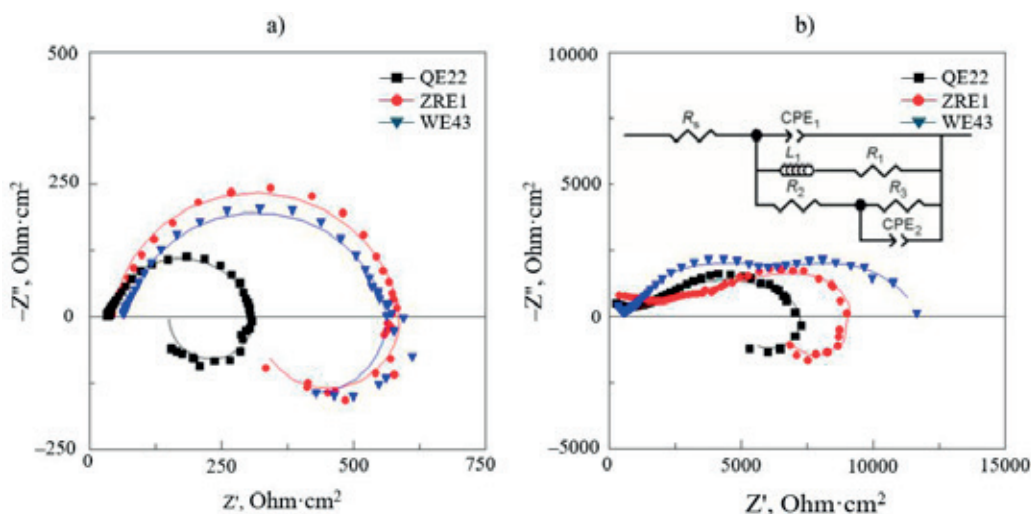


Fig. 5. Impedance spectra of the magnesium alloys presented as Nyquist diagrams without (a) and with (b) conversion coatings.

increase diameters of the capacitive semicircles. The impedance spectra of the QE22 and ZRE1 samples demonstrate an inductive loop in the region of low frequencies. The presence of the loop in the electrochemical impedance spectra of the alloys with conversion coatings might indicate the defectiveness of the formed coating and ionization of magnesium under the formed layer of $\text{CaHPO}_4 \cdot 2\text{H}_2\text{O}$. The impedance hodographs of the WE43 alloy with a conversion coating is characterized by the lack of inductive loops in region of low frequencies, which can be accounted for by the integrity of the formed coating.

An equivalent circuit presented in Fig. 5b was used for the quantitative description of the obtained impedance spectra. In the suggested circuit R_s is the resistance of the electrolyte; R_1 is the resistance of the corrosion products layer; L is the inductance parameter; R_2 is the surface

resistance; CPE_1 is the capacitive response of the corrosion products layer; and R_3 is the charge transfer resistance; CPE_2 is the capacitive response of the electrical double layer. Due to the lack of induction processes, they were not used for the quantitative description of the impedance spectra of the WE43 alloy with a conversion coating.

The obtained results demonstrate that WE43 with a conversion coating has the highest corrosion resistance in Hank’s Balanced Salt Solution. The obtained results are in good agreement with the data obtained by means of linear polarization.

Corrosion of magnesium alloys as accompanied by the release of hydrogen gas, which increases the pH of solutions. Therefore, it is practical to perform a comparative analysis of the protective abilities of the obtained coatings based on the dynamics of the pH of the corrosive environment

Table 5. Selection of the equivalent circuit

Grade alloy	R_s , $\text{Ohm}\cdot\text{cm}^2$	$\text{CPE}_1, 10^{-5} \text{ Ohm}^{-1}\cdot\text{cm}^{-2}\cdot\text{c}^n$	n_1	L, kN	$R_1, \text{kOhm}\cdot\text{cm}^2$	$R_2, \text{kOhm}\cdot\text{cm}^2$	$\text{CPE}_2, 10^{-4} \text{ Ohm}^{-1}\cdot\text{cm}^{-2}\cdot\text{c}^n$	n_2	$R_3, \text{OM}\cdot\text{cm}^2$
Initial alloy samples									
QE22	42.1	2.2	0.91	5.44	0.55	0.54	30.0	0.90	13
ZRE1	32.0	2.8	0.90	1.71	0.17	0.23	40.4	0.30	75
WE43	65.7	5.0	0.85	13.76	0.35	0.50	3.0	0.90	15
Conversion coated alloys									
QE22	48.0	4.4	0.80	190.50	12.90	0.93	0.25	0.48	6902
ZRE1	90.0	9.1	0.20	50.00	11.00	0.60	0.14	0.60	47361
WE43	496.7	1.1	0.65	–	6.90	4.38	1.86	0.73	–

in contact with the studied samples.

Fig. 6 demonstrates dependences of the pH of Hank's Balanced Salt Solution on the time of exposure of the initial magnesium alloys. The initial pH of Hank's Balanced Salt Solution is 7.4. After keeping the QE22 sample in the solution for 24 hours, the pH fluctuated abruptly and was ≈ 11 . After keeping the QE22 sample in the solution for 7 days, the pH did not grow significantly, which can be explained by the formation of a low-soluble layer of corrosion products – magnesium hydroxide and carbonate. Alloys ZRE1 and WE43 are characterized by a lower corrosion rate in Hank's Balanced Salt Solution. Thus, the pH of the corrosive environments 24 hours after putting ZRE1 and WE43 into them was 9.2 and 9.3, and after 7 days it was 10.1 and 10.0 respectively.

The brushite based conversion coating $\text{CaHPO}_4 \cdot 2\text{H}_2\text{O}$ significantly lowers the alkalization rate of Hank's Balanced Salt Solution with the studied samples. After 24 hours of experimenting with the coated QE22 alloy, the pH of the electrolyte was 8.3, and after 3 days the pH grew rapidly to 11.3, which indicated the beginning of active dissolution of the alloy. When the ZRE1 and WE43 alloys with conversion coatings were used, the pH of Hank's Balanced Salt Solution remained the same after 3 days: 7.5 and 7.6 respectively. A comparative analysis of the dynamics of the pH of corrosive environments with phosphated ZRE1 and WE43 demonstrated that between 3

and 5 days after the beginning of the experiment, the alkalization process was more active in the solution with the WE43 alloy. However, after 7 days, the pH of the corrosive environments became practically identical and were ≈ 8.4 .

Fig. 7 and 8 demonstrate the SEM images of the surface of magnesium alloy samples after their exposure in Hank's Balanced Salt Solution for 24 hours and for 7 days respectively. The surface of the QE22 alloy after 24 hours of corrosion testing was almost completely covered in an inhomogeneous layer of corrosion products, whose structure had macrodefects (Fig. 7a). ZRE1 and WE43 are the least susceptible to corrosion in the first 24 hours of testing, which is explained by the formation of a dense layer of corrosion products preventing further dissolution of the alloys. The QE22 sample almost completely dissolves in Hank's Balanced Salt Solution in 7 days. Increasing the exposure time of the ZRE1 alloy in Hank's Balanced Salt Solution up to 7 days results on the formation of pitting corrosion centers.

The surface of the QE22 sample with a conversion coating demonstrated the formation of pores after 24 hours of exposure in Hank's Balanced Salt Solution. The diameter of the pores varies from 10 to 40 μm . After 7 days of exposure, the surface is covered in a continuous layer of corrosion products and the conversion coating is broken down, which can indicate low protective abilities of the coating resulting

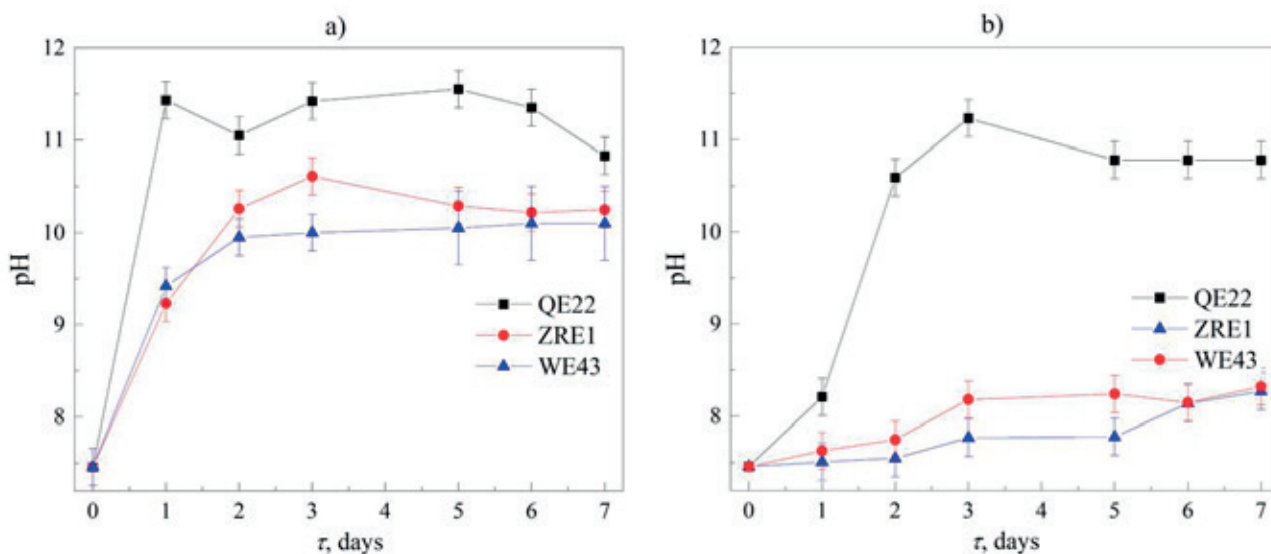


Fig. 6. The dynamics of the pH of Hank's Balanced Salt Solution during corrosion testing of alloys before (a) and after (b) chemical treatment.

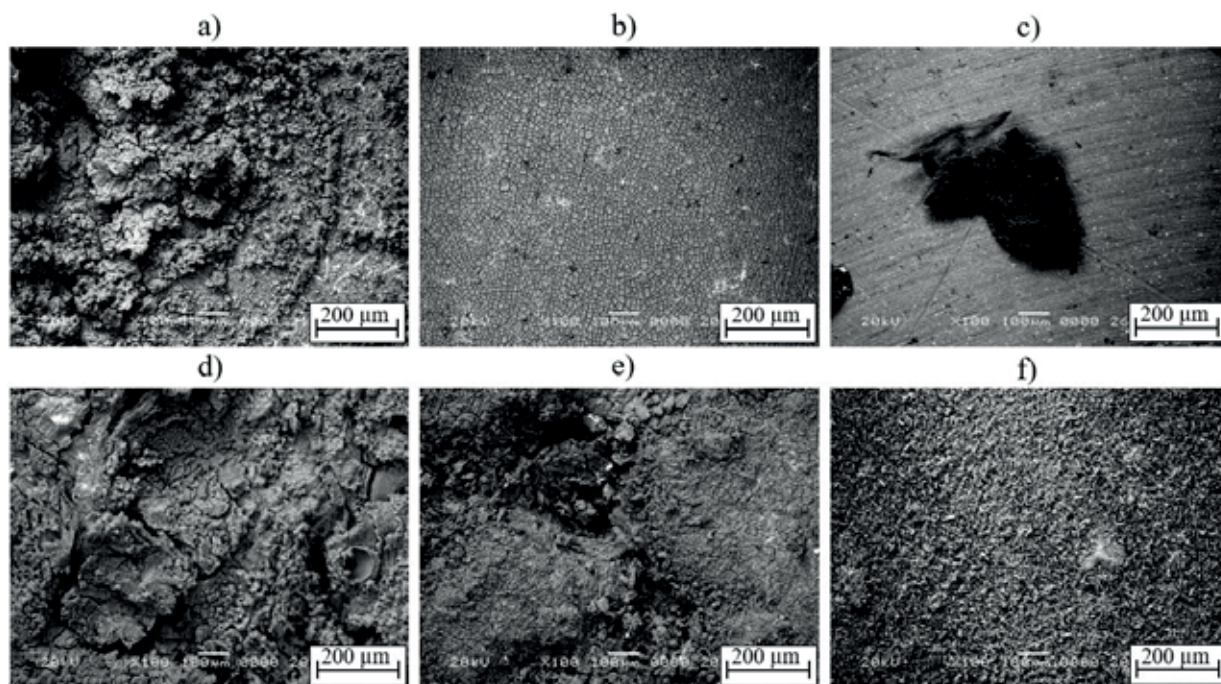


Fig. 7. SEM images of the initial magnesium alloy samples after 24 hours (a-c) and after 7 days (d-f) of corrosion testing in Hank's Balanced Salt Solution. Alloy: a, d – QE22; b, e – ZRE1; c, f – WE43

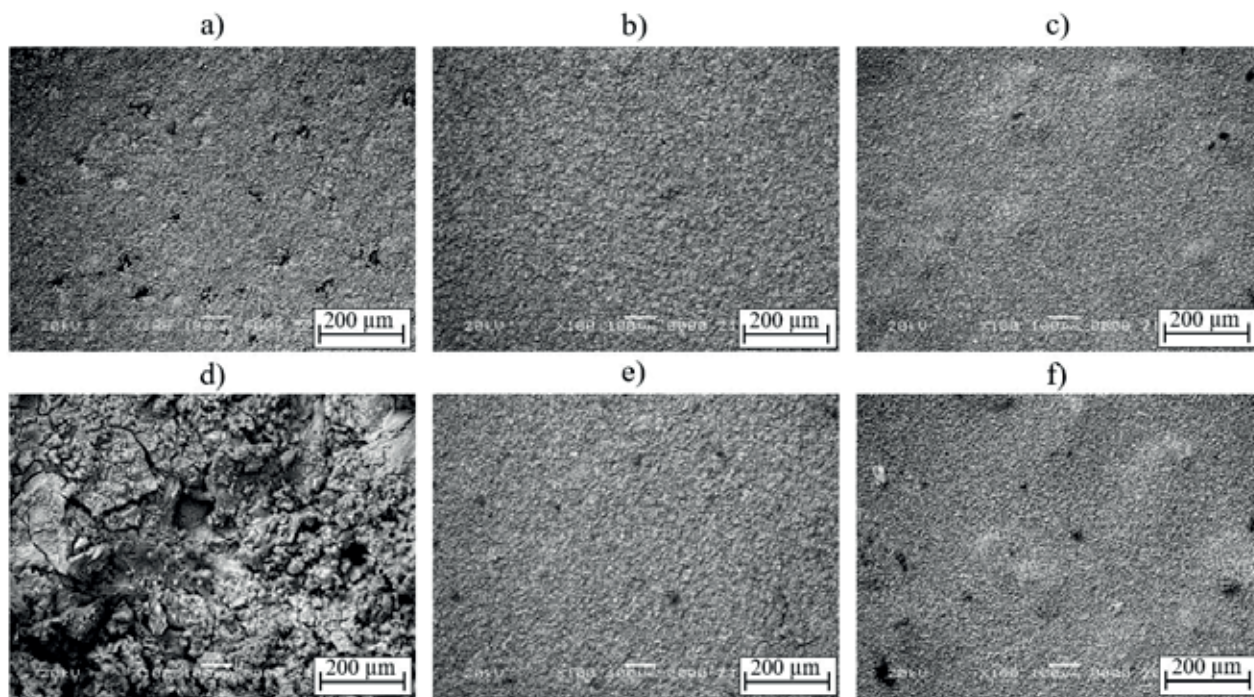


Fig. 8. SEM images of the phosphated magnesium alloy samples after 24 hours (a-c) and after 7 days (d-f) of corrosion testing in Hank's Balanced Salt Solution. Alloy: a, d – QE22; b, e – ZRE1; c, f – WE43

from its inhomogeneity and defectiveness. The microstructure of ZRE1 and WE43 with conversion coatings remains practically the same after 24 hours of corrosion testing in Hank's Balanced Salt Solution. When the time of exposure is

increased up to 7 days, an insignificant number of local corrosion centers (pores) are formed on their surface.

Fig. 9 demonstrates the SEM images of the surface of the studied samples with and without

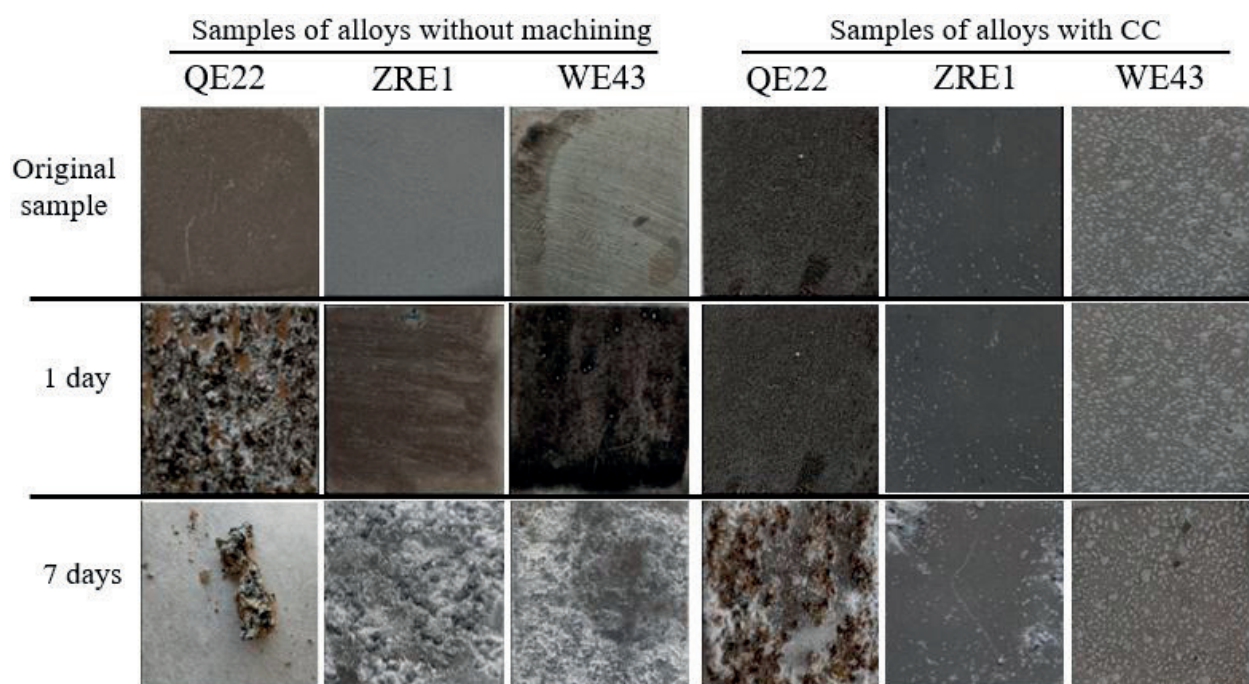


Fig. 9. Images of the surface of magnesium alloy samples after corrosion testing in Hank's Balanced Salt Solution.

conversion coatings after 24 hours and after 7 days of exposure in Hank's Balanced Salt Solution.

After the first 24 hours of corrosion testing, corrosion centers are formed on the surface of the QE22 alloy; the sample completely dissolved in 7 days. Visual assessment of the surface of ZRE1 and WE43 demonstrated that they remained intact after 7 days of testing. The surface of QE22 with a conversion coating does not change significantly after 24 hours of testing. After 7 days of testing, the surface of the alloy was almost completely covered in corrosion products. There were no visible corrosion centers on the surface of coated ZRE1 and WE43 samples after 7 days of testing.

Therefore, conversion coatings based on $\text{CaHPO}_4 \cdot 2\text{H}_2\text{O}$ (brushite) demonstrated a decrease in the corrosion rate of magnesium alloys QE22, ZRE1, and WE43 by 15.2, 7.8, and 6.3 times respectively. The obtained results are in good agreement with those presented in [28,31,32], where similar coatings on magnesium alloys doped with aluminum (series AZ) were demonstrated to reduce the corrosion current density by 19–62 times, while the differences in the protective properties of the conversion coating based on brushite are explained by the impact of

the substrate composition on the structure and defectiveness of the formed coatings. Our study confirmed this assumption and stress the importance of the chemical composition and the structure of magnesium alloys when choosing the technique of deposition of conversion coatings. We should note that despite the high effectiveness of protective conversion coatings on magnesium alloys of the AZ series, the use of these alloys as implant materials is associated with risk due to the presence of aluminum. Excessive amounts of aluminum in the human body has an adverse effect on neurons and osteoblasts and can cause Alzheimer's disease, which makes it even more important to carefully choose magnesium alloys for orthopedic implants.

4. Conclusions

Phosphating of magnesium alloys in solutions containing calcium nitrate results in the formation of low-soluble fine-grained coatings with a pronounced crystal structure including $\text{Ca} \approx 40 \text{ wt.}\%$; $\text{P} \approx 15 \text{ wt.}\%$; and $\text{O} \approx 35 \text{ wt.}\%$ and consisting mainly of brushite ($\text{CaHPO}_4 \cdot 2\text{H}_2\text{O}$). The coating formed on the surface of QE22 is characterized by highest inhomogeneity and the presence of microcracks, which can be explained by the presence of silver in its composition.

The corrosion resistance of magnesium alloys in Hank's Balanced Salt Solution (pH = 7.4), imitating the environment of the human body, decreases in the sequence QE22, ZRE1, WE43, and the corrosion current density i_{corr} is $5.2 \cdot 10^{-5}$, $2.5 \cdot 10^{-5}$ and $2.0 \cdot 10^{-5}$ A/cm², respectively. Conversion coatings reduce the corrosion rate of QE22, ZRE1, and WE43 by 15.2, 7.8, and 6.3 times respectively. Thus, the study demonstrated that conversion coatings formed on WE43 have the best protective abilities. The corrosion testing demonstrated that coated ZRE1 and WE43 alloys can resist corrosion in Hank's Balanced Salt Solution for 7 days without visible damage.

Contribution of the authors

The authors contributed equally to this article.

Conflict of interests

The authors declare that they have no known competing financial interests or personal relationships that could have influenced the work reported in this paper.

References

- Riaz U., Shabib I., Haider W. The current trends of Mg alloys in biomedical applications – A review. *Journal Biomedical Materials Research – Part B Applied Biomaterials*. 2019;107: 1970–1996. <https://doi.org/10.1002/jbm.b.34290>
- Zheng Y. F., Gu X. N., Witte F. Biodegradable metals. *Materials Science Engineering R: Reports*. 2014;77: 1–34. <https://doi.org/10.1016/j.mser.2014.01.001>
- Tan J., Ramakrishna S. Applications of magnesium and its alloys : A review. *Applied Sciences*. 2021;11(15): 6861. <https://doi.org/10.3390/app11156861>
- Król M. Solidification characteristics of Mg-Li-Al alloys. *Solid State Phenomena*. 2018;275: 41–52. <https://doi.org/10.4028/www.scientific.net/SSP.275.41>
- Gusieva K., Davies C. H. J., Scully J. R., Birbilis N. Corrosion of magnesium alloys: The role of alloying. *International Materials Reviews*. 2015;60(3): 169–194. <https://doi.org/10.1179/1743280414Y.0000000046>
- Antoniac I. V., Miculescu M., Mănescu V., ... Earar K. Magnesium-based alloys used in orthopedic surgery. *Materials*. 2022;15(3): 1148. <https://doi.org/10.3390/ma15031148>
- Gu X., Zheng Y., Cheng Y., Zhong S., Xi T. In vitro corrosion and biocompatibility of binary magnesium alloys. *Biomaterials*. 2029;30(4): 484–498. <https://doi.org/10.1016/j.biomaterials.2008.10.021>
- Drynda A., Deinet N., Braun N., Peuster M. Rare earth metals used in biodegradable magnesium-based stents do not interfere with proliferation of smooth muscle cells but do induce the upregulation of inflammatory genes. *Journal of Biomedical Materials Research – Part A*. 2019;91: 360–369. <https://doi.org/10.1002/jbm.a.32235>
- Ma Y., Talha M., Wang Q., Zhou N., Li Z., Lin Y. A multifunctional coating with modified calcium phosphate/chitosan for biodegradable magnesium alloys of implants. *New Journal of Chemistry*. 2022;46: 4436–4448. <https://doi.org/10.1039/d2nj00147k>
- Kozina I., Krawiec H., Starowicz M., Kawalec M. Corrosion resistance of MgZn alloy covered by chitosan-based coatings. *International Journal Molecular Sciences*. 2021;22 (15): 8301. <https://doi.org/10.3390/ijms22158301>
- Huang W., Mei D., Zhang J., ... Guan S. Improved corrosion resistance and cytocompatibility of Mg–Zn–Y–Nd alloy by the electrografted polycaprolactone coating. *Colloids Surfaces A: Physicochemical Engineering Aspects*. 2021;629: 127471. <https://doi.org/10.1016/j.colsurfa.2021.127471>
- Pulido-González N., Torres B., Zheludkevich M. L., Rams J. High Power Diode Laser (HPDL) surface treatments to improve the mechanical properties and the corrosion behaviour of Mg-Zn-Ca alloys for biodegradable implants. *Surface and Coatings Technology*. 2020;402: 126314. <https://doi.org/10.1016/j.surfcoat.2020.126314>
- Liu Y., Curioni M., Dong S., Liu Z. Understanding the effects of excimer laser treatment on corrosion behavior of biodegradable Mg-1Ca alloy in simulated body fluid. *Journal of Magnesium and Alloy*. 2021;10(4): 1004–1023. <https://doi.org/10.1016/j.jma.2021.11.011>
- Hou S., Yu W., Yang Z., Li Y., Yang L., Lang S. Properties of titanium oxide coating on MgZn alloy by magnetron sputtering for stent application. *Coatings*. 2020;10(10): 1–10. <https://doi.org/10.3390/coatings10100999>
- Braga J. de O., Carvalho de S. M., Silva L. M. C., ... Nunes E. H. M. Fabrication and characterization of dicalcium phosphate coatings deposited on magnesium substrates by a chemical conversion route. *Surface and Coatings Technology*. 2020;386: 125505. <https://doi.org/10.1016/j.surfcoat.2020.125505>
- Satharaj M., Ravichandran K., Narayanan S. Controlling the rate of degradation of Mg using magnesium fluoride and magnesium fluoride-magnesium phosphate duplex coatings. *Journal Magnesium and Alloy*. 2022;10(1): 295–312. <https://doi.org/10.1016/j.jma.2021.06.005>
- Cheng S., Wang W., Wang D., ... Zhang Y. An in vitro and in vivo comparison of Mg(OH)₂, MgF₂- and HA-coated Mg in degradation and osteointegration. *Biomaterials Science*. 2020;8: 3320–3333. <https://doi.org/10.1016/j.biomaterials.2020.10.021>

org/10.1039/d0bm00467g

18. Chen X. B., Nisbet D. R., Li R. W., ... Birbilis N. Controlling initial biodegradation of magnesium by a biocompatible strontium phosphate conversion coating. *Acta Biomaterialia*. 2014;10(3): 1463–1474. <https://doi.org/10.1016/j.actbio.2013.11.016>

19. Chunyan Z., Shangju L., Baoxing Y., ... Fuhui W. Ratio of total acidity to pH value of coating bath: A new strategy towards phosphate conversion coatings with optimized corrosion resistance for magnesium alloys. *Corrosion Science*. 2019;150: 279–295. <https://doi.org/10.1016/j.corsci.2019.01.046>

20. Wu Q., Yu B., Zhou P., Zhang T., Wang F. Fabrication of phosphate conversion coatings on rolled AZ31 magnesium alloy: Variation of corrosion resistance on different planes induced by the crystallographic texture. *Materials Chemistry and Physics*. 2021;273: 125121. <https://doi.org/10.1016/j.matchemphys.2021.125121>

21. Chaharmahali R., Fattah-alhosseini A., Nouri M., Babaei K. Improving surface characteristics of PEO coatings of Mg and its alloys with zirconia nanoparticles: a review. *Applied Surface Science Advances*. 2021;6: 100131. <https://doi.org/10.1016/j.apsadv.2021.100131>

22. Seyfi M., Fattah-alhosseini A., Pajohi-Alamoti M., Nikoomanzari E. Effect of ZnO nanoparticles addition to PEO coatings on AZ31B Mg alloy: antibacterial effect and corrosion behavior of coatings in Ringer's physiological solution. *Journal of Asian Ceramic Societies*. 2021;9(3): 1114–1127. <https://doi.org/10.1080/21870764.2021.1940728>

23. Daavari M., Atapour M., Mohedano M., ... Taherizadeh A. Quasi-in vivo corrosion behavior of AZ31B Mg alloy with hybrid MWCNTs-PEO/PCL based coatings. *Journal of Magnesium and Alloys*. 2021;10(11): 3217–3233. <https://doi.org/10.1016/j.jma.2021.09.010>

24. Taranu B.-O., Ianasi P., Rus S. F., Bucur A. I. Simultaneous precipitation and electrodeposition of hydroxyapatite coatings at different temperatures on various metal substrates. *Coatings*. 2022;12(2): 288. <https://doi.org/10.3390/coatings12020288>

25. Yuan B., Chen H., Zhao R., ... Zhang X. Construction of a magnesium hydroxide/graphene oxide/hydroxyapatite composite coating on Mg–Ca–Zn–Ag alloy to inhibit bacterial infection and promote bone regeneration. *Bioactive Materials*. 2022;18: 354–367. <https://doi.org/10.1016/j.bioactmat.2022.02.030>

26. Wang P., Liu J., Shen S., ... Xi T. In vitro and in vivo studies on two-step alkali-fluoride-treated Mg–Zn–Y–Nd alloy for vascular stent application: Enhancement in corrosion resistance and biocompatibility. *ACS Biomaterials Science and Engineering*. 2019;5(7): 3279–3292. <https://doi.org/10.1021/acsbomaterials.9b00140>

27. Van Phuong N., Moon S. Comparative corrosion study of zinc phosphate and magnesium phosphate conversion coatings on AZ31 Mg alloy. *Materials Letters*. 2014;122: 341–344. <https://doi.org/10.1016/j.matlet.2014.02.065>

28. Zai W., Zhang X., Su Y., Man H.C., Li G., Lian J. Comparison of corrosion resistance and biocompatibility of magnesium phosphate (MgP), zinc phosphate (ZnP) and calcium phosphate (CaP) conversion coatings on Mg alloy. *Surface and Coatings Technology*. 2020;397: 125919. <https://doi.org/10.1016/j.surfcoat.2020.125919>

29. Ishizaki T., Shigematsu I., Saito N. Anticorrosive magnesium phosphate coating on AZ31 magnesium alloy. *Surface and Coatings Technology*. 2009;203(16): 2288–2291. <https://doi.org/10.1016/j.surfcoat.2009.02.026>

30. Su Y., Su Y., Lu Y., Lian J., Li G. Composite microstructure and formation mechanism of calcium phosphate conversion coating on magnesium alloy. *Journal of The Electrochemical Society*. 2016;163(9): G138. <https://doi.org/10.1149/2.0801609jes>

31. JIA X., SONG J., QU X., ... PAN F. Effect of scratch on corrosion resistance of calciumphosphate conversioncoated AZ80 magnesium alloy. *Transactions of Nonferrous Metals Society of China*. 2022;32(1): 147–161. [https://doi.org/10.1016/S1003-6326\(21\)65784-9](https://doi.org/10.1016/S1003-6326(21)65784-9)

32. Jia X., Song J., Xiao B., ... Pan F. Influence of indentation size on the corrosion behaviour of a phosphate conversion coated AZ80 magnesium alloy. *Journal of Materials Research and Technology*. 2021;14: 1739–1753. <https://doi.org/10.1016/j.jmrt.2021.07.091>

33. Ong J. L., Chan D. C. N. Hydroxyapatite and their use as coatings in dental implants: A review. *Critical Reviews in Biomedical Engineering*. 2000;28(5&6): 667–707. <https://doi.org/10.1615/CritRevBiomedEng.v28.i56.10>

34. Dorozhkin S. V. Calcium orthophosphate coatings on magnesium and its biodegradable alloys. *Acta Biomaterialia*. 2014;10(7): 2919–2934. <https://doi.org/10.1016/j.actbio.2014.02.026>

35. Duan G., Yang L., Liao S., ... Wang F. Designing for the chemical conversion coating with high corrosion resistance and low electrical contact resistance on AZ91D magnesium alloy. *Corrosion Science*. 2018;135: 197–206. <https://doi.org/10.1016/j.corsci.2018.02.051>

36. Su Y., Guo Y., Huang Z., ... Ren L. Preparation and corrosion behaviors of calcium phosphate conversion coating on magnesium alloy. *Surface and Coatings Technology*. 2016;307(part A): 99–108. <https://doi.org/10.1016/j.surfcoat.2016.08.065>

37. Sun R. X., Wang P. F., Zhao D. D., Sun Z. Z., Li C. Q., Chen K. Z. An environment-friendly calcium phosphate conversion coating on AZ91D alloy and its

corrosion resistance. *Materials and Corrosion*. 2015;66(4): 383–386. <https://doi.org/10.1002/maco.201307424>

38. Braga J. de O., Santos dos D. M. M., Cotting F., ... Nunes E. H. M. Surface modification of magnesium with a novel composite coating for application in bone tissue engineering. *Surface and Coatings Technology*. 2022;433: 128078. <https://doi.org/10.1016/j.surfcoat.2021.128078>

39. Kawahara M, Kato-Negishi M. Link between aluminum and the pathogenesis of Alzheimer's disease: The integration of the aluminum and amyloid cascade hypotheses. *International Journal of Alzheimer's Disease*. 2011;8: 276393. <https://doi.org/10.4061/2011/276393>

40. Zhang S., Zhang X., Zhao C., ... Bian Y. Research on an Mg-Zn alloy as a degradable biomaterial. *Acta Biomaterialia*. 2010;6(2): 626–640. <https://doi.org/10.1016/j.biomaterials.2003.08.009>

41. Khan F., Panigrahi S. K. Age hardening, fracture behavior and mechanical properties of QE22 Mg alloy. *Journal of Magnesium and Alloy*. 2015;3(3): 210–217. <https://doi.org/10.1016/j.jma.2015.08.002>

42. Rzychoń T., Szala J., Kiełbus A. Microstructure, castability, microstructural stability and mechanical properties of ZRE1 magnesium alloy. *Archives of Metallurgy and Materials*. 2012;57(1): 245–252. <https://doi.org/10.2478/v10172-012-0018-3>

Information about the authors

Andrei V. Paspelau, Researcher at the Department of Physical, Colloidal and Analytical Chemistry, Belarusian State Technological University (Minsk, Republic of Belarus).

<https://orcid.org/0000-0002-1287-603X>
andrei29088@mail.ru

Aliaksandr A. Kasach, Cand. Sci. (Chem.), Assistant at the Department of Chemistry, Technology of Electrochemical Productions and Electronic Engineering Materials, Belarusian State Technological University (Minsk, Republic of Belarus).

<https://orcid.org/0000-0001-5522-2928>
kasach2018@bk.ru

Aleksandr R. Tsyganov, Dr. Sci. (Agric.), Academician, First Vice-Rector, Belarusian State Technological University (Minsk, Republic of Belarus).

<https://orcid.org/0000-0001-5521-5613>
tziganov@belstu.by

Irina I. Kurilo, Cand. Sci. (Chem.), Associate Professor, Head at the Department of Physical, Colloidal and Analytical Chemistry, Belarusian State Technological University (Minsk, Republic of Belarus).

<https://orcid.org/0000-0002-0016-6719>
september@tut.by

Received 28.09.2023; approved after reviewing 04.12.2023; accepted for publication 15.12.2023; published online 01.10.2024.

Translated by Yulia Dymant



Condensed Matter and Interphases

Kondensirovannye Sredy i Mezhfaznye Granitsy
<https://journals.vsu.ru/kcmf/>

Original articles

Research article

<https://doi.org/10.17308/kcmf.2024.26/12227>

Residual strain evaluation in GaN/AlN multiperiod superlattices grown on SiC/Si

P. V. Seredin¹✉, Sh. Sh. Sharofidinov², D. L. Goloshchapov¹, N. S. Buylov¹, K. A. Ereemeev², S. A. Yusupova², S. A. Kukushkin³

¹Voronezh State University,
Universitetskaya pl. 1, Voronezh 394018, Russian Federation

²Ioffe Institute,
26 Polytechnicheskaya st., St. Petersburg 194021, Russian Federation

³Institute for Problems in Mechanical Engineering of the Russian Academy of Science,
61 Bolshoy prospekt V.O., St. Petersburg 199178, Russian Federation

Abstract

In our study, we formed a multilayer heterostructure consisting of periodic GaN and AlN layers by means of chloride-hydride epitaxial growth on a hybrid SiC/Si substrate synthesized using the method of the coordinated substitution of atoms.

A comprehensive study of the heterostructure by means of nanoscale mapping of elastic strain demonstrated that in the upper GaN layer the dual-axis strain σ_{xx} is minimal (~ -0.12 GPa). There is practically no strain in the superlattices located in the upper part of the heterostructure.

Keywords: GaN, AlN, Superlattice, Raman spectroscopy

Acknowledgements: Access to scientific equipment was provided by the Ministry of Education and Science of the Russian Federation, agreement No. FZGU-2023-0006 and 075-15-2021-1351. SiC/Si hybrid substrates were synthesized using the equipment of the unique scientific facility “Physics, Chemistry and Mechanics of Crystals and Thin Films” of Institute of Problems of Mechanical Engineering, Russian Academy of Sciences (St. Petersburg).

The content is available under Creative Commons Attribution 4.0 License.

Acknowledgments: Access to the scientific equipment granted by the grant of Ministry of science and higher education of Russia, grant number № FZGU-2023-0006 and № 075-15-2021-1351. Hybrid SiC/Si substrates were synthesized using the equipment of the unique scientific unit “Physics, Chemistry, and Mechanics of Crystals and Thin Films” (Institute for Problems in Mechanical Engineering of the Russian Academy of Sciences, St. Petersburg)

For citation: Seredin P. V., Sharofidinov Sh. Sh., Goloshchapov D. L., Buylov N. S., Ereemeev K. A., Yusupova S. A., Kukushkin S. A. Residual strain evaluation in GaN/AlN multiperiod superlattices grown on SiC/Si. *Condensed Matter and Interphases*. 2024;26(3): 518–525. <https://doi.org/10.17308/kcmf.2024.26/12227>

Для цитирования: Середин П. В., Шарофидинов Ш. Ш., Голощапов Д. Л., Буйлов Н. С., Еремеев К. А., Юсупова Ш. А., Кукушкин С. А. Исследования остаточных упругих напряжений в многопериодных сверхрешетках GaN/AlN, выращенных на подложке SiC/Si. *Конденсированные среды и межфазные границы*. 2024;26(3): 518–525. <https://doi.org/10.17308/kcmf.2024.26/12227>

✉ Pavel V. Seredin, e-mail: paul@phys.vsu.ru

© Seredin P. V., Sharofidinov Sh. Sh., Goloshchapov D. L., Buylov N. S., Ereemeev K. A., Yusupova S. A., Kukushkin S. A., 2024



The content is available under Creative Commons Attribution 4.0 License.

1. Introduction

Group III nitrides (GaN, AlN, AlGaN) have unique physical and chemical properties as compared to other semiconductors [1–3]. They have high hardness, good thermal conductivity, and high resistance to radiation and chemicals. These properties make Group III nitrides good candidates for the role of semiconductors in modern high-frequency equipment [3–6].

Group III nitrides are usually grown on substrates including sapphire and silicon carbide (SiC). However, silicon substrates, including porous ones [7–9], are becoming increasingly popular, because they have large diameters and, what is more important, have the required thermal characteristics and electrical properties. However, due to the considerable mismatch of crystal lattice parameters between group III nitride films and foreign substrates, as well as the difference in the coefficient of thermal expansion (CTE) of these materials, large elastic strain occurs during the growth process [10]. Therefore, it is important to lower the elastic strain in the epitaxial layers of the superlattice. At the same time, the misfit deformation in epitaxial systems with mismatched lattices can be reduced by the high density of structural defects and the growth of transition buffer layers based on multiperiod superlattices. Therefore, strain engineering in group III nitrides and its analysis present an important problem [11]. X-ray powder diffraction is often used to control strain, because it is a powerful and reliable method of nondestructive analysis of heterostructures [12, 13]. However, lately, Raman spectroscopy has been the most preferable method [14, 9]. Its main advantage over X-ray powder diffraction is that it allows for spatially resolved evaluation of inhomogeneous deformations. Raman spectra and motorized sample stages used to adjust the position of the sample within the scanning plane at submicron steps make it possible to register residual strain and its fluctuations in the layers of heterostructures with a high spatial resolution. Considering the fact that strain engineering is one of the most powerful tools for adjusting the optical and electronic properties of III-V semiconductor compounds, it is important to investigate residual strain in epitaxial layers of gallium nitride grown by means of transition

buffer layers based on multiperiod GaN/AlN superlattices.

Earlier experiments demonstrated [15,16] that group III nitrides of good structural quality (AlN, GaN, and AlGaN) can be grown on a hybrid substrate SiC/Si and then separated from it. Thus, in [16] we grew single-crystal crack-free layers of AlN (with a thickness up to 300 μm), AlGaN (with a thickness up to 400 μm , and GaN (with a thickness up to 200 μm), as well as GaN films of the semipolar (11 $\bar{2}$ 4) orientation and a thickness up to 35 μm .

Therefore, the purpose of this study was to analyze residual elastic strain in the epitaxial periodic heterostructure and the corresponding GaN/AlN multiperiod superlattices after the separation from the hybrid substrate.

2. Materials and methods

To grow a bulk GaN layer with a good crystal structure which could then be separated from the substrate, we used hybrid vapor phase epitaxy (HVPE), which is well-known to be a relatively inexpensive method of obtaining bulk III-nitride layers on silicon or sapphire substrates. In our experiment, we used a hybrid SiC/Si(111) substrate synthesized using the method of coordinated substitution of atoms [17–19]. Taking into account the mismatch of crystal lattice parameters and the difference in the coefficients of thermal expansion, to avoid cracking we used the method of deposition of superlattices between the main layers of AlN and GaN. First, we deposited a thin layer of AlN, after which the second element was added (Ga). Then we grew an AlN/GaN superlattice layer in a 50:50 ratio for 20 min. During the next stage, another AlN layer was grown followed by the growth of yet another AlN/GaN superlattice layer. The final layer was a GaN layer with a thickness of about 3.5 μm . The structure was grown in a reactor at high temperatures ($T \sim 1000$ °C). Ammonia (NH₃) and argon (Ar) were used as a gas mixture, the flow rate was 1000 and 4000 ml/min respectively. The flow rate of Al and Ga was 100 ml/min. After the growth of the structure, the substrate was removed.

The diagnostics of the samples was carried out using microstructural and spectroscopic methods. Microscopic studies were performed

using a JSM-7001F scanning electron microscope (Jeol, Japan). Raman spectra were measured using a RamMics 532 confocal Raman microscope (EnSpectr, Moscow, Russia) with a radiation wavelength of 532 nm. The scanning was performed using a 60× lens. The power at the focus was 30 mW. The spectra were registered in the range of 100–2000 cm⁻¹ with a spectral resolution of 1 cm⁻¹. Analysis of the spatial domains of the samples was carried out using a dual-axis motorized stage with a step of 0.25 μm along the whole structure of the samples. As a result, we obtained the spectra in the $z(xy)\bar{z}$ and $x(xy)\bar{x}$ geometry.

3. Results and discussion

Fig. 1 demonstrates a scheme of the GaN/AlN multilayer heterostructure and microscopic images of the cross-section of the sample on different scales obtained using scanning electron microscopy.

We have already mentioned that information about the structural properties of free thin layers based on GaN/AlN multiperiod superlattices was obtained by means of Raman light scattering. Raman spectroscopy is a very effective tool for non-destructive testing of semiconductor nanostructures.

Fig. 2 presents the Raman spectrum of the sample in the $z(xy)\bar{z}$ geometry.

Due to the optical transparency of GaN and AlN and a large depth of the Raman spectroscopy profiling in the $z(xy)\bar{z}$ geometry the spectrum

demonstrates Raman light scattering modes from various layers of the heterostructure.

In accordance with the geometry of Raman light scattering and the selection rules for the wurtzite crystal structure (spatial group $P3m1$) observed in phases GaN and AlN, for each phase the Raman spectra might demonstrate a characteristic set of six longitudinal (LO) and transverse (TO) phonon modes [20,21]. An analysis of the experimental data (Fig. 2) demonstrated that there are four vibrations in the spectrum. The first and the most intense maximum at about 567 cm⁻¹ is the phonon mode E_2^{high} of the wurtzite-like GaN [22,23]. A less intense peak at about 735 cm⁻¹ is the $A_1(\text{LO})$ mode of GaN. The peak at about

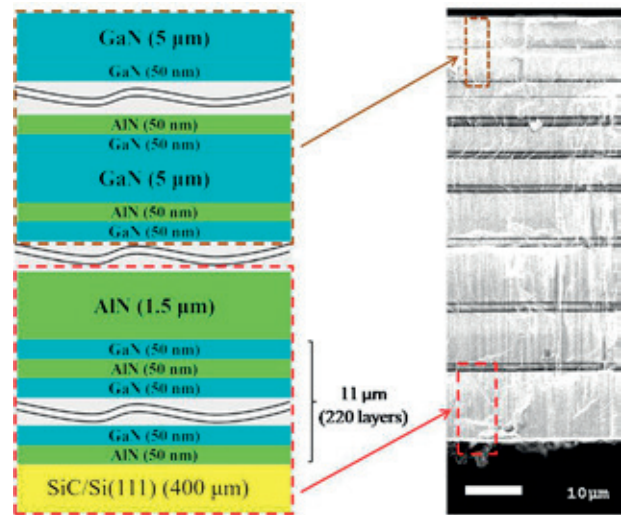


Fig. 1. SEM image of the heterostructure and schematic images of two types of superlattices

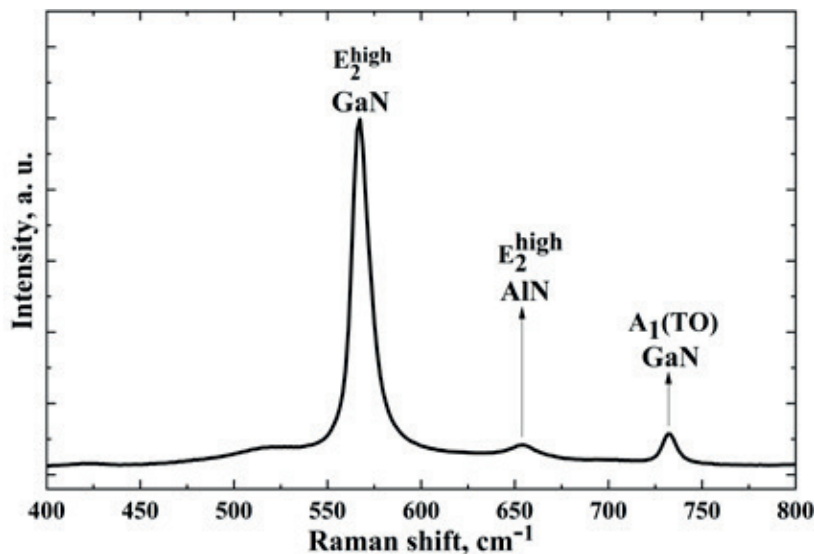


Fig. 2. Raman spectrum of the film in the geometry $z(xy)\bar{z}$

653 cm^{-1} is the E_2^{high} mode of AlN, the strongest of the modes allowed in the films of wurtzite AlN in the $z(xy)z'$ backscattering geometry used in our experiment [24].

To perform a layer-by-layer analysis of the structure with a high spatial resolution we performed the scanning in the $x(xy)\bar{x}$ geometry with a step of 250 nm. As a result, we obtained a set of phonon modes from the region of multiperiod superlattices GaN/AlN (Fig. 3) as well as from AlN buffer layers (Fig. 4)

Based on the obtained results, we can say that in the selected $x(xy)\bar{x}$ geometry, the spectra of the GaN/AlN superlattice (Fig. 3) demonstrate an intense nonpolar phonon mode E_2^{high} of GaN (Fig. 2) together with active polar vibrations $A_1(\text{TO})$ of GaN and $E_1(\text{TO})$ of GaN at about 535 and 555 cm^{-1} respectively. These vibrations are characteristic for GaN crystals with a wurtzite structure [25]. We can see that depending on the distance between the substrate and the studied region, a shift in the frequencies of phonon modes $A_1(\text{TO})$, $E_1(\text{TO})$, and E_2^{high} of GaN is observed as well as a change in their relative intensities.

As for the Raman spectra of the AlN buffer layers (Fig. 4), there are three active modes: E_2^{high} , $A_1(\text{TO})$, and $E_1(\text{TO})$, whose intensity practically

does not depend on the location of the AlN layer in the film. We should also note that the spectra of the AlN buffer layer demonstrate vibrations at about 530–580 cm^{-1} (Fig. 4) attributed to $A_1(\text{TO})$ and E_2^{high} modes of GaN. This can be explained by the fact that during the scanning, the region of generation of the desired signal occupied the neighboring layers of the superlattice, which in turn means that the cleavage plane was not perpendicular to the surface of the sample.

The observed shifts of the phonon modes of various symmetry must be connected with the deformations of the layers caused by the difference in the crystal lattice parameters and the thermal expansion coefficients of the materials of the layers that occurred during the growth of the heterostructure. We can see that the shifts in phonon vibrations belonging to phonons of AlN and GaN in various layers of superlattices and buffer layers have different directions, which indicates different types of deformations in these layers.

By performing micro Raman spectroscopy of the cleavage of the heterostructure using coordinated spectral scanning, we can obtain a scheme of the structure in the cross-section of the layers based on the variations on the intensity

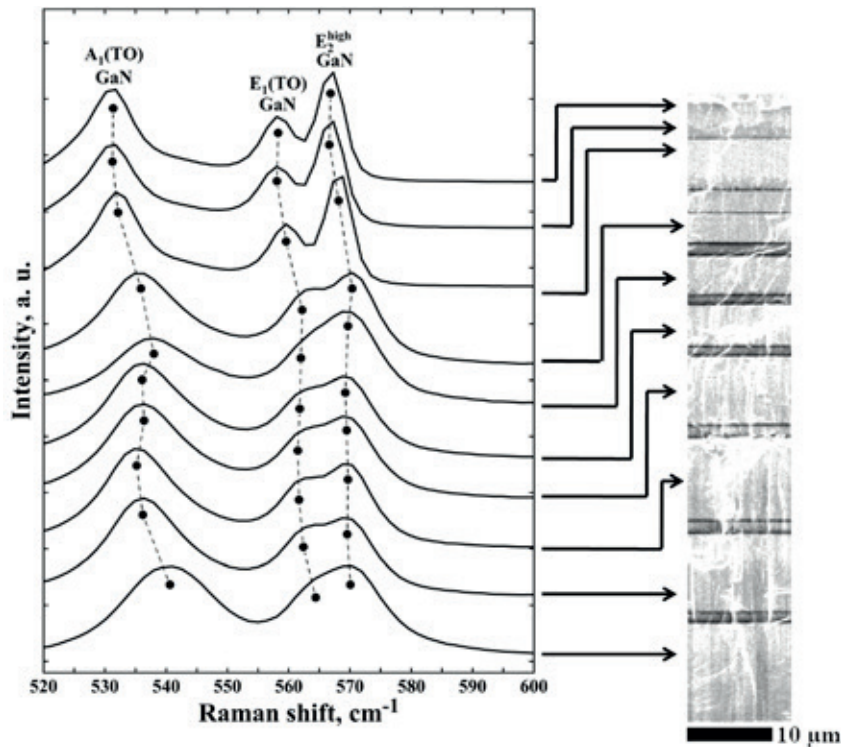


Fig. 3. Raman spectra from regions of GaN/AlN superlattices, taken in geometry $z(xy)\bar{z}$

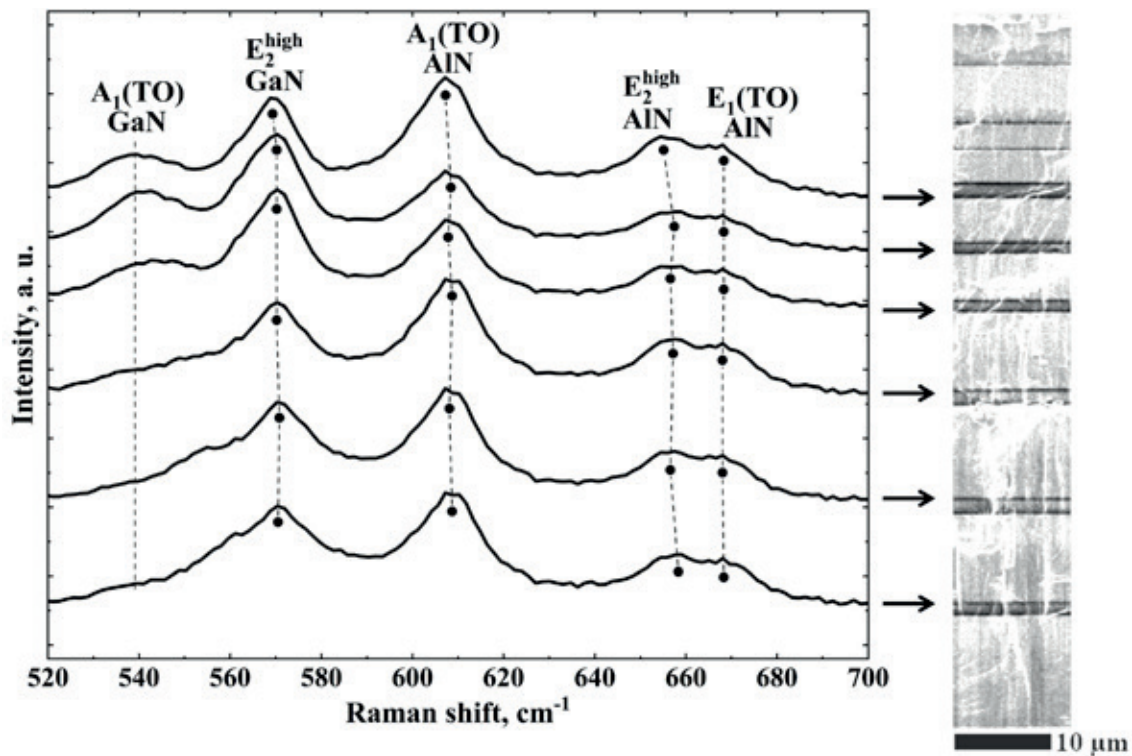


Fig. 4. Raman spectra from AlN buffer layers taken in geometry $z(xy)\bar{z}$

of spectral lines reflecting the distribution of nonpolar E_2^{high} vibrational modes of GaN and AlN near the interface. In order to do this, we determined integral areas under the selected spectral lines in each spectrum corresponding to a particular point in the scanning region.

Fig. 5a, b demonstrate the results of the hyperspectral mapping based on the distribution of intensities of the selected vibrations and a SEM image of the scanned region. The results of the chemical mapping are color coded. The warmer the color, the greater the intensity of the corresponding phonon and therefore the composition of the phase in the region.

An analysis of the results of the hyperspectral mapping (Fig. 5a, b) visualizes the structure of the layers in the sample: the maps demonstrate bands of the greatest/smallest intensity of GaN/AlN, and the distance between the bands correlates well with the SEM image.

At the same time, we should note that in the layers forming the GaN/AlN superlattices, the quantitative composition and the intensity of the localized modes depend on the localization region as well as on the period of the superlattice. We can see that the nonpolar E_2^{high} mode of GaN

has a maximum intensity in upper layers of the superlattices changing gradually from layer to layer.

As we have already mentioned, the residual strain in thin epitaxial films is an important issue for the production of various devices. During the growth of multilayer heterostructures based on group III nitrides on foreign substrates, the residual strain observed in the films is the result of a balance between two competing deformation components: misfit deformation caused by the difference in the thermal expansion coefficients and the deformation caused by the defects in the structure [26]. Results of numerous studies have demonstrated that the frequencies of the E_2^{high} modes of GaN and AlN depend on the deformations in the crystal lattice. Therefore, the evaluation of residual strain in various layers of the heterostructure can be carried out based on the frequency shifts in the Raman spectrum of the main vibrational modes: E_2^{high} modes of GaN and AlN.

The calculation of residual strain at the cleavage of the epitaxial layer was performed based on the frequency of the E_2^{high} mode of GaN using the equation:

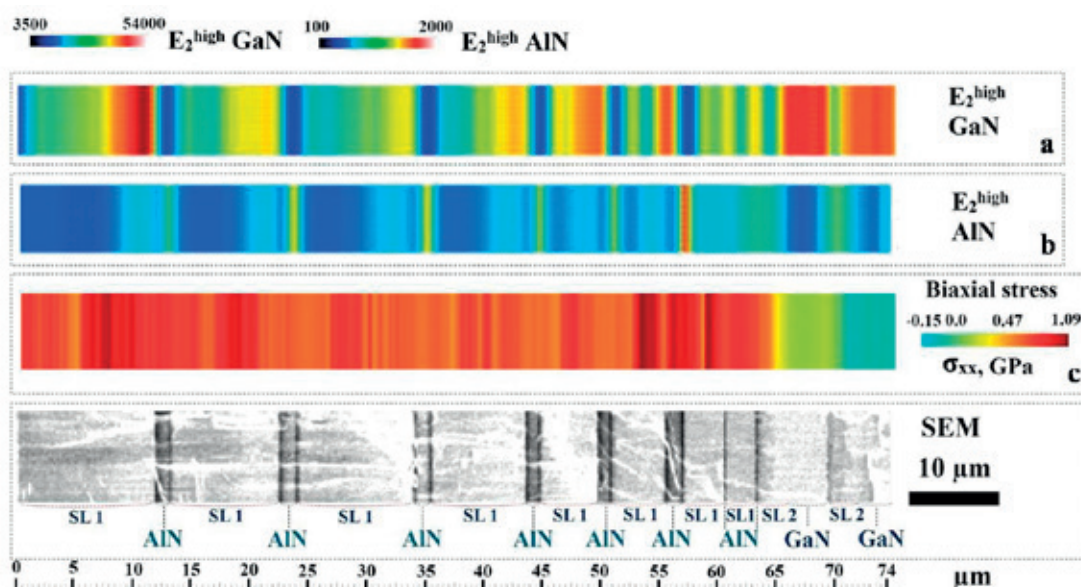


Fig. 5. Hyperspectral Raman mapping of the film cleavage region based on the intensity distribution of the E_2^{high} GaN (a) и E_2^{high} AlN (b), phonon modes, as well as the distribution of elastic stresses in a multilayer heterostructure (c)

$$\sigma_{xx} = \frac{\Delta\omega}{K}. \quad (1)$$

Where $\Delta\omega$ is the Raman shift with regard to the strain-free layer, K is a constant value for GaN $K_{\text{GaN}} = 4.3 \text{ cm}^{-1} \cdot \text{GPa}$

Fig. 5c demonstrates a map of dual-axis strain near the cleavage of the film. We can see that in the upper GaN layer the dual-axis strain σ_{xx} is minimal ($\sim -0.12 \text{ GPa}$). At the same time, the strain is minimal in the upper SL2 superlattices (with a constant period).

4. Conclusions

In our study, we formed a multilayer heterostructure consisting of periodic GaN and AlN layers by means of chloride-hydride epitaxial growth on a hybrid SiC/Si substrate synthesized using the method of coordinated substitution of atoms.

The thickness of the obtained structure was $\sim 78 \mu\text{m}$. Using nanoscale mapping in the upper GaN layers we determined the dual-axis strain σ_{xx} to be minimum ($\sim 0.12 \text{ GPa}$). There is practically no strain in the superlattices located in the upper part of the structure.

Contribution of the authors

The authors contributed equally to this article.

Conflict of interests

The authors declare that they have no known competing financial interests or personal relationships that could have influenced the work reported in this paper.

References

1. Zou C., Zhao Z., Xu M., ... Li S. GaN/Gr (2D)/Si (3D) Combined high-performance hot electron transistors. *ACS Nano*. 2023;17(9): 8262–8270. <https://doi.org/10.1021/acsnano.2c12435>
2. Das P., Wu T.-L., Tallur S. Design and analysis of high electron mobility transistor inspired: III-V electro-optic modulator topologies. *Semiconductor Science and Technology*. 2020;35(9): 095028. <https://doi.org/10.1088/1361-6641/ab9ea9>
3. Kohen D., Nguyen X. S., Yadav S., ... Fitzgerald E. A. Heteroepitaxial growth of In_{0.30}Ga_{0.70}As high-electron mobility transistor on 200 mm silicon substrate using metamorphic graded buffer. *AIP Advances*. 2016;6(8): 085106. <https://doi.org/10.1063/1.4961025>
4. Jang W.-H., Kim H.-S., Kang M.-J., Cho C.-H., Cha H.-Y. Recessed AlGaIn/GaN UV phototransistor. *Journal of Semiconductor Technology and Science*. 2019;19(2): 184–189. <https://doi.org/10.5573/JSTS.2019.19.2.184>
5. Encomendero J., Faria F. A., Islam S. M., ... Xing H.G. New tunneling features in polar III-nitride resonant tunneling diodes. *Physical Review X*. 2017;7(4): 041017. <https://doi.org/10.1103/PhysRevX.7.041017>

6. Singh M. M., Siddiqui M. J., Saxena A. Comparative simulation of GaAs and GaN based double barriers-resonant tunneling diode. *Procedia Computer Science*. 2016; 85581–85587. <https://doi.org/10.1016/j.procs.2016.05.224>
7. Seredin P. V., Lenshin A. S., Mizerov A. M., Leiste H., Rinke M. Structural, optical and morphological properties of hybrid heterostructures on the basis of GaN grown on compliant substrate por-Si(111). *Applied Surface Science*. 2019; 4761049–4761060. <https://doi.org/10.1016/j.apsusc.2019.01.239>
8. Seredin P. V., Goloshchapov D. L., Lenshin A. S., Mizerov A. M., Zolotukhin D. S. Influence of por-Si sublayer on the features of heteroepitaxial growth and physical properties of In_xGa_{1-x}N/Si(111) heterostructures with nanocolumn morphology of thin film. *Physica E: Low-dimensional Systems and Nanostructures*. 2018; 104101–104110. <https://doi.org/10.1016/j.physe.2018.07.024>
9. Seredin P. V., Goloshchapov D. L., Arsentyev I. N., Sharofidinov S., Kasatkin I. A., Prutskij T. HVPE fabrication of GaN sub-micro pillars on preliminarily treated Si(001) substrate. *Optical Materials*. 2021; 117111130. <https://doi.org/10.1016/j.optmat.2021.111130>
10. Ansah-Antwi K. K., Soh C. B., Liu H., Chua S. J. Growth optimization and characterization of GaN epilayers on multifaceted (111) surfaces etched on Si(100) substrates. *Journal of Vacuum Science & Technology A: Vacuum, Surfaces, and Films*. 2015;33(6): 061517. <https://doi.org/10.1116/1.4933201>
11. Gao N., Chen J., Feng X., ... Kang J. Strain engineering of digitally alloyed AlN/GaN nanorods for far-UVC emission as short as 220 nm. *Optical Materials Express*. 2021;11(4): 1282. <https://doi.org/10.1364/OME.422215>
12. Kuchuk A. V., Kryvyi S., Lytvyn P. M., ... Salamo G. J. The peculiarities of strain relaxation in GaN/AlN superlattices grown on vicinal GaN (0001) substrate: Comparative XRD and AFM study. *Nanoscale Research Letters*. 2016;11(1): 252. <https://doi.org/10.1186/s11671-016-1478-6>
13. Seredin P. V., Glotov A. V., Ternovaya V. E., ... Tarasov I. S. Effect of silicon on relaxation of the crystal lattice in MOCVD-hydride Al_xGa_{1-x}As:Si/GaAs(100) heterostructures. *Semiconductors*. 2011;45(4): 481–492. <https://doi.org/10.1134/S106378261104021X>
14. Davydov V., Roginskii E., Kitaev Y., ... Smirnov M. Phonons in short-period GaN/AlN superlattices: Group-theoretical analysis, ab initio calculations, and Raman spectra. *Nanomaterials*. 2021;11(2): 286. <https://doi.org/10.3390/nano11020286>
15. Sharofidinov Sh. Sh., Kukushkin S. A., Red'kov A. V., Grashchenko A. S., Osipov A. V. Growing III–V semiconductor heterostructures on SiC/Si substrates. *Technical Physics Letters*. 2019;45(7): 711–713. <https://doi.org/10.1134/S1063785019070277>
16. Kukushkin S. A., Sharofidinov Sh. Sh. A new method of growing AlN, GaN, and AlGaIn bulk crystals using hybrid SiC/Si substrates. *Physics of the Solid State*. 2019;61(12): 2342–2347. <https://doi.org/10.1134/S1063783419120254>
17. Kukushkin S. A., Osipov A. V. Theory and practice of SiC growth on Si and its applications to wide-gap semiconductor films. *Journal of Physics D: Applied Physics*. 2014;47(31): 313001. <https://doi.org/10.1088/0022-3727/47/31/313001>
18. Kukushkin S. A., Osipov A. V. Nanoscale single-crystal silicon carbide on silicon and unique properties of this material. *Inorganic Materials*. 2021;57(13): 1319–1339. <https://doi.org/10.1134/S0020168521130021>
19. Kukushkin S. A., Osipov A. V. Epitaxial silicon carbide on silicon. Method of coordinated substitution of atoms (a review). *Russian Journal of General Chemistry*. 2022;92(4): 584–610. <https://doi.org/10.1134/S1070363222040028>
20. Olivier A., Wang H., Koke A., Baillargeat D. Gallium nitride nanowires grown by low pressure chemical vapour deposition on silicon substrate. *International Journal of Nanotechnology*. 2014;11(1/2/3/4): 243. <https://doi.org/10.1504/IJNT.2014.059826>
21. Borowicz P., Gutt T., Malachowski T. Structural investigation of silicon carbide with micro-Raman spectroscopy. In: *2009 MIXDES-16th International Conference Mixed Design of Integrated Circuits Systems*. 2009; 177–180.
22. Davydov V. Yu., Kitaev Yu. E., Goncharuk I. N., ... Evarestov R. A. Phonon dispersion and Raman scattering in hexagonal GaN and AlN. *Physical Review B*. 1998;58(19): 12899–12907. <https://doi.org/10.1103/PhysRevB.58.12899>
23. Feng Y., Saravade V., Chung T.-F., ... Lu N. Strain-stress study of Al_xGa_{1-x}N/AlN heterostructures on c-plane sapphire and related optical properties. *Scientific Reports*. 2019;9(1): 10172. <https://doi.org/10.1038/s41598-019-46628-4>
24. Lughu V., Clarke D. R. Defect and stress characterization of AlN films by Raman spectroscopy. *Applied Physics Letters*. 2006;89(24): 241911. <https://doi.org/10.1063/1.2404938>
25. Zeng Y., Ning J., Zhang J., ... Wang D. Raman analysis of E2 (High) and A1 (LO) phonon to the stress-free GaN grown on sputtered AlN/graphene buffer layer. *Applied Sciences*. 2020;10(24): 8814. <https://doi.org/10.3390/app10248814>
26. Hushur A., Manghnani M. H., Narayan J. Raman studies of GaN/sapphire thin film heterostructures. *Journal of Applied Physics*. 2009;106(5): 054317. <https://doi.org/10.1063/1.3213370>

Information about the authors

Pavel V. Seredin, Dr. Sci. (Phys.–Math.), Full Professor, Head of the Department, Department of Solid State Physics and Nanostructures, Voronezh State University (Voronezh, Russian Federation).

<https://orcid.org/0000-0002-6724-0063>
paul@phys.vsu.ru

Shukrilo Sh. Sharofidinov, Cand. Sci. (Phys.–Math.), Research Fellow, Ioffe Institute (St. Petersburg, Russian Federation).

<https://orcid.org/0000-0003-0354-5981>
shukrillo71@mail.ru

Dmitry L. Goloshchapov, Cand. Sci. (Phys.–Math.), Assistant Professor, Department of Solid State Physics and Nanostructures, Voronezh State University (Voronezh, Russian Federation).

<https://orcid.org/0000-0002-1400-2870>
goloshchapov@phys.vsu.ru

Nikita S. Buylov, Cand. Sci. (Phys.–Math.), Educator, Department of Solid State Physics and Nanostructures, Voronezh State University (Voronezh, Russian Federation).

<https://orcid.org/0000-0003-1793-4400>
buylov@phys.vsu.ru

Konstantin A. Eremeev, student, Department of Solid State Physics and Nanostructures, Voronezh State University (Voronezh, Russian Federation).

<https://orcid.org/0009-0004-9798-6642>
kjcncz2001@gmail.com

Shaira A. Yusupova, Cand. Sci. (Phys.–Math.), Researcher, Laboratory of Power Semiconductor Devices, Department of Solid State Electronics, Ioffe Institute (St. Petersburg, Russian Federation).

sh.yusupova@mail.ioffe.ru

Sergey A. Kukushkin, Dr. Sci. (Phys.–Math.), Professor, Head of Laboratory, Institute for Problems in Mechanical Engineering of the Russian Academy of Sciences (St. Petersburg, Russian Federation).

<https://orcid.org/0000-0002-2973-8645>
sergey.a.kukushkin@gmail.com

Received 25.01.2024; approved after reviewing 05.02.2024; accepted for publication 15.02.2024; published online 01.10.2024.

Translated by Yulia Dymant



Condensed Matter and Interphases

Kondensirovannye Sredy i Mezhfaznye Granitsy
<https://journals.vsu.ru/kcmf/>

Original articles

Research article

<https://doi.org/10.17308/kcmf.2024.26/12228>

Structural and spectroscopic studies of epitaxially overgrown GaN, n-GaN, and n⁺-GaN contact layers

P. V. Seredin^{1✉}, D. L. Goloshchapov¹, D. E. Kostomakha¹, Y. A. Peshkov¹, N. S. Buylov¹,
A. A. Gaivoronskaya¹, A. M. Mizerov², S. N. Timoshnev², M. S. Sobolev², E. V. Ubyivovk³,
V. I. Zemlyakov⁴, P. P. Kutsko⁵, P. L. Parmon⁵

¹Voronezh State University,
Universitetskaya pl. 1, Voronezh 394018, Russian Federation

²Alferov University,
8/3 Khlopina st., St. Petersburg 194021, Russian Federation

³Saint-Petersburg State University,
7-9 Universitetskaya emb., St. Petersburg 199034, Russian Federation

⁴National Research University of Electronic Technology,
1, Shokin Square, Zelenograd, Moscow 124498, Russian Federation

⁵Research Institute of Electronic Technology,
5 Staryh Bolshevikov st., Voronezh 394033, Russian Federation

Abstract

The paper demonstrates that the technology of plasma-assisted molecular beam epitaxy (PA MBE) can be used to form epitaxially overgrown GaN, n-GaN, and n⁺-GaN contact layers with a high structural quality on virtual GaN/c-Al₂O₃ substrates under Ga-enriched conditions at relatively low growth temperatures of ~700 °C.

It was shown that the initial stage of growth of the contact layers was accompanied by effective filtration of dislocations threading from the buffer GaN layer of the virtual substrate formed by MOCVD.

The values of residual stresses calculated using the data of Raman microspectroscopy indicate a high structural quality of GaN, n-GaN, and n⁺-GaN contact layers regardless of the level of silicon doping.

The contact resistance reduced to the pad width determined using the transmission line method for the structure with n⁺-GaN contact layer was ~0.11 Ohm-mm and for the n-GaN contact layer it was ~0.5 Ohm-mm.

Keywords: Molecular beam epitaxy, GaN, n-GaN, and n⁺-GaN contact layers, Virtual substrate, Raman microspectroscopy

Funding: The study was carried out within the framework of the grant of the Ministry of Education and Science of the Russian Federation (grant No. FZGU-2023-0006). GaN, n-GaN, and n⁺-GaN contact layers were synthesized in the framework of the grant of the Ministry of Education and Science of the Russian Federation No. FSRM-2023-0006.

Acknowledgements: The authors are grateful to V. V. Lundin, A. E. Nikolaev (Ioffe Physical-Technical Institute, Russia) and Iurii Kim (Aalto University School of Electrical Engineering, Finland) for providing GaN/c-Al₂O₃ templates for PA MBE synthesis of contact layers.

The authors also express their gratitude to the resource center of Saint Petersburg State University for the use of equipment: the TEM results presented in this paper were obtained using the equipment of the Interdisciplinary Resource Center “Nanotechnologies” of Saint Petersburg State University.

✉ Pavel V. Seredin, e-mail: paul@phys.vsu.ru

© Seredin P. V., Goloshchapov D. L., Kostomakha D. E., Peshkov Y. A., Buylov N. S., Gaivoronskaya A. A., Mizerov A. M., Timoshnev S. N., Sobolev M. S., Ubyivovk E. V., Zemlyakov V. I., Parmon P. L., Kutsko P. P., 2024



The content is available under Creative Commons Attribution 4.0 License.

The research was carried out using the equipment of the Laboratory of Gallium Nitride and Silicon Electronics of Voronezh State University and the Research Institute of Electronic Technology.

For citation: Seredin P. V., Goloshchapov D. L., Kostomakha D. E., Peshkov Y. A., Buylov N. S., Gaivoronskaya A. A., Mizerov A. M., Timoshnev S. N., Sobolev M. S., Ubyivovk E. V., Zemlyakov V. I., Parmon P. L., Kutsko P. P. Structural and spectroscopic studies of epitaxially overgrown GaN, n-GaN, and n⁺-GaN contact layers. *Condensed Matter and Interphases*. 2024;26(3): 526–535. <https://doi.org/10.17308/kcmf.2024.26/12228>

Для цитирования: Середин П. В., Голощачпов Д. Л., Костомаха Д. Е., Пешков Я. А., Буйлов Н. С., Гайворонская А. А., Мизеров А. М., Тимошнев С. Н., Соболев М. С., Убийвовк Е. В., Земляков В. И., Пармон П. Л., Куцько П. П. Структурно-спектроскопические исследования эпитаксиально-доращиваемых контактных слоев GaN, n-GaN и n⁺-GaN. *Конденсированные среды и межфазные границы*. 2024;26(3): 526–535. <https://doi.org/10.17308/kcmf.2024.26/12228>

1. Introduction

Many studies conducted in recent decades have been dedicated to group III nitrides (AIIIN) (third-generation semiconductors) and the extension of the range of their applications [1]. However, the key problem in creating viable AIIIN-based device technology solutions is the choice of a substrate for epitaxial synthesis and the method of integration with it [2–4]. In most cases, lattice-matched GaN substrates are not commercially viable despite the fact that they allow synthesizing GaN-based device heterostructures with better material characteristics and crystalline quality. An alternative solution to this problem is to form the active regions of AIIIN heterostructures by using virtual substrates (templates) of the GaN/substrate type, in which the buffer layer has already been synthesized on a commercially available substrate (Si, SiC, sapphire) by epitaxial technologies. Currently, two methods are mainly used to form GaN/substrate templates: metalorganic chemical vapor deposition (MOCVD) and molecular beam epitaxy (MBE) [3].

The second important issue in the development of AIIIN-based devices is the formation of ohmic contacts, which not only provide the connection between the device structure and the signal processing circuitry, but also are the basis for further improving the performance of final devices. The ohmic contact between metal and semiconductor must not only be compatible, but also durable and temperature stable, [5] taking into account the type of conductivity of the contact layer and technological postoperations.

The formation of high-quality ohmic contact in devices based on wide-gap AIIIN compounds is still an unresolved problem [6]. Defects in AIIIN layers and the tendency to metal oxidation at high temperatures can also affect the contact

properties. Therefore, studies aimed at reducing the contact resistance during the formation of ohmic contacts in AIIIN heterostructures are becoming increasingly relevant today.

Currently, there are a number of technological solutions to reduce the contact resistance, including the use of Ti/Al/X/Au multilayers [7]. It was also shown that the formation of fully buried Ti-based ohmic contacts results in good values of contact resistivity [6]. However, along with the traditional technology of annealing ohmic contacts [5], a wide range of studies are currently being conducted to create ohmic contacts without using the procedure of high-temperature annealing, or so-called non-annealed ohmic contacts [8–13]. In particular, papers [10–13] show that it is possible to form such contacts with a relatively low contact resistance by the epitaxial overgrowth of highly silicon-doped n⁺-GaN contact layers with an electron concentration of more than $1 \cdot 10^{19} \text{ cm}^{-3}$ using the PA MBE technique.

This work presents comparative studies of the structural, morphological, and electrical properties of undoped GaN and silicon-doped n-GaN and n⁺-GaN contact layers synthesized by the PA MBE technique on GaN/c-Al₂O₃ virtual substrates grown using the method of pre-epitaxial cleaning of GaN surfaces of substrates previously developed by the authors and described in detail in [14]. The review of scientific literature has shown that there have been no studies of this kind, which emphasizes the relevance of this work.

2. Materials and methods

During the study, GaN, n-GaN, and n⁺-GaN contact layers were formed using the PA MBE technique on an industrial Veeco Gen 200 setup [14]. Synthesis was carried out on

virtual substrates, i.e. undoped GaN layers with a thickness of about 2.5 μm grown on sapphire substrates with (0001) orientation by metal organic chemical vapor deposition (MOCVD) [18].

After MOCVD synthesis, GaN/c-Al₂O₃ virtual substrates were extracted to the atmosphere for standard preparation procedures for PA MBE layer synthesis, which are described in detail in [14].

Immediately before the start of the PA MBE growth of the contact layers, the surfaces of the virtual substrates were cleaned following the procedure in [14]. First, the pre-epitaxial cleaning of virtual substrates was carried out in the growth chamber of the PA MBE system in a flow of activated nitrogen particles with a gradual increase in the temperature of the substrate from $T_s = 400$ °C to $T_s = 600$ °C followed by exposure of the substrate surface to a flow of activated nitrogen at a fixed value of $T_s = 600$ °C for 1 hour. This was followed by the final procedure of GaN surface cleaning based on the deposition of several Ga monolayers on the surface of the virtual substrate followed by thermal desorption of the deposited Ga from the surface. The study involved five periods of gallium precipitation/desorption on the GaN surface of the virtual substrate heated to $T_s = 700$ °C, i.e. to a temperature at which there was still no intensive decomposition of GaN, however, the flow of the thermal desorption of Ga from the liquid phase was $F_{\text{Ga}}^{\text{des}} \sim 0.3$ $\mu\text{m}/\text{h}$ [15]. During each cycle of the stage, the precipitation of gallium atoms was completed within a 10 second exposure of GaN on the surface of the virtual substrate in a gallium flow $F_{\text{Ga}} \sim 0.4$ $\mu\text{m}/\text{h}$, which corresponded to the precipitation of about one Ga monolayer. The Ga flow was then shut off with a valve for 10 seconds to enable thermal desorption of the precipitated gallium from the GaN surface. Throughout the procedure of gallium adsorption/desorption, there was a “linear” pattern of reflected high energy electron diffraction (RHEED) with bright and thin reflexes characteristic of a relatively smooth GaN surface.

Immediately after the pre-epitaxial cleaning of the surfaces of the virtual substrates, undoped (sample A) and silicon-doped (samples B and C) GaN layers with thicknesses of about 250 nm were grown on the virtual substrates by PA MBE

at constant values of $T_s = 700$ °C, $F_{\text{Ga}} \sim 0.25$ $\mu\text{m}/\text{h}$, $F_{\text{N}} \sim 0.05$ $\mu\text{m}/\text{h}$ and different temperatures of the silicon effusion source $T_{\text{Si}} = 1,020$ – $1,110$ °C. The general scheme of samples with GaN, n-GaN, and n⁺-GaN contact layers is shown in Fig. 1.

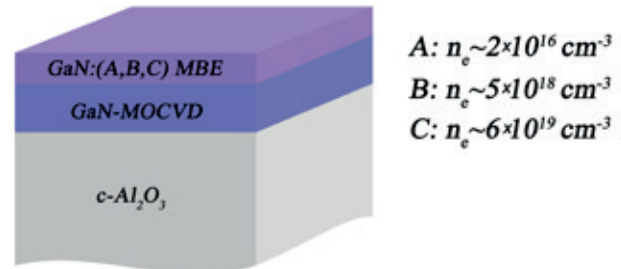


Fig. 1. Schematic representation of heterostructures with contact layers: sample A – GaN; sample B – n-GaN; sample C – n⁺-GaN

The GaN/c-Al₂O₃ virtual substrate with a precisely oriented c-Al₂O₃(0001) substrate were used to synthesize samples A and C, while the c-Al₂O₃ substrate with a deviation of 0.5° from [0001] direction was used to produce sample B.

The crystal structure of the samples was studied using high-resolution X-ray diffraction using a DRON-8T X-ray diffractometer with CuK α radiation and an angular reproducibility of ± 0.0001 °.

A RamMics 532 Raman microscope (EnSpectr, Moscow, Russia) with a radiation wavelength of 532 nm was used to obtain Raman spectra. The scanning was carried out using a 20 \times lens, the focal spot size of ~ 8 μm , and power of 30 mW. Raman spectra were recorded in the (xy)⁻ geometry in the range of 100–2,000 cm^{-1} and a spectral resolution of 1 cm^{-1} . The position of the lines and the values of the full width at half maximum (FWHM) for both the GaN and Al₂O₃ layers was determined by approximating the maxima using a set of Voigt functions [16]. OriginPro software was used for processing. Spectral position of the maxima of the Raman lines was determined by measuring the position of the LO-mode of the Si calibration plate. Calibration was performed both before and after each sample measurement using a $\times 20$ lens.

The quality of surface and hetero-interfaces was studied using scanning transmission electron microscopy (STEM) and high angular annular dark-field scanning transmission electron microscopy (HAADF-STEM) on a Zeiss Libra 200

FE transmission electron microscope with an accelerating voltage of 200 keV.

Ohmic contacts were metalized on a Kurt J. Lesker AXXIS unit for the electron-beam sputtering of metals.

Electrophysical measurements were performed at room temperature in a four-probe van der Pauw configuration on an Ecopia HMS-3000 measurement system.

Contact resistance was measured using the transmission line method (TLM).

3. Results and discussion

The characteristics of the epitaxial layers of GaN, such as surface structure and morphology, crystalline perfection, and density of the threading dislocations, play an important role in determining the characteristics of the heterostructure. Therefore, the surface and hetero-interface were first studied.

Images of the surface and profile of the GaN contact layers obtained at different levels of silicon doping are shown in the STEM and HAADF-STEM images (Fig. 2). For all samples, regardless of the size of the introduced impurity, there was a good smooth surface morphology with pits or V-shaped defects evenly distributed on the surface. These defects had a characteristic shape of inverted hexagonal pyramids (see the insert to Fig. 2a). These pits formed by low-index crystallographic planes can be observed during the deposition of nitride films on various substrates [17,18].

Since GaN/sapphire templates were used to form the GaN, n-GaN, and n⁺-GaN contact layers, it is obvious that the heteropairs should have a significant discrepancy in both the parameters

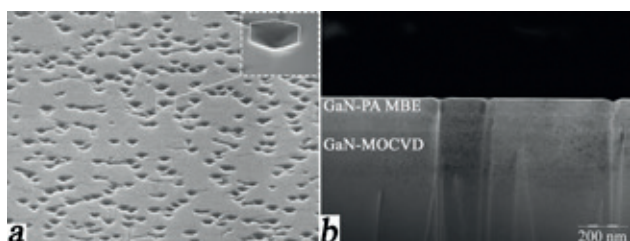


Fig. 2. Image of sample C, in which the contact n⁺-GaN layer was synthesized by the MIIЭ ПIA method on a virtual GaN/c-Al₂O₃ substrate under Ga-enriched growth conditions: STEM image of the surface (a); HAADF-STEM image of the heterointerface (b)

of the crystal lattices and the thermal expansion coefficients (16 and 34%, respectively). Both factors led to deformations and stress distribution gradients in the thick GaN buffer layer [19]. They were also the driving force for the formation of V-shaped pits in the upper contact epitaxial layers.

Previously, it was shown that the bottom of each pit is always associated with a threading dislocation (TD), and the density of the defects is almost always equivalent to the density of TDs [20]. Thus, the formation of V-shaped defects in the upper GaN, n-GaN, and n⁺-GaN contact layers can be explained both by the threading dislocations from the virtual substrate and the emergence of new dislocations on the interface between the surface of the virtual substrate and the GaN contact layer due to insufficiently effective pre-epitaxial cleaning of the template surface.

To study the evolution of threading dislocations during the PA MBE synthesis of GaN layers on GaN/c-Al₂O₃ templates, cross-section of one of the samples with an upper n⁺-GaN contact layer was studied by dark-field scanning transmission electron microscopy. Figure 2b shows a typical HAADF-STEM image of the interface between the GaN layer of the virtual substrate and the upper n⁺-GaN contact layer obtained by PA MBE.

The analysis of the HAADF-STEM data allows concluding that threading dislocations in the GaN, n-GaN, and n⁺-GaN contact layers were filtered. It was seen that the number of threading dislocations in the upper PA MBE layer was smaller than in the lower buffer GaN layer of the GaN/c-Al₂O₃ virtual substrate grown by MOCVD. Some of the TDs were filtered near the interface with the upper GaN contact layer, though some dislocations were still present.

The observed effect of filtration of threading dislocations may be due to the evolution of the surface morphology of the GaN contact layer at the initial stage of PA MBE synthesis on the GaN surface of the virtual substrate. In particular, the relatively low substrate temperatures used in the PA MBE synthesis of GaN could lead to the formation of three-dimensional GaN nucleation islands, which quickly grew and coalesced into a continuous GaN layer with a smooth surface

morphology, as shown in [21]. However, during the initial stage of the island PA MBE growth of GaN, it became energetically more advantageous for the TDs to deviate from the initial vertical direction of their propagation [22]. The energy gain was due to a reduction in the TD energy since the line of the threading dislocation became shorter when it deviated to the edge of the island as compared to the energy of dislocations propagating in the direction of the GaN layer growth.

In addition, TEM studies of the synthesized samples also showed that there were no additional defects in the GaN, n-GaN, and n⁺-GaN contact layers, which could appear as a result of insufficiently effective cleaning of the surface of the GaN MOCVD layer of the virtual substrate from foreign atoms or due to surface degradation that could occur during the process of pre-epitaxial cleaning. This indicates the effectiveness of the used method of pre-epitaxial cleaning of the GaN surface of the virtual substrate.

The crystalline structure and the quality of epitaxial heterostructures were studied using high-resolution X-ray diffraction (XRD), which can provide direct information on the effect of silicon impurity on the crystalline properties of the AIII⁺BV and AIII⁺N semiconductors [23, 24]. Figure 3 shows the results of XRD measurements over a wide range of Bragg angles.

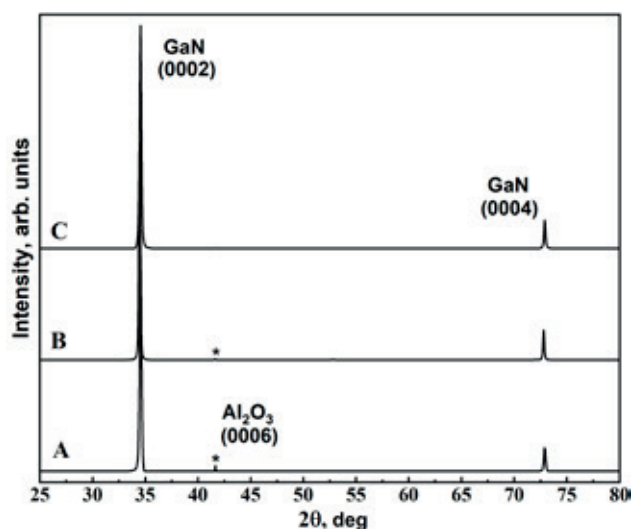


Fig. 3. XRD 2 θ -scans for samples with GaN, n-GaN and n⁺-GaN contact layers. Reflexes from the substrate are indicated by the index*

XRD 2 θ -scans of all samples had maxima that also belonged to 0002 and 0004 GaN reflections with a wurtzite lattice. However, the scans also showed low-intensity reflexes belonging to the sapphire substrate. The presence of diffraction maxima of the same basal series on XRD scans suggests the monocrystalline state of the epitaxial GaN layers.

Additional structural information on the properties of the GaN, n-GaN, and n⁺-GaN contact layers was obtained by Raman spectroscopy, which allows studying the features of the crystal structure of thin epitaxial films and their perfection on the scale of crystal lattice parameters [25]. The Raman spectra of the samples are shown in Fig. 4. The Raman spectra shown in Figure 4 are typical of the *c*-plane (0001) of the GaN single crystal. They have maxima of about ~567 and 734 cm⁻¹ (Fig. 4a,b), which, in accordance with the group theory for GaN with a wurtzite crystal lattice, are transverse A₁(TO) and E₂^{high} phonon modes [26, 27]. However, the peaks present in the spectra in the region of 415 cm⁻¹ and 750 cm⁻¹ are typical characteristic longitudinal optical (LO) modes with A_{1g} and E_{1g}(LO) symmetry, which belong to the sapphire substrate [28].

Attention should be paid to another spectral feature observed in Raman scattering for the n-GaN and n⁺-GaN contact layers (samples B and C, see insert to Fig. 4d). In the region of 465–500 cm⁻¹, there was a low-intensity shoulder, the appearance of which was associated with a high level of silicon impurity in the n-GaN and n⁺-GaN contact layers. It was previously shown that the appearance of this phonon mode in the Raman spectra is associated with the formation of Si clusters in various materials [29, 30]. It should also be noted that n⁺-GaN had low-intensity Raman bands in the region of 505 and 517 cm⁻¹. According to [29, 30], the appearance of these oscillations in the Raman spectra suggests the formation of both silicon nanocrystals of various sizes and amorphous silicon.

The frequency position of active oscillations from GaN and c-Al₂O₃ in Raman spectra recorded using a x20 lens is shown in Table 1.

According to the results of our study, the value of the full width at half maximum (FWHM) of the Raman mode E₂^{high} GaN in the spectra of the GaN, n-GaN, and n⁺-GaN contact layers was ~5.0–

on sapphire substrates [33]. However, the residual biaxial stresses in the n-GaN layer (sample B) were at a higher level of $\sigma_{xx} \sim 0.4$ GPa, which was probably due to the use of a misoriented sapphire substrate when creating a GaN/c-Al₂O₃ virtual substrate (see Methods).

During the last stage of the studies, ohmic Ti/Al contacts (20/100 nm) were formed on the surface of the samples using magnetron sputtering. After that, the mobility and concentration of carriers and resistivity were determined according to Hall measurements using the van der Pauw method. The results are given in Table 2.

Table 2. Hall measurement data by the van der Pauw method

Sample	Mobility of carriers cm ² /Vs	Carrier concentration, cm ⁻³	Resistivity Ohm·cm
A (GaN)	–	2·10 ¹⁶	–
B (n-GaN)	265	–5·10 ¹⁸	4.7·10 ⁻²
C (n ⁺ -GaN)	105	–6·10 ¹⁹	1·10 ⁻²

The contact pads of the test structure of ohmic contacts had an annular geometry with a length of the outer circumference of 400 μm. Using such topology allowed measuring contact resistance without isolating the active elements [34]. As a result, using the transmission line method (TLM) in accordance with [35] allowed determining the contact resistance reduced to the pad width, which for the structure with the n⁺-GaN contact layer (sample C) was ~ 0.11 Ohm·mm, and for the n-GaN contact layer (sample B) ~ 0.5 Ohm·mm. Both values are in agreement with the results of the van der Pauw method (see Table 2).

It should be noted that it appeared challenging to measure the Hall characteristics for the structure with the GaN contact layer (sample A) due to the high values of resistivity (~ 1·10⁴ Ohm·cm), which may indicate a sufficiently low intrinsic conductivity of this layer.

4. Conclusions

The study showed that plasma-assisted molecular beam epitaxy can be used to create overgrown GaN, n-GaN, and n⁺-GaN contact layers on GaN/c-Al₂O₃ virtual substrates under Ga-enriched conditions. This involves effective filtration of dislocations threading from the

buffer GaN layer of the virtual substrate formed by MOCVD.

Residual stresses calculated using the data of Raman microspectroscopy indicate a high structural quality of GaN, n-GaN, and n⁺-GaN contact layers regardless of the level of silicon doping.

Contact resistance reduced to the pad width determined by the transmission line method for the structure with the n⁺-GaN contact layer was ~ 0.11 Ohm·mm, and for the n-GaN contact layer it was ~ 0.5 Ohm·mm.

Contribution of the authors

The authors contributed equally to this article.

Conflict of interests

The authors declare that they have no known competing financial interests or personal relationships that could have influenced the work reported in this paper.

References

1. Liu A.-C., Lai Y.-Y., Chen H.-C., Chiu A.-P., Kuo H.-C. A Brief overview of the rapid progress and proposed improvements in gallium nitride epitaxy and process for third-generation semiconductors with wide bandgap. *Micromachines*. 2023;14(4): 764. <https://doi.org/10.3390/mi14040764>
2. Elwaradi R., Mehta J., Ngo T. H., ... Cordier Y. Effects of GaN channel downscaling in AlGaIn–GaN high electron mobility transistor structures grown on AlN bulk substrate. *Journal of Applied Physics*. 2023;133(14): 145705. <https://doi.org/10.1063/5.0147048>
3. Zeng X., Wu Y., He G., Zhu W., Ding S., Zeng Z. High-pure AlN crystalline thin films deposited on GaN at low temperature by plasma-enhanced ALD. *Vacuum*. 2023;213: 112114. <https://doi.org/10.1016/j.vacuum.2023.112114>
4. Yang L., Huang W., Wang D., ... Wang X. AlN/GaN HEMTs with f_{max} exceeding 300 GHz by using Ge-doped n⁺⁺GaN ohmic contacts. *ACS Applied Electronic Materials*. 2023;5(9):4786–4791. <https://doi.org/10.1021/acsaelm.3c00555>
5. Wu C.-Y., Chao T.-S., Chou Y.-C. A high thermal stability ohmic contact for GaN-based devices. *Nanoscale Advances*. 2023;5(19): 5361–5366. <https://doi.org/10.1039/D3NA00491K>
6. Greco G., Iucolano F., Roccaforte F. Ohmic contacts to gallium nitride materials. *Applied Surface Science*. 2016;383: 324–345. <https://doi.org/10.1016/j.apsusc.2016.04.016>

7. Liu Y. Recent research on ohmic contacts on GaN-based materials. *IOP Conference Series: Materials Science and Engineering*. 2020;738(1): 012007. <https://doi.org/10.1088/1757-899X/738/1/012007>
8. Ambacher O. Growth and applications of group III-nitrides. *Journal of Physics D: Applied Physics*. 1998;31(20): 2653–2710. <https://doi.org/10.1088/0022-3727/31/20/001>
9. Yue Y., Hu Z., Guo J., ... Xing H. InAlN/AlN/GaN HEMTs with regrown ohmic contacts and f_T of 370 GHz. *IEEE Electron Device Letters*. 2012;33(7): 988–990. <https://doi.org/10.1109/LED.2012.2196751>
10. Hong S.J., Kim K. (Kevin). Low-resistance ohmic contacts for high-power GaN field-effect transistors obtained by selective area growth using plasma-assisted molecular beam epitaxy. *Applied Physics Letters*. 2006;89(4): 042101. <https://doi.org/10.1063/1.2234566>
11. Zheng Z., Seo H., Pang L., Kim K. (Kevin). Nonalloyed ohmic contact of AlGaIn/GaN HEMTs by selective area growth of single-crystal n⁺-GaN using plasma assisted molecular beam epitaxy. *Physica Status Solidi (a)*. 2011;208(4): 951–954. <https://doi.org/10.1002/pssa.201026557>
12. Guo J., Cao Y., Lian C., ... Xing H. (Grace). Metal-face InAlN/AlN/GaN high electron mobility transistors with regrown ohmic contacts by molecular beam epitaxy. *Physica Status Solidi (a)*. 2011;208(7): 1617–1619. <https://doi.org/10.1002/pssa.201001177>
13. Bo Song, Mingda Zhu, Zongyang Hu, ... Xing H.G. Ultralow-leakage AlGaIn/GaN high electron mobility transistors on Si with non-alloyed regrown ohmic contacts. *IEEE Electron Device Letters*. 2016;37(1): 16–19. <https://doi.org/10.1109/LED.2015.2497252>
14. Mizerov A. M., Timoshnev S. N., Nikitina E. V., ... Bouravleuv A. D. On the specific features of the plasma-assisted MBE synthesis of n⁺-GaN layers on GaN/c-Al₂O₃ templates. *Semiconductors*. 2019;53(9): 1187–1191. <https://doi.org/10.1134/S1063782619090112>
15. Brandt O., Yang H., Ploog K. H. Surface kinetics of zinc-blende (001) GaN. *Physical Review B*. 1996;54(7): 4432–4435. <https://doi.org/10.1103/PhysRevB.54.4432>
16. Wells R. J. Rapid approximation to the Voigt/Faddeeva function and its derivatives. *Journal of Quantitative Spectroscopy and Radiative Transfer*. 1999;62(1): 29–48. [https://doi.org/10.1016/S0022-4073\(97\)00231-8](https://doi.org/10.1016/S0022-4073(97)00231-8)
17. Zsebök O., Thordson J. V., Andersson T. G. Surface morphology of MBE-grown GaN on GaAs(001) as function of the N/Ga-ratio. *MRS Internet Journal of Nitride Semiconductor Research*. 1998;3: 1–11. <https://doi.org/10.1557/S1092578300000867>
18. Zsebök O., Thordson J. V., Gunnarsson J. R., Zhao Q. X., Ilver L., Andersson T. G. The effect of the first GaN monolayer on the nitridation damage of molecular beam epitaxy grown GaN on GaAs(001). *Journal of Applied Physics*. 2001;89(7): 3662–3667. <https://doi.org/10.1063/1.1345516>
19. Liao H., Wei T., Zong H., ... Hu X. Raman investigation on the surface carrier concentration of single GaN microrod grown by MOCVD. *Applied Surface Science*. 2019;489: 346–350. <https://doi.org/10.1016/j.apsusc.2019.05.346>
20. Lee Y.-J., Kuo H.-C., Lu T.-C., ... Lin S.-Y. Study of GaN-based light-emitting diodes grown on chemical wet-etching-patterned sapphire substrate with V-shaped pits roughening surfaces. *Journal of Lightwave Technology*. 2008;26(11): 1455–1463. <https://doi.org/10.1109/JLT.2008.922151>
21. Seredin P. V., Lenshin A. S., Mizerov A. M., Leiste H., Rinke M. Structural, optical and morphological properties of hybrid heterostructures on the basis of GaN grown on compliant substrate por-Si(111). *Applied Surface Science*. 2019;47(6): 1049–1060. <https://doi.org/10.1016/j.apsusc.2019.01.239>
22. Ruvimov S., Liliental-Weber Z., Washburn J., ... Weber E. R. Effect of N/Ga flux ratio in GaN buffer layer growth by MBE on (0001) sapphire on defect formation in the GaN main layer. *MRS Proceedings*. 1999;572: 295. <https://doi.org/10.1557/PROC-572-295>
23. Seredin P. V., Ternovaya V. E., Glotov A. V., ... Prutskij T. X-ray diffraction studies of heterostructures based on solid solutions Al_xGa_{1-x}As_yP_{1-y}:Si. *Physics of the Solid State*. 2013;55(10): 2161–2164. <https://doi.org/10.1134/S1063783413100296>
24. Seredin P. V., Glotov A. V., Lenshin A. S., ... Rinke M. Structure and optical properties of heterostructures based on MOCVD (Al_xGa_{1-x}As_{1-y}P_y)_{1-z}Si_z alloys. *Semiconductors*. 2014;48(1): 21–29. <https://doi.org/10.1134/S1063782614010217>
25. Seredin P. V., Goloshchapov D. L., Lenshin A. S., Mizerov A. M., Zolotukhin D. S. Influence of por-Si sublayer on the features of heteroepitaxial growth and physical properties of In_xGa_{1-x}N/Si(111) heterostructures with nanocolumn morphology of thin film. *Physica E: Low-dimensional Systems and Nanostructures*. 2018;104: 101–110. <https://doi.org/10.1016/j.physe.2018.07.024>
26. Zeng Y., Ning J., Zhang J., ... Wang D. Raman analysis of E2 (High) and A1 (LO) phonon to the stress-free GaN grown on sputtered AlN/graphene buffer layer. *Applied Sciences*. 2020;10(24): 8814. <https://doi.org/10.3390/app10248814>
27. Davydov V. Yu., Kitaev Yu. E., Goncharuk I. N., ... Evarestov R. A. Phonon dispersion and Raman scattering in hexagonal GaN and AlN. *Physical Review B*. 1998;58(19): 12899–12907. <https://doi.org/10.1103/PhysRevB.58.12899>
28. Behera S., Khare A. Characterization of sapphire (α -Al₂O₃) thin film fabricated by pulsed laser deposition. In: *13th International Conference on Fiber*

Optics and Photonics. Kanpur: OSA; 2016; P1A.15. Available at: <https://opg.optica.org/abstract.cfm?URI=Photonics-2016-P1A.15>

29. Terekhov V. A., Terukov E. I., Undalov Y. K., ... Trapeznikova I. N. Effect of plasma oxygen content on the size and content of silicon nanoclusters in amorphous SiO_x films obtained with plasma-enhanced chemical vapor deposition. *Symmetry*. 2023;15(9): 1800. <https://doi.org/10.3390/sym15091800>

30. Solonenko D., Gordan O. D., Le Lay G., Zahn D. R. T., Vogt P. Comprehensive Raman study of epitaxial silicene-related phases on Ag(111). *Beilstein Journal of Nanotechnology*. 2017;8: 1357–1365. <https://doi.org/10.3762/bjnano.8.137>

31. Park A. H., Seo T. H., Chandramohan S., ... Suh E.-K. Efficient stress-relaxation in InGaN/GaN light-emitting diodes using carbon nanotubes. *Nanoscale*. 2015;7(37): 15099–15105. <https://doi.org/10.1039/C5NR04239A>

32. Tripathy S., Chua S. J., Chen P., Miao Z. L. Micro-Raman investigation of strain in GaN and Al_xGa_{1-x}N/GaN heterostructures grown on Si(111). *Journal of Applied Physics*. 2002;92(7): 3503–3510. <https://doi.org/10.1063/1.1502921>

33. Talwar D. N., Lin H.-H., Chuan Feng Z. Anisotropic optical phonons in MOCVD grown Si-doped GaN/sapphire epilayers. *Materials Science and Engineering: B*. 2020;260: 114615. <https://doi.org/10.1016/j.mseb.2020.114615>

34. Klootwijk J. H., Timmering C. E. Merits and limitations of circular TLM structures for contact resistance determination for novel III-V HBTs In: *Proceedings of the 2004 International Conference on Microelectronic Test Structures (IEEE Cat. No.04CH37516)*. Awaji Yumebutai, Japan: IEEE; 2004; 247–252. Available at: <http://ieeexplore.ieee.org/document/1309489/>

35. Egorkin V. I., Zemlyakov V. E., Nezhentsev A. V., Garmash V. I., Kalyuzhnyi N. A., Mintairov S. A. Investigation of alloyed ohmic contacts in epitaxial tellurium-doped gallium arsenide layers. *Russian Microelectronics*. 2018;47(6): 388–392. <https://doi.org/10.1134/S1063739718060045>

Information about the authors

Pavel V. Seregin, Dr. Sci. (Phys.–Math.), Full Professor, Head of the Department, Department of Solid State Physics and Nanostructures, Voronezh State University (Voronezh, Russian Federation).

<https://orcid.org/0000-0002-6724-0063>
paul@phys.vsu.ru

Dmitry L. Goloshchapov, Cand. Sci. (Phys.–Math.), Assistant Professor, Department of Solid State Physics and Nanostructures, Voronezh State University (Voronezh, Russian Federation).

<https://orcid.org/0000-0002-1400-2870>
goloshchapov@phys.vsu.ru

Danila E. Kostomakha, graduate student, Department of Solid State Physics and Nanostructures, Voronezh State University (Voronezh, Russian Federation).

danilkostomaha@gmail.com

Yaroslav A. Peshkov, Cand. Sci. (Phys.–Math.), Research Assistant, Department of Solid State Physics and Nanostructures, Voronezh State University (Voronezh, Russian Federation).

<https://orcid.org/0000-0003-0939-0466>
tangar77@mail.ru

Nikita S. Buylov, Cand. Sci. (Phys.–Math.), Educator, Department of Solid State Physics and Nanostructures, Voronezh State University (Voronezh, Russian Federation).

<https://orcid.org/0000-0003-1793-4400>
buylov@phys.vsu.ru

Alisa A. Gaivoronskaya, student, Department of Solid State Physics and Nanostructures, Voronezh State University (Voronezh, Russian Federation).

alisa.a.gaivoronskaya@gmail.com

Andrey M. Mizerov, Cand. Sci. (Phys.–Math.), Leading Researcher, Alferov University (St. Petersburg, Russian Federation).

<https://orcid.org/0000-0002-9125-6452>
andrey@mizerov@rambler.ru

Sergey N. Timoshnev, Cand. Sci. (Phys.–Math.), Leading Researcher, Alferov University (St. Petersburg, Russian Federation).

<https://orcid.org/0000-0002-9294-3342>
timoshnev@mail.ru

Maksim S. Sobolev, Cand. Sci. (Phys.–Math.), Acting Head of the Laboratory of Nanoelectronics, Alferov University (St. Petersburg, Russian Federation).

<https://orcid.org/0000-0001-8629-2064>
sobolevsm@gmail.com

Evgeniy V. Ubyivovk, Cand. Sci. (Phys.–Math.), Senior Researcher, Research Laboratory of Mechanics of Advanced Bulk Nanomaterials for Innovative Engineering Applications, Saint Petersburg State University (St. Petersburg, Russian Federation).

<https://orcid.org/0000-0001-5828-4243>
ubyivovk@gmail.com

Valeriy E. Zemlyakov, Cand. Sci. (Eng.), Leading Researcher, Laboratory of Nanoelectronics Element Base, National Research University of Electronic Technology (Moscow, Russian Federation).

<https://orcid.org/0000-0001-5681-9603>
vzml@rambler.ru

Pavel P. Kutsko, Cand. Sci. (Eng.), General Director, Research Institute of Electronic Technology (Voronezh, Russian Federation).

kutsko@niiet.ru

Pavel L. Parmon, Director of Quality, Research Institute of Electronic Technology (Voronezh, Russian Federation).

p.parmon@niiet.ru

Received 26.02.2024; approved after reviewing 26.04.2024; accepted for publication 15.05.2024; published online 01.10.2024.

Translated by Irina Charychanskaya



Condensed Matter and Interphases

Kondensirovannye Sredy i Mezhfaznye Granitsy
<https://journals.vsu.ru/kcmf/>

Original articles

Research article

<https://doi.org/10.17308/kcmf.2024.26/12229>

Nanocrystalline films based on YCrO_3 and LaCrO_3 yttrium and lanthanum chromites doped with strontium ions Sr^{2+} as a basis for semiconductor gas sensors

M. A. Yakimchuk[✉], E. S. Eliseeva, V. F. Kostryukov

Voronezh State University,
Universitetskaya pl. 1, Voronezh 394018, Russian Federation

Abstract

For the production of gas-sensitive sensors, easily obtained nanostructured substances are required. Therefore, one of the most important scientific problems is the search for new compositions and an improvement in the used materials. The aim of this study was the creation of thin-film materials based on yttrium and lanthanum chromite nanopowders YCrO_3 and LaCrO_3 , doped with strontium ions, and the identification of their gas-sensitive properties.

The synthesis of nanopowders was carried out by the sol-gel method for LaCrO_3 and the citrate method for YCrO_3 . Doped powders were obtained using the same synthesis methods as the original samples. The phase and elemental composition of the obtained samples was determined. The result of this study demonstrated that the actual composition of the nanopowders is close to the nominal one. Gas-sensitive properties were determined by measuring the specific surface resistance of the obtained samples to the content of carbon monoxide CO with a concentration of 50 ppm.

It was found that the obtained samples possess *n*-type of conductivity and a good response to the presence of traces of carbon monoxide. Yttrium chromite-based nanofilms exhibit better gas-sensitive response compared to LaCrO_3 . The maximum value was obtained for $\text{Y}_{0.9}\text{Sr}_{0.1}\text{CrO}_3$, demonstrating a gas sensitive response of 2.83 at a temperature of 200 °C.

Keywords: Semiconductors, Gas sensitivity, Yttrium chromite, Lanthanum chromite, Doping, Nanofilms, Nanopowders

Acknowledgements: The results of the research were obtained using the equipment of the Centre for the Collective Use of Scientific Equipment of Voronezh State University.

For citation: Yakimchuk M. A., Eliseeva E. S., Kostryukov V. F. Nanocrystalline films based on YCrO_3 and LaCrO_3 yttrium and lanthanum chromites doped with strontium ions Sr^{2+} as a basis for semiconductor gas sensors. *Condensed Matter and Interphases*. 2024;26(3): 536–546. <https://doi.org/10.17308/kcmf.2024.26/12229>

Для цитирования: Якимчук М. А., Елисеева Е. С., Кострюков В. Ф. Нанокристаллические пленки на основе хромитов иттрия и лантана YCrO_3 и LaCrO_3 , допированных ионами стронция Sr^{2+} как основа полупроводниковых газовых сенсоров. *Конденсированные среды и межфазные границы*. 2024;26(3): 536–546. <https://doi.org/10.17308/kcmf.2024.26/12229>

✉ Milena A. Yakimchuk, e-mail: yakimchuk.720.46@gmail.com

© Yakimchuk M. A., Eliseeva E. S., Kostryukov V. F., 2024



The content is available under Creative Commons Attribution 4.0 License.

1. Introduction

Production safety is one of the main problems today. Emitted toxic gases require immediate detection for subsequent timely elimination. Therefore, gas-sensitive sensors are used; and the search for modern material compositions that allow detecting small concentrations of gases in a short time is carried out.

Today, gas sensors based on *n*-type semiconductors are widely used. The most significant progress was achieved in the development of gas-sensing transistors, Schottky barrier devices, and semiconductor gas-sensing resistors [1]. All semiconductors with the electronic type of conductivity have a sensory response, but wide-bandgap semiconductors are widely used. Such semiconductors include: SnO_2 , ZnO , In_2O_3 , WO_3 , characterized by the highest gas sensitivity. Important physical and chemical properties of these materials are the electronic type of conductivity, transparency in a wide range of the electromagnetic radiation spectrum and high surface reactivity [2–6]. At the same time, semiconductors with *p*-type conductivity can also act as gas sensors [7], however, in this case, oxidizing gases act as priority detected gases.

The need for detector selectivity leads to the search for more complex structural compounds, one of which is the perovskite – orthorhombic structure of the Pbmn spatial group with the general formula ABO_3 . There is a wide variety of gas sensors with a perovskite structure capable of detecting various gases and volatile compounds.

One of common material is a composite of iron oxide and lanthanum oxide, of perovskite type LaFeO_3 . It has both high ionic and electronic conductivity at high temperatures and is suitable for detecting gases such as butane, propane, propylene, butylenes, ethylene, methane, formaldehyde, and carbon dioxide [8–10].

In addition to lanthanum ferrite, its close analogue, lanthanum cobaltite, is also actively used, which exhibits satisfactory sensory properties for reducing gases such as carbon monoxide and ammonia vapors [11].

Alternative gas sensors with a perovskite structure are transition metal chromites. Their main advantage is the ability to detect inorganic gases – carbon monoxide and dioxide, nitrogen oxide (II) [12, 13]. Gas detection occurs at slightly

higher concentrations of gases than when using a lanthanum ferrite-based gas sensor. The response time and recovery time is up to 3 minutes, however, with a higher concentration of the test gas. Chromites are also promising due to their low cost, selectivity for specific gases and mechanical strength, although the operating temperatures of the sensors also remain high [14–16]. Due to its simplicity and cost-effectiveness, the sol-gel method remains the main method of synthesis of such materials [17–19].

Further developments in chromite-based gas sensors are aimed at reducing operating temperatures and gas concentrations required for detection. The aim of this study was to create nanocrystalline films based on yttrium and lanthanum chromite nanopowders doped with strontium ions, as well as to identify their gas-sensitive properties depending on the dopant content.

2. Experimental

Doped nanopowders of lanthanum chromite were obtained by the sol-gel method. The work used a technique used in our laboratory for the synthesis of ferrites [20], and adapted for lanthanum chromite. A mixture of $\text{La}(\text{NO}_3)_3$, $\text{Cr}(\text{NO}_3)_3$, and $\text{Sr}(\text{NO}_3)_2$ solutions was added to boiling water with constant stirring using a magnetic stirrer, based on their stoichiometric ratios to obtain LaCrO_3 , $\text{La}_{0.95}\text{Sr}_{0.05}\text{CrO}_3$, and $\text{La}_{0.9}\text{Sr}_{0.1}\text{CrO}_3$. The resulting solutions were boiled for 5 min. Then, while stirring, ammonia water was added dropwise through a separatory funnel, taken in a quantity sufficient for the complete precipitation of cations, based on the stoichiometric ratio of the reagents. The solutions were stirred for another 5 min. The resulting precipitates were separated on a vacuum filter and dried for several days to constant weight at room temperature. The final nanopowders were obtained by heat treatment of dehydrated precipitates in a muffle furnace (SNOL 8.2/1100) at a temperature of 950 °C for 1 h.

The citrate method was used to obtain yttrium chromite (with and without dopant). The technique was also similar to that of the synthesis of yttrium ferrite [21] and adapted for chromite. The $\text{Cr}(\text{NO}_3)_3 \cdot 9\text{H}_2\text{O}$, $\text{Y}(\text{NO}_3)_3 \cdot 6\text{H}_2\text{O}$, and $\text{Sr}(\text{NO}_3)_2 \cdot 4\text{H}_2\text{O}$ were dissolved in distilled water

in stoichiometric proportion. The solutions were heated for better dissolution of the salts and then cooled. Then, while stirring, the calculated amount of ammonia was added dropwise until precipitate was formed. After the addition of citric acid, it was heated again until the precipitate dissolved. The solutions were then completely evaporated and burned until ash was formed. The resulting powders were annealed in a muffle furnace (SNOL 8.2/1100) at a temperature of 950 °C for 1 h.

For the study of the gas-sensitive properties, the synthesized powders were dispersed in ethyl alcohol with the addition of cetyltrimethylammonium bromide (CTAB) as a surfactant until a paste was formed. Then the synthesized powders were applied to a conductive element (silicon wafer) using the *spin-coating* method (SpinNXG-P1H unit) and annealed for 1 h at 100 °C. The mode of application created a fixed thickness of $150 \pm 5\%$ nm. Electrical contacts to the thin films, located at the vertices of the square silicon wafer, consisted of tungsten carbide with a diameter of 0.5 mm. The distance between contacts was 1 mm.

The phase composition of nanopowders was determined using an X-ray diffractometer Thermo ARL X'TRA (X-ray radiation, $\lambda = 0.154$ nm), which included a computer equipped with software for automatic shooting and processing of diffractograms. The initial shooting angle is $2\theta = 10^\circ$, the final angle is $2\theta = 70^\circ$, step = 0.02. The decoding of the obtained diffractograms was carried out using the JCPDC PCPDFWIN database [22]. In this work, the elemental composition of the obtained powders was studied by local X-ray spectral microanalysis [23] on a JEOL-6510LV installation with a Bruker energy dispersive microanalysis system. The specific surface resistance of the obtained thin films was studied by the Van der Pauw method at the CIUS-4 installation. The specific surface resistance of the samples, necessary to establish gas-sensitive properties, was measured in air, as well as in the presence of the test gas (CO) with a concentration of 50 ppm. The technique was similar to that described in [24]. The required concentration of carbon monoxide was achieved by diluting the certified gas mixture with dry synthetic air. The measurements were carried out in a stationary

system (a closed chamber with a volume of 50 liters). The electrical contacts to the thin films, located at the vertices of the square, consisted of tungsten carbide with a diameter of 0.5 mm. The distances between the contacts were 1 mm. Heating was carried out at a rate of 1° C/min. During the experiment, temperature control was carried out continuously. A chromel-kopel thermocouple was used for this purpose. The value of the sensor signal was determined as the ratio of the specific surface resistance in air to the specific surface resistance of samples in the presence of carbon monoxide: [25]

$$S_G = R_G / R_A,$$

where S_G – sensory signal, R_A – specific surface resistance of films in air, R_G – specific surface resistance of films in the presence of a reducing gas.

3. Results and discussion

3.1. X-ray phase analysis (XPA)

For the conformation of the expected composition, the phase composition of the nanopowders was determined using X-ray phase analysis (XPA). The obtained diffraction patterns are shown in Figs. 1 and 2. According to the results of X-ray diffractometry, the sample LaCrO_3 synthesized by the sol-gel method, consisted of one phase, orthorhombic lanthanum chromite. The sample YCrO_3 obtained by the citrate method, had one phase of yttrium chromite. Impurity phases were not detected.

According to X-ray diffraction data, $\text{La}_{0.95}\text{Sr}_{0.05}\text{CrO}_3$, $\text{La}_{0.9}\text{Sr}_{0.1}\text{CrO}_3$, $\text{Y}_{0.95}\text{Sr}_{0.05}\text{CrO}_3$, and $\text{Y}_{0.9}\text{Sr}_{0.1}\text{CrO}_3$ samples were characterized by the presence of a single phase, YCrO_3 and LaCrO_3 respectively. A shift of the peaks compared to the initial phases and a decrease in the interplanar distances of the unit cell were observed, which indicates the successful incorporation of strontium ions into the crystal lattices of yttrium chromite and lanthanum chromite. The increase in shifts and decrease in interplanar distances of unit cells for doped yttrium chromite samples correlated with the percentage content of strontium ions.

The size of the obtained particles was determined from the coherent scattering region using the Debye–Scherrer formula and was 25–

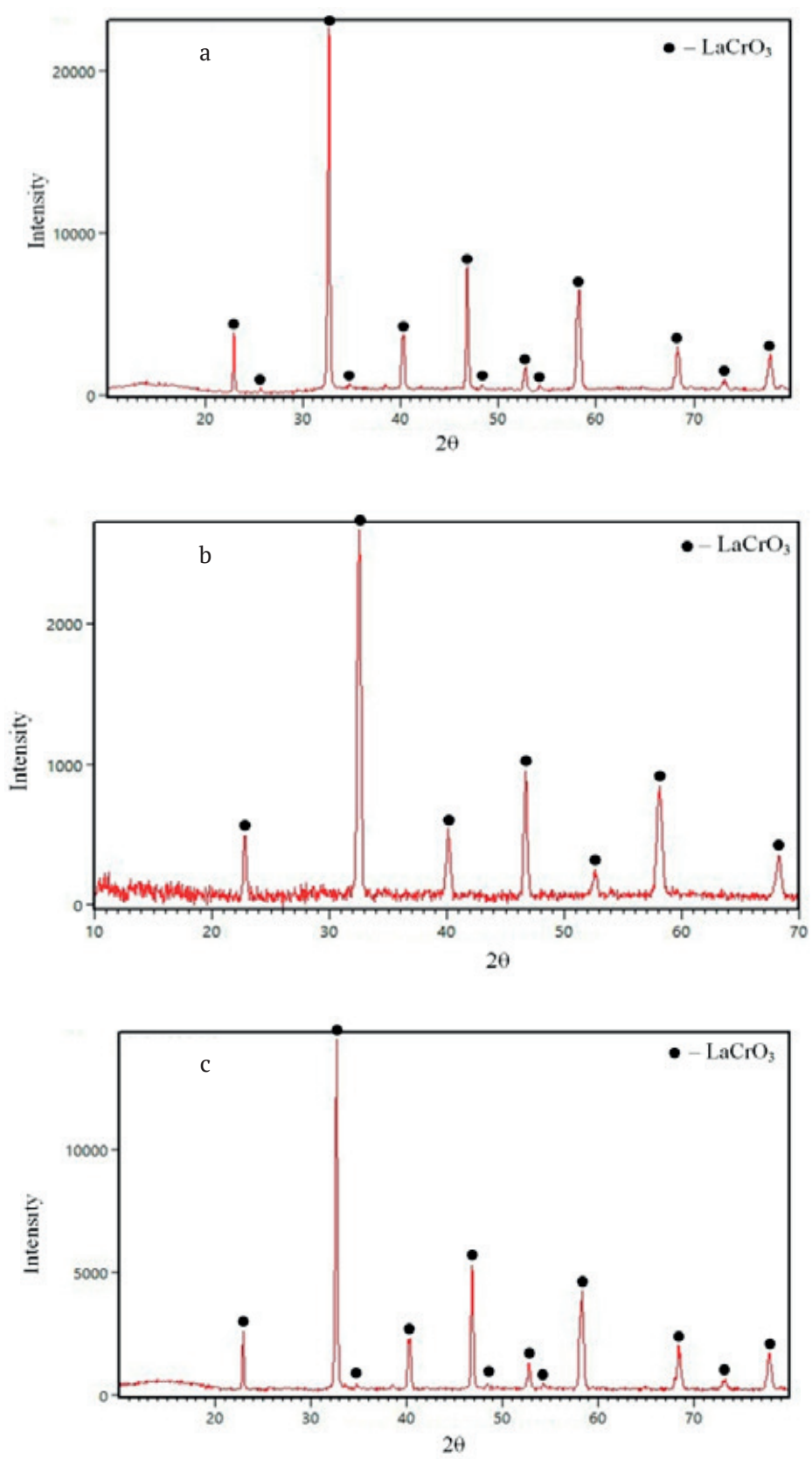


Fig. 1. X-ray diffraction patterns: a) LaCrO_3 ; b) $\text{La}_{0.95}\text{Sr}_{0.05}\text{CrO}_3$; c) $\text{La}_{0.9}\text{Sr}_{0.1}\text{CrO}_3$

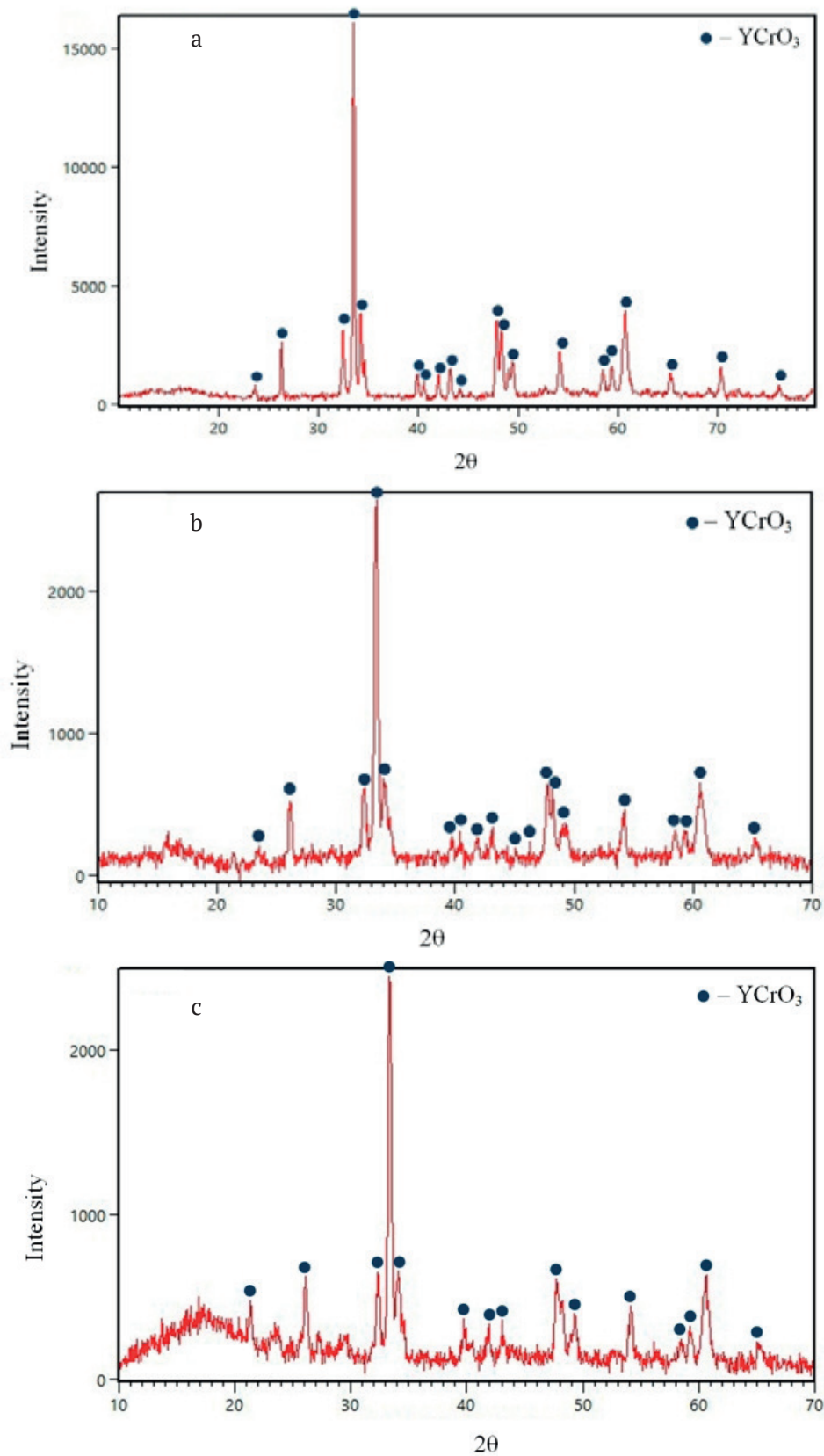


Fig. 2. X-ray diffraction patterns: a) YCrO_3 ; b) $\text{Y}_{0.95}\text{Sr}_{0.05}\text{CrO}_3$; c) $\text{Y}_{0.9}\text{Sr}_{0.1}\text{CrO}_3$

27 nm for yttrium-substituted chromites and 11–22 nm for lanthanum-substituted chromites.

3.2. Electron probe X-ray microanalysis (EPXMA)

The elemental composition of nanopowders was studied using the local X-ray spectral microanalysis (EPXMA) method. The results obtained are presented in Tables 1 and 2. The EPXMA data confirm the inclusion of strontium in LaCrO₃ and YCrO₃ lattice. The results showed that the actual composition of nanoparticles is close to their nominal composition. However, the lack of oxygen in all samples compared to the expected composition should be noted. This was a consequence of the formation of oxygen vacancies during the synthesis process and should have a beneficial effect on gas-sensitive properties, especially for yttrium ferrite.

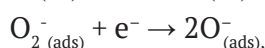
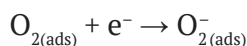
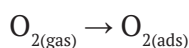
3.3. Measurement of surface resistivity by the Van der Pauw method

Based on the results of measuring the specific surface resistance, it was found that yttrium chromite reacts to the presence of CO gas at a concentration of 50 ppm, which is shown in Fig. 3. As can be seen in Fig. 4 a response was also observed for lanthanum chromite samples, however, compared to yttrium chromite, the resistance curves had a smoother character.

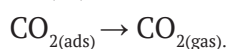
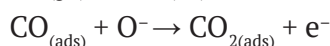
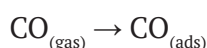
The resistance of thin films of yttrium chromites at temperatures from 20 to 200 °C and samples of lanthanum chromite from 20 to 180 °C in the presence of carbon monoxide dropped

sharply, which was due to the interaction of adsorbed CO molecules with atmospheric oxygen adsorbed on the surface of the film. The following interactions occurred:

with the involvement of oxygen:



with the involvement of detectable gas (CO):



The released electrons are conduction electrons, and an increase in their concentration led to the observed decrease in surface resistance. This, in turn, indicated the electronic type of conductivity of the samples, probably caused by vacancies in the anion sublattice, the presence of which follows from the EPXMA data. At the same time, there is evidence in the literature about the possibility of lanthanum chromite and hole conduction [26].

The graphs of the dependence of the gas-sensitive response on temperature, which indicate the susceptibility of sensors based on YCrO₃ and LaCrO₃ to the studied gas are shown in Fig. 5. A directly proportional dependence of the sensory signal on the degree of doping was observed. The sensory signal increased with the increase in the strontium content.

Table 1. Results of elemental analysis of LaCrO₃, La_{0.95}Sr_{0.05}CrO₃, La_{0.9}Sr_{0.1}CrO₃ powder, synthesized by the sol-gel method

Nominal composition of nanoparticles	Elemental composition, at. %				The actual composition of the samples
	La	Sr	Cr	O	
LaCrO ₃	19.41	0	20.28	60.31	La _{0.96} CrO _{2.97}
La _{0.95} Sr _{0.05} CrO ₃	19.11	1.01	20.31	59.57	La _{0.94} Sr _{0.05} CrO _{2.95}
La _{0.9} Sr _{0.1} CrO ₃	18.26	2.04	20.42	59.28	La _{0.89} Sr _{0.1} CrO _{2.9}

Table 2. Results of elemental analysis of YCrO₃, Y_{0.95}Sr_{0.05}CrO₃, Y_{0.9}Sr_{0.1}CrO₃ powder, obtained by the citrate method

Nominal composition of nanoparticles	Elemental composition, at. %				The actual composition of the samples
	Y	Sr	Cr	O	
YCrO ₃	20.03	0	20.78	59.19	Y _{0.96} CrO _{2.85}
Y _{0.95} Sr _{0.05} CrO ₃	19.84	0.98	20.74	58.44	Y _{0.96} Sr _{0.047} CrO _{2.82}
Y _{0.9} Sr _{0.1} CrO ₃	19.53	1.97	20.66	57.84	Y _{0.95} Sr _{0.095} CrO _{2.8}

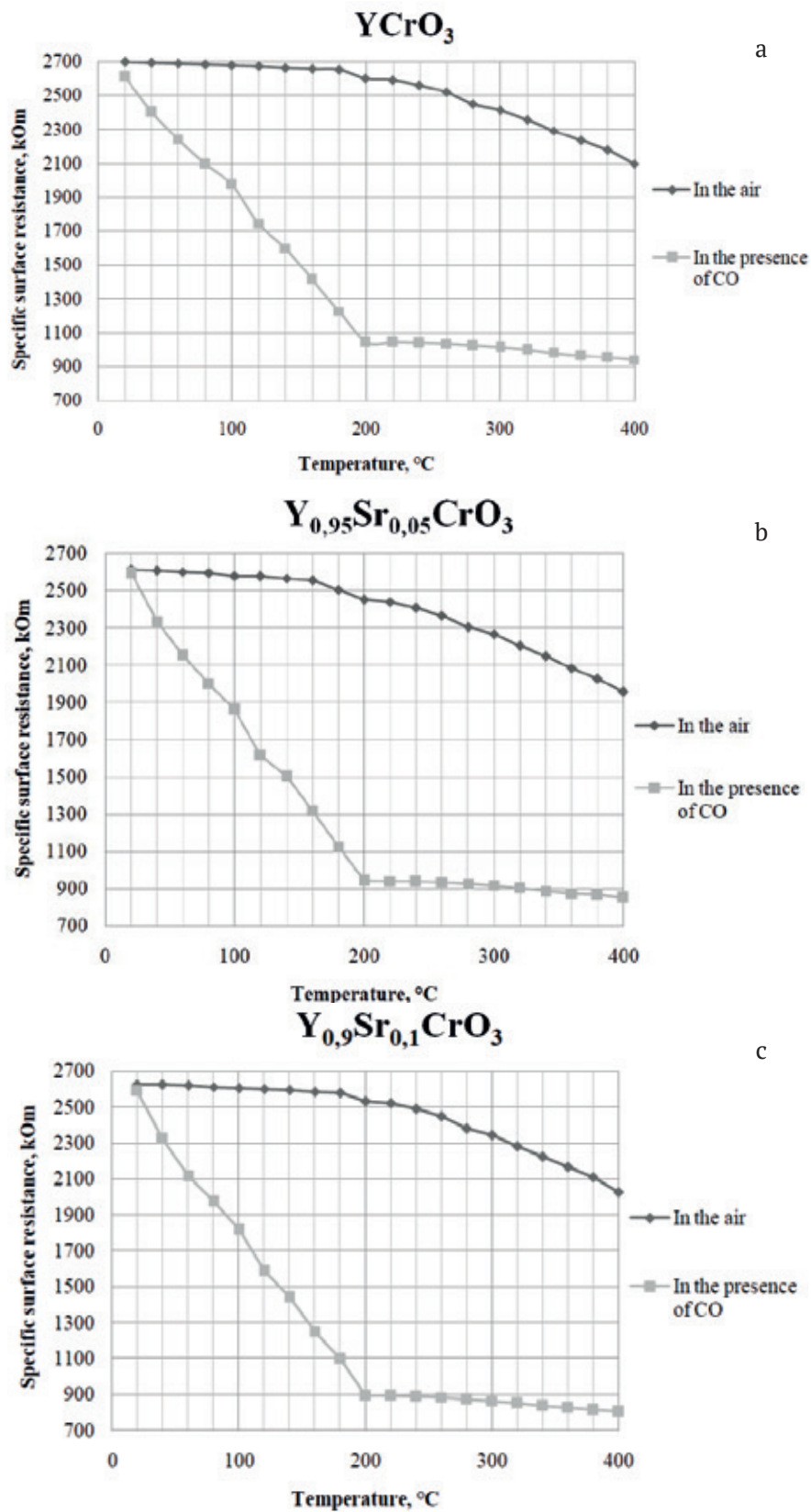


Fig. 3. Dependence of specific surface resistance on temperature in air and in the presence of CO for: a) YCrO_3 ; b) $\text{Y}_{0.95}\text{Sr}_{0.05}\text{CrO}_3$; c) $\text{Y}_{0.9}\text{Sr}_{0.1}\text{CrO}_3$

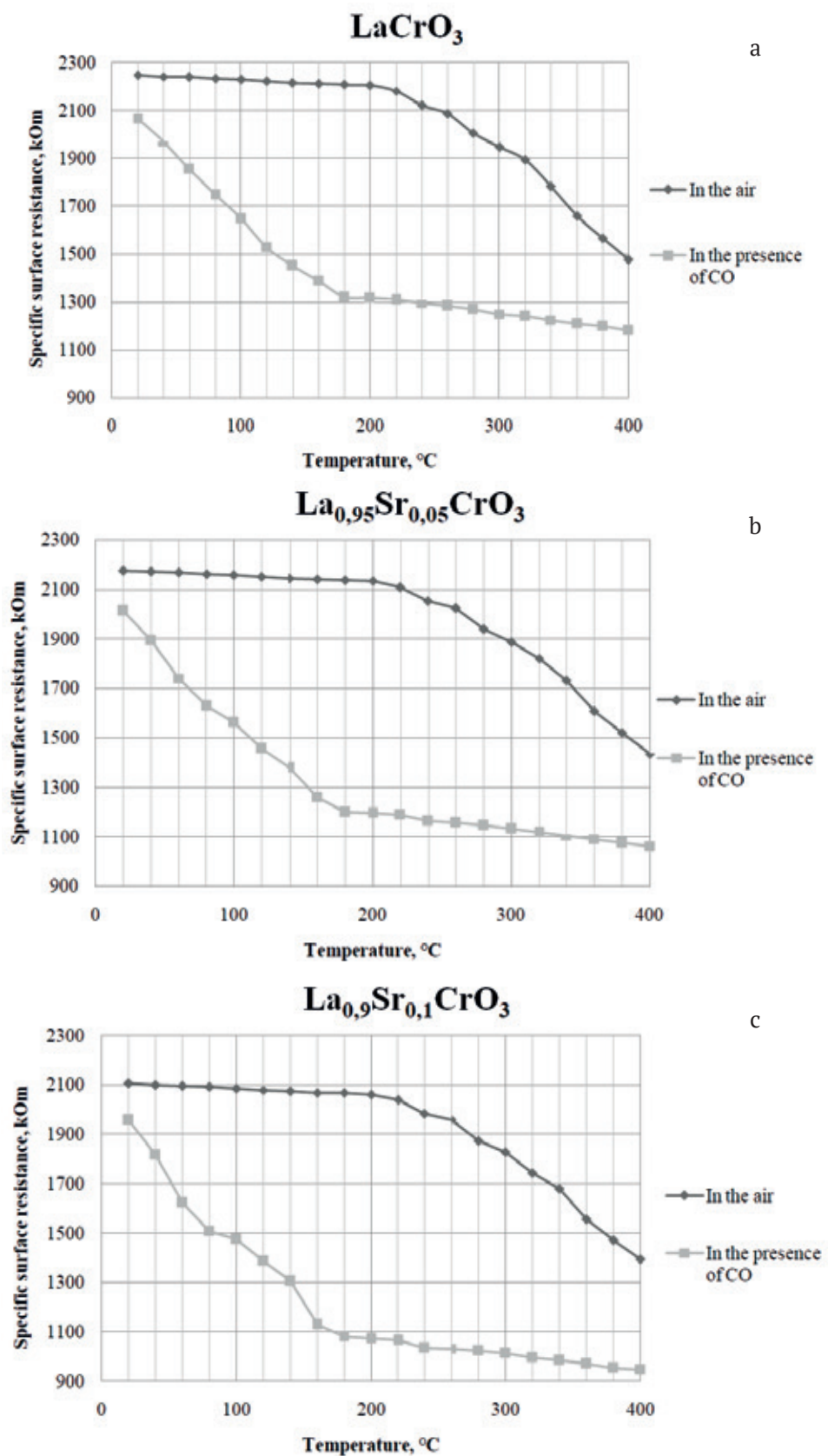


Fig. 4. Dependence of specific surface resistance on temperature in air and in the presence of CO for: a) LaCrO₃; b) La_{0.95}Sr_{0.05}CrO₃; c) La_{0.9}Sr_{0.1}CrO₃

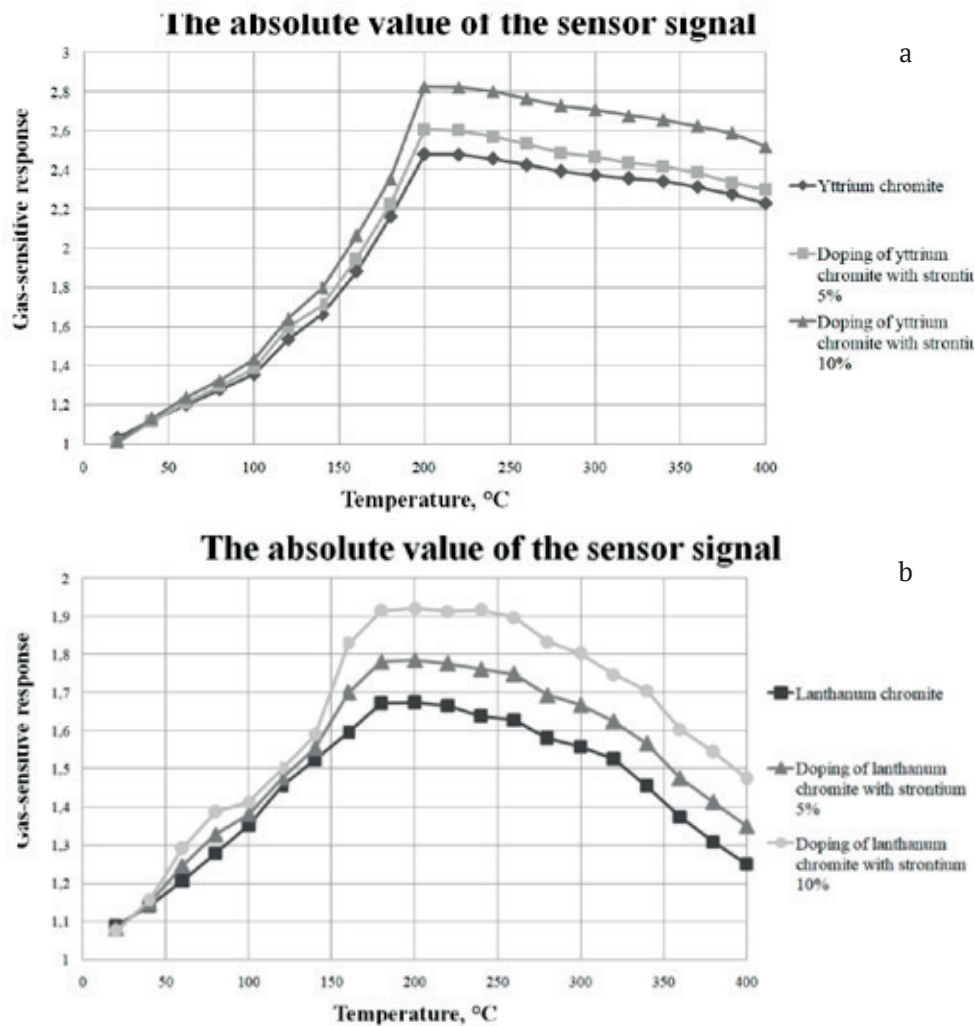


Fig. 5. Gas sensitive response as a function of temperature for: a) YCrO_3 ; b) LaCrO_3

At room temperature, the sensitivity of sensors in the presence of carbon monoxide was virtually absent. As the temperature increased, CO adsorption occurred on the surface of the samples. Electrons passed from adsorbed molecules into the surface layer, which reduced the specific surface resistance of nanomaterials. The maximum value of the sensor response of gas-sensitive thin films was achieved at a temperature of 200 °C for yttrium chromites. For lanthanum chromites, clearly defined maximum was not identified, and the similar value of the sensory signal was maintained in the temperature range of 180–240 °C, which was especially distinct for the sample with the maximum dopant content. The YCrO_3 , $\text{Y}_{0.95}\text{Sr}_{0.05}\text{CrO}_3$, $\text{Y}_{0.9}\text{Sr}_{0.1}\text{CrO}_3$, LaCrO_3 , $\text{La}_{0.95}\text{Sr}_{0.05}\text{CrO}_3$, and $\text{La}_{0.9}\text{Sr}_{0.1}\text{CrO}_3$ samples had a tendency to a linear decrease in resistance, explained by the desorption

of carbon monoxide molecules with increasing temperature, and consequently, the breaking of bonds between gas molecules and surface atoms of the samples. With an increase in the strontium content, lower resistance values are detected, and the difference between the resistance in the air and in the gas under study increases.

The obtained values of the sensory signal exceed similar results known from the literature for both lanthanum chromite proper [17] and lanthanum cobaltite analogous to it [11]. It should be noted that, in comparison with the work [17], such a result was achieved simultaneously with a decrease in the concentration of the detected gas at a comparable temperature. In the case of yttrium cobaltite, the superior value of the sensor signal was achieved at a significantly higher temperature (200 °C instead of 100).

4. Conclusions

Thin films based on synthesized YCrO_3 and LaCrO_3 nanopowders were obtained using sol-gel and citrate methods and doped with 5 and 10 at. % Sr. The synthesized samples were single-phase and had a good agreement between the actual and nominal compositions. Good gas sensitivity was detected in the presence of carbon monoxide at a concentration of 50 ppm using the Van der Pauw method. The dependence of the sensory signal on the dopant content was established. The maximum sensor signal value of 2.82 corresponded to $\text{Y}_{0.9}\text{Sr}_{0.1}\text{CrO}_3$ sample at a temperature of 200 °C.

Contribution of the authors

The authors contributed equally to this article.

Conflict of interests

The authors declare that they have no known competing financial interests or personal relationships that could have influenced the work reported in this paper.

References

- Ranga R., Kumar A., Kumari P., Singh P., Madaan V., Kumar K. Ferrite application as an electrochemical sensor: A review. *Materials Characterization*. 2021;178: 111269. <https://doi.org/10.1016/j.matchar.2021.111269>
- Uma S., Shobana M. K. Metal oxide semiconductor gas sensors in clinical diagnosis and environmental monitoring. *Sensors and Actuators: A. Physical*. 2023;349: 114044. <https://doi.org/10.1016/j.sna.2022.114044>
- Masuda Y. Recent advances in SnO_2 nanostructure based gas sensors. *Sensors and Actuators: B. Chemical*. 2022;1(2): 1–27. <https://doi.org/10.1016/j.snb.2022.131876>
- Chen Y., Li H., Huang D., ... Han G. Highly sensitive and selective acetone gas sensors based on modified ZnO nanomaterials. *Materials Science in Semiconductor Processing*. 2022;43(4): 1–10. <https://doi.org/10.1016/j.mssp.2022.106807>
- Petrov V. V., Bayan E. M. Investigation of rapid gas-sensitive properties degradation of ZnO- SnO_2 . *Chemosensors*. 2020;8: 1–13. <https://doi.org/10.3390/chemosensors8020040>
- Ryabtsev S. V., Obvintseva N. Yu., Chistyakov V. V., ... Domashevskaya E. P. Features of the resistive response to ozone of semiconductor PdO sensors operating in thermomodulation mode. *Condensed Matter and Interphases*. 2023;25(3): 392–397. <https://doi.org/10.17308/kcmf.2023.25/11263>
- Rumyantseva M. N., Ivanov V. K., Shaporev A. S., ... Arbiol J. Microstructure and sensing properties of nanocrystalline indium oxide prepared using hydrothermal treatment. *Russian Journal of Inorganic Chemistry*. 2009;54(2): 163–171. <https://doi.org/10.1134/s0036023609020016>
- Yadav A. K., Singh R. K., Singha P. Fabrication of lanthanum ferrite based liquefied petroleum gas sensor. *Sensors and Actuators B: Chemical*. 2016;229: 25–30. <https://doi.org/10.1016/j.snb.2016.01.066>
- Hu J., Chen X., Zhang Y. Batch fabrication of formaldehyde sensors based on LaFeO_3 thin film with ppb-level detection limit. *Sensors and Actuators: B. Chemical*. 2021;349: 130738. <https://doi.org/10.1016/j.snb.2021.130738>
- Qina J., Cui Z., Yanga X., Zhua S., Li Z., Lianga Y. Synthesis of three-dimensionally ordered macroporous LaFeO_3 with enhanced methanol gas sensing properties. *Sensors and Actuators B: Chemical*. 2015;209: 706–713. <https://doi.org/10.1016/j.snb.2014.12.046>
- Chumakova V. T., Marikutsa A. V., Rumyantseva M. N. Nanocrystalline lanthanum cobaltite as a material for gas sensors. *Russian Journal of Applied Chemistry*. 2021;94(12): 1651–1698. <https://doi.org/10.1134/s1070427221120119>
- Tiwari S., Saleem M. Varshney M., Mishra A., Varshney D. Structural, optical and magnetic studies of YCrO_3 perovskites. *Physica B: Condensed Matter*. 2018;546: 67–72. <https://doi.org/10.1063/1.5122339>
- Kadu A. V., Bodade A. B., Bodade A. B., Chaudhari G. N. Structural characterization of nanocrystalline $\text{La}_{1-x}\text{Sr}_x\text{CrO}_3$ thick films for H_2S gas sensors. *Journal of Sensor Technology*. 2012;2: 13–18. <https://doi.org/10.4236/jst.2012.21003>
- Khetre S. M., Chopade A. U., Khilare C. J., Jadhav H. V., Jagadale P. N., Bamane S. R. Electrical and dielectric properties of nanocrystalline LaCrO_3 . *Journal of Materials Science: Materials in Electronics*. 2013;24: 4361–4366. <https://doi.org/10.1007/s10854-013-1411-z>
- Matulkova I., Holec P., Pacakova B., ... Vejpravova J. On preparation of nanocrystalline chromites by co-precipitation and autocombustion methods. *Sensors and Actuators A: Physical*. 2015;195: 66–73. <https://doi.org/10.1016/j.mseb.2015.01.011>
- Rao V., Rajamani M., Ranjith R., David A., Prellier W. Local structural distortion and interrelated phonon mode studies in yttrium chromite. *Materials Research Society*. 2017;32(8): 1541–1547. <https://doi.org/10.1557/jmr.2017.5>
- Prashant B. K., Kailas H. K., Uday G. D., Umesh J. T., Sachin G. S. Fabrication of thin film sensors by spin coating using sol-gel LaCrO_3 perovskite material modified with transition metals for sensing

environmental pollutants, greenhouse gases and relative humidity. *Environmental Challenges*. 2021;3: 1–13. <https://doi.org/10.1016/j.envc.2021.100043>

18. Chadli I., Omari M., Abu Dalo M., Albiss B. Preparation by sol–gel method and characterization of Zn-doped LaCrO_3 perovskite. *Journal of Sol-Gel Sci Technol*. 2016;80: 598–605. <https://doi.org/10.1007/s10971-016-4170-5>

19. Zarrin N., Husain S., Khan W., Manzoor S. Sol-gel derived cobalt doped LaCrO_3 : Structure and physical properties. *Journal of Alloys and Compounds*. 2019;784(5): 541–555. <https://doi.org/10.1016/j.jallcom.2019.01.018>

20. Nguyen A. T., Tran H. L. T., Nguyen Ph. U. T., ... Nguyen T. L. Sol-gel synthesis and the investigation of the properties of nanocrystalline holmium orthoferrite. *Nanosystems: Physics, Chemistry, Mathematics*. 2020;11(6): 698–704. <https://doi.org/10.17586/2220-8054-2020-11-6-698-704>

21. Mittova I. Ya., Perov N. S., Alekhina Iu. A., ... Sladkopevtsev B. V. Size and magnetic characteristics of YFeO_3 nanocrystals. *Inorganic Materials*. 2022;58(3): 271–277. <https://doi.org/10.1134/S0020168522030116>

22. JCPDC PCPDFWIN: A Windows Retrieval. Display program for Accessing the ICDD PDF. 2 Data base, International Centre for Diffraction Data. 1997.

23. Krishtal M. M., Jasnikov I. S., Polunin V. I., Filatov A. M., Ul'janenkov A. G. *Scanning electron microscopy and X-ray microanalysis**. Moscow: Tehnosfera Publ.; 2009. 208 p.

24. Kostryukov V. F., Parshina A. S., Sladkopevtsev B. V., Mittova I. Ya. Thin films on the surface of GaAs, obtained by chemically stimulated thermal oxidation, as materials for gas sensors. *Coatings (MDPI)*. 2022;12(12): 1819–1828. <https://doi.org/10.3390/coatings12121819>

25. Kostryukov V. F., Balasheva D. S., Parshina A. S. Creation of thin films on the surface of InP with a controlled gas-sensitive signal under the influence of $\text{PbO} + \text{Y}_2\text{O}_3$ compositions. *Condensed Matter and Interphases*. 2021;23(3): 406–412. <https://doi.org/10.17308/kcmf.2021.23/3532>

26. Shevchik A. P., Suvorov S. A. Jeletroprovodjashhie svojstva materialov na osnove hromita lantana. *Izvestija sankt-peterburgskogo gosudarstvennogo tehnologicheskogo instituta (tehničeskogo universiteta)*. 2008;3(29): 36–41.

Information about the authors

Milena A. Yakimchuk, Master's student of the Department of Materials Science and Industry of Nanosystems, Voronezh State University (Voronezh, Russian Federation).

yakimchuk.720.46@gmail.com

Eugenia S. Eliseeva, student of the Department of Materials Science and Industry of Nanosystems, Voronezh State University (Voronezh, Russian Federation).

eliseewa.zhenya@yandex.ru

Victor F. Kostryukov, Dr. Sci. (Chem.), Associate Professor, Associate Professor of the Department of Materials Science and Industry of Nanosystems, Voronezh State University (Voronezh, Russian Federation).

<https://orcid.org/0000-0001-5753-5653>

vc@chem.vsu.ru

Received 23.04.2024; approved after reviewing 02.08.2024; accepted for publication 15.08.2024; published online 01.10.2024.

Translated by Valentina Mittova



Condensed Matter and Interphases

Kondensirovannye Sredy i Mezhfaznye Granitsy
<https://journals.vsu.ru/kcmf/>

Original articles

Research article

<https://doi.org/10.17308/kcmf.2024.26/12230>

Preparation of composite micro-nanofibers based on nano-sized magnetite by electrospinning

R. P. Yakupov¹, V. Yu. Buzko^{1,2,3}, S. N. Ivanin^{1,3}✉, M. V. Papezhuk¹

¹Kuban State University,
149 Stavropolskaya st., Krasnodar 350040, Russian Federation

²Kuban State Technological University,
2 Moskovskaya st., Krasnodar 350072, Russian Federation

³Federal State Budgetary Educational Institution of Higher Education “Kuban State Agrarian University named after I. T. Trubilin”,
13 Kalinina st., Krasnodar, 350044, Russian Federation

Abstract

Composite materials with magnetic fillers play an important role in a number of industries, from functional coatings in electronics to electromagnetic wave absorption and microwave-shielding materials. An important feature is the selection of a magnetic nano-sized filler that does not cause increased degradation of the polymer binder, and the selection of a polymer that ensures the weather resistance of the nanocomposite material. In this study, composite samples of micro- and nanofibers based on fabricated particles of nanosized magnetite (Fe_3O_4) as a cheap electromagnetic wave absorption material were investigated.

Magnetic polymer-dielectric fibers polystyrene- Fe_3O_4 were obtained by electrospinning. The X-ray diffraction analysis showed that the synthesized Fe_3O_4 nanoparticles have a cubic space group structure $Fd\bar{3}m$ with crystal lattice parameter $a = 8.422 \pm 0.026$ Å. The analysis of the ferromagnetic resonance spectrum showed the ferromagnetic nature of the obtained magnetite nanoparticles. It has been shown that during the production of composite fibers by electrospinning, a dispersion of nano-sized magnetite powder can be included in the spinning solution, which, as a result of the electrospinning process, allows obtaining magnetic composite micro- and nanofibers. The average size of the included magnetite particles was 15 ± 3 nm.

The resulting non-woven magnetic material is predominantly composed of two types of fibers with an average diameter of 680 ± 280 nm and larger associated fibers with a diameter of 1500 ± 300 nm. Based on a certain frequency dependence of losses upon reflection RL in the frequency range 15 MHz – 7.0 GHz, the synthesized fibrous material can be considered to be an effective electromagnetic wave absorption material.

Keywords: Nano-sized magnetite, Electrospinning, Composite fiber, Structural characteristics, Magnetic materials, Radio absorption

Funding: The study was supported by the Ministry of Science and Higher Education of the Russian Federation (state task project FZEN-2023-0006).

Acknowledgements: studies using powder X-ray diffraction and laser granulometric analysis methods were carried out using the equipment of the Centre for the Collective Use “X-Ray Diagnostics of Materials” of Kh. M. Berbekov Kabardino-Balkarian State University.

For citation: Yakupov R. P., Buzko V. Yu., Ivanin S. N., Papezhuk M. V. Preparation of composite micro-nanofibers based on nano-sized magnetite by electrospinning. *Condensed Matter and Interphases*. 2024;26(3): 547–557. <https://doi.org/10.17308/kcmf.2024.26/12230>

Для цитирования: Якупов Р. П., Бузько В. Ю., Иванин С. Н., Папезжук М. В. Получение композитных микро- и нановолокон на основе наноразмерного магнетита методом электроформования. *Конденсированные среды и межфазные границы*. 2024;26(3): 547–557. <https://doi.org/10.17308/kcmf.2024.26/12230>

✉ Sergey N. Ivanin, e-mail: Ivanin18071993@mail.ru

© Yakupov R. P., Buzko V. Yu., Ivanin S. N., Papezhuk M. V., 2024



The content is available under Creative Commons Attribution 4.0 License.

1. Introduction

The diverse applications of magnetic nano-sized particles or materials are widely explored by scientists and researchers around the world for various industrial, engineering, structural, and biomedical applications. This interest is due to the exceptional physical and chemical properties of nanoscale objects, such as large specific surface area, small size, surface functionalization, and magnetism. Magnetic nanoparticles usually consist of pure metals (Fe, Co, Ni), metal alloys (CoPt, FePt) and metal oxides or ferrites [1]. In the last decade, magnetic nanoparticles have gained enormous interest due to their use in specialized areas such as medicine: as a carriers in targeted drug delivery [2, 3], cancer theranostics [4, 5], biosensors [6, 7], contrast agents for magnetic resonance imaging [8–10]; electromagnetic wave absorption and radio-shielding materials of electromagnetic radiation [11–14], fillers of composite materials for FDM printing [15, 16], production of magnetorheological fluids for systems of controlled hydraulic automation devices, in which such particles are a component of the complex dispersed phase [17], magnetic ink [18], etc. Magnetic nanoparticles of magnetite (Fe_3O_4) and maghemite ($\gamma\text{-Fe}_2\text{O}_3$) are of particular interest [19].

Nanoscale Fe_3O_4 is a cheap, effective magnetic, electromagnetic wave absorption and radio-shielding nanomaterial with a combination of unique magnetic, optical and photocatalytic properties [20–23]. Composite fibrous materials based on Fe_3O_4 are of particular interest due to the development of new materials with magnetic and conductive properties [24–26]. In [27], the authors obtained composite fibers by electrospinning based on a polyacrylonitrile/DMSO fiber-forming system with the inclusion of magnetite nanoparticles, in [28] the authors studied the effect of the concentration of magnetite nanoparticles in a colloidal solution on the process of their loading into calcium carbonate microparticles grown on polycaprolactone fibers; in [29] the authors obtained composite fibers by electrospinning based on the polyvinylpyrrolidone/water fiber-forming system containing magnetite nanoparticles. Composite fibrous materials based on nanosized magnetite can be used both for effective electromagnetic microwave absorption

and for ensuring electromagnetic compatibility of radio-electronic equipment at ultrahigh frequencies [28–35]. From practical experience it is known that ultrafine Fe_3O_4 nanoparticles, which have strong catalytic properties, cause increased degradation of polymer binders, leading to poorly predictable changes in the properties of electromagnetic wave absorption and radio-shielding nanocomposite materials based on Fe_3O_4 on time and temperature. In addition, an important problem is the provision of the protection of nano-sized magnetic filler in a composite material from chemical leaching by precipitation.

A solution to this problem may be the creation of fibrous composite materials in which Fe_3O_4 nanoparticles are “encapsulated” in a weather-resistant polymer binder (polystyrene or acrylate-styrene copolymer) using fiber electrospinning technology. This approach fundamentally allows reducing the temporary degradation of the operational properties of electromagnetic wave absorption and radio-shielding nanocomposite materials based on Fe_3O_4 under atmospheric conditions.

The purpose of this study was the creation and investigation of the characteristics of a fibrous composite material based on nano-sized magnetite in a polystyrene matrix using electrospinning.

2. Experimental

A sample of nanosized magnetite was obtained using the ammonium hydroxide method. As iron salts $\text{FeSO}_4 \cdot 7\text{H}_2\text{O}$ (chemically pure) and $\text{Fe}_2(\text{SO}_4)_3$ (reagent grade) which were dissolved in double-distilled water at a concentration of 0.05 M were used. Next, the salt solution in the required proportions was heated on a laboratory electric stove with a power stirrer to a temperature of 65 °C and the calculated amount of a 25% ammonium hydroxide solution ($\text{NH}_3 \cdot \text{H}_2\text{O}$ with density $\rho = 0.9070$ g/ml) with a 1% excess was poured drop by drop with constant stirring at a slow rate upon reaching pH = 8.5. The formation of magnetite took place in accordance with the ionic equation:

$$\text{Fe}^{2+} + 2\text{Fe}^{3+} + 8\text{OH}^- \rightarrow \text{Fe}_3\text{O}_4 \downarrow + 4\text{H}_2\text{O}.$$

After pouring in the ammonia precipitant, the solution was kept for 20 min at a temperature

of 65 °C for the formation of the magnetite nanoparticles. The resulting magnetite nanoparticles were separated from the resulting solution using magnetic decantation with a permanent magnet. The powder was thoroughly washed four times with bidistilled water. The resulting black wet powder was dried in air for 3-4 days. The dried magnetite powder was then ground in a ceramic mortar until homogeneity was achieved.

The microstructure of the synthesized magnetite powder was analyzed using a JEOL JSM-7500F electron scanning microscope. The microstructure was studied using the secondary electron registration mode. The advantage of using the secondary electron registration mode is the ability to study the surface morphology, taking into account the dependence of the contrast on the relief [36]. Elemental analysis was performed using an Inca X Sight EDX Spectrometer X-ray energy dispersive microanalysis attachment. The X-ray spectral analysis method allows both qualitative and quantitative analysis of samples without compromising their integrity [37]. Laser granulometric analysis was performed using laser particle size analyzer Analysette 22 of JEOL JES-FA300X ESR/FMR X-ray spectrometer. X-ray phase analysis of a sample of nanosized magnetite powder was carried out using a powder diffractometer D2 Phaser. The sample was examined at room temperature in the 2θ angle range from 10° to 70° with a scanning step of 0.02° .

The synthesis of individual and composite polystyrene nano- and microfibers was carried out

using an independently developed installation for needle-free electrospinning. Emulsion-type polystyrene was dissolved in toluene (chemically pure) until the mass fraction of polystyrene in the solution reached 18%. To obtain nanocomposite fibers based on nanomagnetite and polystyrene, a concentrated aqueous dispersion of purified magnetite nanoparticles was used. Magnetite nanoparticles were removed from the aqueous dispersion by magnetic decantation using a permanent magnet. The solution for electrospinning fibers was prepared in order to obtain a composite fiber with a mass content of nanosized magnetite of 25%. The electroforming process was carried out at a electric potential difference between the electrodes of 18 kV and an interelectrode distance of 10 cm.

For the determination of the electromagnetic wave absorption properties of the fabricated fibrous composite based on polystyrene fiber with nano-sized magnetite, the reflection loss characteristics of its compressed layer with the thickness of 2.54 mm were measured in a 10-cm HP-11566A coaxial cell with toroid dimensions of 7.0×3.05 mm. A KC901V Deepace vector network analyzer was used in the operating frequency range from 15 MHz to 7.0 GHz. Losses upon reflection RL for the nanocomposite was determined experimentally by measuring the complex transmission coefficient S_{11} in a short-circuited line.

3. Results and discussion

Based on the data obtained by processing photographs of the microstructure at high

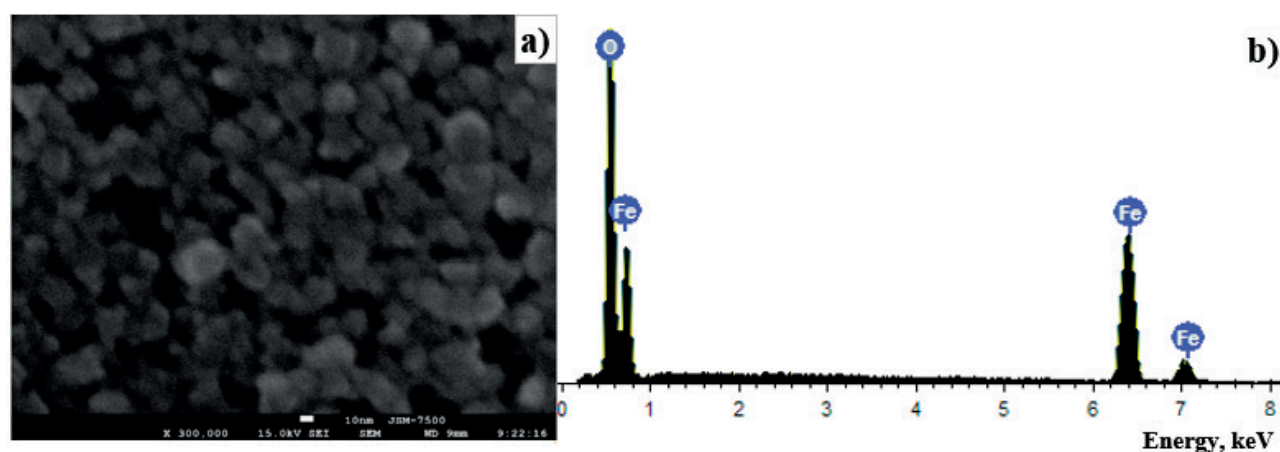


Fig. 1. Photograph of nanoparticles (a) and EDA spectrum (b) of the resulting nano-sized magnetite powder

resolution (Fig. 1), the size of magnetite nanoparticles in the synthesized sample was 15 ± 3 nm. Our results are consistent with the results of [38], in which a similar synthesis method was used, but with iron chlorides and low temperature, short exposure of the resulting nanomagnetite in the mother solution, and are in good agreement with the data of [39]. In this case, the synthesis product, according to energy-dispersive microanalysis, in terms of the percentage of Fe and O atoms corresponded to the expected composition of Fe_3O_4 without impurities in significant quantities.

Laser granulometric analysis of the synthesized magnetite powder showed (Fig. 2a) significant agglomeration of particles in it; therefore, an aqueous dispersion of purified magnetite nanoparticles was used to obtain nanocomposite fibers based on magnetite and polystyrene. Before adding the magnetite dispersion to the polymer molding solution, the nanoparticles were

dispersed using an AG SONIC TC-50 ultrasonic bath for 20 min at room temperature.

FMR spectrum of synthesized nanosized Fe_3O_4 magnetite powder is shown in Fig. 2b. Based on the shape of the FMR spectrum, the studied sample of Fe_3O_4 nano-sized magnetite powder is a typical ferromagnetic material with a highly symmetrical nanoparticle shape.

The powder X-ray diffraction pattern of the studied sample of synthesized nanosized magnetite is shown in Fig. 3. Based on X-ray diffraction analysis, it was found that Fe_3O_4 nanopowder has a typical cubic space group structure $Fd\bar{3}m$ with crystal lattice parameter $a = 8.422 \pm 0.026$ Å and an average Fe-O distance of 2.55 Å, which correlates well with known literature data for Fe_3O_4 ($a = 8.407$ - 8.414 Å [40], $a = 8.40$ - 8.42 Å [41], $a = 8.397$ Å [42] or JCPDS19-0629 $a = 8.396$ Å [43]). This confirms that the sample was composed of Fe_3O_4 without possible traces of $\gamma\text{-Fe}_2\text{O}_3$.

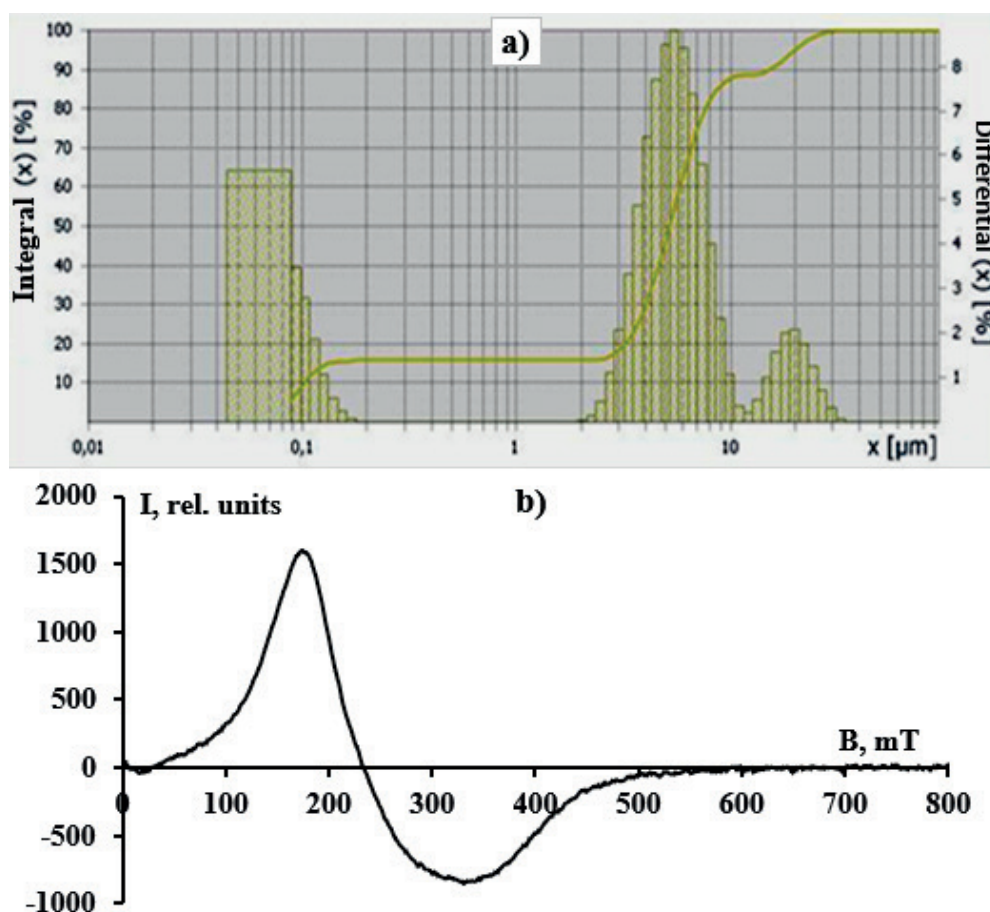


Fig. 2. Laser granulometric analysis (a) and FMR spectrum (b) of the resulting nano-sized magnetite powder

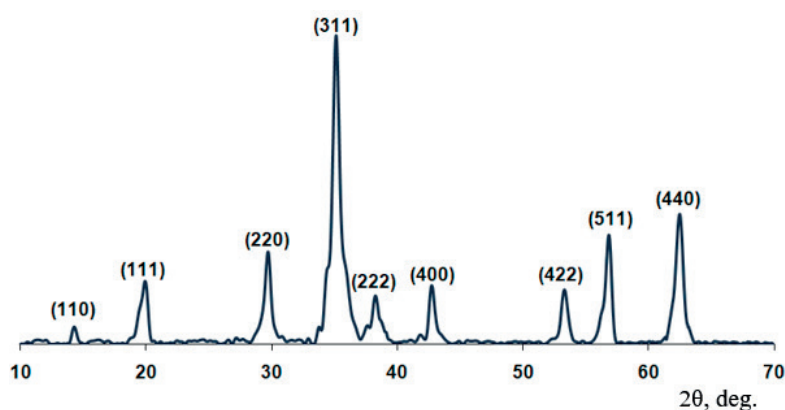


Fig. 3. Powder diffraction pattern of a sample of nano-sized magnetite

Average size of coherent scattering regions (CSR) - D for a sample of nano-sized magnetite was calculated based on X-ray diffraction data for all peaks using the Scherrer formula:

$$D = \frac{k \times \lambda}{\beta \times \cos \theta}$$

where $k = 0.9$ – for spherical particles; λ – wavelength of the x-ray radiation used ($\lambda = 0.15405$ nm), nm; θ – Bragg angle, rad; β – half-width of integral peaks at half-maximum, rad.

The calculated CSR value for magnetite crystallites using the Scherrer method for the main diffraction peak was $D = 15.1$ nm, which was consistent with the results of electron microscopy, and according to all observed diffraction peaks $D = 19.5 \pm 6$ nm. Our results are in good agreement with the data of [44], in which the size of synthesized magnetite nanoparticles based on electron microscopy data of 15 nm was lower than the size calculated based on powder X-ray diffractometry data of 19.4 nm.

Calculation of CSR sizes and microstresses for a sample of the studied Fe_3O_4 nanopowder using the Williamson-Hall method, provided the following results: CSR sizes $D = 17.2$ nm, which agreed with the value obtained using Scherrer's formula, the microstresses value $\varepsilon = 4.6 \cdot 10^{-4}$.

It should be noted that a electrospinning spinneret in the form of a hollow needle is usually used to produce non-woven materials by electrospinning. However, the use of a hollow needle has the following limitations and disadvantages: clogging of the needle channel with a dispersion of filler particles of the spinning solution due to the narrow

internal diameter of the hole, which may not allow encapsulation of particles that can improve the properties of the resulting fibers and/or functionalize the resulting non-woven material; limited productivity (up to 0.1 grams per hour), nonlinear scaling [45]; a needle-down spinneret placement can result in droplets forming at the needle tip, which can fall onto the collector, preventing the formation of uniform fibers [46]. To overcome these disadvantages, needleless electrospinning units can be used to produce polymer nano- and microfibers filled with nanoparticles. Needleless electrospinning is the process of producing nanofibers by electrospinning of a polymer solution directly from the exposed surface of a liquid/liquid dispersion of a spinning solution with nanoparticles using various structural elements as a spinning electrode [46], such as a conical wire supported by gravity [47], metal plate [48], rotating cone [49], gear [50], spinneret with a mechanical shift [51], etc. Such structural elements are partially immersed and rotated in the polymer molding solution, resulting in the formation of a thin polymer solution layer on their surface and thus from the surface of the thin polymer layer, multiple cones are formed, which, after applying an electric field, initiate electrospinning. In our unit the fibers were formed from a polymer solution flowing under the influence of gravitational force along a vertically oriented spinning electrode. The forming electrode consisted of a metal rod made of surgical stainless steel with a diameter of 1 mm, on top of which a wire with a diameter of 0.2 mm was wound as a spiral.

The microstructure of the resulting polystyrene micro- and nanofibers according to scanning electron microscopy data are shown in Fig. 4. According to the studies, the average thickness of the obtained polystyrene microfibers was 910 ± 160 nm (Fig. 4a). At the same time, the resulting fibrous material also contained a small fraction of thin nanofibers with a thickness of 89 ± 7 nm (Fig. 4b).

The results of studying the microstructure of the obtained composite polystyrene fibers with included magnetite nanoparticles are shown in Fig. 5. According to studies conducted in the resulting fibrous material, polystyrene- Fe_3O_4 the fraction of submicron fibers with a thickness of 680 ± 280 nm predominated. At the same time, the discussed material also contained a small fraction of large microfibers with a thickness of 1500 ± 300 nm, probably being pairs of submicron fibers. We concluded

that the obtained composite fibers based on nanosized magnetite had an average diameter almost 2-3 times higher compared to the results for composite nanofibers based on nanosized magnetite from [8] with a diameter of 200-350 nm and [13] with a diameter of 200-320 nm. This was due to the use of low potential difference of 18 kV in the electrospinning process, compared to the electrospinning process carried out at 30 kV in [8] and at 65 kV in [13].

The frequency dependence of losses upon RL reflection for a manufactured fiber composite with nanosized magnetite particles in the frequency range from 15 MHz to 7.0 GHz is shown in Fig. 6. According to the data in Fig. 6, the resulting fibrous nanocomposite material in compressed form had wide-range radio absorption and electromagnetic wave absorption properties in the microwave range acceptable for practical use, taking into account its microporosity and the low

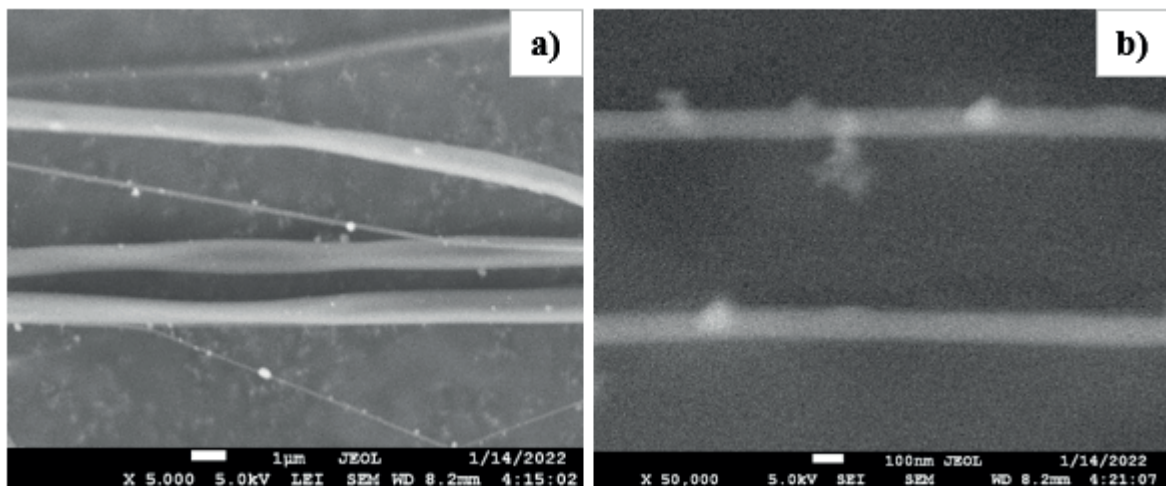


Fig. 4. Structure of polystyrene microfibers obtained at a magnification of 5000x (a) and 50,000x (b)

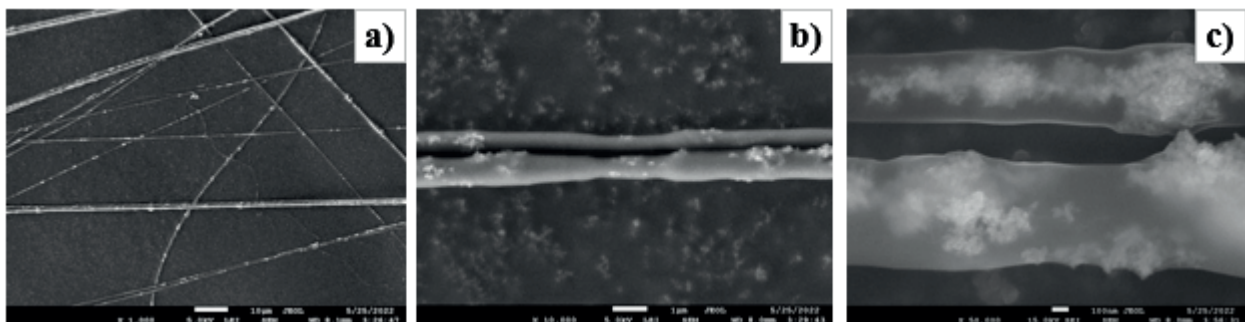


Fig. 5. Photographs of the structure of synthesized composite fibers, obtained at magnifications of 1000 (a), 10,000 (b) and 50,000x (c)

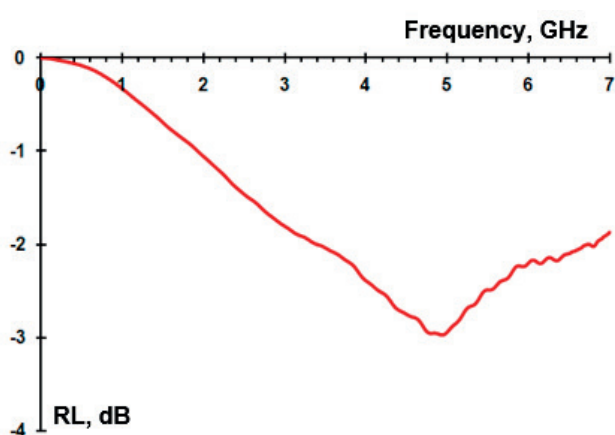


Fig. 6. Frequency dependence of reflection loss RL for a fabricated fiber composite based on polystyrene fiber with nanosized magnetite

proportion of magneto-dielectric filler in the form of nano-sized magnetite in it.

Previously published data on the electromagnetic wave absorption properties of composites with different thicknesses and concentrations of magnetite particles are shown in Table 1. The size of magnetite particles used in various studies ranged from 15 nm to 1000 nm. As can be seen from the data in Table 1, the material made of Fe_3O_4 nanoparticles had the highest radio absorption of -8.2 d, with a diameter of 30 nm in a silicone binder [57], however, it should

be noted that the thickness of this sample was 4 mm, and the percentage of magnetite was 30% by weight. Our sample had a microwave absorption of -2.97 dB with a thickness of 2.54 mm and a magnetite concentration of 25% in polystyrene. Taking into account the thickness of the studied materials, the proportion and size of filler particles, and the used polymer binder, we can suggest the using the material of submicron polystyrene fibers with included magnetite nanoparticles, as a cheap non-woven electromagnetic wave absorption material.

4. Conclusions

Thus, we can conclude that the combination of a simple solution method for the synthesis of magnetite nanoparticles without the use of expensive stabilizing polymers or surfactants in combination with the encapsulation technique of Fe_3O_4 nanoparticles into polystyrene submicron fibers during electrospinning allowed to develop elements of the technology for creating fibrous magnetic and electromagnetic wave absorption nanocomposite materials based on magnetic Fe_3O_4 nanoparticles. According to their characteristics, the resulting micro- and nanofibers with nanosized magnetite particles we can suggest the promise of the obtained material for use as a cheap non-woven electromagnetic wave absorption material.

Table 1. Radio absorption properties of various composites based on magnetite particles of various natures

Material	Filler (Fe_3O_4), %	Sample thickness, mm	Reflection loss, dB	Reference
Fe_3O_4 nanoparticles 15 nm in submicron polystyrene fibers	25	2.54	-2.97 at 4.96 GHz	this article
Fe_3O_4 nanoparticles 20–30 nm in submicron polyvinyl chloride fibers	40	2.4	-6.6 at 9.7 GHz	[52]
natural Fe_3O_4 in paraffin	50	5	-5.47 at 7.44 GHz	[53]
cubic Fe_3O_4 nanoparticles 15–20 nm in paraffin	40	5.5	-7.6 at 5.1 GHz	[54]
Fe_3O_4 microspheres 300 nm in paraffin	50	2	-1.0 at 5.6 GHz	[55]
hedgehog-like microspheres Fe_3O_4 500–1000 nm in paraffin	50	5	-4.1 at 8.4 GHz	[56]
Fe_3O_4 nanoparticles 30 nm in silicone polymer	30	4	-8.2 at 6.7 GHz	[57]
Fe_3O_4 microspheres 200–1000 nm in paraffin	20	4	-7.5 at 7.6 GHz	[58]

Author contributions

Yakupov R. P. – synthesis of polystyrene fibers and polystyrene-Fe₃O₄, discussion of the results, c. Buzko V. Yu. – experimental planning, synthesis of Fe₃O₄ dispersion, organization of measurements, analysis of powder diffraction results, analysis of electron microscopy data, discussion of results, writing an article. Ivanin S. N. – planning of the experiment, scanning electron microscopy of samples, measurement of reflection losses, discussion of results, design and editing of the text. Papezhuk M. V. – organization of measurements, discussion of results.

Conflict of interests

The authors declare that they have no known competing financial interests or personal relationships that could have influenced the work reported in this paper.

References

- Mittal A., Roy I., Gandhi S. Magnetic nanoparticles: An overview for biomedical applications. *Magnetochemistry*. 2022;8(9): 107. <https://doi.org/10.3390/magnetochemistry8090107>
- Zargar T., Kermanpur A. Effects of hydrothermal process parameters on the physical, magnetic and thermal properties of Zn_{0.5}Fe_{2.7}O₄ nanoparticles for magnetic hyperthermia applications. *Ceramics International*. 2017;43: 5794–5804. <https://doi.org/10.1016/j.ceramint.2017.01.127>
- Sulaiman N. H., Ghazali M. J., Majlis B. Y., Yunas J., Razali M. Superparamagnetic calcium ferrite nanoparticles synthesized using a simple sol-gel method for targeted drug delivery. *Bio-Medical Materials and Engineering*. 2015;26: S103–S110. <https://doi.org/10.3233/bme-151295>
- Li X., Li W., Wang M., Liao Z. Magnetic nanoparticles for cancer theranostics: Advances and prospects. *Journal of Controlled Release*. 2021;335: 437–448. <https://doi.org/10.1016/j.jconrel.2021.05.042>
- Jiao W., Zhang T., Peng M., Yi J., He Y., Fan H. Design of magnetic nanoplatforms for cancer theranostics. *Biosensors*. 2022;12(1): 38. <https://doi.org/10.3390/bios12010038>
- Rocha-Santos T. A. P. Sensors and biosensors based on magnetic nanoparticles. *TrAC Trends in Analytical Chemistry*. 2014;62: 28–36. <https://doi.org/10.1016/j.trac.2014.06.016>
- Chen Y. T., Kolhatkar A. G., Zenasni O., Xu S., Lee T. R. Biosensing using magnetic particle detection techniques. *Sensors*. 2017;17(10): 2300. <https://doi.org/10.3390/s17102300>
- Avasthi A., Caro C., Pozo-Torres E., Leal M. P., García-Martín M. L. Magnetic nanoparticles as MRI contrast agents. *Topics in Current Chemistry*. 2020;378: 40. <https://doi.org/10.1007/s41061-020-00302-w>
- Ivanin S. N., Buz'ko V. Y., Panyushkin V. T. Research of the properties of gadolinium stearate by EPR Spectroscopy. *Russian Journal of Coordination Chemistry/Koordinatsionnaya Khimiya*. 2021;47(3): 219–224. doi: 10.1134/S1070328421030027
- Narmani A., Farhood B., Haghi-Aminjan H., ... Abbasi H. Gadolinium nanoparticles as diagnostic and therapeutic agents: Their delivery systems in magnetic resonance imaging and neutron capture therapy. *Journal of Drug Delivery Science and Technology*. 2018;44: 457–466. <https://doi.org/10.1016/j.jddst.2018.01.011>
- Goryachko A. I., Ivanin S. N., Buz'ko V. Yu. Synthesis, microstructural and electromagnetic characteristics of cobalt-zinc ferrite. *Condensed Matter and Interphases*. 2020;22(4): 446–452. <https://doi.org/10.17308/kcmf.2020.22/3115>
- Bhingardive V., Woldu T., Biswas S., ... Bose S. Microwave absorption in MWNTs-based soft composites containing nanocrystalline particles as magnetic core and intrinsically conducting polymer as a conductive layer. *Chemistry Select*. 2016;1: 4747–4752. <https://doi.org/10.1002/slct.201601056>
- Lai T., Qin W., Cao C., Zhong R., Ling Y., Xie Y. Preparation of a microwave-absorbing UV coating using a BaFe₁₂O₁₉-polypyrrole nanocomposite filler. *Polymers*. 2023;15(8): 1839. <https://doi.org/10.3390/polym15081839>
- Buzko V., Babushkin M., Ivanin S., Goryachko A., Petriev I. Study of electromagnetic shielding properties of composites based on glass fiber metallized with metal films. *Coatings*. 2022;12(8): 1173. <https://doi.org/10.3390/coatings12081173>
- Ehrmann G., Blachowicz T., Ehrmann A. Magnetic 3D-printed composites—production and applications. *Polymers*. 2022;14(18): 3895. <https://doi.org/10.3390/polym14183895>
- Buzko V., Ivanin S., Goryachko A., Shutkin I., Pushankina P., Petriev I. Magnesium spinel ferrites development for FDM 3D-printing material for microwave absorption. *Processes*. 2023;11: 60. <https://doi.org/10.3390/pr11010060>
- Haiduk Yu. S., Korobko E. V., Shevtsova K. A., ... Pankov V. V. Synthesis, structure, and magnetic properties of cobalt-zinc nanoferrite for magnetorheological liquids. *Condensed Matter and Interphases*. 2020;22(2): 28–38. <https://doi.org/10.17308/kcmf.2020.22/2526>
- Vaseem M., Ghaffar F. A., Farroqui M. F., Shamim A. Iron oxide nanoparticle-based magnetic ink development for fully printed tunable radio-

frequency devices. *Advanced Materials Technologies*. 2018;3: 1700242. <https://doi.org/10.1002/admt.201700242>

19. Korsakova A. S., Kotsikau D. A., Haiduk Yu. S., Pankov V. V. Synthesis and physicochemical properties of $Mn_xFe_{3-x}O_4$ solid solutions. *Condensed Matter and Interphases*. 2020;22(4): 466–472. <https://doi.org/10.17308/kcmf.2020.22/3076>

20. Shaou C.-N., Chao C.-G., Wu T. M., Shy H.-J. Magnetic and optical properties of isolated magnetite nanocrystals. *Materials Transactions*. 2007;48(5): 1143–1148. <https://doi.org/10.2320/matertrans.48.1143>

21. Urbanova V., Magro M., Gedanken A., Baratella D., Vianello F., Zboril R. Nanocrystalline iron oxides, composites and related materials as a platform for electrochemical, magnetic, and chemical biosensors. *Chemistry of Materials*. 2014;26(23): 6653–6673. <https://doi.org/10.1021/cm500364x>

22. Liu M., Ye Y., Ye J., ... Song Z. Recent advances of magnetite (Fe_3O_4)-based magnetic materials in catalytic applications. *Magnetochemistry*. 2023;9(4): 110. <https://doi.org/10.3390/magnetochemistry9040110>

23. Goryachko A. I., Ivanin S. N., Buz'ko V. Y. Study of electrodynamic parameters of composite materials based on natural Fe_3O_4 . *Journal of Radio Electronics*. 2020;7. <https://doi.org/10.30898/1684-1719.2020.7.4>

24. Tanaka K., Ishii J., Katayama T. Influence of magnetite dispersion on tensile properties of magnetite/PLA nanofiber nonwoven fabrics. *Key Engineering Materials*. 2019;827: 190–195. <https://doi.org/10.4028/www.scientific.net/KEM.827.190>

25. Chowdhury T., D'Souza N., Berman D. Electrospun Fe_3O_4 -PVDF nanofiber composite mats for cryogenic magnetic sensor applications. *Textiles*. 2021;1: 227–238. <https://doi.org/10.3390/textiles1020011>

26. Mamun A., Klöcker M., Blachowicz T., Sabantina L. Investigation of the morphological structure of needle-free electrospun magnetic nanofiber mats. *Magnetochemistry*. 2022;8(2): 25. <https://doi.org/10.3390/magnetochemistry8020025>

27. Mansurov Z. A., Smagulova G. T., Kaidar B. B., Lesbayev A. B., Imash A. Production of fibers based on polyacrylonitrile with magnetite nanoparticles. *Powder Metallurgy and Functional Coatings*. 2021;15(4): 68–76. (In Russ.). <https://doi.org/10.17073/1997-308x-2021-4-68-76>

28. Kildisheva V. A., Velikanov I. S., Andreev A. A. Synthesis of composite structures with magnetite nanoparticles included in calcium carbonate microparticles. *Trends in the development of science and education*. 2021;72(2): 155–158. (In Russ.). <https://doi.org/10.18411/lj-04-2021-80>

29. Teng Y., Li Yu., Li Y., Song Q. Preparation of Fe_3O_4 /PVP magnetic nanofibers via in situ method with electrospinning. *Journal of Physics: Conference Series*. 2020;1549: 032087. <https://doi.org/10.1088/1742-6596/1549/3/032087>

30. Gu H., Huang Y., Zhang X., ... Guo Z. Magnetoresistive polyaniline-magnetite nanocomposites with negative dielectrical properties. *Polymer*. 2012;53: 801–809. <https://doi.org/10.1016/j.polymer.2011.12.033>

31. Guo J., Gu H., Wei H., ... Guo Z. Magnetite-polypyrrole metacomposites: Dielectric properties and magnetoresistance behavior. *The Journal of Physical Chemistry C*. 2013;117: 10191–10202. <https://doi.org/10.1021/jp402236n>

32. Tahmasebipour M., Paknahad A. A. Unidirectional and bidirectional valveless electromagnetic micropump with PDMS- Fe_3O_4 nanocomposite magnetic membrane. *Journal of Micromechanics and Microengineering*. 2019;29(7): 075014. <https://doi.org/10.1088/1361-6439/ab1dbe>

33. Chiscan O., Dumitru I., Postolache P., Tura V., Stancu A. Electrospun PVC/ Fe_3O_4 composite nanofibers for microwave absorption applications. *Materials Letters*. 2012;68: 251–254. <https://doi.org/10.1016/j.matlet.2011.10.084>

34. Zhang T., Huang D., Yang Y., Kang F., Gu J. Fe_3O_4 /carbon composite nanofiber absorber with enhanced microwave absorption performance. *Materials Science and Engineering: B*. 2013. 178(1): 1–9. <https://doi.org/10.1016/j.mseb.2012.06.005>

35. Samadi A., Hosseini S. M., Mohseni M. Investigation of the electromagnetic microwaves absorption and piezoelectric properties of electrospun Fe_3O_4 -GO/PVDF hybrid nanocomposites. *Organic Electronics*. 2018;59: 149–155. <https://doi.org/10.1016/j.orgel.2018.04.037>

36. Petriev I., Pushankina P., Shostak N., Baryshev M. Gas-transport characteristics of PdCu-Nb-PdCu membranes modified with nanostructured palladium coating. *International Journal of Molecular Science*. 2022;23(1): 228. <https://doi.org/10.3390/ijms23010228>

37. Petriev I. S., Pushankina P. D., Lutsenko I. S., Baryshev M. G. Anomalous kinetic characteristics of hydrogen transport through Pd–Cu membranes modified by pentatwinned flower-shaped palladium nanocrystallites with high-index facets. *Technical Physics Letters*. 2021;47(11): 803–806. <https://doi.org/10.1134/s1063785021080216>

38. Martínez-Mera I., Espinosa-Pesqueira M. E., Pérez-Hernández R., Arenas-Alatorre J. Synthesis of magnetite (Fe_3O_4) nanoparticles without surfactants at room temperature. *Materials Letters*. 2007;61: 4447–4451. <https://doi.org/10.1016/j.matlet.2007.02.018>

39. Zhao Y., Qiu Z., Huang J. Preparation and analysis of Fe_3O_4 magnetic nanoparticles used as targeted-drug carriers. *Chinese Journal of Chemical Engineering*. 2008;16(3): 451–455. [https://doi.org/10.1016/s1004-9541\(08\)60104-4](https://doi.org/10.1016/s1004-9541(08)60104-4)
40. Wang P., Shi T., Mehta N., ... Zhu Z. Changes in magnetic properties of magnetite nanoparticles upon microbial iron reduction. *Geochemistry, Geophysics, Geosystems*. 2022;23(3): e2021GC010212. <https://doi.org/10.1029/2021GC010212>
41. He H., Zhong Y., Liang X., Tan W., Zhu J., Wang C. Y. Natural magnetite: an efficient catalyst for the degradation of organic contaminant. *Scientific Reports*. 2015;5: 10139. <https://doi.org/10.1038/srep10139>
42. Fischer A., Schmitz M., Aichmayer B., Fratzl P., Faivre D. Structural purity of magnetite nanoparticles in magnetotactic bacteria. *Journal of the Royal Society Interface*. 2011;8(60): 1011–1018. <https://doi.org/10.1098/rsif.2010.0576>
43. Blaney L. Functionalized magnetite nanoparticles—synthesis, properties, and bio-applications. *The Lehigh Review*. 2007;15: 32–81. <https://doi.org/10.1080/10408430701776680>
44. Wu S., Sun A., Zhai F., ... Volinsky A. A. Fe_3O_4 magnetic nanoparticles synthesis from tailings by ultrasonic chemical co-precipitation. *Materials Letters*. 2011;65: 1882–1884. <https://doi.org/10.1016/j.matlet.2011.03.065>
45. Beaudoin É. J., Kubaski M. M., Samara M., Zednik R. J., Demarquette N. R. Scaled-up multi-needle electrospinning process using parallel plate auxiliary electrodes. *Nanomaterials*. 2022;12(8): 1356. <https://doi.org/10.3390/nano12081356>
46. Partheniadis I., Nikolakakis I., Laidmäe I., Heinämäki J. A Mini-review: Needleless electrospinning of nanofibers for pharmaceutical and biomedical applications. *Processes*. 2020;8(6): 673. <https://doi.org/10.3390/pr8060673>
47. Wang X., Niu H., Lin T., Wang X. Needleless electrospinning of nanofibers with a conical wire coil. *Polymer Engineering and Science*. 2009;49: 1582–1586. <https://doi.org/10.1002/pen.21377>
48. Thoppey N. M., Bochinski J. R., Clarke L. I., Gorga R. E. Unconfined fluid electrospun into high quality nanofibers from a plate edge. *Polymer*. 2010;51: 4928–4936. <https://doi.org/10.1016/j.polymer.2010.07.046>
49. Wu D., Huang X., Lai X., Sun D., Lin L. High throughput tip-less electrospinning via a circular cylindrical electrode. *Journal of Nanoscience and Nanotechnology*. 2010;10: 4221–4226. <https://doi.org/10.1166/jnn.2010.2194>
50. Ahmad A., Ali U., Nazir A., ... Abid S. Toothed wheel needleless electrospinning: A versatile way to fabricate uniform and finer nanomembrane. *Journal of Materials Science*. 2019;54: 13834–13847. <https://doi.org/10.1007/s10853-019-03875-0>
51. Kara Y., He H., Molnár K. Shear-aided high-throughput electrospinning: A needleless method with enhanced jet formation. *Journal of Applied Polymer Science*. 2020;137: e49104. <https://doi.org/10.1002/app.49104>
52. Chiscan O., Dumitru I., Postolache P., Tura V., Stancu A. Electrospun PVC/ Fe_3O_4 composite nanofibers for microwave absorption applications. *Materials Letters*. 2012;68: 251–254. <https://doi.org/10.1016/j.matlet.2011.10.084>
53. Mashuri X., Lestari W., Triwikantoro X., Darminto X. Preparation and microwave absorbing properties in the X-band of natural ferrites from iron sands by high energy milling. *Materials Research Express*. 2018;5(1): 014003. <https://doi.org/10.1088/2053-1591/aa68b4>
54. Liu X., Cao K., Chen Y., ... Peng D. L. Shape-dependent magnetic and microwave absorption properties of iron oxide nanocrystals. *Materials Chemistry and Physics*. 2017;192: 339–348. <https://doi.org/10.1016/j.matchemphys.2017.02.012>
55. Zhang B., Du Y., Zhang P., ... Xu P. Microwave absorption enhancement of Fe_3O_4 /polyaniline core/shell hybrid microspheres with controlled shell thickness. *Journal of Applied Polymer Science*. 2013;130(30): 1909–1916. <https://doi.org/10.1002/app.39332>
56. Tong G., Wu W., Guan J., Qian H., Yuan J., Li W. Synthesis and characterization of nanosized urchin-like $\alpha\text{-Fe}_2\text{O}_3$ and Fe_3O_4 : Microwave electromagnetic and absorbing properties. *Journal of Alloys and Compounds*. 2011; 509: 4320–4326. <https://doi.org/10.1016/j.jallcom.2011.01.058>
57. Kolev S., Yanev A., Nedkov I. Microwave absorption of ferrite powders in a polymer matrix. *Physica Status Solidi c*. 2006;3(5): 1308–1315. <https://doi.org/10.1002/pssc.200563116>
58. Ni S., Sun X., Wang X., ... He D. Low temperature synthesis of Fe_3O_4 micro-spheres and its microwave absorption properties. *Materials Chemistry and Physics*. 2010;124: 353–358. <https://doi.org/10.1016/j.matchemphys.2010.06.046>

Information about the authors

Roman P. Yakupov, graduate student of the Department of General, Inorganic Chemistry and IVT in Chemistry, Kuban State University (Krasnodar, Russian Federation).

<https://orcid.org/0000-0002-8872-1640>
yakupov@sfedu.ru

Vladimir Yu. Buzko, Cand. Sci. (Chem.), Associate Professor, Department of Radiophysics and Nanotechnology, Kuban State University, Kuban State Agrarian University named after I. T. Trubilin (Krasnodar, Russian Federation).

<https://orcid.org/0000-0002-6335-0230>
Buzkonmr@mail.ru

Sergey N. Ivanin, Cand. Sci. (Chem.), Lecturer at the Department of Radiophysics and Nanotechnology, Kuban State University, Kuban State Agrarian University named after I. T. Trubilin (Krasnodar, Russian Federation).

<https://orcid.org/0000-0001-9352-5970>
Ivanin18071993@mail.ru

Marina V. Papezhuk, Lecturer at the Department of General, Inorganic chemistry and IVT in Chemistry, Kuban State University (Krasnodar, Russian Federation).

<https://orcid.org/0000-0001-8187-9819>
marina-marina322@mail.ru

Received 25.01.2024; approved after reviewing 19.03.2024; accepted for publication 15.04.2024; published online 01.10.2024.

Translated by Valentina Mittova



Original articles

Research article

<https://doi.org/10.17308/kcmf.2024.26/12304>**XPS investigations of thin epitaxial and magnetron tin layers surface physico-chemical state**O. A. Chuvenkova¹, N. I. Boikov¹, S. V. Ryabtsev¹, E. V. Parinova¹, R. G. Chumakov²,
A. M. Lebedev², D. Smirnov³, A. Makarova⁴, S. S. Titova¹, K. A. Fateev¹, S. Yu. Turishchev¹✉¹Voronezh State University,
1 Universitetskaya pl., Voronezh 394018, Russian Federation²National Research Center «Kurchatov Institute»,
1 Akademika Kurchatova pl., Moscow 123182, Russian Federation³Free University of Berlin,
Arnimallee 22, Berlin 14195, Germany⁴Dresden University of Technology,
Zellescher Weg 18, Dresden 01069, Germany**Abstract**

Thin layers of the tin-oxygen system with nanometer thicknesses and structures based on them are relevant objects of development for use in modern devices, for example in microelectronics. The general miniaturization of electronic devices, the achievement of energy efficiency in the operation of such devices, and the optimal modes of their operation determine the strategies for using the tin-oxygen system structures. First of all, the justification of the tin-oxygen system nanolayers formation technique. The dependence of the formed nanolayers properties on the state of their surface is significant.

The article contains the results of direct experimental studies of the composition and physico-chemical state of the tin-oxygen system thin nanolayers surface. To form the studied structures, the popular and in-demand methods of magnetron sputtering and molecular beam epitaxy were used. The X-ray photoelectron spectroscopy was applied with the use of the synchrotron radiation which has a high intensity and the possibility of spectrum excitation energy optimal selection, which is important for a small amount of the studied material. After formation, the research objects were stored in laboratory conditions for several weeks before synchrotron studies.

Differences in the surface composition and physico-chemical state of the thin tin layers formed by magnetron sputtering or epitaxially, and then oxidized naturally, are shown. Five monolayers of tin formed by the molecular beam epitaxy make it possible to diffuse atmospheric oxygen, which oxidizes the Si buffer layer located under the Sn nanolayer on a silicon substrate. At the same time, the surface of the tin film obtained by magnetron sputtering is close to the natural oxide SnO_{2-x} in its physico-chemical state.

The results of the work can be useful for determining the optimal approaches to the formation and subsequent modification of thin and ultrathin layers of tin oxides for the tasks of creating active layers of modern electronic devices.

Keywords: Tin and its oxides, Physico-chemical state, Composition, Epitaxial nanolayers, Magnetron nanolayers, X-ray photoelectron spectroscopy, Synchrotron studies

Funding: The study was supported by Russian Science Foundation (Project 23-22-00465).

For citation: Chuvenkova O. A., Boikov N. I., Ryabtsev S. V., Parinova E. V., Chumakov R. G., Lebedev A. M., Smirnov D., Makarova A., Titova S. S., Fateev K. A., Turishchev S. Yu. XPS investigations of thin epitaxial and magnetron tin layers surface physico-chemical state. *Condensed Matter and Interphases*. 2024;26(3): 558–564. <https://doi.org/10.17308/kcmf.2024.26/12304>

✉ Sergey Yu. Turishchev, e-mail: tsu@phys.vsu.ru

© Chuvenkova O. A., Boikov N. I., Ryabtsev S. V., Parinova E. V., Chumakov R. G., Lebedev A. M., Smirnov D., Makarova A., Titova S. S., Fateev K. A., Turishchev S. Yu., 2024



The content is available under Creative Commons Attribution 4.0 License.

Для цитирования: Чувенкова О. А., Бойков Н. И., Рябцев С. В., Паринаева Е. В., Чумаков Р. Г., Лебедев А. М., Смирнов Д., Макарова А., Титова С. С., Фатеев К. А., Турищев С. Ю. XPS исследования физико-химического состояния поверхности тонких эпитаксиальных и магнетронных слоев олова. *Конденсированные среды и межфазные границы*. 2024;26(3): 558–564. <https://doi.org/10.17308/kcmf.2024.26/12304>

1. Introduction

Nanostructures of the tin-oxygen system attract wide interest of researchers and are used to solve various modern problems of science, engineering and technology [1–3]. Tin oxide SnO_2 is actively used in microelectronics, for example, to create structures of resistive gas sensors [4–6] and a number of other devices. Planar layered tin oxide structures including ones characterized by nanometer thicknesses are an important class of objects with high manufacturability realization of them together with relative simplicity of their creation [7–9]. By varying the formation and processing techniques, it is possible to control the morphology, composition, structure, physico-chemical state as a whole and, as a result, the properties of the structures being formed, obtaining optimal sizes, energy consumption of devices based on them, response speed and other functional characteristics. The molecular beam epitaxy makes it possible to obtain ordered layers of tin of minimal thickness (up to few nanometers) that may have a set of unique characteristics with variations in their composition e.g. after certain subsequent modification. The use of layered epitaxial heterostructures of tin and silicon for thermoelectrics may be promising [10]. At the same time, the magnetron sputtering is a common formation approach of the tin-oxygen system thin layered structures [11]. This technique allows significant variations of the composition and structure of the formed and modified tin layers in combination with simplicity and flexibility in managing the formation regimes. It is obvious that the properties of thin tin-oxygen layers will be significantly influenced by the composition of the surface and interface boundaries, largely determining the properties of structures based on them. Therefore, the use of direct experimental techniques for studying the composition-sensitive, surface physico-chemical state of thin layers is extremely important. Such techniques include X-ray photoelectron spectroscopy (XPS). XPS allows us to obtain high-precision experimental data on the charge state of atoms that make up several nanometers of the object

under study surface without destruction, and to study the phase composition. The use of high-intensity synchrotron radiation makes it possible to select the quantum energy for excitation of the photoelectron spectrum. This makes the XPS technique an accurate universal tool for studying the physico-chemical state of the surface even with a small amount of matter, which is typical for layers of nanoscale thickness, including the tin-oxygen system [12–15]. This paper presents the results of XPS studies using synchrotron radiation on the physico-chemical state of the surface of thin epitaxial and magnetron layers of tin formed on crystalline silicon substrates.

2. Experimental

The molecular beam epitaxy was used to obtain tin nanolayers on a 50 nm thick Si buffer layer grown on a Si (001) substrate [10]. We will call these samples «Epitaxy Sn/Si». The substrates prepared after cleaning and drying were moved to an ultrahigh vacuum chamber. After desorption of thermal oxide at a temperature of 840 °C, 5 monolayers of tin atoms (~ 1.6 nm) from an effusion cell were grown (deposited) on the formed 50 nm thick silicon buffer layer. After formation, the samples were kept in the laboratory for several weeks before synchrotron studies. The control by atomic force microscopy showed the continuity and uniformity of the formed tin layer.

Magnetron sputtering was used to form 30 nm thickness tin layers on silicon substrate. We will call these samples «Magnetron Sn/Si». Sputtering of a tin target with a purity of 99.999% was carried out in a direct current argon plasma. Prepared and cleaned Si (100) substrates were used. The argon pressure in the working chamber was 10^{-3} Torr, the discharge current was 60 mA, the voltage was 360 V. The film thickness was determined by the deposition time. The morphology was controlled by scanning electron microscopy. Solid uniform granular nanolayers with granule sizes comparable to the layer thickness have been formed. The «Magnetron Sn/Si» samples

were also stored in the laboratory for several weeks before measuring the photoelectron spectra.

Investigations of the samples surface physico-chemical state were carried out using the non-destructive XPS technique. The XPS is based on the kinetic energies spectrum analysis for photoelectrons emitted by atoms under the irradiation of X-rays (synchrotron) radiation and allows determining the binding energies of electrons levels excited by radiation [e.g. 12, 16]. The high-intensity radiation of the ultra-soft X-ray range of BESSY-II synchrotron, the Russian-German beamline (Helmholtz - Zentrum-Berlin, Berlin, Germany) [17] and KISI-Kurchatov synchrotron, the NANOPES beamline (National Research Center «Kurchatov Institute», Moscow, Russia) [18] were used. The photon flux was 10^9 – 10^{11} photons/s, the storage ring current was 50–300 mA. The depth of the analyzed surface layer [12] and the instrumental broadening were ~2 nm and 0.1 eV, respectively. The photon energies of synchrotron radiation of 800 eV were used, which corresponded to the

maximum intensity of synchrotron radiation of both beamlines. The vacuum in the experimental chambers was $\sim 10^{-10}$ Torr. Calibration and normalization of the spectra were carried out using a pure gold film based on the position of the core 4f gold level and the Fermi level under the same registration conditions as for the studied samples. Additionally, the position of the core levels was also controlled by C1s level of carbon-containing contaminants on the surface of the samples, reduced to a value of 285.0 eV according to [16]. To ensure charge drain during spectra registration, standard sample mounting on Omicron flag type holders was used.

3. Results and discussion

Fig. 1 shows the survey XPS spectra of the studied samples with epitaxial (Epitaxy Sn/Si) and magnetron (Magnetron Sn/Si) tin layers. The spectrum of the sample obtained by magnetron sputtering of tin (Magnetron Sn/Si) shows intense lines of oxygen O 1s, tin Sn $3d_{3/2,5/2}$, Sn 4d, carbon C 1s, and Auger $M_{5,4}N_{4,5}N_{4,5}$ and $M_{4,4}N_{4,5}N_{4,5}$ lines [14, 16, 19]. The C 1s line is clearly defined,

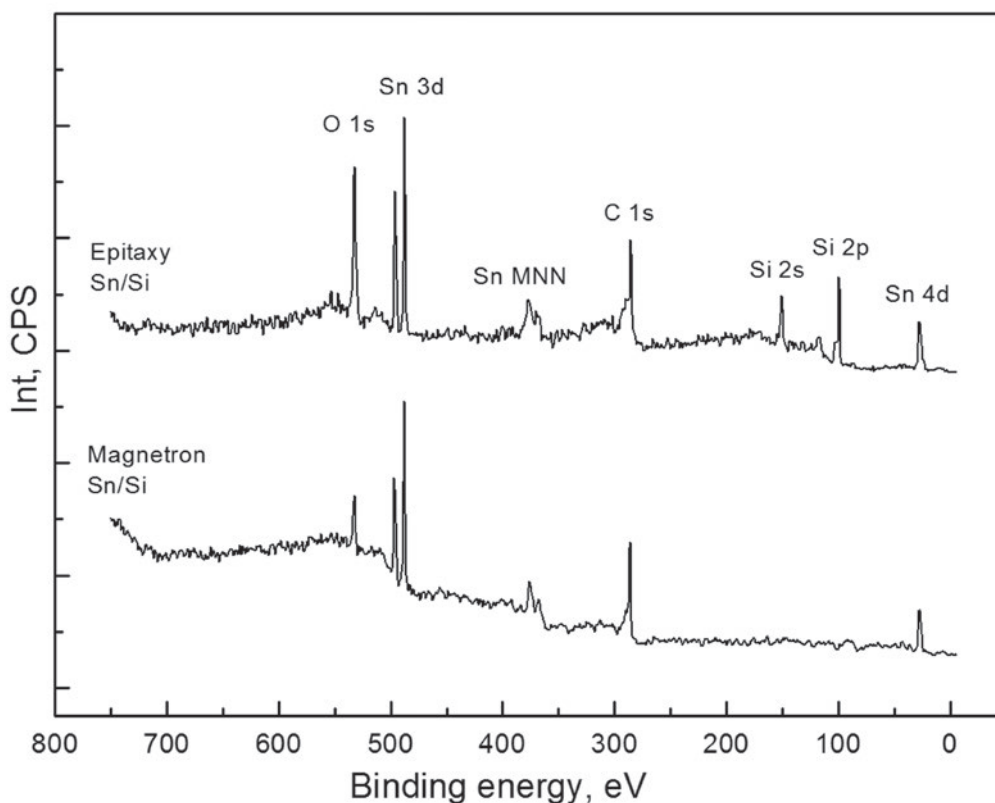


Fig. 1. Survey XPS spectra of the studied samples of epitaxial (Epitaxy Sn/Si) and magnetron (Magnetron Sn/Si) tin layers

which indicates a sufficient carbon-containing contaminants amount formed on the surface as a result of samples storage in the laboratory conditions. In the spectrum of the sample obtained by molecular beam epitaxy (Epitaxy Sn/Si), in addition to the above, silicon lines $Si\ 2p_{1/2,3/2}$, $Si\ 2s$ are observed. The observation of the lines related to the silicon buffer layer is the result of the small thickness of the formed layer of epitaxial tin. This means that the tin-silicon layer interface is available for study. At the same time, the oxygen line $O\ 1s$ in its intensity is noticeably higher than that in the «Magnetron Sn/Si» sample. The intensity of this line, in our opinion, consists of a signal from the naturally oxidized upper epitaxial Sn layer, as well as from oxygen atoms bound to the surface of the silicon buffer layer. This observation, in our opinion, is the result of atmospheric oxygen diffusion through the epitaxial tin layer to its interface with the more electronegative silicon of the buffer layer. The $C\ 1s$ carbon line is also quite intense, which may indicate the presence of a sufficiently large amount of carbon on the surface of this sample in the form of carbon-containing contaminants.

For a detailed analysis of the physico-chemical state of the surfaces and interfaces of the studied samples, the spectra of the main core lines of tin and oxygen were taken with high resolution. Fig. 2 shows the XPS spectra of tin $Sn\ 3d_{5/2}$ of the reference sample of tin dioxide SnO_2 [15], epitaxial «Epitaxy Sn/Si» and magnetron «Magnetron Sn/Si» in the binding energy range 483 – 491 eV. It can be seen that the $Sn\ 3d_{5/2}$ line of the sample obtained by magnetron sputtering is single-component, with a binding energy of 486.7 eV, which is slightly lower than the binding energy of this line for the reference tin dioxide SnO_2 , which is 487.2 eV [14–16]. This value of the binding energy of tin atoms indicates a relatively incomplete oxidation of the surface of the «Magnetron Sn/Si» sample to SnO_2 and corresponds to the binding energy value for the intermediate oxide SnO_{2-x} previously shown in [15, 20, 21], e.g. for the surface of a metal foil. In the spectrum of the «Epitaxy Sn/Si» sample obtained by molecular beam epitaxy, two components are observed at binding energies of 487.5 eV and 486.0 eV, respectively (Fig. 2). The high-energy component shows a binding energy value close

to the SnO_2 reference sample. The low-energy component of low intensity corresponds to the binding energy of tin atoms in SnO monoxide, specified in [20]. Thus, the surface of the studied «Magnetron Sn/Si» tin layers with a thickness of 30 nm is single-phase and is characterized by an intermediate «surface» tin oxide SnO_{2-x} . The formation of such an oxide occurs with a sufficient number of tin atoms in a layer available for natural

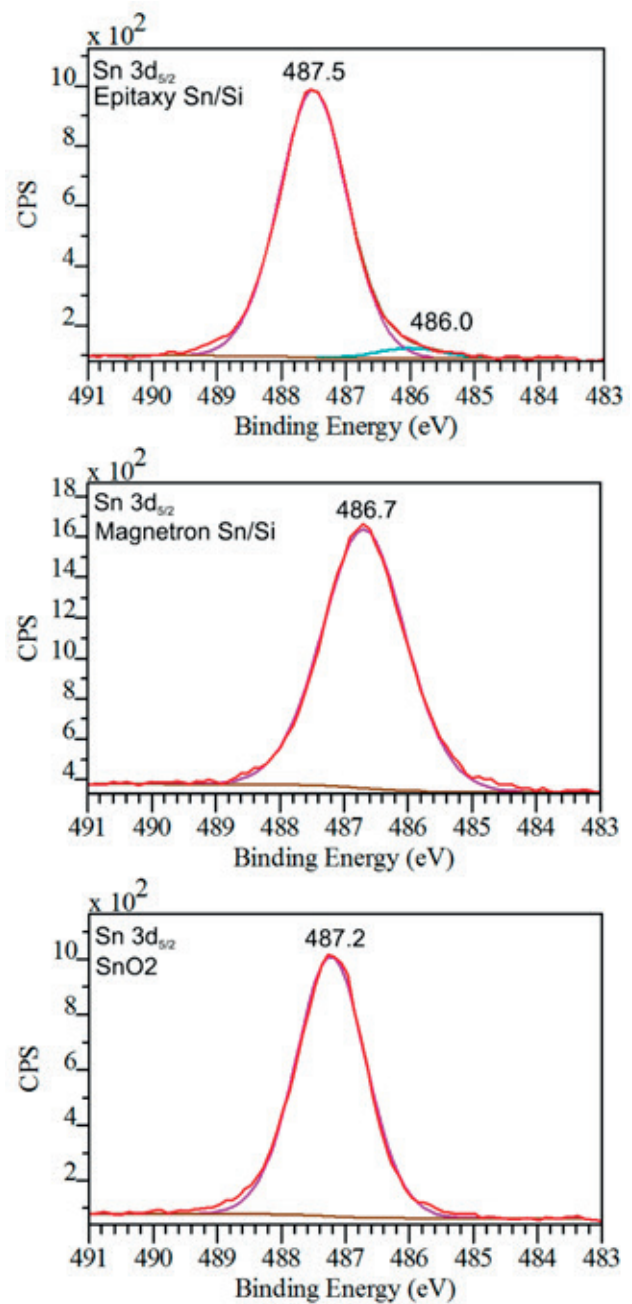


Fig. 2. XPS spectra of $Sn\ 3d_{5/2}$ of the reference SnO_2 and the studied samples of epitaxial (Epitaxy Sn/Si) and magnetron (Magnetron Sn/Si) tin layers

oxidation during storage in the laboratory. The thickness of the epitaxial layer of tin is extremely small, moreover, there is a surface of more electronegative buffer silicon under it. In the process of interaction with atmospheric oxygen, during storage in laboratory conditions, complete oxidation of tin atoms of the entire epitaxial layer occurs, with the formation of a thin transition layer of SnO. In our opinion, this layer borders on a buffer layer of silicon, which is also oxidized as a result of atmospheric oxygen diffusion, as was suggested above when considering the intensities of the tin and oxygen core level lines of the survey spectrum. The mutual oxidation of the tin and silicon epitaxial layers interface occurs before the equilibrium state is established, keeping the thin transition layer of tin in the SnO state. A detailed study of the fine structure of high-resolution photoelectron spectra of 2p silicon states seems to us to be a priority task in further studying the epitaxial structures of tin-silicon.

Fig. 3 shows the XPS O 1s spectra of the reference SnO₂ and the studied samples of epitaxial «Epitaxy Sn/Si» and magnetron «Magnetron Sn/Si» tin layers. The spectrum of the «Magnetron Sn/Si» sample has two components with a binding energy of 530.5 eV and a binding energy of 532.1 eV, which correspond to oxygen atoms in the surface oxide SnO_{2-x} [15, 20, 21] and various types of atmospheric oxygen compounds adsorbed by the surface [see for example 14–16]. In a sample with an epitaxial tin nanolayer, 3 components are observed in the O 1s spectrum at energies 531.5, 532.6 and 533.3 eV. The states of oxygen atoms with the binding energy of 531.5 are close to SnO₂ dioxide (Fig. 3). A slight increase in the binding energy of the states of oxygen atoms (as well as tin atoms, see above) may be due to the influence of an additional surface charge forming by the layered structure of the sample during its phase transformations as a result of natural oxidation [12]. The components of the O 1s spectrum with binding energies of 533.3 and 532.6 eV are connected, in our opinion to various types of atmospheric oxygen compounds adsorbed by the surface [see for example 14–16] and are observed in the spectrum of the reference SnO₂ (Fig. 3). However, the peak at 532.6 eV has a significantly higher intensity compared to the SnO₂ standard, which is associated with the

binding energies of silicon oxide, having a close value. This confirms the above assumption about the oxidation of the silicon buffer layer located under the epitaxial layer of tin. Finally, the fact that we do not observe a state in the O1s spectrum of the «Magnetron Sn/Si» sample with the binding energy of ~ 533.3 eV indicates somewhat different storage conditions for this sample.

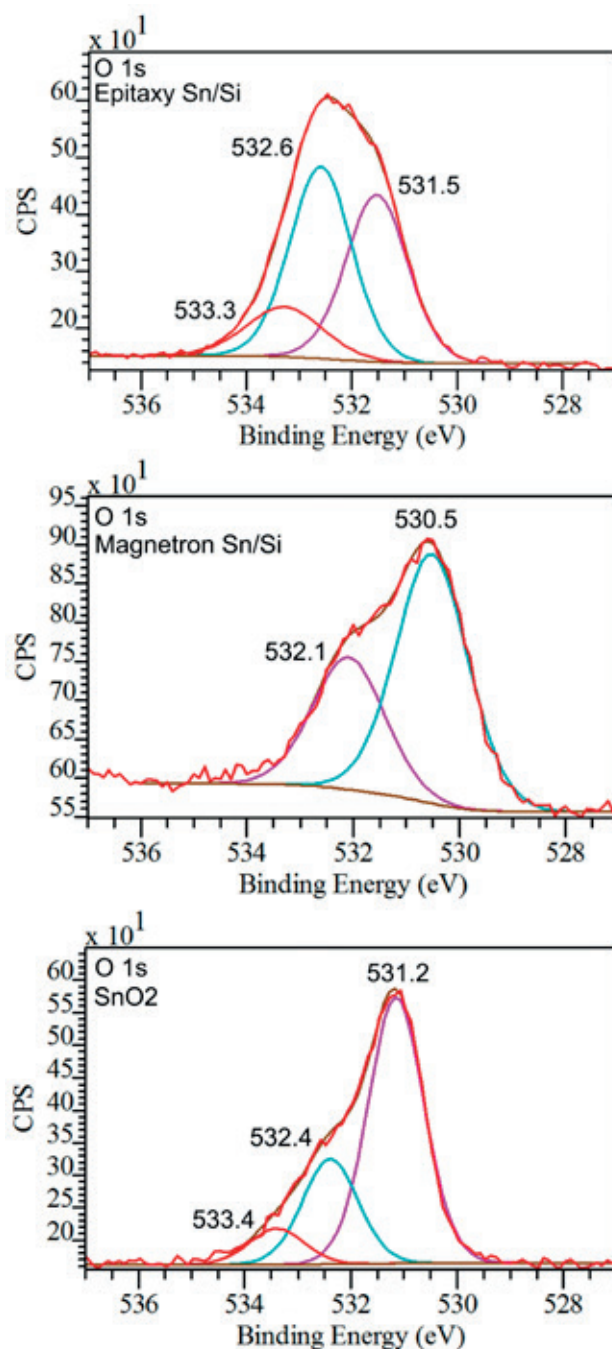


Fig. 3. XPS spectra of O 1s of the reference SnO₂ and the studied samples of epitaxial (Epitaxy Sn/Si) and magnetron (Magnetron Sn/Si) tin layers

4. Conclusions

The physico-chemical state of the thin tin layers surface obtained by magnetron sputtering and molecular beam epitaxy after storage in laboratory conditions is studied. There is a general agreement of data on the analysis of synchrotron photoelectron spectra, including high-resolution data for the Sn $3d_{5/2}$ and O 1s lines. The differences in the composition of the studied structures surface layers are shown. When using the magnetron sputtering to form a 30 nm Sn layer with subsequent storage in laboratory conditions, a single-phase surface of natural tin oxide SnO_{2-x} is formed. The tin layer formed by the molecular beam epitaxy after storage of the same duration in laboratory conditions is completely oxidized to SnO_2 . The surface of the silicon buffer layer is oxidized by atmospheric oxygen atoms as a result of their diffusion through the epitaxial layer of tin, while a thin transition layer of SnO is formed. The results obtained can be used in the controlled formation of functional nanolayers of the tin-oxygen system and structures based on them for various tasks, for example, in the creation of modern microelectronic devices.

Contribution of the authors

All authors made an equivalent contribution to the preparation of the publication.

Conflict or interests

The authors declare that they have no known competing financial interests or personal relationships that could have appeared to influence the work reported in this paper.

References

1. Kong Y., Li Y., Cui X., ... Wang Y. SnO_2 nanostructured materials used as gas sensors for the detection of hazardous and flammable gases: A review. *Nano Materials Science*. 2022;4: 339–350. <https://doi.org/10.1016/j.nanoms.2021.05.006>
2. Huang J., Yu K., Gu C., ... Liu J. Preparation of porous flower-shaped SnO_2 nanostructures and their gas-sensing property. *Sensors and Actuators B*. 2010;147: 467–474. <https://doi.org/10.1016/j.snb.2010.03.085>
3. Turishchev S., Schleusener A., Chuvankova O., ... Sivakov V. Spectromicroscopy studies of silicon nanowires array covered by tin oxide layers. *Small*. 2023;19 (10): 22063221-6. <https://doi.org/10.1002/sml.202206322>

4. Wu Q.-H., Li J. Sun S.-G. Nano SnO_2 gas sensors. *Current Nanoscience*. 2010;6: 525–538. <https://doi.org/10.2174/157341310797574934>
5. Vilaseca M., Coronas J., Cirera A., Cornet A., Morante R. J., Santamaria J. Gas detection with SnO_2 sensors modified by zeolite films. *Sensors and Actuators B*. 2007;124: 99–110. <https://doi.org/10.1016/j.snb.2006.12.009>
6. Shaposhnik A. V., Shaposhnik D. A., Turishchev S. Yu., ... Morante J. R. Gas sensing properties of individual SnO_2 nanowires and SnO_2 sol-gel nanocomposites. *Beilstein Journal of Nanotechnology*. 2019;10: 1380–1390. <https://doi.org/10.3762/bjnano.10.136>
7. Gaggiotti G., Galdikas A., KaEiulis S., Mattogno G., Setkus A. Temperature dependencies of sensitivity and surface chemical composition of SnO, gas sensors. *Sensors and Actuators B*. 1995;24-25: 516–519. [https://doi.org/10.1016/0925-4005\(95\)85111-9](https://doi.org/10.1016/0925-4005(95)85111-9)
8. Kwoka M., Ottaviano L., Passacantando M., Santucci S., Czempik G., Szuber J. XPS study of the surface chemistry of L-CVD SnO_2 thin films after oxidation. *Thin Solid Films*. 2005;490: 36 – 42. <https://doi.org/10.1016/j.tsf.2005.04.014>
9. Ryabtsev S. V., Shaposhnik A. V., Lukin A. N., Domashevskaya E. P. Application of semiconductor gas sensors for medical diagnostics. *Sensors and Actuators B: Chemical*. 1999;59 (1): 26–29. [https://doi.org/10.1016/S0925-4005\(99\)00162-8](https://doi.org/10.1016/S0925-4005(99)00162-8)
10. Tonkikh A. A., Zakharov N. D., Eisenschmidt C., Leipner H. S., Werner P. Aperiodic SiSn/Si multilayers for thermoelectric applications. *Journal of Crystal Growth*. 2014;392: 49–51. <http://doi.org/10.1016/j.jcrysgro.2014.01.047>
11. Gangwar A. K., Godiwal R., Jaiswal J., ... Singh P. Magnetron configurations dependent surface properties of SnO_2 thin films deposited by sputtering process. *Vacuum*. 2020;177: 109353-1-9. <https://doi.org/10.1016/j.vacuum.2020.109353>
12. Hufner S. (ed.) Very high resolution photoelectron spectroscopy. In: *Lecture Notes in Physics*. Springer Berlin Heidelberg; 2007. 397 p. <https://doi.org/10.1007/3-540-68133-7>
13. Jimenez V. M., Mejias J. A., Espinos J. P., Gonzalez-Elipe A. R. Interface effects for metal oxide thin films deposited on another metal oxide II. SnO_2 deposited on SiO_2 . *Surface Science*. 1996;366: 545-555. [https://doi.org/10.1016/0039-6028\(96\)00831-x](https://doi.org/10.1016/0039-6028(96)00831-x)
14. Domashevskaya E. P., Chuvankova O. A., Ryabtsev S. V., ... Turishchev S. Yu. Electronic structure of undoped and doped SnO_x nanolayers. *Thin Solid Films*. 2013;537(30): 137–144. <https://doi.org/10.1016/j.tsf.2013.03.051>
15. Chuvankova O. A., Domashevskaya E. P., Ryabtsev S. V., ... Turishchev S. Yu. XANES and XPS investigations of surface defects in wire like SnO_2 crys-

tals. *Physics of the Solid State*. 2015;57(1): 153–161. <https://doi.org/10.1134/s1063783415010072>

16. Crist B. V. *XPS International Inc., 1999. V. 1.* Режим доступа: www.xpsdata.com

17. Fedoseenko S. I., Iossifov I. E., Gorovikov S. A., ... Kaindl G. Development and present status of the Russian–German soft X-ray beamline at BESSY II. *Nuclear Instruments and Methods in Physics Research Section A: Accelerators, Spectrometers, Detectors and Associated Equipment*. 2001;470: 84–88. [https://doi.org/10.1016/S0168-9002\(01\)01032-4](https://doi.org/10.1016/S0168-9002(01)01032-4)

18. Lebedev A. M., Menshikov K. A., Nazin V. G., Stankevich V. G., Tsetlin M. B., Chumakov R. G. Nano PES photoelectron beamline of the Kurchatov Synchrotron Radiation Source. *Journal of Surface Investigation: X-ray, Synchrotron and Neutron Techniques*. 2021;15: 1039–1044. <https://doi.org/10.1134/S1027451021050335>

19. Davis L. E., MacDonald N. C., Palmberg P. W., Riach G. E., Weber R. E. *Handbook of Auger electron spectroscopy. Second Edition*. Physical Electronics Industries, Inc; 1976.

20. Chuvenkova O. A., Domashevskaya E. P., Ryabtsev S. V., ... Turishchev S. Yu. Photoelectron spectroscopy study of commercial metal tin foil SnO and SnO₂ oxides in two energy ranges of synchrotron radiation. *Condensed Matter and Interfaces*. 2014;16(4): 513–522. (In Russ., abstract in Eng.). Available at: http://www.kcmf.vsu.ru/resources/t_16_4_2014_015.pdf

21. Turishchev S. Yu., Chuvenkova O. A., Parinova E. V., ... Sivakov V. XPS investigations of MOCVD tin oxide thin layers on Si nanowires array. *Results in Physics*. 2018;11: 507–509. <https://doi.org/10.1016/j.rinp.2018.09.046>

Information about the authors

Olga A. Chuvenkova, Cand. Sci. (Phys.-Math.), Senior Researcher, Joint Scientific and Educational Laboratory «Atomic and Electronic Structure of Functional Materials» of Voronezh State University and the National Research Center «Kurchatov Institute», Voronezh State University (Voronezh, Russian Federation).

<https://orcid.org/0000-0001-5701-6909>
chuvnkova@phys.vsu.ru

Nikolai I. Boikov, Engineer-physicist, Joint Scientific and Educational Laboratory «Atomic and Electronic Structure of Functional Materials» of Voronezh State University and the National Research Center «Kurchatov Institute», Voronezh State University (Voronezh, Russian Federation).

<https://orcid.org/0000-0002-0512-8666>
boikov-hfmm@bk.ru

Stanislav V. Ryabtsev, Dr. Sci. (Phys.-Math.), Head of the Institute of physics, Voronezh State University (Voronezh, Russian Federation).

<https://orcid.org/0000-0001-7635-8162>
ryabtsev@phys.vsu.ru

Elena V. Parinova, Cand. Sci. (Phys.-Math.), Assistant Professor, General Physics Department, Voronezh State University (Voronezh, Russian Federation).

<https://orcid.org/0000-0003-2817-3547>
parinova@phys.vsu.ru

Ratibor G. Chumakov, Cand. Sci. (Phys.-Math.), Senior Researcher of the National Research Center «Kurchatov Institute» (Moscow, Russian Federation).

<https://orcid.org/0000-0002-3737-5012>
ratibor.chumakov@gmail.com

Alexei M. Lebedev, Cand. Sci. (Phys.-Math.), Senior Researcher of the National Research Center «Kurchatov Institute» (Moscow, Russian Federation).

<https://orcid.org/0000-0002-4436-6077>
lebedev.alex.m@gmail.com

Dmitry Smirnov, Cand. Sci. (Phys.-Math.), Researcher, Institut für Festkörper- und Materialphysik, Technische Universität Dresden (Dresden, Germany).

anna.makarova@fu-berlin.de

Anna Makarova, Cand. Sci. (Phys.-Math.), Researcher, Institut für Chemie und Biochemie, Freie Universität Berlin (Berlin, Germany).

anna.makarova@fu-berlin.de

Sofiia S. Titova, Teacher of General Physics Department, Voronezh State University, (Voronezh, Russian Federation).

<https://orcid.org/0000-0001-6860-401X>
titova@phys.vsu.ru

Kirill A. Fateev, Laboratory assistant in physics of General Physics Department, Voronezh State University, (Voronezh, Russian Federation).

<https://orcid.org/0009-0005-5352-9594>
fateev@phys.vsu.ru

Sergey Yu. Turishchev, Dr. Sci. (Phys.-Math.), Associate Professor, Head of the General Physics Department, Voronezh State University (Voronezh, Russian Federation).

<https://orcid.org/0000-0003-3320-1979>
tsu@phys.vsu.ru

Received 17.10.2023; approved after reviewing 04.12.2023; accepted for publication 06.12.2023; published online 01.10.2024.

Translated by Sergey Turishchev